Support and promoter effects in automotive exhaust catalysis

Drager- en promotoreffecten in de katalyse van auto-uitlaatgassen

(met een samenvatting in het Nederlands)

Proefschrift

ter verkrijging van de graad van doctor aan de Universiteit Utrecht
op gezag van de rector magnificus, prof.dr. J.C. Stoof,
ingevolge het besluit van het college voor promoties in het openbaar te verdedigen
op maandag 22 juni 2009 des middags te 2.30 uur

door

Muriel Monique Maria Lepage

geboren op 13 mei 1975 te Namen, België

Promotor: Prof. dr. ir. B. M. Weckhuysen

Co-promotor: Dr. T. Visser

Support and promoter effects in automotive exhaust catalysis

“Inspiration acts as a catalyst for success.”

Sam Veda

“Science never solves a problem without creating ten more.”

George Bernard Shaw

Dit proefschrift werd mede mogelijk gemaakt met financiële steun van Toyota Motor Europe nv/sa.

ISBN: 978-90-39350737

Cover lay-out by the author

ZuidamUithof Drukkerijen, Utrecht

Table of content

Chapter 1	Automotive catalysis: From engine exhaust emissions over current catalyst technology to new challenges	1
Chapter 2	Promotion effects in the oxidation of CO over zeolite-supported Pt nanoparticles	41
Chapter 3	Pore curvature and support composition effects on the electronic properties of supported Pt catalysts: An infrared spectroscopy study with CO as probe molecule	67
Chapter 4	Atomic XAFS as a tool to probe the electronic properties of supported noble metal nanoclusters	85
Chapter 5	Promotion effects in the oxidation of CO over zeolite-supported Rh nanoparticles	99
Chapter 6	Promotion effects in the reduction of NO by CO over zeolite-supported Rh nanoparticles	129
Chapter 7	Concluding remarks and perspectives	155
Samenvatting		165
Annex	List of acronyms, special units and chemicals	171
Acknowledgements		175
Curriculum Vitae		179
List of publications		181

Chapter 1

Automotive catalysis: From engine exhaust emissions over current catalyst technology to new challenges

1 Car exhaust emissions

1.1 Origin, evolution and associated concerns

Most cars are propelled thanks to the energy produced by an internal combustion engine, which burns fossil fuels such as gasoline, diesel or compressed natural gas (CNG).[1-3] The main chemical reaction taking place in such engine, as represented by equation (1.1), produces water and carbon dioxide (CO_2).[3-4] These species are therefore the most abundant products of internal combustion. However, due to the imperfect mixture between the transportation fuel and air as well as the limited contact time between the reactants, the combustion is usually incomplete (equation (1.2)). Hence, unburned hydrocarbons (HC) and carbon monoxide (CO) are also emitted. These unburned hydrocarbons are found in the form of volatile organic compounds (VOC) or aerosols, called soot or particulate matter (PM). Furthermore, fossil fuels also contain small amounts of N- and S-compounds, which will yield nitrogen oxides (NO_x) and sulphur oxides (SO_x) during the combustion.[3-4] Finally, NO_x emissions are as well produced at higher temperatures and pressures due to the large excess of N_2 from the air.

$$C_mH_n + \left(m + \frac{n}{4}\right) O_2 \rightarrow m\, CO_2 + \frac{n}{2} H_2O \tag{1.1}$$

$$C_mH_n + \left(x + \frac{y}{2} + \frac{z}{2}\right) O_2 \rightarrow x\, CO_2 + y\, H_2O + z\, CO + w\, C_pH_q \tag{1.2}$$

with x + z + w . p = m and 2 . y + w . q = n and where p and q can have values varying between 1 and m or n, respectively.

As shown in Figure 1.1, the global atmospheric CO_2 concentration has been increasing exponentially since the industrial period due to the extensive use of fossil fuels. It is the most important anthropogenic greenhouse gas (GHG) and it is now by far exceeding the natural concentration, as determined by ice cores analysis, which was ranging between 180 and 300 ppm over the last 650000 years.[5] Figure 1.2 highlights the contribution from the passenger cars to the CO_2 emissions in Europe as 12%, which is not negligible.[6] Additionally, reports from the European Environment Agency (EEA) show that the contribution from the transport sector to the GHG emissions in Europe in 2004 and 2005 was about 21 %, from which, 93 % is coming from road transportation.[7-8] These GHG from the transport sector mainly

consist of CO_2 with a minor share from methane (CH_4) and nitrous oxide (N_2O), the latter coming from the catalytic converters used as PM traps or loosing efficiency due to aging. Between 1990 and 2004, the GHG emissions have been decreasing in most sectors of 15 European Member States, except for the transportation where they increased by 26 %. The main factors contributing to this increase are larger road transport volumes, an aging car fleet and an increased mileage, the latter being illustrated by Figure 1.3.[6,8-11] Estimations for 2010 predict that they will further grow up to 35 % from the 1990 level if the currently existing measures are implemented.[8]

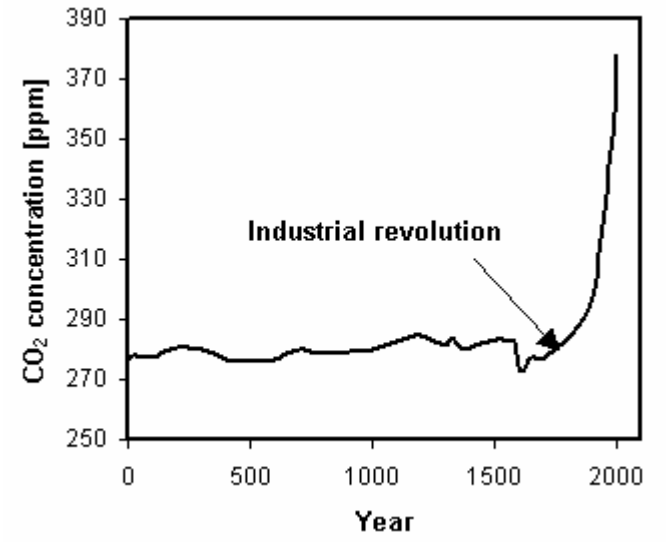

Figure 1.1: Global atmospheric concentration of carbon dioxide over the last 2000 years. Adapted from reference [5].

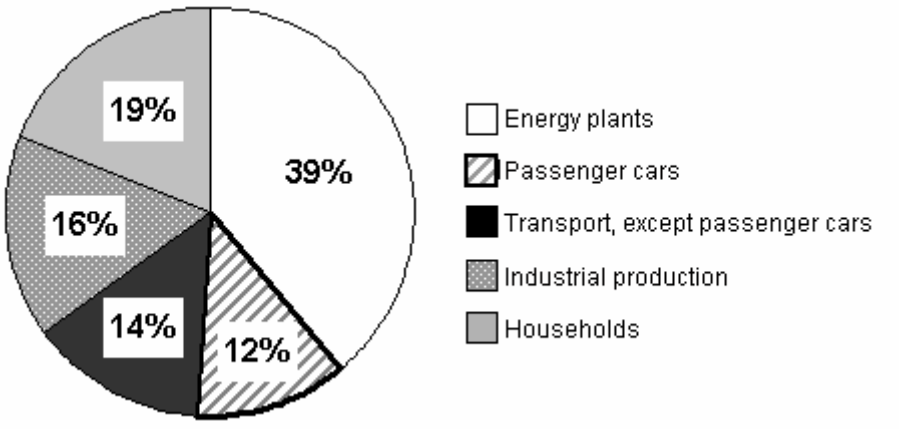

Figure 1.2: Repartition of the man-made CO_2 emissions from the 25 European Members States by sectors based on data from 2004.[6]

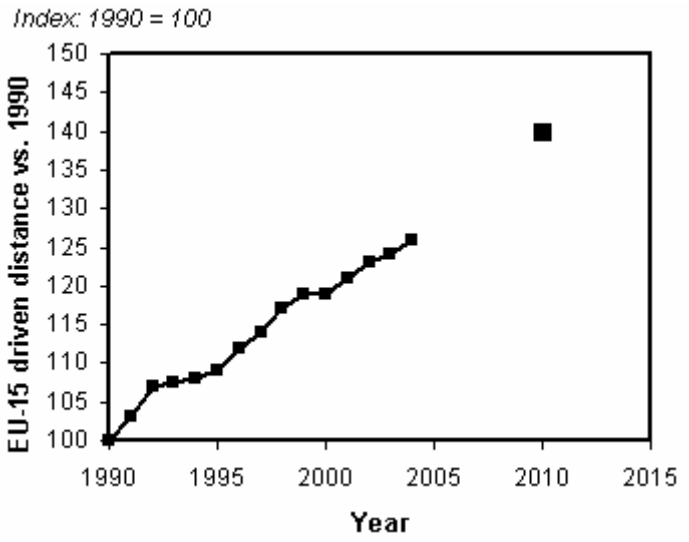

Figure 1.3: Evolution in the usage, as compared to the year 1990 (index 100), of passenger cars in 15 European Members States based on data from 2004. Adapted from reference [7].

In Europe, when it comes to NO_x, HC and CO emissions from the transport sector the picture is even worse as they account for 58 %, 50 % and 75 % of the respective total man-made emissions.[9] Figure 1.4 shows the distribution by sector in emissions of NO_x and PM with an aerodynamic diameter of less than 2.5 μm ($PM_{2.5}$) in 2000 and the estimated distribution by 2020. As can be seen in Figure 1.5, the decrease in share of automotive NO_x and PM emissions is due to a drastic decrease, since 1990, in such emissions from the road transport sector, which on average consists of 80 % passenger cars.[10-12] These results are attributed to measures implemented in the framework of the Auto-Oil Programme I.[11] Without technical improvements, *i.e.* the introduction of catalysts and better engine combustion, and strict legislations, it is estimated that road transport emissions would have been 50 to 100 % higher by 2010 as compared to the 1990-level.[11,13]

Finally, SO_x emissions were not considered in these numbers because vehicles are no essential emission sources anymore thanks to the introduction of low-sulphur-content transportation fuels. In 1995, 1.5 % of the total SO_x emissions came from the road transport sector and this should further decrease to less than 0.5 % by 2010.[11]

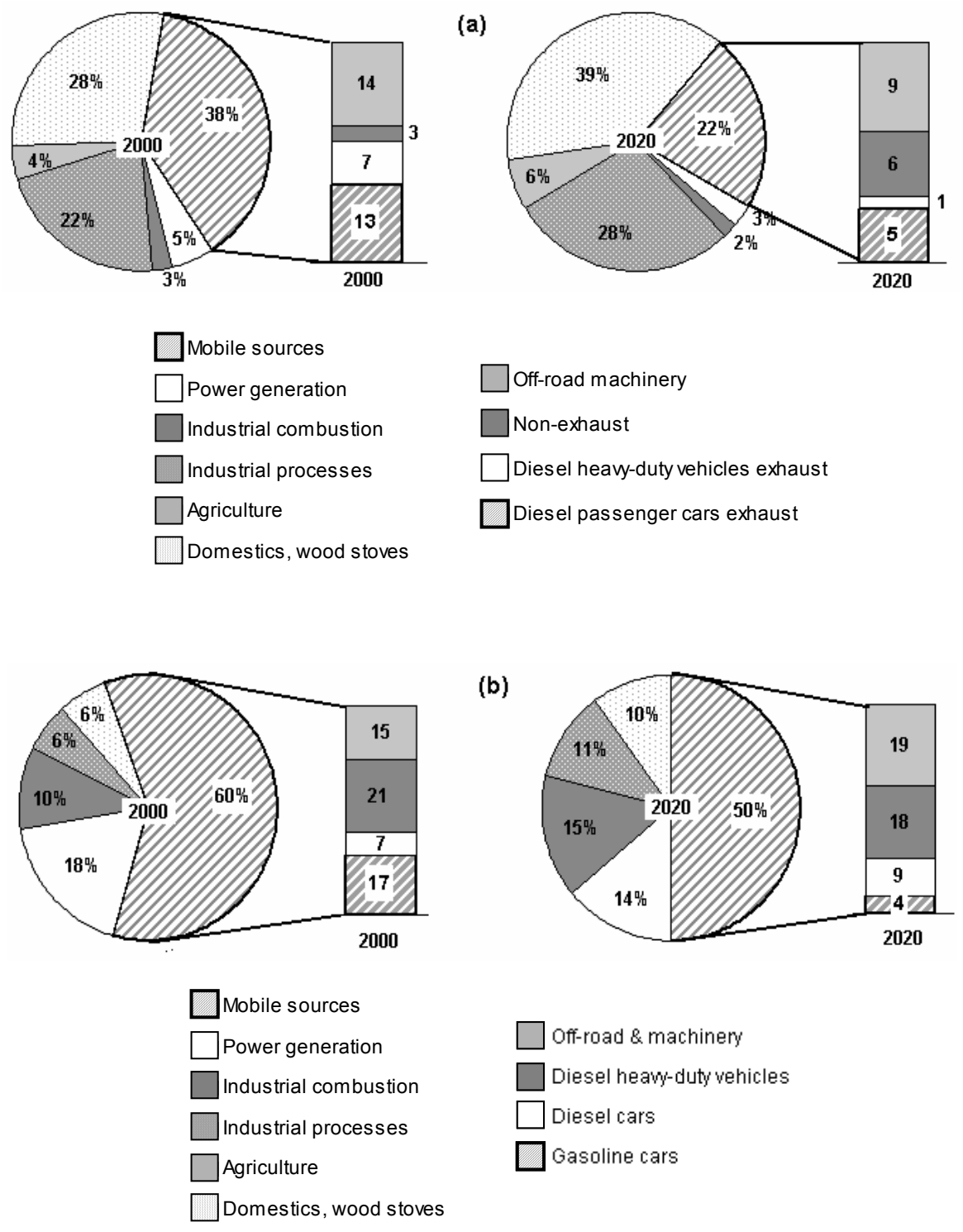

Figure 1.4: Repartition of the land-based PM2.5 (a) and NO_x (b) emissions from the 15 European Members States by sectors and, for the transport sector, by type of mobile sources based on data from 2000 and on estimations for 2020. Adapted from reference [10].

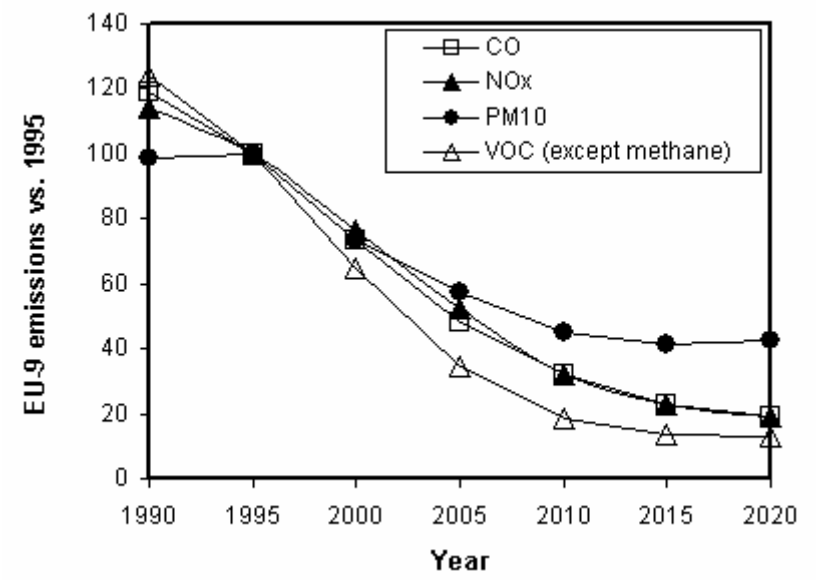

Figure 1.5: Evolution of the road transport emissions of CO (□), NO_x (▲), PM_{10} (●) and non-methane VOC (∆) as compared to the year 1995 (index 100), in the 15 European Members States based on data collected up to 2000 and on estimations up to 2020, the latest assuming the implementation of the ACEA Agreement and the Auto-Oil I legislation, which gave rise to the Euro 3 and Euro 4 (see point 1.2). Adapted from reference [11].

The automotive exhaust emissions should be limited as much as possible as most of their constituents have firstly an impact on human health and environment, but also on buildings and infrastructure.[1,9,14] In principle, the following products with their potential harmful effects can be distinguished:

- CO_2 is the most important gas contributing to global warming; it has an impact on biodiversity, ecosystems, plant photosynthesis, species distribution and the occurrence of diseases, such as malaria;
- NO_x play a big role in the acidification and eutrophication problems, in the ground-level ozone and smog formation and in the mobility of heavy metals; they therefore have an impact on biodiversity, ecosystems, reproduction, distribution of species, lung damage, asthma and respiratory problems;
- CO has also an effect on the tropospheric ozone and is additionally an odourless poison that can lead to unconsciousness or kill at high concentrations;
- SO_x are responsible for acid deposition and corrosion; they can affect lung tissues and favour cancer or respiratory infections;

- PM has the tendency to accumulate in the lung and depending on its size to infiltrate the tissues; it has a large role on asthma and bronchitis, reduces the life expectancy through a rise in mortality from respiratory, cardiac and circulatory diseases and it is assumed to favour cancer; and
- VOC's are a very large group of pollutants from which some are fairly harmless and others extremely toxic:
    - Benzene among others is carcinogenic; and
    - Some VOC's lead to ground-level ozone and smog through photochemical reactions, which in turn causes respiratory problems.

1.2 Legislation

In order to improve the air quality and to limit the impact of automotive pollutants harmful for humans and climate change, the European Commission has taken several legal measures. The most important ones will be discussed in this section.

1.2.1 CO_2 emissions

In March 1998, the European Automobile Manufacturers Association (ACEA) signed a voluntary agreement with the European Union (EU) commission. It is linked to the commitment of the latter to reduce GHG emissions by 8 % in the scope of the Kyoto protocol concluded in 1997.[6,9,15] This ACEA agreement consists in a two-steps objective for the reduction in fleet-average CO_2 emissions from new passenger cars. The first aim is to reach 140 g CO_2/km in average for new cars introduced from 2008 on and this mainly through new vehicle technology. The second objective is a further reduction to 120 g CO_2/km from 2012 through extra technical improvement, taxation and labelling.

Thanks to an improved fuel efficiency and a shift from gasoline to diesel powered cars, the CO_2 emissions from new cars have been reduced by 12 % from 186 to 162 g/km between 1995 and 2004.[6,8,16] However, as can be seen from Figure 1.6, the target will be missed if the current reduction pace is kept.[17,18] So, the EU Commission has issued a legislative proposal to put more pressure on the European automotive industry.[19-21] By 2012, new passenger cars should not emit in average more than 130 g/km (based on engine bench results with the European Test Mode) with the aim to reach in total 120 g/km in the integrated approach including better

tyres and air conditioning systems as well as by using biofuels instead of fossil-based transportation fuels. In case of failure, an emissions premium scheme is foreseen. The European Federation for Transport and Environment even suggested to further reduce CO_2 emissions to 80 and 60 g/km by 2020 and 2025, respectively.[18,22]

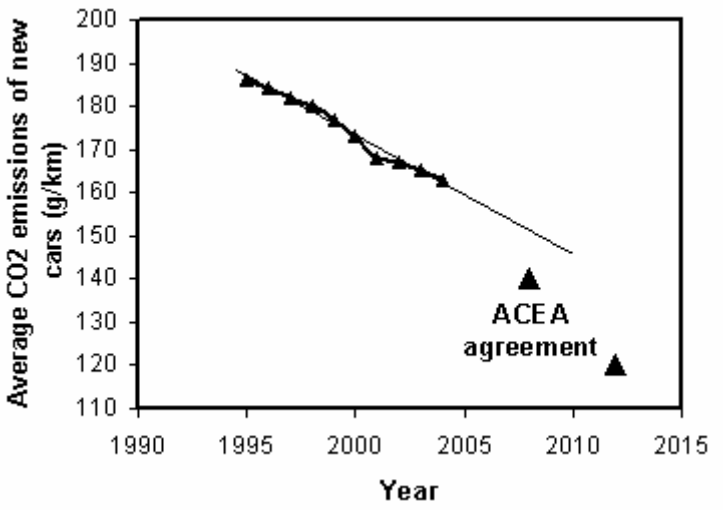

Figure 1.6: Evolution in average CO_2 emissions of new passenger cars in 15 European Members States based on data from 2004. Adapted from reference [7].

1.2.2 NO_x, PM, CO and HC emissions

NO_x, PM, CO and HC emissions from cars are regulated since the 1970 Directive 70/220/EEC.[23] The limits have evolved with several amendments following different programmes of the EU Commission proposed to improve air quality in Europe and mainly to reduce acidification and ground-level ozone formation. In that view two programmes should be cited: the Auto-Oil Programme I & II, from 1992 to 2000, and the Clean Air For Europe (CAFE), which started in 2002.[11,24,25] They have led to the 98/69/EC directive (Euro 3 and Euro 4) and to the regulation (EC) No 715/2007 (Euro 5 and Euro 6) for passenger cars and light commercial vehicles. They specify, amongst other requirements such as the testing conditions, the catalysts durability and the need for on-board diagnostic systems (OBD), emission standards for NO_x, HC, CO and small PM for 2000 and 2005 as well as 2009 and 2014, respectively. Their fulfilment is directly linked to the type-approval process of the vehicle, which is the authorisation to sell it in the European Union. The evolution of the maximum allowed emissions in CO, HC, NO_x and PM from new cars is illustrated in Figure 1.7, covering the Euro 1 to Euro 6 standards for gasoline and diesel cars. For the future,

the main focus will be on the reduction in PM from 2009 and on the abatement of NO_x from 2014.

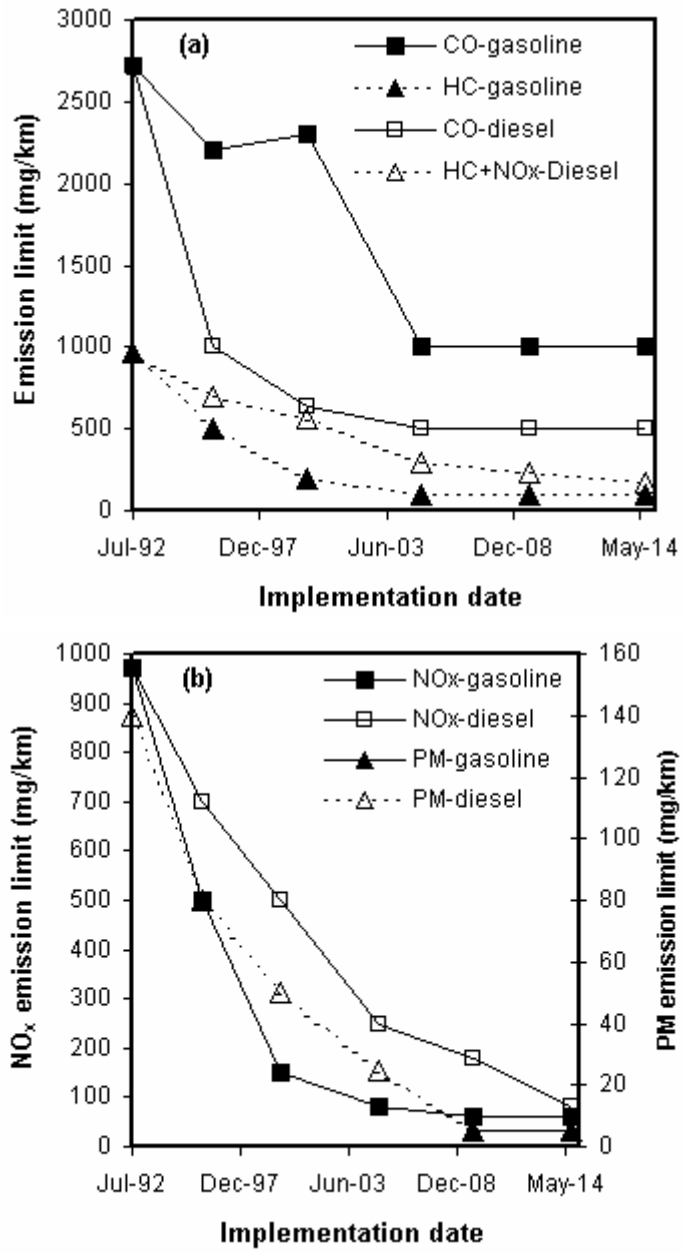

Figure 1.7: Evolution of the maximum authorised emissions in CO and HC (a) and in NO_x and PM (b) from new gasoline- and diesel-powered cars as a function of time throughout the period covering the Euro 1 to Euro 6 standards.

1.2.3 Other legislations having an impact on emissions

As the combustion products will be influenced by the fuel composition and because the exhaust purification systems lose performance over time due to poisoning, the directive on fuel quality, 98/70/EC as amended by 2003/17/EC, has a big impact on the different emissions levels.[1,9,11,22-23,26-30] It, for instance, suppresses

lead (Pb) and prescribes a maximum sulphur (S) content of 50 ppm as from 2005 and a further lowering of this limit to 10 ppm by 2009.

The biofuel directive 2003/30/EC is aimed to reduce CO_2 emissions, but will most probably cause an increase in NO_x emissions, while having a positive effect on PM and CO due to a higher content in oxygenates.[11,27-28,30-31] This directive requires that biofuels should replace 2 % of all transport fossil fuels by the end of 2005 and 5.75 % by 2010.

Safety related legislations have had a negative impact on emissions as their fulfilment required the installation of additional equipments, *e.g.* airbags, anti-lock braking systems (ABS), sensors, etc., which increased the vehicle weight and hence lowered the fuel economy.[6,16,18]

The car labelling directive 1999/94/EC allowing the customer to buy a car based on its fuel economy and CO_2 emissions did not have a big impact up to now, but might be more important in the future as the public awareness on global warming is steadily increasing in view of recent press releases and the related media coverage in general.[16,32]

1.3 Strategies to reduce emissions

As shown above, part of the strategy to reduce emissions is based on the legislations on vehicles emissions, fuel quality and labelling. The first one imposes to car manufacturers to develop technical solutions, which will be explained in more detail in the next section, while the second helps them to achieve the targets. Additionally, inspection and maintenance policies can hinder the (further) use of highly polluting cars, while a good communication can help consumers to make aware choices.[11,29-30,32-33] Finally, several governmental actions can have an effect on the emissions from the transport sector.[11] Fiscal measures have the largest potential in influencing the customer choices and behaviours, especially at the local level.[11,16,19,29,32,33] They cover the promotion of:

- Enhanced environmentally-friendly vehicles (EEV), which are emitting substantially less than prescribed by the legislation, through fiscal incentives and CO_2-based taxation;
- Public transportation through the implementation of parking charges, differentiated road pricing, etc.;

- Replacement of old polluting vehicles by new ones; and
- Alternative fuels and city fuels, which cause lower PM emissions.

The infrastructure also plays a role. Road capacity, traffic management (*e.g.* dynamic lights) and reduced road surface rolling resistance can all improve fuel economy and decrease CO_2 production.[11,34] Moreover, as the driver himself can influence the consumption, the introduction of an eco driving module in drivers' learning package could lead to about 8 % fuel economy.[6,29,33,35] Up to now, the largest reductions in emissions have, however, been achieved thanks to technological improvements.[2,6,11,16]

2 Technology to reduce emissions

2.1 CO_2 reduction

The CO_2 emissions cannot be reduced by car exhaust aftertreatment systems. They are directly linked to the vehicle fuel type and fuel economy. The latter one is in turn a function of the engine efficiency, resistance forces and energy demand and losses.[6,16,36]

The engine efficiency has mainly been improved through a better combustion and a reduction in friction losses.[26-27,33,37-41] The former one was partially achieved through developments in the injection systems, *e.g.* direct injection or piezo injectors, and in variable valve technology. But also through engine downsizing, turbo-charging and lean operation, which, by an excess of air, guarantees a larger contact between fuel and oxygen. Finally, the powertrain heat losses can be reduced thanks to optimised cooling and exhaust gas heat recovery.

Hybrid cars combine a conventional gasoline or diesel engine with an electrical motor. Their higher efficiency mainly lies in aspects such as the regenerative braking system, which will convert the braking energy into electrical energy instead of heat, or the start-stop function, which ensures that the electrical motor is exclusively used in idle mode.[33,38,41] Low friction lubricants applied to engine and transmission parts have the potential to lower CO_2 emission by 2.5 %.[33,39] Further improvement to the car drivetrain were obtained thanks to the introduction of 6-speeds gearbox with optimised gear ratios, gear shift indicator, continuous variable transmission, electric power steering, etc.[33,37-39,41]

The main resistance forces are coming from the air and from the tyres. They can be lowered with better vehicle body aerodynamics and low rolling resistance tyres.[29,33,37-39,41-42] The efficiency of the latter ones can be further improved with a tyre pressure monitoring system. Furthermore, controlling the vehicle mass is primordial as 1 % weight decrease is associated with a reduction of 0.8 % in CO_2 emissions.[18,33,37-38,41] It is achieved by the introduction of light weight materials, such as high strength steel, aluminium, magnesium, plastics and composites as well as by new designs.

Additional fuel savings can be achieved through energy management, including better air conditioning systems, and systems that help the driver to adapt to the traffic, such as active cruise control, navigation with eco-routing and telematics.[33,36-37,39,41] Finally, CO_2 emissions can be reduced by the usage of alternative fuels, *e.g.* biofuels or gas, and new drivetrains, such as electrical motor or fuel cells.[27,33,37-41,43-44] However, most of them are still under development and can only be used in cities due to their limited driving range.

2.2 Other emissions reduction

HC and CO emissions are the products of incomplete oxidation and can therefore be partially reduced with the technologies listed above that improve the fuel combustion. On the other hand, NO_x emissions from the engine can be reduced thanks to exhaust gas re-circulation (EGR) and high pressure injection, the latter having a positive impact on PM production as well.[4,26-27,40,45] However, as it was hard to meet the legislation only by engine adaptations, automotive exhaust catalytic converters have been introduced since the 1970's.[4,46-51] Considering the fact that diesel and gasoline engines function in very different ways and their emissions are therefore not completely alike, the exhaust gas purification systems are varying as well. As a consequence, the technologies developed for diesel and gasoline engines will now be discussed separately.

2.2.1 Gasoline

Gasoline engines mainly emit CO, HC and NO_x at a temperature typically varying between 250 °C and 900 °C (523 K and 1173 K).[48,52] The original automotive exhaust converters were Pt- or Pt/Pd-based oxidation catalysts used to remove CO

and HC in net oxidising conditions, *i.e.* in excess of oxygen.[4,50-51] However, under real driving conditions modes, like the start or accelerations, net reducing conditions are produced. Therefore, these converters further evolved in a combined system consisting of a Pt-Rh-based reduction catalyst followed by an oxidation catalyst with air injection in between. Finally the three-way catalyst (TWC), which is the best known automotive catalyst, has been introduced in 1977 in the USA and Japan and in the early 1980's in Europe. It treats at once the exhaust gas of gasoline engines operated at stoichiometry.[3-4,30,46,48-54] Its name comes from the three reactions that simultaneously take place on the active surface: the CO and HC oxidation and the NO_x reduction. As shown by Figure 1.8, TWC are efficient in a limited region around stoichiometry and are therefore used in combination with a lambda sensor, *i.e.* an oxygen sensor, electronic feedback and electronic fuel injection. In the stoichiometric region, the HC, CO and NO_x conversions on modern TWC are almost complete.

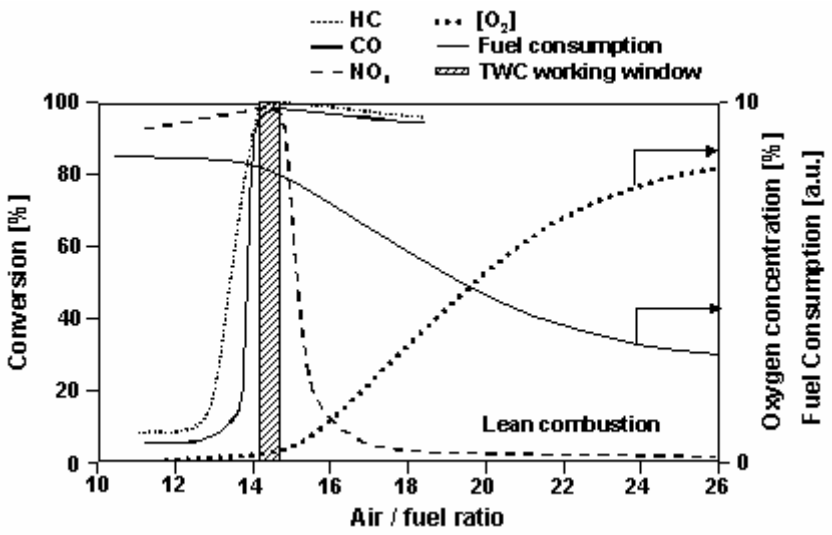

Figure 1.8: HC, CO and NO_x conversion on a TWC as well as fuel consumption and oxygen concentration as a function of A/F. The dashed zone indicates the working window of the TWC. Adapted from reference [53].

Recently, in order to lower the fuel consumption, gasoline engines, however, tend to be operated in lean conditions. This means that HC and CO are easily removed, but NO_x, even if emitted at lower levels by this type of engine, cannot be reduced anymore by the conventional TWC.[3-4,48,50,52-53,55] Therefore, new de-NO_x technologies, which work at high oxygen concentrations, had to be developed.[4,11,27,50] One of them is the NO_x storage-reduction (NSR) or lean NO_x-

trapping (LNT) catalyst.[4,46,48,50,53,55-57] Its principle and the evolution of the NO_x concentration in the exhaust as a function of time is shown in Figure 1.9. During the lean operation of the engine, NO is oxidised on a Pt catalyst into nitrogen dioxide (NO_2), which is captured by the storage material, *e.g.* BaO, in the form of nitrates. Those nitrates are then reduced to N_2 during a short stoichiometric or rich spike thanks to the presence of CO, HC and H_2 on Pt or Rh metal.

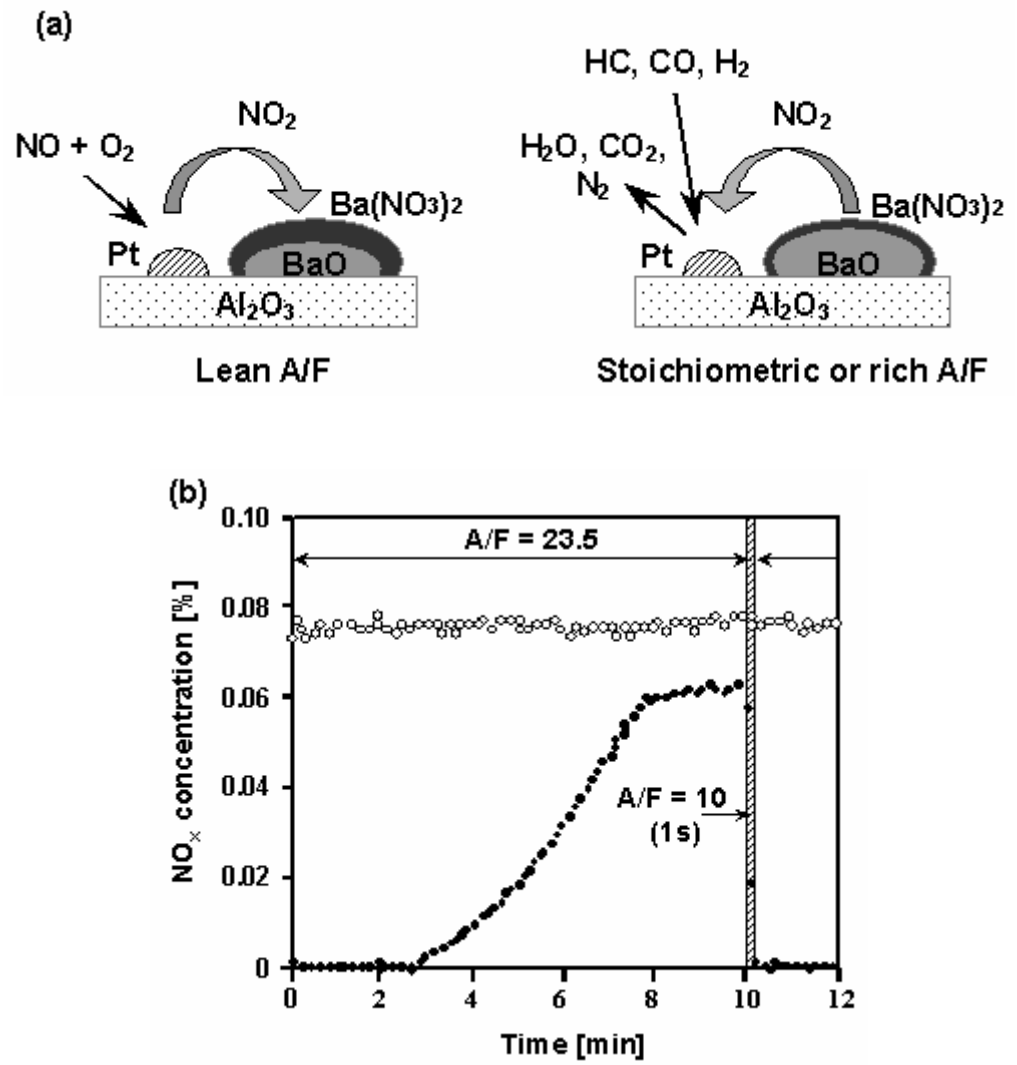

Figure 1.9 b: (a) Mechanism of the NO_x storage and reduction on a NSR catalyst; and (b) NO_x concentration in the inlet (○) and in the outlet (●) of a NSR catalyst ($Pt/Rh/BaO/CeO_2/\gamma\text{-}Al_2O_3$) as a function of time just after a rich spike; test performed at 400 °C (673 K) on an engine bench with a 1.8 dm³ catalyst installed on the exhaust of a lean-burn engine operated at 2000 rpm and 75 kPa. Adapted from references [53] and [55].

Another strategy is based on the direct decomposition of NO_x into nitrogen and oxygen in the lean environment.[4,50,56] In these conditions, the active surface is

quickly poisoned by oxygen, which can be removed periodically by reductants, such as the combustion fuel itself or urea used as a source of ammonia, directly introduced in the exhaust line. This approach is called the selective catalytic reduction by HC (HC-SCR) or by NH_3 (NH_3-SCR).

Additionally, with time, the PM emissions from gasoline engines are getting as high as the ones from diesel engines. Therefore, if the engine improvements are not sufficient, PM filters might have to be introduced alongside the Otto engines from Euro 6 on.[11,27]

2.2.2 Diesel

Diesel engines are very popular in Europe because of their better fuel economy. Practically, they always function in large excess of oxygen, *i.e.* with air/fuel ratios (A/F) higher than 17, which means few CO is formed and the main issue should be the NO_x.[48,52] However, due to the nature of the combustion process, more PM are generated by diesel engines than by gasoline ones.[4,48] Moreover, due to the low temperature of the exhaust gases, usually 200-300 °C (473-573 K) and rarely above 600 °C (873 K), the oxidation of HC and CO is not straightforward.[4,48]

Up to the Euro 5, the NO_x and PM emission standards have been met by engine adaptations exclusively.[4,45] Meanwhile, HC and CO concentrations in the exhaust as well as the PM mass were reduced by diesel oxidation catalysts (DOC) made of highly dispersed and well-stabilised Pt and/or Pd catalysts.[3-4,48] The Euro 5 limits will require PM filters on all diesel vehicles, whereas de-NO_x gas aftertreatment systems will only be necessary from the Euro 6 on.[4,10,45,48,58]

For the PM reduction, PM filters or traps, also called diesel particulate filters (DPF), are already getting standard.[3,10,40,59] They can be of 2 types, foam or wall filters.[4,60] The latter are the most common and usually consist of a ceramic monolith with alternately plugged channels, which forces the gases through the porous walls, as shown in Figure 1.10.[4,48] Another type is a roll made of a perforated and corrugated metal foil, creating the flow-through structure, combined with a fleece sheet that serves as filter.[60] In these systems, the filtration efficiency related to a particulate size has to be kept, whereas the control of the backpressure is the most critical parameter as it directly affects the engine performance.[4,50] Therefore, the filter has to be regenerated, *i.e.* the PM have to be oxidised into CO_2, on a

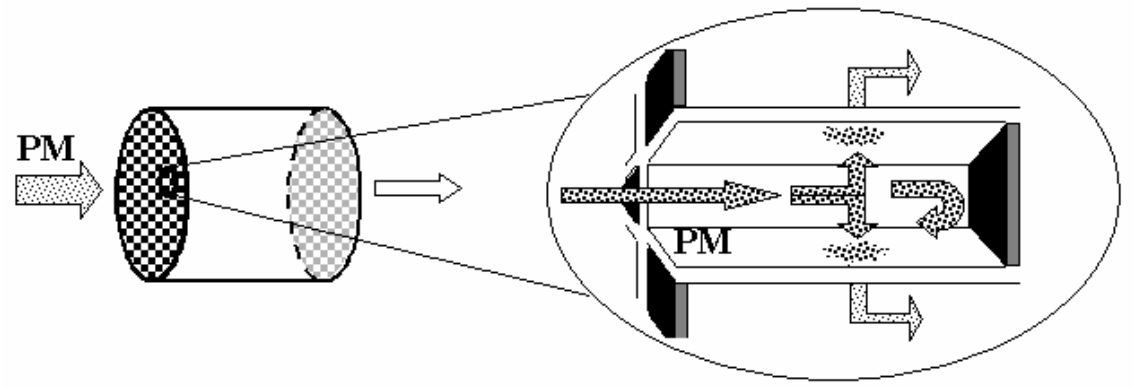

Figure 1.10: Schematic showing the principle of a DPF made of porous ceramic walls. Because of the alternately blocked channels, the exhaust gas flow is forced through the porosity of the walls in which most of the PM is trapped.

regular basis. For this purpose, several regeneration strategies have been developed.[4,26-27,30,48,50] The most obvious is the thermal regeneration at 600 °C (873 K) or more. In passenger cars, it is obtained by an intermittent fuel injection before a pre-catalyst, which via CO and HC conversion, is creating an exotherm utilised to burn the PM accumulated on the filter walls. With this approach, the fuel economy is affected and the thermal stress encountered by the filter can cause cracks, which will lower the PM filtration efficiency. For this reason, the self-regenerating trap is a better concept as it continuously oxidises the soot at lower temperature. This can be achieved in 3 different ways. The first one, mainly used for heavy duty vehicles thanks to their higher exhaust gas temperature (250-400 °C – 523-673 K), is the continuous regeneration DPF (CR-DPF) where the soot is burned at about 300 °C (573 K) with a strong oxidant like NO_2. This NO_2 is usually generated through the conversion of NO on a Pt based oxidation catalyst. The second approach is the oxidation of the trapped PM by air on a catalysed DPF (CDPF). In this case, the DPF walls are coated with a catalyst based on precious metals or complex oxides, such as iron. The last method is the use of fuel additives, such as Cu, Ce, Sr or Fe, introduced in the fuel in the form of liquid organometallics. Thanks to the intimate contact achieved between the PM and the catalyst, the oxidation of soot by air will be promoted at a temperature about 200 °C (473 K) lower than on non-catalysed DPF. The disadvantage of this approach is the need for a tank and a precise injection system for the additives. Therefore, the second system is often favoured as it has the advantage to oxidise HC, CO and NO at the same time as the soot, which

produces some heat and a stronger oxidant *in situ*. Its drawback is the necessity to control the exhaust gas temperature.

Concerning the NO_x reduction, catalysts developed for the lean-burn gasoline engines can also be used for diesel engines as their exhaust gas composition is more similar.[52] These technologies are already being installed on some vehicles, but are not yet mature. At this point, most of the research activities are focussing on NSR, HC-SCR and NH_3-SCR durability and sulphur tolerance.[4,26,45,48,52,57,61]

In order to reduce the space and the cost, several systems have been developed to integrate separated functions. The CDPF described here above is a first example with the combination of an oxidation catalyst with a filter.[4] Additionally, Toyota integrated a NSR function into a DPF with its diesel particulate-NO_x reduction (DPNR) system.[62] For trucks, an oxidation catalyst was combined with a filter and a NH_3-SCR catalyst.[4]

3 Automotive catalysts

3.1 Catalyst components and layout

Depending on the type of fuel, the space around the engine and the selected emissions reduction strategy, including engine control, the exhaust parts layout can vary a lot. As an example, Figure 1.11 illustrates the configuration developed by Toyota for the DPNR system. The diesel direct injection is performed at high pressure and an exhaust port injector is added to the exhaust gas collector. The latter serves as a fuel injection system for the intermittent PM and NO_x reduction. Part of the exhaust gas is re-circulated after cooling in order to lower the combustion temperature, which limits the NO_x production. The exhaust purification system consists of three different catalyst bricks. The first two are placed in a close-coupled position, *i.e.* nearby the engine, in order to benefit from the heat of the combustion, while the last one is positioned under-floor. The first catalytic converter is a NSR, directly followed by a DPNR, which will trap the PM and the NO_x in the lean operation. The last one is a DOC used to remove the remaining CO and HC in the exhaust gas, especially during the rich operation. In order to control the good operation of the total system, several sensors are used. Two pressure sensors are measuring the backpressure building up in the DPNR due to the soot accumulation. When a critical value is reached, the regeneration process is triggered. Furthermore,

two temperature sensors are utilised to make sure the DPNR is operated in the right temperature window as well as to avoid thermal damage. Finally, a lambda sensor is adopted to control the DPNR proper functioning and feedback to the engine management unit.

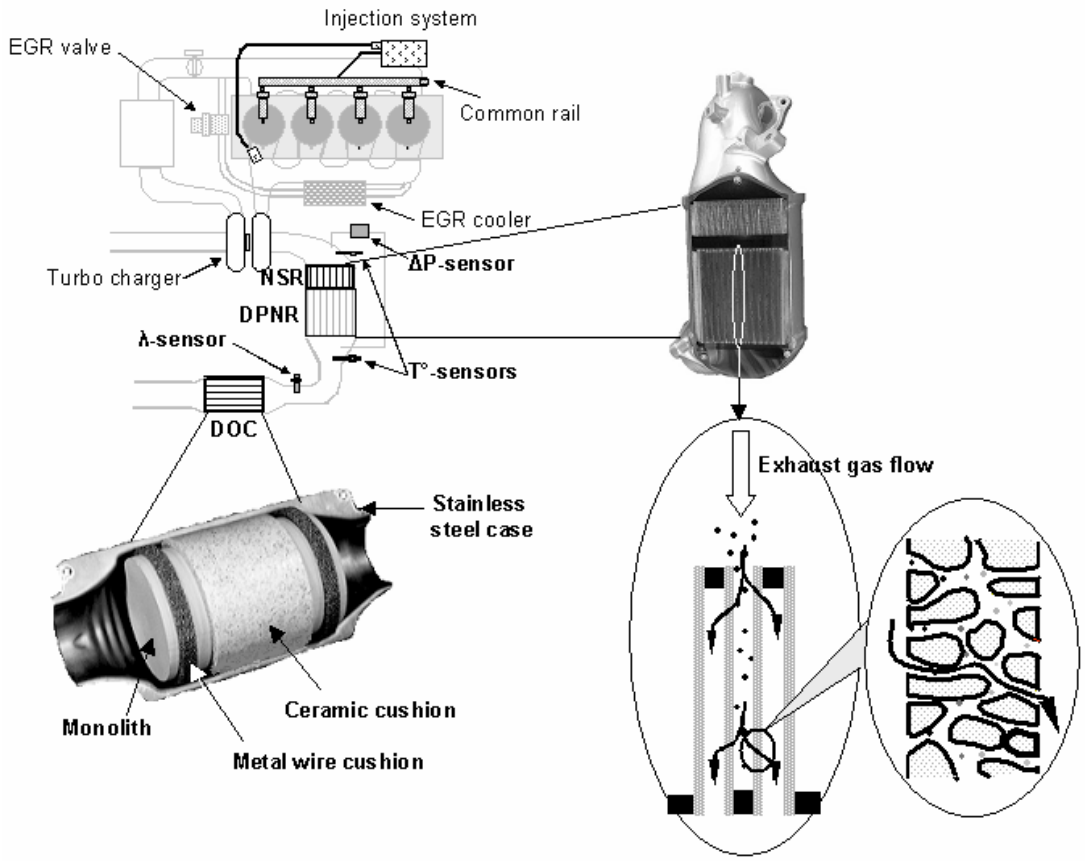

Figure 1.11: Schematic showing the layout developed by Toyota for the DPNR system. Its main elements are a diesel engine with EGR and high pressure fuel injection, a diesel post-injection for the regeneration of PM and NO_x, a SCR, a DPNR and a DOC catalysts and finally a series of sensors for the control of the complete system. Adapted from reference [62].

When cold-start oxidation catalysts are used, they are usually placed in close-coupled position for a fast warm-up and, more rarely, under-floor with isolation of the pipes.[30,46,48,50-52,63] Their efficiency may be further improved by, for instance, electrical heating or fuel burners.[30,46,51-52] DPF and TWC are found in the two configurations, close-coupled or under-floor, depending on their optimal operation temperature range and on their thermal resistance.[40,51-52]

The OBD's usually make use of two oxygen sensors, one placed upstream and one downstream from the TWC. Their signal is used to control the oxygen storage capacity (OSC) of the catalyst material, a direct measure of the catalyst

performance.[4,30,51,54] In rare cases, NO_x sensors are placed behind de-NO_x systems, but they are still very expensive and exhibit slow response.[54,64]

When the DPF regeneration is done with fuel additives or when NO_x are reduced by NH_3-SCR, both an additional storage tank and an injection system have to be foreseen. In the latter case, a NH_3 sensor can also be useful.[54]

The exhaust of an internal combustion engine is a very demanding environment, far from the steady-state operation of most chemical plant catalytic processes.[3-4,49-50] It requires to cope with variable inlet temperature and pressure, elevated and pulsating space velocities and with a complex inlet composition. Additionally, it has to be active at low temperature and withstand temperatures as high as 1000 °C (1273 K) as well as thermal shock. Finally, it should tolerate poisons and mechanical vibrations, while excessive pressure drops should be avoided. Therefore, packed pellets, which are sensitive to attrition, were quickly abandoned and replaced by a new catalyst skeleton made of parallel channels oriented in the direction of the exhaust gas flow, the monolith. As shown for the DOC in Figure 1.11, the monolith is retained with a ceramic cushion sometimes accompanied by metallic mats in a stainless steel mantel fitted into the exhaust system by connecting cones. The ceramic cushions are typically made of vermiculite, a natural mineral that expands when heated for the first time and will keep its holding function for the rest of the car life.

The monolith itself is often made of porous cordierite ($2MgO.2Al_2O_3.5SiO_2$) because of its low coefficient of thermal expansion. It is manufactured by extrusion of a mixture of talc, alumina and clay mixed with water and organic additives, followed by drying and firing at high temperature.[3-4,52,60] An alternative to the ceramic monolith is the rolled metal foil, which has as advantage its low back pressure and short warm-up time.[3-4,51-52,60] For DPF, several filter materials are used: metal, silicon carbide (SiC), cordierite and aluminium titanate ($Al_2O_3.TiO_2$); the SiC material being to date the most common.[3,60,62,65] Improvements in the TWC ceramic monolith were achieved through thinner walls (down to about 60 µm thick) with higher cell densities (up to 900 or even 1200 cpsi), which increases the geometric surface area and lowers the thermal mass for a fast light-off.[4,51,63] Sometimes, the substrate is foreseen with a hole that can incorporate a sensor.[51] The benefits are then a faster usability of the sensor, a quicker closed-loop control and the possibility to reduce the amount of monoliths.

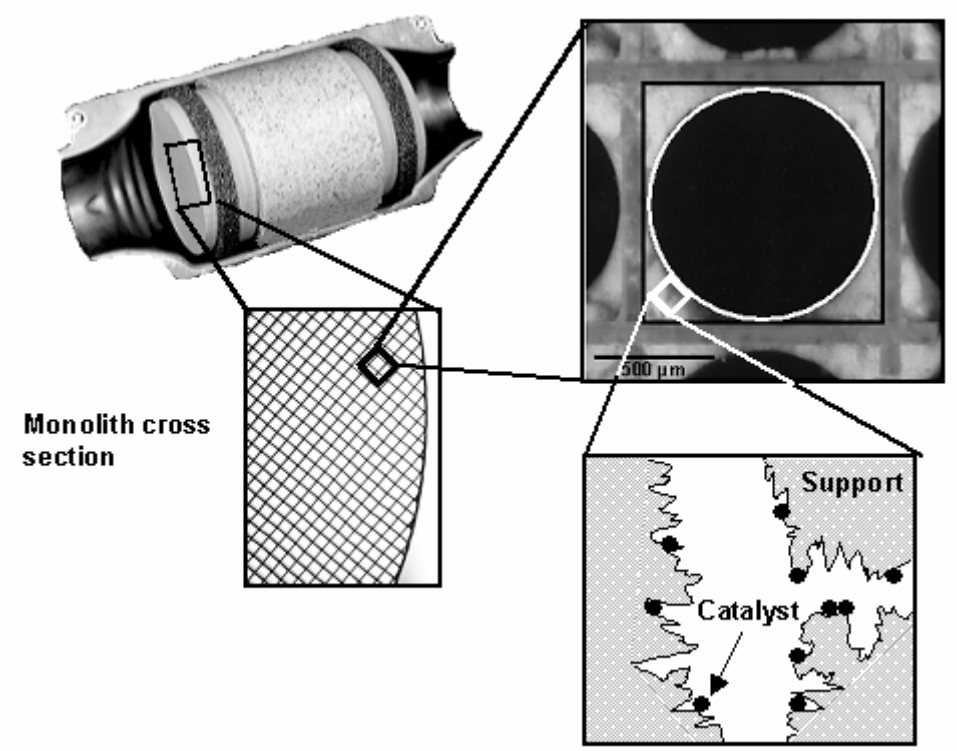

Figure 1.12: Photograph of a DOC catalyst with in successive inserts, a portion of the monolith cross-section, a magnification of the cell arrangement showing the monolith structure and the wash-coat layer and, finally, a schematic of the wash-coat material morphology.

As the monolith porosity is limited to guarantee the mechanical strength, it does not represent a good catalyst support material. So a thin coating layer, 20-150 µm thick, of a high specific surface area (SSA) material supporting the catalytically active components is deposited on the walls (see Figure 1.12).[3-4,49,52] This layer, called the wash-coat, is obtained by slurry deposition followed by calcination. For specific needs, this wash-coat layer also encounters several adaptations in order to improve the exhaust gas purification. First of all, as illustrated by Figure 1.13, the thickness of the wash-coat can be decreased through the use of a different monolithic cell structure. The adoption of hexagonal cells will for instance have a positive impact on the mass transport limitations, especially in the corners, where the film thickness can be reduced by a factor of 2.[53,57,61] Such limitations have a drastic impact on the catalyst regeneration after poisoning.[52-53,57,61] Secondly, the wash-coat can consist of multiple layers as schematised for a two-layers coating by Figure 1.14. In this case, the aim is to maximise the desirable interactions between the catalyst material constituents, while minimising the potential undesirable

interactions, such as solid-state reactions, by physical separation.[3-4,46,50-51,63] It was demonstrated that this segregation shows advantages in the low-temperature and NO_x reduction performance as well as in catalyst durability. Finally, the wash-coat can be applied in zones of different composition, with for example higher metal loadings in the front zone in order to increase the light-off performance.[46,51,63,66] This leads to a more efficient use of the precious metals and allows for a sharpened segregation, which was shown efficient in the case of Pd-Rh catalysts because they tend to form alloys through migration over distances in the order of 10 µm.

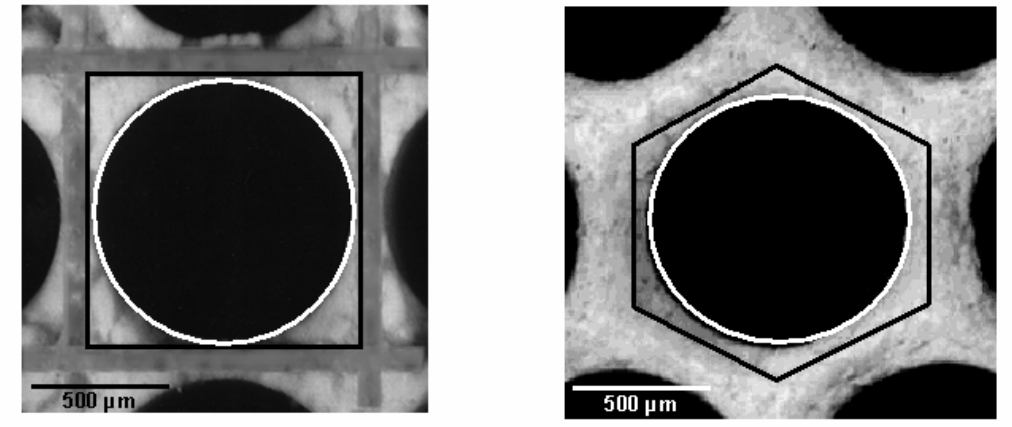

Figure 1.13: Photograph of the wash-coat layer on square-cell (left) and hexagonal-cell (right) monolithic substrate, the wash-coat amount being the same on both monoliths. Adapted from references [53] and [61].

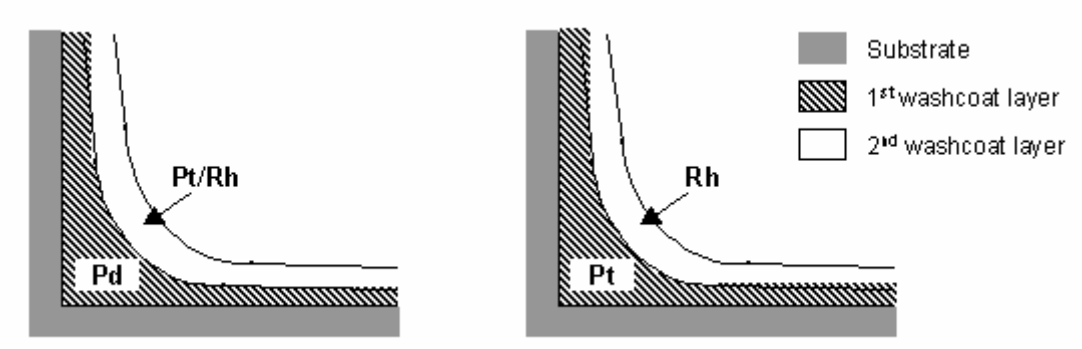

Figure 1.14: Schematic showing a bilayer wash-coat with the typical precious metals location.

3.2 Catalyst materials in the wash-coat

A typical TWC wash-coat can contain up to 3 noble metals, 3 to 4 support materials and 4 to 5 stabilisers or additives to ensure high performance and durability.[46] Its main constituent is a high SSA support, typically 100 m²/g, usually

made of 70 to 80 wt% gamma-alumina (γ-Al_2O_3) with lately an increasing use of zirconia (ZrO_2) as a support for Rh.[3,48-49,52,63] This support material is modified by additives, which are improving the catalyst thermal stability, resistance to poisoning, activity and storage properties.[3,48-52,61,67-68]

The second important ingredient of the wash-coat represents 10 to 30 wt% and is made of rare-earth metal oxides. The most common is ceria (CeO_2), which is mainly used as an oxygen storage material.[3-4,30,48-53,57] The concept of oxygen storage capacity (OSC) was introduced to extend the operating window of the TWC around the stoichiometric point in order to compensate for the delay time between the λ-sensor signal and the feedback to the engine. CeO_2 works as a buffer thanks to the two easily accessible oxidation states of Ce according to the redox reaction (1.3)

$$CeO_2 \leftrightarrow CeO_{2\,(1-x)} + x\,O_2 \qquad (1.3)$$

where $0 \leq x \leq 0.25$. Under reducing conditions, CeO_2 is releasing oxygen and extending the TWC activity for the CO and HC oxidation to richer atmospheres. While, under oxidising conditions, the material is storing oxygen allowing for higher NO_x conversions during the lean excursions. Figure 1.15 is illustrating this mechanism. This process is facilitated by a high SSA and close contact of CeO_2 with Pt.[52-53] Theoretically, the x value in reaction (1.3) can reach 0.25 and the OSC is directly related to the total amount of CeO_2 in the catalyst material composition. However, in real conditions, the maximum storage capacity is not achieved due to kinetic limitations.[4,30] The addition of lanthanum oxide (La_2O_3) or ZrO_2 to CeO_2 to form solid solutions both improves its thermal stability and its OSC.[4,46,51,53,57,68] The effect of La_2O_3 on the OSC is explained by the creation of oxygen vacancies through replacement of a tetravalent Ce ion by a trivalent La ion. The efficacy of ZrO_2 can be attributed to the difference in cation size easing the migration of oxygen from the bulk under reducing conditions. The latter pushes the ceria OSC close to its theoretical limit when an equimolar solid solution of CeO_2-ZrO_2 (CZ) is produced in a regular arrangement. CZ has however the disadvantage to present a much too small SSA to be used in real conditions. This issue was solved by mixing Al_2O_3, which serves as a barrier to CZ sintering, with the CZ solid solution and resulted in lower light-off temperatures.[53,57,63]

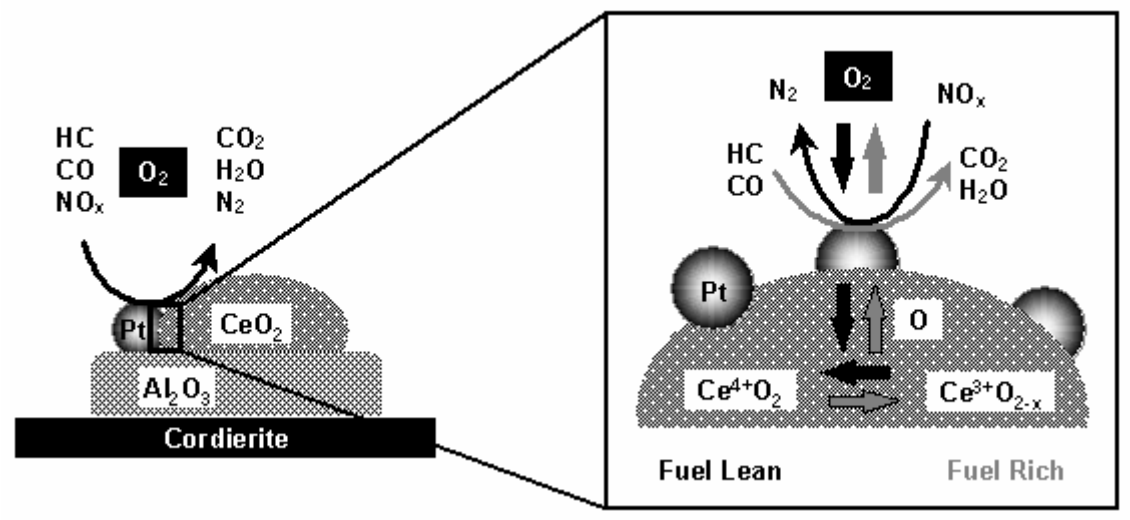

Figure 1.15: Schematic showing a TWC using ceria as oxygen storage material as well as the oxygen transfer in lean and rich operation.

Ceria has complementary roles besides the OSC. It, for instance, improves the catalytic activity at low temperatures, except for Pd, which is interesting for the cold start.[46,52] Mixed with ZrO_2 and yttria (Y_2O_3), it also inhibits the Pt sintering behaviour and allows for Pt re-dispersion through the formation of a strong Pt-O-Ce bond in oxidising conditions, which is desired for an enhanced catalyst durability.[57,67,69] One of its drawbacks is that it increases the sulphur storage capacity of the support and therefore prolongs the detrimental effect of sulphur on the catalytic activity.[52]

Low concentrations of rare-earth oxides, such as La_2O_3 or CeO_2, and alkaline earth oxides, *e.g.* barium oxide (BaO), are added to Al_2O_3 as a thermal stabiliser.[48-50,52,57,63,66,68] They also help stabilise the precious metals.[50,67,69] Finally, they can enhance the catalytic activity, which for instance allowed the use of Pd as a TWC.[4,52,63,66,68]

Furthermore, alkali metals and alkaline earth metals, *e.g.* Ba, Sr or K, usually act as catalyst promoters, oxygen buffers or NO_x storage materials.[4,48-51,55-57,70-71] They are able to stabilise the surface oxygen atoms or to promote the water gas shift reaction. The latter favours both CO and NO conversions thanks to the consumption of CO and the formation of molecular hydrogen (H_2), which is a good NO_x reductant.

Ni, Fe or Mn oxides, Ge- and Cu-based systems are used as scavengers of hydrogen sulphide (H_2S).[4,46,49-50,52] This gas is formed in rich conditions through the reduction of sulphates accumulated on basic support materials during the lean operation. As it causes a very bad odour and it is toxic, it should be avoided. It is

therefore stored in the form of sulphides under reducing conditions, via formation of water, and released as sulphur dioxide (SO_2), which is less odorous, in oxidising conditions.

Titania (TiO_2) or Fe-compounds are introduced as additives in Al_2O_3 to enhance the sulphur tolerance of NSR catalysts.[53,57,61] These systems are indeed very sensitive to the presence of sulphur in the fuel because their NO_x storage materials tend to form sulphates, which are more stable than their nitrate counterparts, and therefore reduce the NO_x storage capacity of the catalyst.[4,48,53,55-57,61] Here, the strategy to reduce the sulphur poisoning problem is to inhibit the sulphate formation, through the control of the support acidity, and to favour its desorption, thanks to the inhibition of the sulphate particles growth.[53,57,61] When Fe-compounds are used, the TWC performance is increased thanks to their OSC properties and to a reduction in the CO poisoning of the Pt active sites.[57]

TiO_2 stabilised by tungsten oxide (WO_3) can be used as support material for vanadium-based NH_3-SCR types of catalyst. They are mainly used for heavy duty vehicles.[4,48,57]

As already mentioned above, ZrO_2 is used as a support for Rh or as a component of oxygen storage materials. Additionally, it is a good support when K is used as NO_x storage material at high temperature. When combined with 30 % TiO_2, the K storage capacity after aging in a sulphur containing atmosphere is improved thanks to the reduction in both sulphate formation and solid-phase reaction.[57] As for the CZ-type of supports, the formation of a nano-composite consisting of Al_2O_3 and ZrO_2-TiO_2 improves the thermal stability of the latter.[57]

Perovskite-type of oxides have been tested as a support material in HC-SCR applications and introduced in the self-regenerating TWC developed by Daihatsu. In the latter case, the precious metals sintering is inhibited thanks to their alternative capture and release by the perovskite oxide structure when the exhaust atmosphere switches between oxidising and reducing conditions, respectively.[48,51,57,72]

Zeolites are introduced in DOC or TWC materials as a HC trap during the cold start.[3-4,46,48,50,63] The HC are stored at low temperature and then released and oxidised when the temperature of the catalyst is high enough. They therefore improve the Pt catalytic performance for the CO oxidation and the apparent performance for HC (due to absorption). A too soon desorption of the HC can be avoided by the addition of Ag to the adsorbent material.[63] Zeolites can also enhance

the activity for the NO_x reduction reaction through the increased local HC concentration.[4]

Metal-exchanged zeolites, usually of the MFI-type, have been tested for NO direct decomposition, NH_3-SCR and HC-SCR applications, but they have a low activity or are easily damaged at high space velocities and at temperatures higher than 600 °C (873 K). They are additionally sensitive to sulphur and water, which has limited their commercial introduction until now.[4,30,48,52,56-57] In combination with an oxidation and a NSR catalyst, Cu/zeolite exhibits an enhanced activity for the NO_x reduction.[57] It is assumed that NH_3 and HC are stored under the reductive conditions and released to react with NO during the lean operation.

All materials described here above constitute the support and the promoters of the automotive catalyst materials. The active phase is made of 1-2 wt% precious metals, in the form of dispersed nanoparticles obtained by incipient wetness impregnation of the support, followed by drying and calcination.[3,52] Pt and Rh are the most commonly used noble metals, their amount usually varying between 1 g/l and 2 g/l of catalyst with a typical Pt:Rh ratio of 5-20:1.[3,48-49,52] Recently, with the increase in Pt prices, Pd is often replacing Pt with loadings ranging between 2 g/l and 10 g/l.[3,46-49,52] Of course, as the formulation choice depends on the exhaust gas purification strategy, on the engine type and its calibration, on the emission levels to be reached and on the converter cost target, those numbers can change a lot.[3,47,51] Early oxidation catalysts and TWC were often using Pt/Pd or Pt/Rh combinations, respectively. Today's TWC's tend to contain Pd/Rh formulations, but Pt/Rh or Pd only compositions are also found.[3-4,46-47,50-51] When the NO_x regulation is strict, Rh has to be used and, for diesel applications, Pt is often selected.[3,50-52,57] Pd is an alternative to Pt/Rh catalysts, especially for light-off applications. It is then employed with higher loadings for a similar cost as Pd is cheaper.[3,46,50]

Pt, Pd and Rh have been rapidly selected because of their combined high activity for TWC reactions, good thermal stability and high resistance to poisons as compared to base metals, such as Ni, Cu, Co, Mn, etc., and other platinum group metals (PGM), like Ir or Ru.[3-4,46-47,50,63,73] A comparison of the NO reduction by CO in excess of oxygen on Pt, Pd, Rh and Ir has shown that Ir is the best candidate because it is the only one showing a prevalence for the CO + NO reaction over the CO + O_2 reaction even at high temperatures.[73] However, in practice, Ir cannot be used because it forms volatile oxides in typical automotive exhaust conditions.[4,46,73]

Ru is also very active and selective, but its oxides are so volatile that the catalyst is rapidly lost during usage.[4,46] Base metals are usually less active and more easily oxidised, which further impact their activity. They are additionally not very thermally stable as they can react with the support material and are not resistant to sulphur, lead and halides poisoning.[3-4,46-47,50,63]

Rh is mainly used for its activity in the selective NO reduction reaction, while Pt and Pd are employed for the HC and CO oxidation.[30,46-47,49-50,52,57] Rh is already active for the CO + NO reaction at low temperatures and it tolerates an excess of O_2 as illustrated by Figure 1.16.[49,66,73] As opposed to Pt and Pd, NO dissociatively adsorbs on Rh and can form dinitrosyls with Rh, which favours the N_2 formation.[49] Furthermore, Rh supported on ZrO_2 catalyses the steam reforming reaction (1.4).[3,30,49,61] This property has shown advantages in the reduction of sulphates thanks to the *in situ* production of H_2, which was the most efficient reductant.[61]

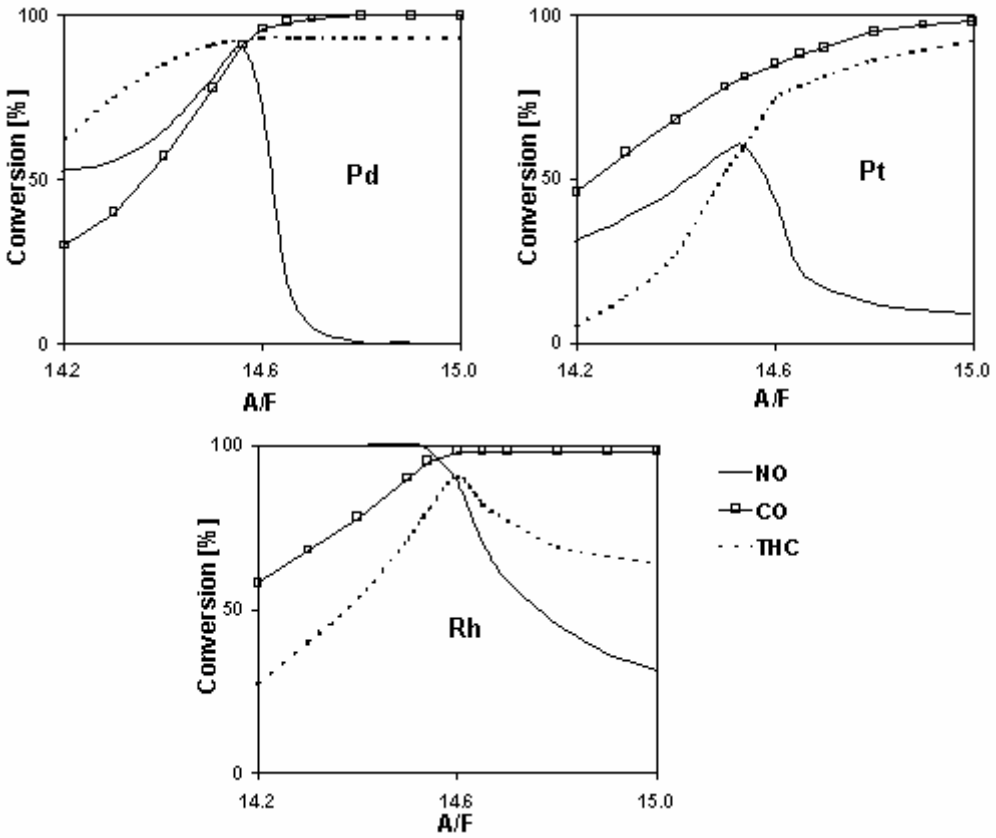

Figure 1.16: NO, CO and total hydrocarbons (THC) conversions as a function of A/F on Pt, Pd and Rh catalysts with respective loadings of 0.5 g/l, 0.05 g/l and 0.05 g/l. The measurements have been performed on an engine exhaust in static conditions. Adapted from reference [66].

$$C_mH_n + 2\ m\ H_2O \rightarrow m\ CO_2 + (2\ m + 0.5\ n)\ H_2 \quad (1.4)$$

Pt is an active player in the regeneration of CR-DPF and in the oxygen storage and NSR processes.[50,52-53,55-57] In the latter case, the action range of the Pt is a few μm for the reduction of $Ba(NO_3)_2$ but only a few nm for $Ba(SO_4)$.[57] In both the CR-DPF regeneration and the NO_x storage step in NSR catalysts, Pt is employed for its ability to oxidise NO to NO_2.[57] Pt is also a good catalyst for HC-SCR and NH_3-SCR applications, but in the former type it tends to form excessive amounts of N_2O.[4,48,50] It also shows activity in the water-gas shift reaction (1.5).[30] Pd is efficient for the HC oxidation in cold-start catalysts and for the oxidation of methane emitted by engines fuelled with CNG.[30,63]

$$CO + H_2O \rightarrow CO_2 + H_2 \quad (1.5)$$

Pt, Pd and Rh are very good active sites for automotive catalysts but each of them has its own problem. Pt tends to sinter under long exposure to oxidising conditions at high temperature, which is causing a lost in catalytic activity with increasing mileage.[4,46-47,67] Pd forms a stable oxide, PdO, which is active for oxidation reactions but not for the NO reduction. It therefore leads to a narrow A/F ratio window for high NO_x conversions.[4,30,52] Pd is also more sensitive to lead, sulphur and phosphorus (P) poisoning than Pt, which is the reason why it was not used in TWC until 1989.[30,46,50,52,63] Rh easily forms Rh oxide (Rh_2O_3), which can react with support materials, such as alumina. Furthermore, as Rh is mainly used for the NO reduction where its metallic state is active, the latter should be easily recovered during excursions in slightly reducing conditions, which is not the case on alumina.[3-4,46] When Pd and Rh are mixed in the catalyst formulation, PdO tends to segregate on the Rh surface or they can form alloys after migration of the pure metals over distances as big as 10 μm.[30,46,63,66] This usually has an impact on the NO reduction performance. Some of those issues have been partially solved through the development of better support materials or new coating technologies.[4,46,48,50-52,57,66-67,72]

In an attempt to reduce the amount of PGM, especially Rh, in the automotive exhaust aftertreatment systems, other metals have been tested as active sites. For HC-SCR in lean conditions, Ag supported on Al_2O_3 and Cu or Co in zeolites are attractive catalysts but they lack durability.[4,30,48-49,52] For NH_3-SCR, vanadia (V_2O_5) is used in heavy duty vehicles applications and could be replaced by metal-exchanged

zeolites containing Cu, Co, Fe or Ce.[4,48,57] Base metal oxides and mixed oxides, *e.g.* Cu, Mn, Co, Cr oxides, have been tested as CO and HC oxidation catalysts and showed good light-off characteristics for those reactions, but were not durable enough.[63] Au could be a promising active site for the CO oxidation in case it is finely dispersed on a reducible support, such as CeO_2 or TiO_2.[63]

3.3 Challenges

As was shown in paragraph 1.2, the legislation regulating emissions from passenger cars is getting stricter and stricter, which means the catalyst performance and its durability have to be further improved. At the same time, the engine fuel consumption has to continuously decrease, leading to a shift to lean-burn combustion, which has an impact on the exhaust gas composition and temperature. This includes a trade-off between the fuel economy, the PM and the NO_x emissions to be taken into account when designing the complete engine-catalyst system.[4,60,74] The regeneration of a DPF and the pressure drop it causes are usually increasing the fuel consumption by 2-5 %. A better combustion will decrease both the PM and the fuel consumption but increase the NO_x, which if reduced by HC-SCR or NSR, will require more fuel. Finally, as shown by Figure 1.17, the PGM prices are fluctuating a lot and increasing tremendously since 3 years, especially for Pt and Rh. Furthermore, about 66 % of the Pt and 87 % of the Rh global supplies go to the automotive catalysts.[47] It means that a change in the legislation or automotive catalyst technology can affect both the supply and the price of the PGM.[3] This is a very uncomfortable economical situation for the car industry given the fact that it takes about 3 years to develop a car, which will be on the market for approximately 6 years.[39]

This means that the challenges for future automotive catalysts are threefold. First of all, the material weaknesses, such as their limited thermal resistance and their susceptibility to sulphur poisoning, have to be tackled. Secondly, their performance has to be extended to a larger range of operation covering for instance the low temperatures from the cold start and the high oxygen concentrations obtained in lean conditions. At last, the PGM amount should be reduced as much as possible, while keeping or even improving the catalytic activity.

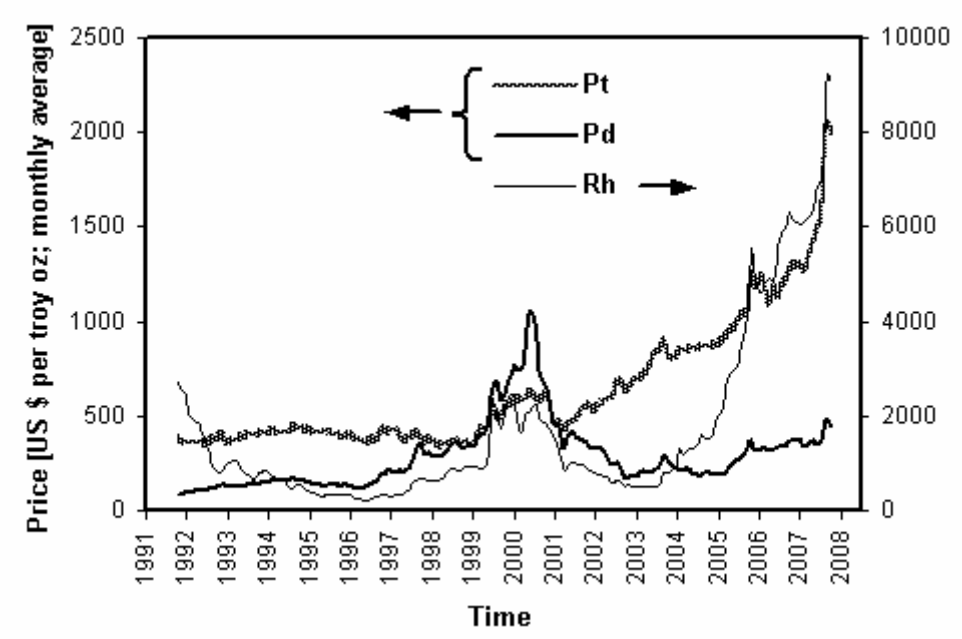

Figure 1.17: Evolution of the average monthly prices of Pt, Pd (left y-axis) and Rh (right y-axis) from July 2002 to April 2008 as published by Johnson Matthey.[75] 1 troy ounce (troy oz) is equivalent to 0.0311 kg; it is the weight unit traditionally used for precious metals such as Pt.

3.3.1 Reduction of catalyst materials weaknesses

In order to improve the fuel economy, more engines are run in lean conditions, which means the exhaust gases usually have a lower temperature.[50] One way to compensate for this lower temperature causing a decrease in the catalytic activity is to place the catalyst in close-coupled position. This means it is then at risk for thermal damage during modes at which elevated temperatures are reached. It has been observed that the OSC of TWC is decreasing with the mileage due to the sintering of both ceria and the PGM particles.[30,46,51,68] This can be responsible for CO and NO_x breakthrough emissions. NSR catalysts require a close contact between the Pt and the NO_x storage material and are therefore very sensitive to sintering and to side solid reactions with other components of the wash-coat.[53,55-56] For that reason, precious metal particles anchoring, improved metal-support interactions and supports with a high thermal stability are desirable.[3,48,57,67-69,72]

Nowadays, even though the sulphur content of transportation fuels has reached very low levels, it is still causing problems, especially in aged catalysts and for NSR and CR-DPF applications.[3-4,26-27,48,50,52-53,61] Sulphur causes both a reduction in maximum conversion and in low temperature performance of TWC.[52] It competes

with NO in the NO oxidation reaction used for the DPF continuous regeneration; it then forms sulphur trioxide (SO_3), which combines with water and adsorbs on the soot, increasing their weight.[27,30,50] Both events have a negative effect on the filter regeneration efficiency. Finally, sulphur is stored as sulphates in NSR catalyst materials, requiring high temperature regeneration and therefore thermally resistant materials.[4,48,50,53,61] This recovery process is not ideal as it can cause smell problems due to the production of H_2S. This means that new sulphur-resistant NO_x absorbers or systems that can easily regenerate the NSR material by producing SO_2 under mild conditions, are needed.[48,50] Zn, Ca, P, Si and Mn are other typical poisons of automotive catalysts that can block the monolith channels and the active sites. They can also produce undesirable products by reaction with catalyst components, *e.g.* cerium phosphate.[3,51] Those problems should be solved by the introduction of better fuels, modified lubricants formulations and less sensitive TWC compositions.

3.3.2 Extension of the catalyst operation range

A poor flow distribution in the monolith can be responsible for local high temperature peaks that can cause heavy damage to the catalyst.[48] It will also have some influence on the catalyst performance and aging.[3,30] So, attention should be paid to the design of the monolith, connecting cones and exhaust pipes.

The PM filtration and filter regeneration strategies are very important. The elimination of nanoparticles with a diameter of less than 50 nm, which form the largest number of particles, is a big challenge.[4] A sudden combustion of a thick layer of carbon can lead to very high temperatures and hence to cracking of the filter walls.[30,50] Therefore, materials with a high heat resistance and an appropriate porosity are essential. The continuous regeneration might in this view be an advantage, but in this case one has to pay special attention to the coating, which should not block the interconnecting pores of the walls.[50] Moreover, for CR-DPF, the exhaust gas temperature is a critical parameter.[4,46,50] Therefore, soot oxidation catalysts active below 250 °C (523 K) should be developed.

Several engine technologies have been introduced to improve the fuel economy, such as downsizing, direct injection, turbo-charging, EGR, etc. They have an impact on the exhaust gas composition and its temperature but also on the backpressure

requirements of the converters.[51] Lean-burn combustion is pushed to higher A/F ratios, challenging the catalyst designers to reduce NO_x in large excess of oxygen at low temperatures.[4,30,46,48,50,52-53] In these conditions, the NO_x reduction by HC-SCR or NH_3-SCR is favoured compared to the competitive oxidation reactions, but only in a restricted temperature window and with a limited NO_x conversion, especially for the HC-SCR. Furthermore, N_2O and NH_3 emissions, due to partial reduction of NO and to NH_3 slip, respectively, can be an issue. So, further improvements in NO_x SCR activity and selectivity are a must.

With the increasing legal requirements on HC and CO emissions, the cold start is now becoming an issue.[3,30,46,52,63] They require oxidation catalysts active at very low temperature, while their light-off is typically around 200-300 °C (473-573 K).[3,30,63] The same holds for the exhaust gas purification from lean-burn engines, where the temperature can be as low as 120 °C (393 K).[50,51] To help solving this issue, the close-coupled configuration is often used with, as implication, the need for highly thermally stable materials that remain active after exposure to temperatures as high as 1050 °C (1323 K).[3,63]

The introduction of alternative fuels as a mean to reduce CO_2 emissions also has an impact on the TWC requirements.[3,30,51] CNG will mainly produce CH_4 as HC, which has a higher activation energy than HC's usually produced by gasoline engines. The use of ethanol in gasoline leads to lower exhaust gas temperatures and aldehydes can be produced, especially on a cold catalyst.

3.3.3 Catalyst cost reduction

Huge improvements in the performance of automotive catalysts systems have already been achieved, especially for oxidation catalysts and TWC, but the most dramatic ones have been achieved through combined technologies including engine management, control systems and exhaust gas converters design.[50,63] This will most probably remain true for the future where computer modelling might become an asset to compare the efficiency of several converters configurations and sizes with different catalysts formulations at varying engine exhaust conditions.[30,51] All these improvements, including the ones that would cover the issues of paragraphs 3.3.1 and 3.3.2, have of course a direct impact on the cost as each of them can be accompanied by a reduction in PGM usage or a decrease in emissions at equal

price. The largest efforts should therefore be focussing on simplified catalyst material formulations, improved thermal stability, low temperature oxidation catalysts, DPF technology and de-NO_x systems able to work in lean conditions.[46,51] Taking the challenge to reduce the cost is worth as estimations of the impact of the compliance to the Euro 5 and Euro 6 legislations vary between 202 € and 900 € per vehicle.[10]

Additional cost reductions could be achieved by a more appropriate usage of the PGM. Firstly, the PGM loading and ratio should be optimised as they have for instance an impact on the HC light-off temperature, which can be of almost 100 °C (373 K).[3,63] The same holds for the PGM choice for each monolith and the monoliths sequence when multibrick converters are used as they influence the total conversion.[3] Secondly, the ideal precious metal particle should be determined, synthesised and kept after catalyst aging. As examples, the NO reduction by CO was shown to be sensitive to the Rh particle size and the CO oxidation on Rh is structure sensitive.[52,76] Finally, the support material should be carefully selected as it can have a strong influence on the PGM catalytic activity, their dispersion, their valence state and their aging behaviour, *i.e.* their tendency to sinter, get poisoned and be involved in solid state reactions.[3,67] The former is illustrated for Rh by Figure

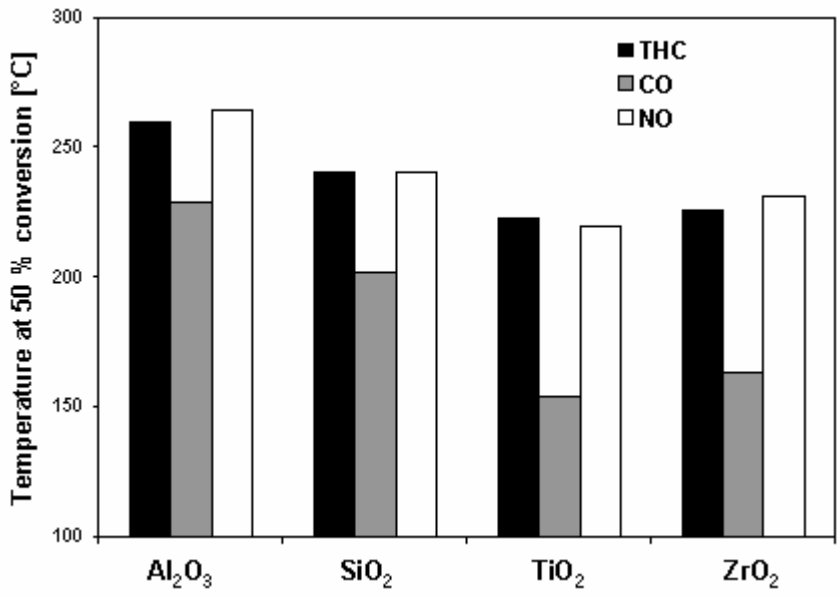

Figure 1.18: Temperature at 50 % conversion of HC, CO and NO for 0.5 wt% Rh supported on Al_2O_3, SiO_2, TiO_2 and ZrO_2. The measurements have been performed on 1.5 g of catalyst in a gas mixture containing 0.65 % CO, 10 % CO_2, 0.7 % O_2, 2200 ppm NO, 2500 ppmC C_3H_6, 10 % H_2O with N_2 balance and flowing at 6 l/min with a ramp up temperature of 10 °C/min.

1.18, which shows the influence of the support on the light-off of Rh for the TWC reactions.

A last challenge for the PGM usage is to keep the formulations as much as possible close to the mining ratio in order not to disturb the market.[66]

3.3.4 Strategy to meet the material-related challenges

Automotive catalysis being a mature technology, it can only be improved by the introduction of new breakthroughs. The ideas generating these technical advances in material science can be found thanks to the synthesis and study of model systems with controlled geometries, compositions, interactions and dimensions in well-known environments. This approach limits the amount of possible parameters influencing the experimental results, facilitates their interpretation and permits their integration in or extrapolations to more complex combinations. The determination of the active sites and the best interactions in these model systems can be done by fundamental surface science studies.[76] The powerfulness of surface science applied to automotive catalysis has also been nicely illustrated by Bowker[77] and Newton.[78] They show the importance to study the catalysts at the atomic level, under working conditions and in an environment as close as possible to the reality.

4 Scope and outline of the thesis

The aim of this PhD thesis was to enlarge insight into the fundamental issue of metal-support interactions for Pt- and Rh-based exhaust gas emission catalysts. This has been done by synthesising model catalysts made of well-defined Pt and Rh nanoparticles dispersed on various oxide supports, differing in their chemical composition and pore architecture. Infrared spectroscopy (IR) in combination with CO or NO as probe molecule, together with detailed X-ray Absorption Fine Structure spectroscopy (XAFS) studies allowed shedding light on the electronic properties of these supported Pt and Rh nanoparticles. In addition, the catalyst materials have been evaluated for two reactions relevant to the automotive exhaust gas converters: the CO oxidation and the NO reduction by CO. Combining all results, it has been possible to derive relationships between the chemical composition of the support material, the electronic density of the supported metal nanoparticles and their catalytic activity.

In **Chapter 2**, a systematic study on Pt-support interactions has been undertaken by using a series of zeolite Y supports containing different monovalent (H^+, Na^+, K^+, Rb^+, and Cs^+) and divalent (Mg^{2+}, Ca^{2+}, Sr^{2+}, and Ba^{2+}) cations. Well-defined Pt nanoparticles occluded in the supercages of zeolite Y have been studied by CO IR spectroscopy at 50 °C (323 K) and during temperature programmed desorption (TPD). The tendencies in IR band red-shift and in linear to bridge band relative intensities could be correlated to intrinsic properties of the cation promoting the Pt, such as the Lewis acidity. Furthermore, it was possible to directly associate the changes in the IR signal and the light-off temperature of the different samples.

The results presented in Chapter 2 for zeolite Y-supported Pt nanoparticles have been extended to the study of different porous oxides in **Chapter 3**. More specifically, Pt particles have been loaded on all-silica supports varying by their pore size. ITQ-1 was used as a microporous support, Si-MCM-41, Si-MCM-48 and Si-SBA-15 as mesoporous ones and amorphous silica to cover the macroporous materials. Additionally, the composition effect observed in Chapter 2 for the zeolite Y series was verified on four silica-supported Pt catalysts promoted by Na^+, Cs^+, Mg^{2+}, and Ba^{2+}, respectively. The impact of the pore-size and the chemical composition were correlated to the activity of the different samples and compared to the results obtained in Chapter 2.

As was demonstrated in Chapters 2 and 3, IR spectroscopy is a powerful method to characterise the electron density of supported Pt particles. It, however, presents at least one disadvantage as it is an indirect measurement method requiring a probe molecule like CO or NO. Consequently, it cannot be used to analyse Pt in realistic reaction conditions. Therefore, in **Chapter 4**, a new spectroscopic method has been explored for probing the electronic properties of supported Pt nanoparticles in porous oxides. The method is based on the use of Atomic X-ray Absorption Fine Structure spectroscopy (AXAFS) and has been applied to 14 of the supported Pt catalysts mentioned above. The intensity of the AXAFS signal is compared with the CO linear to bridge band intensity ratios as determined by IR spectroscopy on the same set of samples. Since the method does not need any probe molecule, it offers potential for measuring the electronic properties of supported metal nanoparticles under reaction conditions in real time.

Inspired by the results of Chapter 2 on promoted zeolite Y-supported Pt nanoparticles, we have extended our approach to zeolite Y-supported Rh

nanoparticles in **Chapter 5**. For this purpose, well-defined Rh particles of about 1 nm to 1.5 nm diameter in average have been deposited on zeolite Y in its proton form as well as ion exchanged with alkaline (Na^+, K^+, Rb^+, and Cs^+) and alkali-earth (Mg^{2+}, Ca^{2+}, Sr^{2+}, and Ba^{2+}) metal ions. As for the Pt catalysts, the influence of the support composition on the Rh was studied by CO IR spectroscopy and related to its catalytic activity in the CO oxidation reaction.

As Rh is a very important catalyst for the NO reduction reaction in automotive exhaust gas converters, the work done in Chapter 5 was extended in **Chapter 6** to the study of NO reduction on zeolite Y-supported Rh. Therefore, NO was used as a probe molecule in IR spectroscopy and the NO reduction by CO reaction was selected for the evaluation of the promoter impact on the Rh catalytic activity.

Finally, in **Chapter 7**, conclusions are drawn from the experimental work described in this PhD thesis. Based on the systematic fundamental study presented, catalyst designers should be able to better understand the impact of more complex catalyst material formulations.

References

[1] Elvingson, P.; Agren, C. *Air and the Environment* Swedish NGO Secretariat on Acid Rain, Box 7005, SE 402 31 Göteborg, Sweden, ISBN 91-973691-7-9, **2004**.

[2] EU Commission Communication to the Council and the European Parliament *Implementing the Community Strategy to reduce CO_2 emissions from cars: sixth annual communication on the effectiveness of the strategy*, COM(2006) 463, 24 August **2006**.

[3] Ertl, G.; Knozinger, H.; Weitkamp, J. (Eds.) *The Handbook of Heterogeneous Catalysis*, Wiley-VCH, Weinheim; Volume 4, **1997**.

[4] Twigg, M. V. *Appl. Catal. B: Environmental* **2007**, *70*, 2.

[5] Forster, P.; Ramaswamy, V.; Artaxo, P.; Berntsen, T.; Betts, R.; Fahey, D.W.; Haywood, J.; Lean, J.; Lowe, D.C.; Myhre, G.; Nganga, J.; Prinn, R.; Raga, G.; Schulz, M.; Van Dorland, R. 2007: *Changes in Atmospheric Constituents and in Radiative Forcing*. In: Climate Change 2007: The Physical Science Basis. Contribution of Working Group I to the Fourth Assessment Report of the Intergovernmental Panel on Climate Change [Solomon, S.; Qin, D.; Manning, M.; Chen, Z.; Marquis, M.; Averyt, K.B.; Tignor, M.; Miller, H.L. (eds.)]. Cambridge University Press, Cambridge, United Kingdom and New York, NY, USA (ISBN 978 0521 88009-1 Hardback; 978 0521 70596-7 Paperback).

[6] European Automobile Manufacturers' Association (ACEA) *Reducing CO_2 emissions from cars towards an integrated approach* on ACEA website: http://www.acea.be/images/uploads/pub/CO2_Leaflet_ENG.pdf, July **2007**.

[7] European Environment Agency; EEA Report No 9/2006, *Greenhouse gas emission trends and projections in Europe 2006*, ISSN 1725-9177, Luxembourg: Office for Official Publications of the European Communities, 2006, ISBN 92-9167-885-6, © EEA, Copenhagen, **2006**.

[8] European Environment Agency; EEA Report No 5/2007, *Greenhouse gas emission trends and projections in Europe 2007*; ISSN 1725-9177, Luxembourg: Office for Official Publications of the European Communities, 2007, ISBN 978-92-9167-973-7, © EEA, Copenhagen, **2007**.

[9] Goossens, Y.; Meneghini, G. P. *Air Pollution* in European Parliament Fact Sheets, July 2006, 4.9.6. on the European Parliament website: http://www.europarl.europa.eu/facts/4_9_6_en.htm.

[10] European Automobile Manufacturers' Association (ACEA) *Air quality: Cost-effectiveness must guide progress*, **2007**, on the ACEA website: http://www.acea.be/index.php/news/category/air_quality/.

[11] Directorates General for Economic and Financial Affairs, Enterprise, Transport and Energy, Environment, Research and Taxation and Customs Union *The Auto-Oil II Programme – Final report*, **October 2000**, on the European Commission, DG Environment website: http://ec.europa.eu/environment/autooil/index.htm.

[12] Proost, S.; De Ceuster, G.; van Herbruggen, B.; Logghe, S.; Ivanova, O.; Carlier, K. *TREMOVE 2 – Final report - Part 3: Policy runs*, **15 December 2006**.

[13] Giannouli, M.; Samaras, Z.; Keller, M.; deHaan, P.; Kallivoda, M.; Sorenson, S.; Georgakaki, A., *Sci. Total Environ.* **2006**, *357*, 247.

[14] World Health Organization *Health aspects of air pollution: Results from the WHO project "Systematic review of health aspects of air pollution in Europe*, World Health Organization, Regional Office for Europe, Scherfigsvej 8, DK-2100 Copenhagen, **2004**.

[15] Commission Recommendation 1999/125/EC of 5 February 1999 relating to the *reduction of CO_2 emissions from passenger cars*, Official Journal of the European Communities, **1999**, L 40:49–50.

[16] Markus, M.; Vance, C.; Gühnemann, A.; Buchheim, S. *Preparation of the 2003 review of the commitment of car manufacturers to reduce CO_2 emissions from M1 vehicles - Final Report of Task A: Identifying and assessing the reasons for the CO_2 reductions achieved between 1995 and 2003*, German Aerospace Centre-Institute of Transport Research, Rutherfordstrasse 2, 12489 Berlin, Germany, 8 December **2004**.

[17] European Federation for Transport and Environment *How clean is your car brand? - The car industry's commitment to the EU to reduce CO_2 emissions: a brand-by-brand progress report*, T&E publication, rue de la Pépinière 1, B-1000 Brussels, October **2006**.

[18] European Federation for Transport and Environment *Reducing CO_2 emissions from new cars: A study of major car manufacturers' progress in 2006*, T&E publication, rue de la Pépinière 1, B-1000 Brussels, November **2007**.

[19] Commission of the European Communities *Results of the review of the community strategy to reduce CO_2 emissions from passenger cars and light-commercial vehicles - Executive summary of the impact assessment*, **2007**, Commission Staff Working Document, SEC(2007) 61, 7 February 2007.

[20] EU Commission Press Release *Commission proposal to limit the CO_2 emissions from cars to help fighting climate change, reduce fuel costs and increase European competitiveness*, IP/07/1965, 19 December **2007**.

[21] EU Commission Communication *Proposal for a regulation of the European Parliament and of the Council: Setting emissions performance standards for new passenger cars as part of the Community's integrated approach to reduce CO_2 emissions from light-duty vehicles*, COM(2007) 856, 2007/0297 (COD), **2007**.

[22] European Federation for Transport and Environment *Transport and climate change policies in Environment Council of 20 February in Brussels*, Letter from the T&E to the Council of 2 December **2007**.

[23] European Union *Motor vehicles with trailers: polluting emissions*, Gateway website: http://europa.eu/scadplus/leg/en/lvb/l21047.htm; July **2007**.

[24] Agren, C. *EU Legislation on air pollution and acidification*, Environmental Factsheets n° 10, June **2002**, Swedish NGO Secretariat on Acid Rain; Box 7005, 40231 Götenborg, Sweden.

[25] Schulte-Braucks, R. *European emissions legislation for mobile sources*, CAPoC7 Conference, Brussels, August **2006**.

[26] ACEA *Car emissions and Euro 5*; ACEA, FIA & ADAC workshop, Brussels, **2005,** http://www.fiafoundation.com/resources/documents/2371837 66__acea_fia_adac_meeting_5_april.pdf.

[27] ACEA; Alliance; EMA; JAMA *Worldwide fuel charter*, Fourth edition, **2006**.

[28] Communication from the Commission to the Council and the European Parliament *Proposal for a Directive amending Directive 98/70/EC (...) and introducing a mechanism to monitor and reduce GHG emissions from the use of road transport fuels and amending Council Directive 1999/32/EC (...) and repealing Directive 93/12/EEC*, COM(2007) 18 final, 2007/0019 (COD), **2007**.

[29] Jensen, P.; Karlsson, J.; Huntington, J. Den Boer, E.; Klein, L.; Radovanac, M. *Sectors that drive environmental change: Transport*, Europe's environment - The fourth assessment, Chapter 7, Section 7.2, European Environment Agency, Kongens Nytorv 6, 1050 Copenhagen, Denmark, ISBN 978-92-9167-932-4, **2007**.

[30] Koltsakis, G. C.; Stamatelos, A. M. *Prog. Energy Combust. Sci.* **1997**, *23*, 1.

[31] European Parliament and Council *On the promotion of the use of biofuels or other renewable fuels for transport*, Directive 2003/30/EC, OJ L123, 15.05.**2003,** 42.

[32] Bockwinkel, A.; Vanham, B. *Selling CO_2: Impact of marketing, advertising and CO_2 labelling on consumer behaviour & CO_2-related car taxes and incentives in the EU*, European Automotive Forum 2008, Brussels, January 23, **2008**.

[33] Smokers, R.; Vermeulen R.; van Mieghem, R.; Gense, R.; Skinner, I.; Fergusson M.; MacKay, E.; ten Brink, P.; Fontaras, G.; Samaras, Z. *Review and analysis of the reduction potential and costs of technological and other measures to reduce CO2-emissions from passenger cars*, Nederlandse Organisatie voor Toegepast-Natuurwetenschappelijk Onderzoek (TNO), Final report 06.OR.PT.040.2/RSM, Schoenmakerstraat 97, Delft, The Netherlands October **2006**.

[34] Knudsen, T. *Better roads: A denied source of emissions reduction*, European Automotive Forum 2008, Brussels, January 23, **2008**.

[35] De Strooper, J.; Caster, R. *E^+ project in Belgium: Ecodriving in practice*, European Automotive Forum 2008, Brussels, January 23, **2008**.

[36] Vikas, A. *CO_2 saving potential of complementary car technologies*, European Automotive Forum 2008, Brussels, January 23, **2008**.

[37] ten Brink, P.; Skinner, I.; Fergusson M.; Haines, D.; Smokers, R.; van der Burgwal, E.; Gense, R.; Wells, P.; Nieuwenhuis, P. *Service contract to carry out economic analysis and business impact assessment of CO_2 emissions reduction measures in the automotive sector*, Institute for European Environmental Policy (IEEP), Final report B4-3040/2003/366487/MAR/C2, Queen Anne's Gate 28; London, UK, June **2005**.

[38] Zachariadis, T. *Energy Policy* **2006**, *34*, 1773.

[39] Faive-Duboz, M. *Concept to car: understanding the complexity of car engineering*, European Automotive Forum 2008, Brussels, January 23, **2008**.

[40] Rinolfi, R. *Policy to practice: Implementing environmental challenges in affordable cars*, European Automotive Forum 2008, Brussels, January 23, **2008**.

[41] Freymann, R. *Efficient dynamics: Innovative technologies to solve the target conflict between driving dynamics and fuel consumption*, European Automotive Forum 2008, Brussels, January 23, **2008**.

[42] Ozoux, P. *The tyre's potential to bring down the car's CO_2 emissions*, European Automotive Forum 2008, Brussels, January 23, **2008**.

[43] Hass, H. *Alternative fuels: State of play*, European Automotive Forum 2008, Brussels, January 23, **2008**.

[44] Jacometti, J. *The future for road transport fuels*, European Automotive Forum 2008, Brussels, January 23, **2008**.

[45] European Commission *Impact assessment for Euro 6 emission limits for light duty vehicles*; Commission staff working document of 20 September **2006**.

[46] Gandhi, H. S.; Graham, G. W.; McCabe, R. W. *J. Catal.* **2003**, *216*, 433.

[47] Tollefson, J. *Nature* **2007**, *450*, 334.

[48] Cornils, B.; Herrmann, W. A.; Schlögl, R.; Wong, C.-H. (Eds.) *Catalysis from A to Z: A concise encyclopedia*, Wiley-VCH, Weinheim; **2000**.

[49] Thomas, J. M.; Thomas, W. J. (Eds.) *Principles and Practice of Heterogeneous Catalysis*, Wiley-VCH, Weinheim; **1996**.

[50] Webster, D. E. *Top. Catal.* **2001**, *16/17*, 33.

[51] Collins, N. R.; Twigg, M. V. *Top. Catal.* **2007**, *42-43*, 323.

[52] Taylor, K. C. *Catal. Rev.* **1993**, *35*, issue 4, 457.

[53] Matsumoto, S. *Catal. Today* **2004**, *90*, 183.

[54] Alkemade, U. G.; Schumann, B. *Solid State Ionics* **2006**, *177*, 2291.

[55] Takahashi, N.; Shinjoh, H.; Iijima, T.; Suzuki, T.; Yamazaki, K.; Yokota, K.; Suzuki, H.; Miyoshi, N.; Matsumoto, S.; Tanizawa, T.; Tanaka, T.; Tateishi, S.; Kasahara K. *Catal. Today* **1996**, *27*, 63.

[56] Miyoshi, N.; Matsumoto, S.; Katoh, K.; Tanaka, T.; Harada, J.; Takahashi, N.; Yokota, K.; Sugiura, M.; Kasahara, K. *SAE Technical Paper* **1995**, 950809.

[57] Matsumoto, S.; Shinjoh, H. *Adv. Chem. Eng.* **2007**, 33, 1.

[58] Good, P. *An overview of European emissions legislation for light duty vehicles*, International Conference on Transport and Environment, Milan, March 19-21, **2007**.

[59] Joubert, E.; Seguelong, T. *Diesel particulate filters market introduction in Europe: review and status*, 2004 Diesel Engine Emissions Reduction (DEER) Conference, Coronado (CA), August 29-September 2, **2004**.

[60] Adler, J. *Int. J. Appl. Ceramic Techn.* **2005**, *2*, 429.

[61] Matsumoto, S.; Ikeda, Y.; Suzuki, H.; Ogai, M.; Miyoshi, N. *Appl. Catal. B: Environmental* **2000**, *25*, 115.

[62] Suzuki, J.; Matsumoto, S. *Top. Catal.* **2004**, *28*, 171.

[63] Skoglundh, M.; Fridell, E. *Top. Catal.* **2004**, *28*, 79.

[64] Hamamoto, K.; Fujishiro, Y.; Awano, M. *Solid State Ionics* **2008**, *179*, 1648.

[65] Ogunwumi, S. B.; Tepesch, P. D.; Chapman, T.; Warren, C. J.; Melscoet-Chauvel, I. M.; Tennent, D. L. *SAE Technical Paper* **2005,** 2005-01-0583.

[66] Muraki, H. *Catal. Soc. Japan* **1992**, *34*, No 4, 225.

[67] Nagai, Y.; Hirabayashi, T.; Dohmae, K.; Takagi, N.; Minami, T.; Shinjoh, H.; Matsumoto, S. *J. Catal.* **2006**, *242*, 103.

[68] Miyoshi, N.; Matsumoto, S.; Ozawa, M.; Kimura, M. *SAE Technical Paper* **1989,** 891970.

[69] Nagai, Y.; Dohmae, K.; Ikeda, Y.; Takagi, N.; Tanabe, T.; Hara, N.; Guilera, G.; Pascarelli, S.; Newton, M. A.; Kuno, O.; Jiang, H.; Shinjoh, H.; Matsumoto, S. *Angew. Chem. Int. Ed.* **2008**, *47*, 9303-9306.

[70] Shinjoh, H.; Isomura, N.; Sobukawa, H.; Sugiura M. *Effect of alkaline addition on hydrocarbon oxidation activities of palladium three-way catalyst*. In: Catalysis and Automotive Pollution Control IV; Kruse N.; Frennet, A.; Bastin, J.-M. (Eds.) *Stud. Surf. Sci. and Catal.* **1998**, *116*, 83.

[71] Shinjoh, H.; Tanabe, T.; Sobukawa, H.; Sugiura, M. *Top. Catal.* **2001**, *16/17*, 95.

[72] Tanaka, H.; Taniguchi, M.; Uenishi, M.; Kajita, N.; Tan, I.; Nishihata, Y.; Mizuki, J.; Narita, K.; Kimura, M.; Kaneko, K. *Angew. Chem. Int. Ed.* **2006**, *45*, 5998-6002.

[73] Taylor, K. C.; Schlatter, J. C. J. Catal. **1980**, *63*, 53.

[74] European Automobile Manufacturers' Association *ACEA's views on Euro 5*, ACEA website: http://www.acea.be/images/uploads/aq/EURO5.pdf, November 26, **2006**.

[75] Johnson Matthey *Platinum today: PGM prices*, Platinum today on Johnson Matthey's website http://www.platinum.matthey.com/.

[76] Bagot, P. A. J. *Mat. Sci. Techn.* **2004**, *20*, 679.

[77] Bowker, M. *Chem. Soc. Rev.* **2008**, *47*, 2204.

[78] Newton, M. A. *Chem. Soc. Rev.* **2008**, *47*, 2644.

Chapter 2

Promotion effects in the oxidation of CO over zeolite-supported Pt nanoparticles

Abstract

Well-defined Pt-nanoparticles with an average diameter of 1 nm supported on a series of zeolite Y samples containing different monovalent (H^+, Na^+, K^+, Rb^+ and Cs^+) and divalent (Mg^{2+}, Ca^{2+}, Sr^{2+} and Ba^{2+}) cations have been used as model systems to investigate the effect of promoter elements in the oxidation of CO in excess oxygen. Time-resolved infrared spectroscopy measurements allowed to study the temperature-programmed desorption of CO from supported Pt nanoparticles in order to monitor the electronic changes in the local environment of adsorbed CO. It was found that the red shift of the linear Pt-coordinated C≡O vibration compared to that of gas-phase CO increases with an increasing cation radius-to-charge ratio. In addition, a systematic shift from linear (L) to bridge (B) bonded C≡O was observed for decreasing Lewis acidity, as expressed by the Kamlet-Taft parameter α. A decreasing α results in an increasing electron charge on the framework oxygen atoms and therefore an increasing electron charge on the supported Pt nanoparticles. Furthermore, it was found that the CO coverage increases with increasing electron density on the Pt nanoparticles. This increasing electron density was found to result in an increased CO oxidation activity; *i.e.*, the $T_{50\%}$ for CO oxidation decreases with decreasing α. In other words, basic promoters facilitate the chemisorption of CO on the Pt particles. The most promoted CO oxidation catalyst is a Pt/K-Y sample, which has a $T_{50\%}$ of 390 K and a L:B intensity ratio of 2.7. The obtained results provide guidelines to design improved CO oxidation catalysts.

1 Introduction

Understanding the effect of a support oxide on the properties of noble metal particles is a challenging subject since it opens a way towards modelling and tuning of the catalytic properties by a deliberate choice of the support. The catalytic activity of supported Pt nanoparticles is well-known to be sensitive to the support composition, acid-base properties and pore curvature[1-3], but despite many studies that have been undertaken to elucidate the exact nature of the relationship, many questions still remain open.

A very useful, but often underestimated technique is infrared spectroscopy (IR) since the IR spectrum of chemisorbed carbon monoxide (CO) can be regarded as a sensitive and local probe of the electronic properties of supported Pt nanoparticles.[4,5] Its application is based on the fact that differences in electronic state are reflected in changes in the vibrational characteristics of the Pt-CO adduct. The result is a red shift of the CO stretching frequency compared to that of the gas phase and the appearance of two principal IR bands; one in the region 2100-1900 cm^{-1}, which is assigned to CO that is coordinated linear to Pt and a bridge bonded one between 1900 and 1700 cm^{-1}, which is attributed to 2, 3 or even 4-fold coordinated CO. Next to the stretching frequency, the intensity ratio of the linear and bridge bonded bands (L:B ratio) can be used as a measure for the electronic state of the Pt nanoparticles.[6] It has been found that Pt nanoclusters on basic supports are relatively more electron-rich than on acidic supports, which is reflected by an increased red shift of the CO stretching frequency and a decreased L:B ratio.[6-8] Another attractive feature of the IR technique is that it can be used to perform real-time temperature programmed desorption (TPD) studies in order to obtain direct information on changes in the Pt-C(O) bond strength. Surprisingly, only a few IR thermal desorption studies of Pt-CO systems have been reported in literature, mainly dealing with stepped single Pt crystals.[4,9-14] To our best knowledge, IR-CO-TPD studies on supported Pt catalysts have only been reported by Barth *et al.*[4,13] and Gandao *et al.*[14]. The former group compared the CO desorption process from Pt/SiO_2 and Pt/Al_2O_3 upon heating and cooling, whereas the latter team used the technique to determine the presence of three types of Pt bonded CO on Pt/Mg(Al)O catalysts.

It is clear that systematic studies on well-defined Pt nanoparticles supported on a wide range of porous oxides are lacking in the literature, preventing the generalisation of some of the above-mentioned conclusions. As a consequence, the aim of the present research is to investigate the effect of monovalent (H^+, Na^+, K^+, Rb^+ and Cs^+) and divalent cations (Mg^{2+}, Ca^{2+}, Sr^{2+} and Ba^{2+}) on the electronic properties of Pt particles encaged in the supercages of zeolite Y by means of the IR-CO-TPD technique. It will be shown that an increasing electron charge on the supported Pt nanoparticles indirectly induced by alkali and alkaline earth metal ions *via* the framework oxygen atoms promotes the CO oxidation activity due to an increased CO surface coverage. Furthermore, the systems under investigation can be envisaged as model systems for the NO_x storage-reduction catalysts (*e.g.* Pt-BaO/Al_2O_3) currently used in cars. The results of the present study shows that BaO plays most likely a dual role since it acts as a NO_x trap, but also promotes the CO oxidation activity of the supported Pt nanoparticles. The work therefore provides guidelines for the development of improved three-way exhaust catalytic converters.

2 Experimental section

Prior to preparation and characterisation, it should be emphasised that the CO stretching vibration of Pt-chemisorbed CO is not only sensitive to the support characteristics, but also to a large number of experimental parameters. According to literature, the loading, dispersion, particle size and coordination number of Pt[9,15-19], the reduction temperature[20,21] and CO exposure pressure[22,23] can affect the observed IR data, while sample pre-treatment[24], CO exposure temperature[12], CO adsorption[25] and CO interaction with support cations[7,26] may play a role as well. In order to prevent erroneous assignments and conclusions, special attention has been paid to keep all experimental parameters and instrumental settings the same.

2.1 Catalyst preparation

H-Y (Si:Al ratio of 2.71) has been obtained from Linde, whereas the starting material for ion exchange was a Na-Y (Si:Al ratio of 2.49) material from Ventron. The zeolite materials were put in their Na^+, K^+, Rb^+, Cs^+, Mg^{2+}, Ca^{2+}, Sr^{2+} and Ba^{2+} form by four successive ion exchanges for 12 h with an aqueous 1 M solution of NaCl (Aldrich, p.a.), KCl (Aldrich, p.a.), RbCl (Merck, p.a.), CsCl (Merck, p.a.), $MgCl_2$

(UCB, p.a.), $CaCl_2$ (UCB, p.a.), $SrCl_2$ (Aldrich, p.a.) and $BaCl_2$ (Aldrich, p.a.), respectively. The samples were washed chlorine-free and dried in air at room temperature overnight. The crystallinity before and after ion exchange was confirmed by X-ray diffraction (XRD) and scanning electron microscope (SEM) techniques. Chemical analysis of the zeolite materials indicated that after four successive ion exchange steps the degree of exchange was above 98 % for all materials under study. Details of the zeolite materials can also be found elsewhere.[27] As will be shown, the zeolite materials, with the exception of H-Y, are almost free of Brønsted acid sites, ensuring that the ion exchange of the promoter cations does not introduce H^+-sites in the catalyst materials.

1 wt% supported Pt particles were prepared *via* dry impregnation of the support materials with the appropriate aqueous solutions of $Pt(NH_3)_4(NO_3)_2$. After impregnation and drying at 353 K in N_2 (quality 4.0; Hoekloos) for 12 h, calcination was carried out by drying in a high airflow (30 ml/min) during 12 h followed by increasing the temperature to 573 K at a heating rate of 0.2 K/min to achieve complete removal of NH_3 prior to reduction. Reduction was performed in pure H_2 (quality 5.0; Hoekloos) with a flow of 10 ml/min at 573 K for 2 h. After reduction and flushing with N_2 at room temperature, passivation was carried out by admitting a small amount of air (10 ml/min) into the system to prevent aggregation of Pt particles. Table 2.1 summarises the different supported Pt catalysts under study in this work.

2.2 Catalyst characterisation

X-ray fluorescence (XRF) was carried out on all samples to determine the Pt loadings using a Spectro X-lab 2000 instrument. N_2 physisorption was performed at 77 K with a Micromeretics ASAP 2400 apparatus (quality 4.0; Hoekloos). Prior to these measurements, the samples were degassed for 24 h at 573 K in vacuum. Surface area, pore volume and pore size distribution were calculated with standard BET theory. Hydrogen chemisorption measurements were performed in a conventional static volume apparatus (Micromeretics ASAP 2010C). The samples were first dried under evacuation at 373 K overnight, then reduced in pure H_2 at 573 K for 1 h (ramp: 5 K/min). The samples were cooled in H_2 down to 523 K and evacuated at this temperature for 1 h. Subsequently, the samples were cooled in a

Table 2.1: Overview of the supported Pt catalysts under study, together with some physico-chemical properties.

Sample name	Pt loading [wt%] [a]	Pt particle size [nm] and their relative abundance [b]	Surface area [m^2/g] [c]	Pore volume [ml/g] [c]	Dispersion of Pt [%] [d]	H^+ amount [mmol/g] [e]
Pt/H-Y	1.2	≤ 1 (exclusive)	700	0.28	93	1.97
Pt/Na-Y	1.0	≤ 1 (exclusive)	686	0.27	95	0.16
Pt/K-Y	1.1	≤ 1 (main fraction); 3 nm (traces)	690	0.27	82	0.15
Pt/Rb-Y	1.0	≤ 1 (main fraction); 3 nm (traces)	678	0.27	88	0.16
Pt/Cs-Y	0.8	≤ 1 (fraction); 5 nm (significant fraction)	542	0.23	69	0.18
Pt/Mg-Y	1.3	≤ 1 (main fraction); 10 nm (traces)	679	0.27	82	0.22
Pt/Ca-Y	1.2	≤ 1 (main fraction); 5 nm (traces)	687	0.27	83	0.17
Pt/Sr-Y	0.9	≤ 1 (main fraction); 5 nm (traces)	690	0.27	82	0.15
Pt/Ba-Y	1.0	≤ 1 (exclusive)	696	0.27	92	0.18

[a] As determined by X-ray fluorescence (XRF).

[b] As determined from high resolution transmission electron microscope (HRTEM) pictures.

[c] As determined from N_2 physisorption measurements.

[d] As determined by H_2 chemisorption measurements.

[e] As determined by NH_3 temperature programmed desorption (TPD).

vacuum to room temperature and H_2 adsorption isotherms were taken at 309 K. At room temperature, the samples were evacuated and a second isotherm was recorded. The hydrogen chemisorption capacity was calculated at the difference between the two isotherms extrapolated to zero pressure. The Pt dispersions were calculated on the basis of the assumption that one hydrogen atom is adsorbed per platinum surface atom. The number of support protons was determined by ammonia temperature programmed desorption (NH_3 TPD) for catalysts containing only chemisorbed NH_3. Approximately 1 g of catalyst was saturated in a flow of 5 % NH_3 in N_2 at room temperature. To remove physisorbed NH_3, the catalyst was washed three times in 50 ml of H_2O at 353 K, filtered and dried at 373 K. The quantity of desorbed NH_3 was determined by titration with a standard solution of 0.1 M HCl. The number of protons was calculated on the basis of the assumption that one NH_3 molecule was chemisorbed per acid site. High-resolution transmission electron microscopy (HRTEM) was done with a Philips CM 30 UT electron microscope equipped with a field emission gun as the source of electron operated at 300 kV. Samples were mounted on a microgrid carbon polymer supported on a copper grid by placing a few droplets of a suspension of ground sample in ethanol on the grid, followed by drying at ambient conditions. Extended X-ray absorption fine structure (EXAFS) measurements were carried out at Hasylab (Germany) at station X1.1 and at the ESRF (France) at CRG DUBBLE (BM26A). Both beamlines were equipped with a double crystal monochromator with Si{111} crystals. Measurements were performed in transmission, and ion chambers were used for detection with a gas fill to absorb 20% in the first and 80% in the second ion chamber. Reduction of the higher harmonic radiation at Hasylab was established by detuning the second crystal to 50% of the maximum intensity, and at the DUBBLE station by using a secondary mirror. The samples were prepared by pressing 0.120 to 0.140 g powder to a self-supporting wafer. Next, the wafer was placed in a treatment cell. Prior to measurement, the sample was dried at 423 K for 30 min in a flow of dry He and then slowly heated to 573 K under a flow of 10 % H_2 in He to reduce the passivated Pt. Next, the samples were measured at liquid N_2 temperature. EXAFS data analysis was carried out with the XDAP program.[28]

IR measurements were performed on self-supporting catalyst wafers that were pressed from 0.010-0.020 g of calcined and reduced sample material. A pressure of 3 bar was applied during 10 s to prevent destruction of the pore structure of the

support.[24] The wafer was placed in an IR transmission cell equipped with CaF_2 windows as previously described.[29] The cell was evacuated to 10^{-8} bar followed by drying of the wafer at 393 K overnight prior to reduction by a 10 ml/min flow of H_2 (quality 4.6; Hoekloos). During reduction the temperature was raised from 393 K with vacuum and after 1 h at 573 K, cooled to 323 K at a rate of 3 K/min where it was maintained for 1h. We believe on the basis of the absence of a Pt-H stretching vibration at around 2050 cm^{-1} in the Pt-loaded samples that this vacuum treatment removed all the hydrogen from the supported Pt nanoparticles. Next the system was switched to 10 % CO (quality 4.7; Hoekloos) in He (quality 4.6; Hoekloos) at a starting pressure of 0.2 bar. After 30 min of static pressure, the system was re-evacuated and after another 30 min, temperature programmed desorption (TPD) was started by increasing the temperature from 323 K to 573 K (at 3 K/min) where it was maintained for 30 min. IR spectra were recorded on a Perkin-Elmer 2000 FTIR instrument with a data point resolution of 4 cm^{-1}. For each spectrum 25 scans were co-added. As a background, the spectrum of the catalyst wafer was taken after drying, reduction and cooling down to 323 K, 2 min prior to CO exposure. During adsorption and TPD, time-resolved scanning was carried out by automatically acquiring spectral data every 2 min, using Perkin-Elmer Time-Base software. In order to obtain spectra of the adsorbed CO during CO exposure, the gas phase spectrum of CO was subtracted from the spectrum that was taken prior to re-evacuation of the cell. Intensity data were acquired by calculating the integrated area of baseline corrected spectra using the Perkin-Elmer Spectrum software. The reproducibility of all IR-TPD measurements was verified by carrying out the experiments in duplo in two ways: (1) by analysing two different wafers from the same sample and (2) by repeating the exposure and desorption process to the same wafer without opening the IR cell.

2.3 Catalytic testing

The Pt-catalysts were tested for the oxidation of CO in a 6-flow reactor set-up described in detail elsewhere.[30] For this purpose, 20 mg of each catalyst diluted with 200 mg of SiC was loaded in the reactors. The reacting gas consists of 1000 ppm of CO in an excess of 10 % of O_2. The flow rate was 250 ml/min and the heating and

cooling rates were 0.3 K/min. The catalysts were tested reversibly and CO and CO_2 gas analysis was done with a non-dispersive IR analyser.

3 Results and discussion

3.1 Catalyst characterisation

Table 2.1 summarises some physicochemical properties of the materials under study as obtained with N_2 and H_2 physisorption, NH_3 TPD and XRF. The surface area and pore volume of the Pt catalysts are typical for zeolite Y. Neither the surface area, nor the pore volume of the zeolite support is significantly affected by the introduction of Pt nanoparticles in the micropores of zeolite Y. An exception is the Pt/Cs-Y sample, which shows a decreased surface area and pore volume. A possible explanation could be pore blocking by Pt particles at the outer surface of the zeolite crystals or zeolite destruction due to extensive Pt particle growth.[31] The Pt content of the different catalysts as determined by XRF varied between 0.7 wt% (Pt/Cs-Y) and 1.3 wt% Pt (Pt/Mg-Y), but most of the Pt loadings are close to the target value of 1 wt%. The H_2 chemisorption results indicate that the Pt nanoparticles are well-dispersed, although Pt/Cs-Y shows the lowest Pt dispersion, an observation in line with the N_2 chemisorption data. Finally, NH_3 TPD was used to estimate the number of acid sites in the Pt-loaded zeolite materials. It was found that, with the exception of Pt/H-Y, the catalyst materials do not contain substantial amounts of protons. More importantly, we do not see any systematic trend as a function of the introduced promoter cations.

The size and size distribution of the supported Pt nanoparticles have been determined with EXAFS and HRTEM. Whereas EXAFS determines an average number for the Pt size (*via* the number of Pt scatterers), HRTEM gives insight in the size distribution of the supported Pt nanoparticles. Table 2.2 summarises the results of the EXAFS analysis on all the samples under study. The data show that for most samples a Pt-Pt coordination number of around 5.5-6.0 was found, which corresponds to a spherical Pt particle size of around 1 nm, most probably located in the supercage of zeolite Y. The three exceptions to this observation are the Pt-Pt coordination number of 6.7 for the Pt/Cs-Y and Pt/Ca-Y samples and the Pt-Pt coordination number of 7.1 for the Pt/Rb-Y sample. We did not observe scattering against the introduced co-cations, indicating that there is no direct chemical contact

between the Pt nanoparticles and the promoter ions. However, because some of the cations introduced (*e.g.*, Ba and Sr) can be regarded as high Z elements, such a Pt absorber-Z backscatter pair still may exist, although we did not try to fit the higher shell contributions of the EXAFS data. In this respect, it is worthwhile to mention the work of Vaarkamp *et al.* in which 1.4 Ba atoms were found at a distance of 3.76 Å from a Pt particle with a coordination number of 3.7 in a Pt/BaKL zeolite material.[32] The small amount of oxygen in the EXAFS fits (see Table 2.2) is a support oxygen originating from the zeolite material. A formal Pt-O bond does not exist because the small Pt clusters are reduced in hydrogen. Therefore, an oxygen atom from the support material is the observed scatterer. This results in an increased Pt-O bond distance in comparison with platinum oxide. The spread in the Pt-O distances is due to changes induced by the presence of cations as well reflects the affinity of the Ptparticles for the support. Finally, the relatively high E_0 or inner potential value has to be addressed for this scatterer. There is an ongoing discussion on the accepted variance in E_0 values. The standard, used in the current calculations, is the Pt-O bond in $Na_2Pt(OH)_6$. For the type of bond, this is the best possible standard, but not

Table 2.2: EXAFS fit parameters of the supported Pt catalysts under study.

Sample	Scatterer	N	$\Delta\sigma^2$ [Å^2]	R [Å]	E_0 [eV]
Pt/H-Y	Pt	5.4	3.4	2.74	1.9
	O	0.2	3.0	2.10	− 12.3
Pt/Na-Y	Pt	5.7	4.6	2.73	2.5
	O	0.6	3.8	2.07	− 15.0
Pt/K-Y	Pt	6.2	4.4	2.74	2.2
	O	0.2	3.4	2.07	− 13.0
Pt/Rb-Y	Pt	7.1	6.1	2.72	1.9
	O	0.4	5.6	2.00	− 12.0
Pt/Cs-Y	Pt	6.6	3.8	2.74	2.2
	O	0.5	1.4	2.05	− 12.0
Pt/Mg-Y	Pt	5.8	6.1	2.73	2.0
	O	0.4	1.0	2.19	− 10.3
Pt/Ca-Y	Pt	6.7	5.1	2.74	2.5
	O	0.3	5.3	2.03	− 13.0
Pt/Sr-Y	Pt	5.1	3.1	2.74	1.9
	O	0.5	1.3	2.10	− 12.0
Pt/Ba-Y	Pt	5.1	4.7	2.73	2.7
	O	0.4	2.1	2.09	− 13.0

fully covering the identity of the zeolite oxygen scatterer, which results in a more then normally accepted variance in E_0 value.

Figure 2.1 shows as examples the HRTEM pictures of Pt/Na-Y and Pt/Cs-Y. Whereas in the case of Pt/Na-Y no large Pt nanoparticles can be observed, HRTEM of Pt/Cs-Y shows a significant portion of Pt nanoparticles of 1-5 nm on top of the zeolite Y crystals. This observation explains, most probably, the decreased surface area and pore volume of this material as well as the higher Pt-Pt coordination number. Another explanation could be that the Pt particles further grow in the Pt/Cs-Y sample exceeding the supercage size, leading to mesopores formation. Evidence for such effects has been reported for the formation of CdS and ZnS in Na-X, Ir clusters in Na-X and Pt clusters in ZSM-5 zeolites.[31]

Table 2.1 summarises the observations made by HRTEM. It can be concluded that all samples, with the exception of the Pt/Cs-Y material, contain exclusively or as a main fraction Pt nanoparticles of 1 nm or smaller. As expected, the Pt/Ca-Y and Pt/Rb-Y samples contain Pt particles of 3-5 nm as well. Thus, although some differences are noticed between the different samples, EXAFS, H_2 chemisorption and HRTEM indicate that well-defined Pt-loaded zeolite Y samples have been prepared. These samples contain predominantly 1 nm Pt nanoparticles, which are most probably occluded in the supercages of zeolite Y.

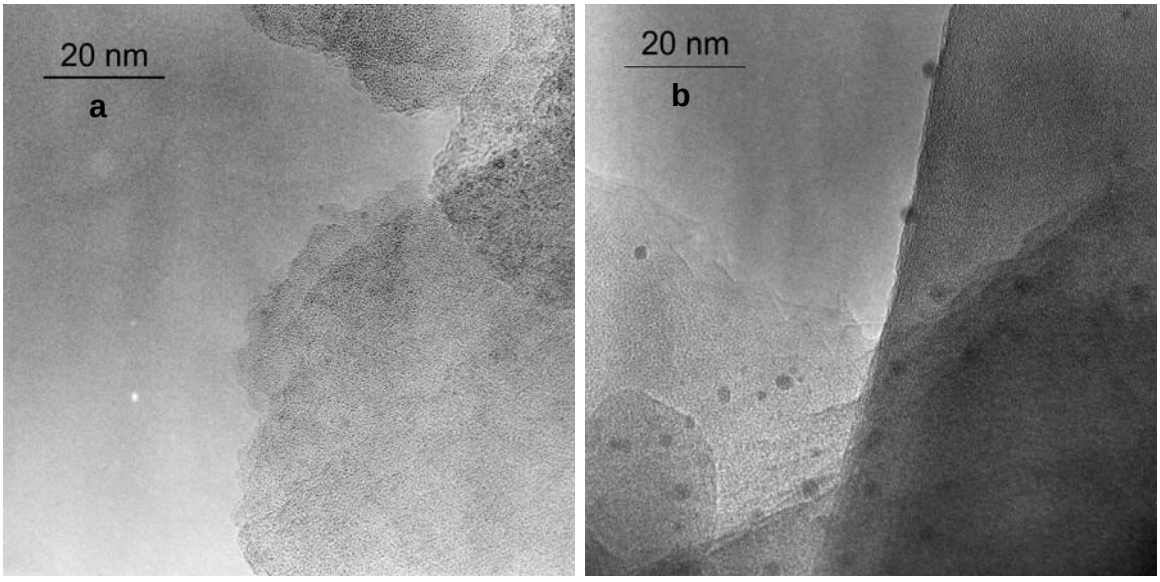

Figure 2.1: HRTEM micrographs of (a) Pt/Na-Y and (b) Pt/Cs-Y catalyst samples.

3.2 Infrared spectroscopy

Figures 2.2 to 2.4 show the time- and temperature-resolved IR spectra of the different supported Pt catalysts obtained during the CO-TPD procedure. It is important to recall that the results of two subsequent measurements of the same self-supported wafer were practically identical, which implies that the samples were not affected by the treatment and that reproducible results were obtained. We also verified the stability of the Pt-zeolite samples during the CO TPD measurements and have noticed with HRTEM no disintegration or aggregation of the supported Pt nanoparticles. In other words, the applied methodology did not affect the Pt size and size distribution of the Pt nanoparticles in the different zeolite samples.

Figure 2.2 shows the CO IR TPD spectra of Pt/H-Y. The 3D-set of spectra in Figure 2.2a are the raw IR data. It is clear that the spectra show a strong IR absorption band at around 2000 cm^{-1} and a weaker one at around 1800 cm^{-1}. The former band is assigned to the stretching vibration of a linearly Pt-coordinated CO, whereas the latter band is due to bridge Pt-CO stretching vibrations.[20,33-35] Both IR absorption bands decrease in intensity with increasing TPD temperature due to CO desorption. In addition, background absorption is arising, which complicates the analysis at higher TPD temperatures. One can apply a baseline correction leading to the spectra shown in Figure 2.2b.

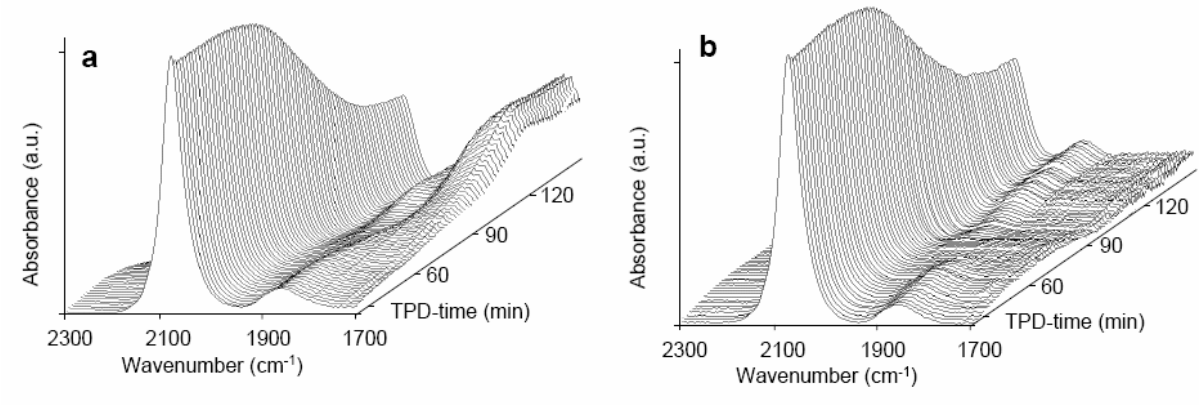

Figure 2.2: Time-resolved IR spectra during temperature programmed CO desorption from Pt/H-Y; (a) raw spectra and (b) baseline corrected spectra.

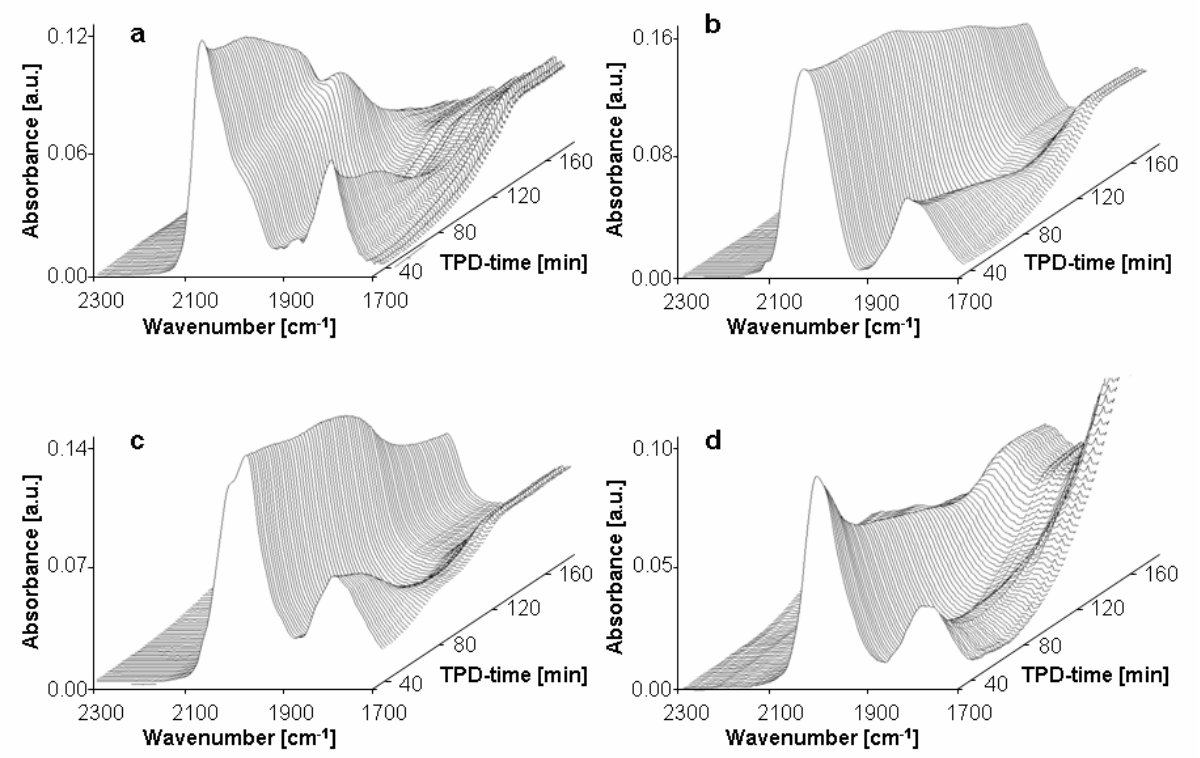

Figure 2.3: Time-resolved IR spectra during temperature programmed CO desorption from (a) Pt/Na-Y, (b) Pt/K-Y, (c) Pt/Rb-Y and (d) Pt/Cs-Y.

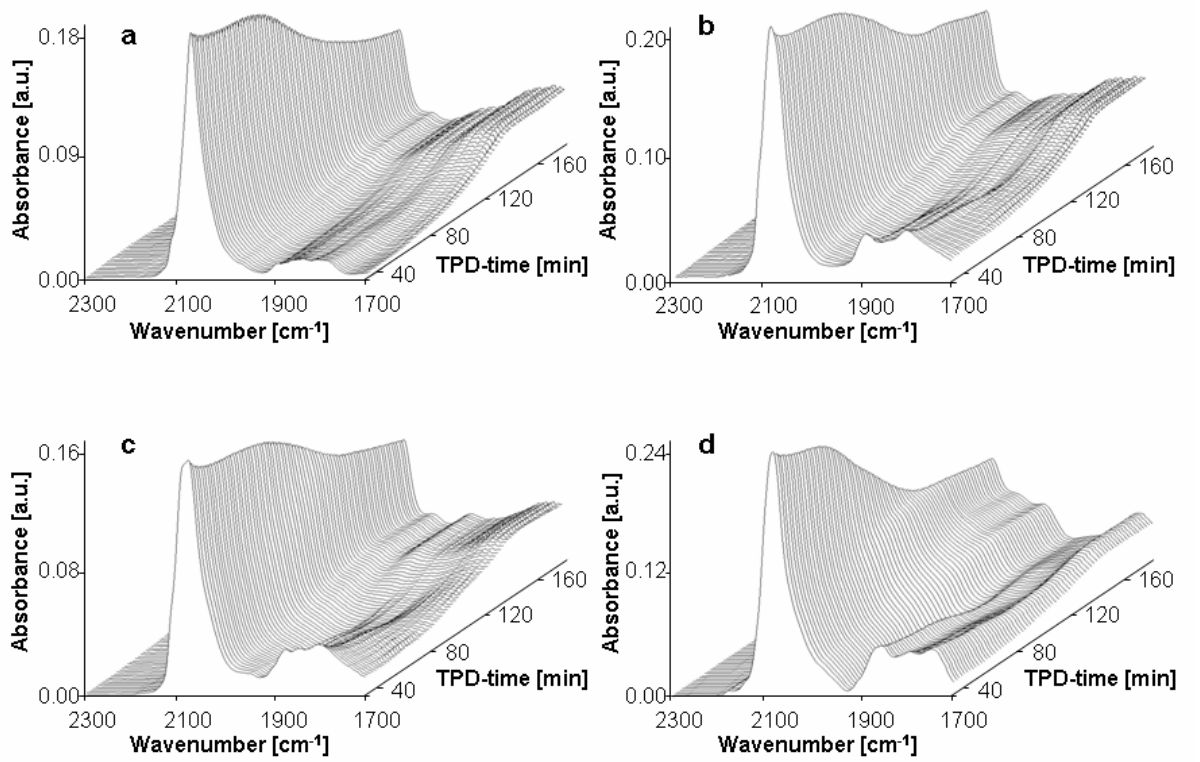

Figure 2.4: Time-resolved IR spectra during temperature programmed CO desorption from (a) Pt/Mg-Y, (b) Pt/Ca-Y, (c) Pt/Sr-Y and (d) Pt/Ba-Y.

On the basis of Figures 2.2 to 2.4 one can make the following qualitative observations:

(1) The linear CO absorption bands of Pt/H-Y (Figure 2.2) are sharp and symmetrical, whereas alkali metal (Figure 2.3) and alkaline earth metal (Figure 2.4) cation-containing samples possess broad asymmetrical bands with shoulders. Indeed, the band width is small (half band width (HBW) of 49 cm^{-1}) for Pt/H-Y compared to those of the alkali metal cation-exchanged (HBW of 90-110 cm^{-1}) and the alkaline earth metal cation-exchanged (HBW of 55-70 cm^{-1}) zeolite Y samples. In the case of Pt/H-Y, the HBW points to the presence of a single type of linear coordinated CO and hence, to a uniform coordination number for the supported Pt particles.[33] On the other hand, the large HBWs for the cation-containing zeolite Y samples implies that either different Pt adsorption sites are present or that different CO orientations are possible as a result of local interactions within the zeolite supercage. The former is rather unlikely, since the Pt particle sizes are practically the same for all the samples, with the exception of Pt/Cs-Y (Table 2.1 and Figure 2.1). The most plausible explanation is to assume the presence of non-bonding electrostatic interactions. Two types of non-bonding interaction of the CO-oxygen can affect the CO vibration and result in different CO orientations: (a) a repulsive electrostatic interaction with oxygen atoms of the framework[36,37] and (b) an attractive ion-dipole interaction with framework cations.[7] Compared to the Pt/H-Y sample, the presence of cations seems crucial in the band broadening effect and so it is most likely that the attractive ion-dipole interactions play the largest role. Next, the presence of cation-affected and "free" CO positions explains to some extent the complex linear CO band in the IR. In addition, reorientation of CO as a result of changing interactions might explain the increasing band complexity at higher temperature. This phenomenon is particularly visible in the IR-CO-TPD pattern of Pt/Na-Y (Figure 2.3 a) by the increasing intensity of the shoulder at 2000 cm^{-1} upon heating.

(2) The differences and shifts of the band maxima for both linear and bridge Pt-coordinated CO for the different samples upon TPD are summarised in Table 2.3. Comparison of the linear Pt-coordinated CO stretching band position under experimental conditions demonstrates that the maximum decreases upon

Table 2.3: Positions of the absorption bands of linearly and bridge Pt-coordinated CO for the supported Pt catalysts measured at different temperatures.

Sample	Temperature [K]							
	323	373	473	573	323	373	473	573
	Linear Pt-coordinated −C≡O stretching band [cm^{-1}]				Bridge Pt-coordinated =C=O stretching band [cm^{-1}]			
Pt/H-Y	2083	2078	2072	2066	1856	1854	1751	1750
Pt/Na-Y	2073	2036	1995	1957	1823	1806	1775	1720
Pt/K-Y	2045	2022	1996	1964	1821	1797	1736	1723
Pt/Rb-Y	1992	1984	1971	1963	1803	1792	1725	1718
Pt/Cs-Y	2001	1959	1937	1918	1813	1753	1720	1719
Pt/Mg-Y	2087	2075	2066	2054	1892 1837 1808	 1855 1786	 1855 1784	
Pt/Ca-Y	2093	2083	2069	2047	1887 1798	 1855 1786	 1855	
Pt/Sr-Y	2076	2070	2059	2041	1872 1844 1802	1868 1845 1773	1868 1845	1897
Pt/Ba-Y	2076	2049	2026	2021	1845 1788 1760	1843 1785 1754	1834 1728	1813 1723

substitution of the framework protons by alkali or alkaline earth metal ions more or less in the same order as their position in the periodic system; *i.e.*, H > Na > K > Rb ≈ Cs and Mg ≈ Ca > Sr > Ba. Similar trends can be observed for the bridge Pt-coordinated CO stretching band. Besides, the spread of about 100 cm^{-1} for alkali metal cation-containing samples and of about 20 cm^{-1} for alkaline earth metal cation-containing samples indicates a large difference in the CO bond strength. These results point to a correlation of the $\nu_{C\equiv O}$ with the electronic properties of M^{+}/M^{2+}. Assuming an inversely proportional relationship of $\nu_{C\equiv O}$ and the Pt−C(O) bond strength, one would expect an order in the CO-desorption rate of Pt/Cs-Y > Pt/Rb-Y > Pt/K-Y > Pt/Na-Y > Pt/H-Y. A closer examination of the IR-desorption patterns in 3D-projection (Figure 2.3) does not show such trend, indicating that there is no simple correlation between the $\nu_{C\equiv O}$ with the Pt−C(O) bond strength. Apparently, a high CO stretching frequency is not by definition related to a weak Pt−C(O) bonding and *vice*

versa. This is in line with a recent conclusion of Wasileski *et al.* that there is no simple correlation between the field dependent Pt bonded CO vibrational frequency and the Pt−C(O) bonding energy.[38]

(3) Both alkali and alkaline earth metal ion-containing samples possess a complex bridge Pt-coordinated CO stretching band pattern and at least three broad and ill-resolved absorption bands are observed (Table 2.3). This is the most evident for materials loaded with the divalent cations. As can be seen from Figure 2.4, the intensity decrease of the bridge bonded CO band at around 1800 cm^{-1} is partially offset by an increase of the baseline and in principle the latter might also be due to the formation of 3- or 4-fold coordinated CO. However, upon cooling, the baseline decreases to its initial values, while the linear and 2-fold coordinated bands do not increase in intensity. For that reason, we reject the formation of the latter type of Pt bonded CO. It implies that the intensity of the bridge band decreases faster than that of the linear Pt−C≡O band at around 2000 cm^{-1}. Comparison between Figures 2.2 to 2.4 also indicate that the IR band intensities of linear and bridge Pt-coordinated CO decrease with increasing measurement temperature and the relative extent of the band intensity decrease is influenced by the presence of alkali and alkaline earth metal cations. Furthermore, the ratio of the IR band intensities of linear to bridge Pt-coordinated CO decreases in the order: Pt/H-Y > Pt/M^{2+}-Y > Pt/M^{+}-Y.

In what follows, we will elaborate on these differences and present a more quantitative comparison between the materials under investigation. For this purpose, the summed integrated intensities of linear and bridge Pt-coordinated C≡O stretching bands have been used after normalising for the Pt contents of the self-supported wafers. Figure 2.5 relates the red shift of linear Pt-coordinated C≡O compared to gas-phase C≡O (positioned at 2143 cm^{-1}) with the cation radius-to-charge ratio of the different metal promoters under study. It is evident that there exists a correlation and a large red shift corresponds to a large cation radius-to-charge ratio. Similar trends are observed for the bridge Pt-coordinated C≡O stretching band, although due to the complexity and broadness of these bands less straightforward conclusions can be drawn.

Next, the effect of the different co-cations on the intensity ratio of the linear (L) to bridge (B) coordinated bands was examined and the results are summarised in Table 2.4. Comparison of the IR L:B intensity ratios of the spectra recorded at 323 K

reveal much lower L:B values of 2.7-2.9 for the alkali ion-exchanged Pt-zeolites compared to 10 for the Pt/H-Y sample. Alkaline earth ion-exchanged Pt-zeolites have intermediate L:B values of 3.5-8.0, but importantly the values follow the trend expected from the ordering in the periodic table. It should be noted that the inaccuracy of the L:B values of the Pt/M^{+}-Y and Pt/M^{2+}/Y catalysts is larger than for Pt/H-Y due to the asymmetry of the bands, but the trends remain clear. In addition, we could not find a simple relationship between the red shift for linear bonded C≡O to Pt and the IR L:B intensity ratio. Instead, we have found a relationship between

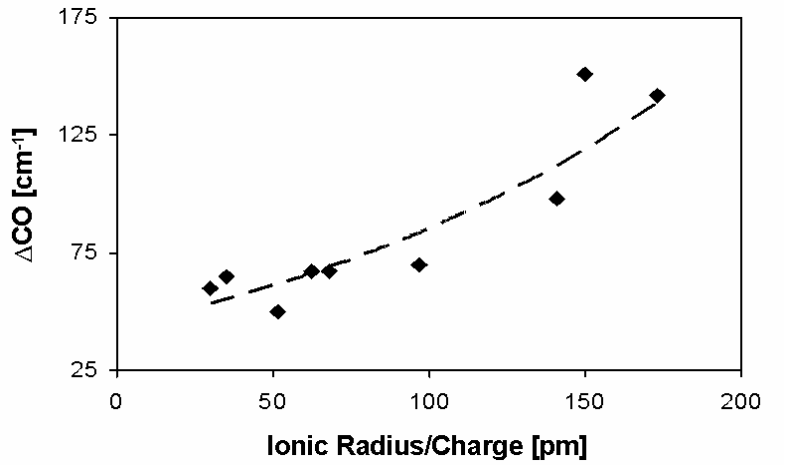

Figure 2.5: Red shift of linearly bonded C≡O on supported Pt nanoparticles compared to gas-phase C≡O as a function of the promoter cation radius-to-charge ratio.

Table 2.4: Overview of the infrared L:B ratios and catalytic activity data of the supported Pt catalysts under study[a].

Sample	Infrared L:B ratio at 323 K	$T_{50\%}$ [K] for the CO conversion	E_{act} [kJ/mol] for the CO conversion
Pt/H-Y	10	460	92
Pt/Na-Y	2.9	410	92
Pt/K-Y	2.7	390	93
Pt/Rb-Y	2.8	405	97
Pt/Cs-Y	2.8	355	98
Pt/Mg-Y	8	450	94
Pt/Ca-Y	4.5	420	94
Pt/Sr-Y	4	395	85
Pt/Ba-Y	3.5	420	79

[a] The L:B ratios have been obtained from the IR spectra after baseline correction.

the L:B intensity ratios and the Lewis acid properties of the cations introduced in zeolite Y. The results are summarised in Figure 2.6. A parameter, describing the Lewis acid behaviour of the cations under investigation, is the Kamlet-Taft parameter α.[39] This parameter expresses the ability of a cation to accept an electron pair and a high α value corresponds with a strong Lewis acid character. It is clear that a weak Lewis acid, such as K^+ (α = 0.85), results in an increasing electron charge on the framework oxygen atoms and therefore an increasing electron charge on the supported Pt nanoparticles. This rise results in an increasing occupancy of the d-levels, resulting in an enhanced back-donation and therefore a decreasing infrared L:B ratio. The reverse situation can be rationalised for a strong Lewis acid site, such as Mg^{2+} (α = 4.66).

Finally, one can use the integrated band intensities of the linear and bridge Pt-coordinated CO molecules to determine the surface coverage of these species as a function of the desorption temperature from the different supported Pt nanoparticles. The obvious assumptions are that (1) the extinction coefficients of linear and bridge Pt-coordinated C≡O molecules do not change with increasing desorption temperature, (2) the CO surface coverage does not affect too much the CO band intensities, and (3) the extinction coefficients are not affected to a great extent by the electron properties of the supported Pt nanoparticles. The second assumption is only valid if Pt nanoparticles of similar size and shape are under study, which is the

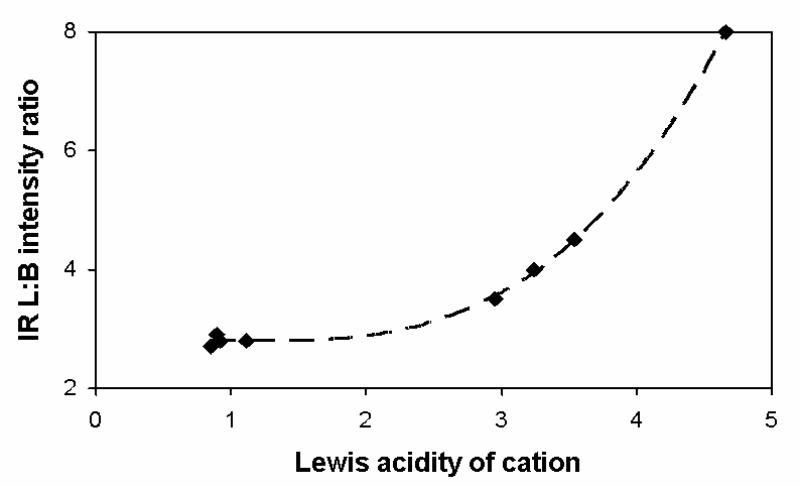

Figure 2.6: Relationship between IR L:B intensity ratios and Lewis acid properties of the cations introduced in zeolite Y as expressed by the Kamlet-Taft parameter α. The Pt/H-Y sample could not be introduced in this plot since no α-values for H^+ are available.

case based on our EXAFS and HRTEM data, with the exception of Pt/Cs-Y. With respect to the third assumption, it should be mentioned that extinction coefficients of a carbonyl function (a C=O unit comparable to a C≡O) in aldehydes and ketones are not dramatically altered when the surrounding R groups are changed. Examples are the extinction coefficients for molecules, such as $CH_3C(=O)CH_3$ (ε = 8.5 cm^2/mol) and $ClCH_2C(=O)C_6H_5$ (ε = 7.9 cm^2/mol).[40] In other words, changes in the electron properties of the supported Pt particle due to the presence of a different promoter element are only expected to slightly influence the extinction coefficient of an adsorbed CO molecule.

Figure 2.7 illustrates the CO surface coverage for Pt/K-Y, Pt/Ca-Y, Pt/Mg-Y and Pt/H-Y zeolites as a function of the desorption temperature. The values have been obtained by taking into account the weight and Pt content of the IR wafers for each sample as well as by assuming that the extinction coefficient of linearly Pt-coordinated C≡O molecules is twice as large as that of the bridge Pt-coordinated C≡O molecules. The latter assumption has been obtained from the work of Vannice and Twu.[41] Figure 2.7 shows that in each zeolite sample the CO coverage on the supported Pt particles decreases with increasing desorption temperature. In addition, the relative amount of adsorbed CO is the highest on Pt/K-Y and the lowest on Pt/H-Y, whereas the two other Pt-loaded zeolites have intermediate CO coverage. To elaborate further on this point we have plotted the CO coverage values at 450 K as a function of the corresponding IR L:B ratios of the different

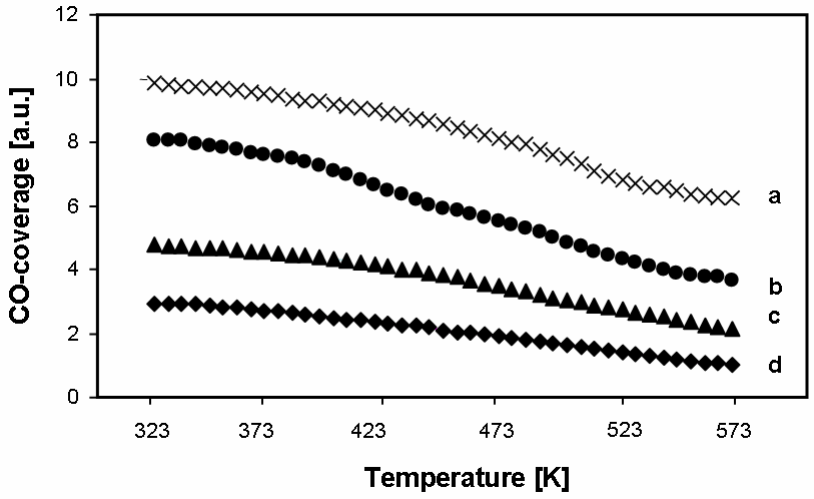

Figure 2.7: CO coverage on supported Pt nanoparticles as a function of the desorption temperature: (a) Pt/K-Y, (b) Pt/Ca-Y, (c) Pt/Mg-Y and (d) Pt/H-Y.

samples. The result is illustrated in Figure 2.8. The CO coverage on supported Pt nanoparticles tends to increase with decreasing IR L:B ratio or increasing electron density of the Pt metal.

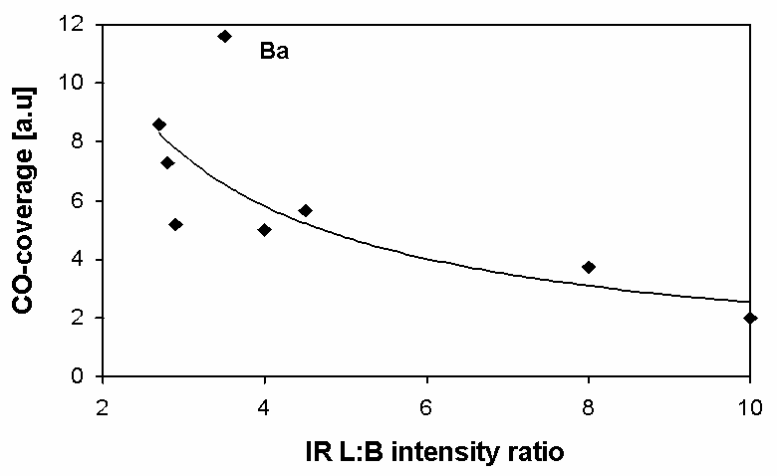

Figure 2.8: CO coverage on supported Pt nanoparticles measured at 450 K as a function of the IR L:B intensity ratio. The Pt/Ba-Y sample behaves atypical and has a very high CO coverage.

3.3 CO oxidation activity

The supported Pt catalysts under investigation show clearly different catalytic behaviour in the oxidation of CO in the presence of excess oxygen. The temperatures at which 50% of the CO is converted ($T_{50\%}$) for the different materials are summarised in Table 2.4. It is evident that depending on the cation present in the parent zeolite Y the $T_{50\%}$ can differ with more than 100 K. The catalytic results can also be plotted as a function of the corresponding IR L:B intensity ratios of the materials, which expresses the electron charge on the supported Pt nanoparticles. The obtained correlation is shown in Figure 2.9. It is evident that electron-rich supported Pt nanoparticles promote CO oxidation activity, whereas electron-poor supported Pt nanoparticles oxidise CO at much higher temperature. It is important to stress that because the Pt/Cs-Y sample contains larger Pt particles we have not included this data point in Figure 2.9; however, the trend remains clear. A more detailed analysis of the catalytic data also revealed that the activation energy for CO conversions between 1 % and 10 % was between 79 and 98 kJ/mol (Table 2.4). This is in line with literature data,[42] indicating that there was no mass transfer limitations in the catalytic systems under study.

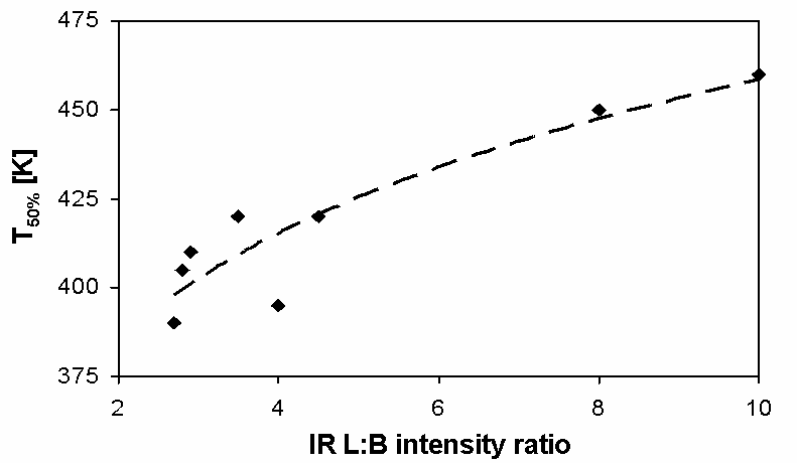

Figure 2.9: CO oxidation activity over supported Pt nanoparticles expressed by $T_{50\%}$ as a function of the IR L:B intensity ratio.

It is well known that the CO oxidation on Pt proceeds *via* a three-steps Langmuir-Hinshelwood reaction scheme:[43-45]

$$CO_{gas} \leftrightarrow CO_{ads} \quad (1)$$

$$(O_2)_{gas} \rightarrow 2\ O_{ads} \quad (2)$$

$$CO_{ads} + O_{ads} \rightarrow (CO_2)_{gas} \quad (3)$$

where the indices “gas” and “ads” refer to the gas phase and adsorbed species, respectively. Under ultra high vacuum conditions CO adsorbs associatively and starts to desorb above about 350 K, while O_2 adsorbs dissociatively above about 100 K, and desorbs associatively above 720 K.[45-46] CO diffuses rapidly over the surface and reacts with O to yield CO_2, which immediately desorbs into the gas phase. Based on the reaction scheme (1)-(3) one can assume that in an excess of oxygen (as is the case for our catalytic experiments) and at temperatures around the desorption temperature of CO (350 K) the rate of the reaction r is determined by the relative surface concentration of adsorbed CO; *i.e.*, the CO surface coverage ($\theta_{C\equiv O}$). One could then write the reaction equation as follows:

$$r = - \{d[(CO_2)_{gas}]/dt\} = k' \theta_{C\equiv O} \quad (4)$$

As shown before, we were able based on the IR measurements to estimate values for the different catalysts under study. The combined information from Figures 2.8 and 2.9 allows us to state that there exists a relationship between $T_{50\%}$ and $\theta_{C\equiv O}$; *i.e.*, CO oxidation over supported Pt particles is facilitated by a higher CO coverage and *vice versa*. This is in line with reaction equation (4). This effect can be

achieved by adding the adequate promoter element to the catalyst system. With the exception of Cs^+, from which the material exhibited larger particles and could not be directly compared with the other samples, K^+ seems to be the best promoting element for tuning the electronic properties of the supported Pt nanoparticles.

One should, however, be aware that the spectroscopic and catalytic measurements are not done under the same environmental conditions, *i.e.*, reducing *vs.* oxidising environments. Indeed, the characterisation by EXAFS and IR does not necessarily represent the state of the active catalyst material and the reduced Pt particles can be (partially) oxidised under the catalytic conditions employed. An alternative explanation could be that the differences in electron density of the Pt nanoparticles on the different support materials lead to higher fraction of surface oxidation. An alternative explanation could therefore be that differences in oxygen coverage on the Pt nanoparticles lead to the observed differences in the CO oxidation performances. In any case, the electronic properties of the supported Pt nanoparticles influence the catalytic behaviour of the materials under study.

Finally, it should be emphasised that the addition of promoter elements has, besides electronic effects, also structural or stabilisation effects, which have not been the subject of this work. Much literature exists in which BaO has been studied in relation to its NO_x storage properties.[47-55] Here, we show that besides this NO_x adsorption capability, BaO also induces an electronic effect on the supported Pt nanoparticles. In this respect, zeolite Y-supported Pt particles of uniform sizes can be regarded as model systems to study in a controlled manner the effect of the addition of alkali and alkaline earth metal cations to the electronic properties of Pt.

4 Conclusions

Based on this work the following conclusions can be made:

(1) Time-resolved infrared spectroscopy proves to be a feasible tool to monitor desorption of CO from highly dispersed supported Pt catalysts as a function of temperature and time. Next to the surface coverage, the position and shape of the linear and bridge Pt-bonded CO stretching band appear to be very sensitive to the chemical composition of the support and the desorption temperature. The work also demonstrates that a high CO stretching frequency is not by

definition related to the desorption rate of CO, which is not correlated to a strong Pt−C≡O bonding and *vice versa*.

(2) The red shift of the linear Pt-coordinated C≡O vibration compared to that of gas-phase CO increases with an increasing cation radius-to-charge ratio. In addition, a systematic shift from linear to bridge bonded CO was observed for decreasing Lewis acidity, as expressed by the Kamlet-Taft parameter α. A decreasing α results in an increasing electron charge on the framework oxygen atoms and therefore an increasing electron charge on the supported Pt nanoparticles.

(3) The CO coverage on the supported Pt nanoparticles increases with increasing electron density on Pt. This increasing electron density was found to result in an increased CO oxidation activity and basic promoters facilitate the chemisorption of CO on the Pt nanoparticles. This adsorbed CO reacts with adsorbed O according to a Langmuir-Hinshelwood mechanism to give rise to the formation of CO_2. The most promoted CO oxidation catalyst, except for Pt/Cs-Y which had a different particle size distribution, is a Pt/K-Y sample, with a $T_{50\%}$ of 390 K and a L:B ratio of 2.7.

References

[1] (a) Arena, G.E.; Centi, G., *Top. Catal.* **2004**, *30-31*, 147; (b) Centi, G.; Arena, G.E., *J. Mol. Catal. A: Chem.* **2003**, *204*, 663; (c) Fornasari, G.; Trifiro, F.; Vaccari, A.; Prinetto, F.; Ghiotti, G.; Centi, G., *Catal. Today* **2002**, *75*, 421; (d) Liotta, L.F.; Macaluso, A.; Arena, G.E.; Livi, M.; Centi, G., *Catal. Today* **2002**, *75*, 439.

[2] (a) Schmauke, T.; Eichel, R.A., Schweiger, A.; Roduner, E., *Phys. Chem. Chem. Phys.* **2003**, *5*, 3076; (b) Schmauke, T.; Menzel, M.; Roduner, E., *J. Mol. Catal. A: Chem.* **2003**, *194*, 211; (c) Zheng, J.; Schmauke, T.; Roduner, E.; Dong, J.L.; Xu, Q.H., *J. Mol. Catal. A: Chem.* **2001**, *171*, 181; (d) Schmauke, T.; Moller, E.; Roduner, E., *Chem. Commun.* 1998, 2589.

[3] (a) Miller, J.T.; Koningsberger, D.C., *J. Catal.* **1996**, *162*, 209; (b) Koningsberger, D.C.; Ramaker, D.E.; Miller, J.T.; De Graaf, J.; Mojet, B.L., *Top. Catal.* **2001**, *15*, 35; (c) De Graaf, J.; van Dillen, A.J.; de Jong, K.P.; Koningsberger, D.C., *J. Catal.* **2001**, *203*, 307.

[4] Barth, R.; Pitchai, R.; Anderson, R.L.; Verykios, X., *J. Catal.* **1989**, *116*, 61.

[5] Blyholder, G.J., *J. Phys. Chem.* **1968**, *60*, 2772.

[6] Mojet, B.L.; Miller, J.T.; Koningsberger, D.C., *J. Phys. Chem. B* **1999**, *103*, 2724.

[7] Kappers, M.J.; Vaarkamp, M.; Miller, J.T.; Modica, F.S.; Barr, M.K.; van der Maas, J.H.; Koningsberger, D.C., *Catal. Lett.* **1993**, *21*, 235.

[8] Ramaker, D.E.; de Graaf, J.; van Veen, J.A.R.; Koningsberger, D.C., *J. Catal.* **2001**, *203*, 7.

[9] Xu, J.; Yates, J.T., *Surf. Sci.* **1995**, *327*, 193.

[10] Xu, J.; Hendriksen, P.N.; Yates, J.T., *Langmuir* **1994**, *10*, 3663.

[11] Hayden, B.E.; Kretzschmar, K.; Bradshaw, A.M., *Surf. Sci.* **1985**, *149*, 394.

[12] Mukerji, R.J.; Bolina, A.S.; Brown, W.A., *Surf. Sci.* **2003**, *527*, 198.

[13] Barth, A.; Ramachandran, A., *J. Catal.* **1990**, *125*, 467.

[14] Gandao, Z.; Coq, B.; de Ménorval, L.C.; Tichit, D*., Appl. Catal. A:General* **1996**, *147*, 395.

[15] Bourane, A.; Bianchi, D., *J. Catal.* **2003**, *218*, 447.

[16] Welch, P.C.; Mills, P.S.W.; Mason, C.; Hollins, P., *J. Electr. Spectrosc. Rel. Phenom.* **1993**, *64/65*, 151.

[17] Hollins, P., *Surf. Sci. Rep.* **1992**, *16*, 51.

[18] Koper, M.T.M.; van Santen, R.A.; Wasileski, S.A.; Weaver, M.J., *J. Chem. Phys.* **2000**, *113*, 4392.

[19] Greenler, R.G.; Brandt, R.K., *Physicochem. Eng. Aspects* **1995**, *105*, 19.

[20] Hippe, C.; Lamber, R.; Schulz-Ekloff, G.; Schubert, U., *Catal. Lett.* **1997**, *43*, 195.

[21] Silvestre-Albero, J.; Sepulveda-Escribano, A.; Rodriguez-Reinoso, F.; Anderson, J.A., *Phys. Chem. Chem. Phys.* **2003**, *5*, 208.

[22] Sharma, R.K.; Brown, W.A.; King, D.A., *Surf. Sci.* **1998**, *414*, 68.

[23] Stoop, F.; Toolenaar, F.J.C.M.; Ponec, V., *J. Catal.* **1982**, *73*, 50.

[24] Geidel, E.; Lechert, H.; Dobler, J.; Jobic, H.; Calazferri, G.; Bauer, F., *Micropor. Mesopor. Mat.* **2003**, *65*, 31.

[25] Otero Arean, C.; Turnes Palomino, G.; Zecchina, A.; Spoto, G.; Bordiga, S.; Roy, P., *Phys. Chem. Chem. Phys.* **1999**, *1*, 4139.

[26] De Mallman, A.; Barthomeuf, D., *Stud. Surf. Sci. Catal.* **1989**, *46*, 429.

[27] Gijzeman, O.L.J.; Mens, A.J.M.; van Lenthe, J.H.; Mortier, W.J.; Weckhuysen, B.M., *J. Phys. Chem. B* **2003**, *107*, 678.

[28] Vaarkamp, M.; Linders, J.C.; Koningsberger, D.C., *Physica B* **1995**, *208/209*, 9825.

[29] Vaarkamp, M.; Mojet, B.L.; Kappers, M.J.; Miller, J.T.; Koningsberger, D.C., *J. Phys. Chem.* **1995**, *99*, 16067.

[30] Nijhuis, T.A.; Makkee, M.; van Langeveld, A.D.; Moulijn, J.A., *Appl. Catal. A: General* **1997**, *164*, 237.

[31] Schulz-Ekloff, G. *Stud. Surf. Sci. Catal.* **1991**, *69*, 65, Wark, M.; Schulz-Ekloff, J.N.I.; Zukal, A. *Stud. Surf. Sci. Catal.* **1991**, *69*, 189.

[32] Vaarkamp, M.; Grondell, J.V.; Miller, J.T.; Sajkowski, D.J.; Modica, F.S.; Lane, G.S.; Gates, B.C.; Koningsberger, D.C. *Catal. Lett.* **1990**, *6*, 369.

[33] Sheppard, N.; Nguyen, T.T., *Adv. Infrared Raman Spectrosc.* **1978**, *5*, 67.

[34] Bourane, A.; Dulaurent, O.; Bianchi, D., *J. Catal.* **2000**, *196*, 115.

[35] Greenler, R.G.; Brandt, R.K., *Coll. Surf. A : Physicochem. Eng. Asp.* **1995**, *105*, 19.

[36] Larin, A.V.; Leherte, L.; Vercauteren, D.P., *Phys. Chem. Chem. Phys.* **2002**, *4*, 2416.

[37] Larin, A.V.; Vercauteren, D.P.; Lamberti, C.; Bordiga, S.; Zecchina, A., *Phys. Chem. Chem. Phys.* **2002**, *4*, 2424.

[38] Wasileski, S.A.; Weaver, M.A.; M.T.M. Koper, *J. Electroanal. Chem.* **2001**, *500*, 344.

[39] Marcus, Y., *Ion properties*, Marcel Dekker, New York, Basel, Hong Kong, **1997**, p. 193.

[40] Renema, J. Structural information from carbonyl stretching frequencies. Ph.D. Thesis. Utrecht University, **1972**.

[41] Vannice, M.A.; Twu, C.C., *J. Chem. Phys.* **1981**, *75*, 5944.

[42] Venderbosch, R.H.; Prins, W.; van Swaaij, W.P.M. *Chem. Eng. Sci.* **1998**, *53*, 3355.

[43] Ertl, G.; Engel, T., *Adv. Catal.* **1979**, *28*, 1.

[44] Ertl, G., *Adv. Catal.* **1990**, *37*, 1.

[45] Nolan, P.D.; Lutz, B.R.; Tanaka, P.L.; Davis, J.E.; Mullins, C.B., *J. Chem. Phys.* **1999**, *111*, 3696.

[46] Artsyukhovich, A.N.; Ukraintsev, V.A.; Harrison, I., *Surf. Sci.* **1996**, *347*, 303.

[47] Broqvist, P.; Gronbeck, H.; Fridell, E.; Panas, I., *J. Phys. Chem.* **2004**, *108*, 3523.

[48] Nova, I.; Castoldi, L.; Prinetto, F.; Dal Santo, V.; Lietti, L.; Tronconi, E.; Forzatti, P.; Ghiotti, G.; Psaro, R.; Recchia, S., *Top. Catal.* **2004**, *30-31*, 181.

[49] Fridell, E.; Skoglundh, M.; Westerberg, B.; Johansson, S.; Smedler, G., *J. Catal.* **1999**, *183*, 196.

[50] Olsson, L.; Persson, H.; Fridell, E.; Skoglundh, M.; Andersson, B., *J. Phys. Chem. B* **2001**, *105*, 6895.

[51] Lesage, T.; Verrier, C.; Bazin, P., Saussey, J.; Daturi, M., *Phys. Chem. Chem. Phys.* **2003**, *5*, 4435.

[52] Lesage, T.; Verrier, C.; Bazin, P., Saussey, J.; Malo, S.; Hedouin, C.; Blanchard, G.; Daturi, M., *Top. Catal.* **2004**, *30-31*, 31.

[53] Shinjoh, H.; Tanabe, T.; Sobukawa, H.; Sugiura, M., *Top. Catal.* **2001**, 16-17, 95.

[54] Takahashi, N.; Shinjoh, H.; Iijima, T.; Suzuki, T.; Yamazaki, K.; Yokota, K.; Suzuki, H.; Miyoshi, N.; Matsumoto, S.; Tanizawa, T.; Tanaka, T.; Tateishi, S.; Kasahara, K., *Catal. Today* **1996**, *27*, 63.

[55] Shinjoh, H.; Takahashi, N.; Yokota, K.; Sugiura, M., *Appl. Catal. B: Environmental* **1998**, *15*, 189.

Chapter 3

Pore curvature and support composition effects on the electronic properties of supported Pt catalysts: An infrared spectroscopy study with CO as probe molecule

Abstract

Supported 1 wt% Pt-based catalyst materials have been used as model systems to study pore curvature and support composition effects on the electronic properties of supported Pt nanoparticles. For this purpose, Pt nanoparticles have been loaded onto all-silica microporous (ITQ-1), mesoporous (MCM-41, MCM-48 and SBA-15) and macroporous (SiO_2) supports, as well as onto a macroporous SiO_2 support, impregnated with monovalent (Na^+, Cs^+) and divalent (Mg^{2+}, Ba^{2+}) cations. Time- and temperature-dependent infrared spectroscopy with CO as probe molecule has been used to investigate the adsorption and desorption properties of CO from these supported Pt nanoparticles. At 323 K, a narrow and smooth linear Pt-coordinated C≡O vibration band at 2070 cm^{-1} was observed for the all-silica catalysts. The IR CO-TPD results revealed a slightly higher desorption rate for the micro- and mesoporous supports, probably due to larger non-bonding electrostatic interactions between CO and the pore walls. A systematic shift from linear (L) to bridge (B) bonded C≡O upon a decrease of the radius of curvature, which would indicate an increasing electron charge on the supported Pt nanoparticles, is however not observed. In contrast, a relationship between the L:B band intensity ratio and the Lewis acidity of the monovalent and divalent cations, as expressed by the Kamlet-Taft parameter α, was observed for the Pt/SiO_2 catalysts. This effect is less pronounced than for zeolite-supported Pt nanoparticles (as studied in Chapter 2), but the results demonstrate that the correlation can be easily transferred from one support type to another, thus providing further guidelines for the design of improved automotive catalysts.

1 Introduction

The catalytic properties of supported nano-sized noble metal particles are known to be tuneable by changing the chemical composition, porosity and structure of the support material. However, despite many characterisation studies that have been undertaken to elucidate the exact nature of this metal-support effect,[1-6] many questions still remain, preventing the design of improved catalyst systems based on an intelligent choice of the support material. In principle, three effects of the support on the catalytic activity of the metal particles can be distinguished: *i.e.*, (1) the support composition, (2) the support pore size and curvature and (3) the presence of promoting elements. In Chapter 2, well-defined Pt nanoparticles supported on a microporous crystalline aluminosilicate material were studied by Pt−C≡O temperature programmed desorption infrared spectroscopy (TPD-IR). More specifically, we have investigated the effect of monovalent (Na^+, K^+, Rb^+ and Cs^+) and divalent (Mg^{2+}, Ca^{2+}, Sr^{2+} and Ba^{2+}) cations on the electronic properties of Pt nanoparticles entrapped in the supercages of zeolite Y. It was found that the Pt electron density increased with decreasing Lewis acidity of the cation introduced in the zeolite matrix. Simultaneously, the CO coverage increased with increasing electron density, which resulted in an enhanced CO oxidation activity.

In order to further shed light into the origin of these intriguing metal-support interactions, it is worthwhile to perform a similar systematic study on the effect of the support pore curvature. For that reason, we have decided to investigate the physicochemical properties of supported Pt nanoparticles in a series of catalysts with different curvatures of the support wall by means of CO TPD-IR spectroscopy. To exclude effects of the chemical composition, we have investigated a series of Pt-loaded all-silica supports with an architecture ranging from micropores over mesopores to macropores. ITQ-1 is an all-silica microporous molecular sieve with a pore structure similar to that of zeolite Y,[7-9] while MCM-41, MCM-48 and SBA-15 are different mesoporous all-silica solids also possessing amorphous silica walls.[10-11] Finally, SiO_2 is an amorphous all-silica material containing macropores. It will be shown that the effect of the pore curvature of an all-silica support on the electron density of supported Pt nanoparticles plays only a minor role. As a consequence, the chemical composition of the support must play the dominant role. For that reason, it was a logical next step to investigate whether the effect on the electronic

properties of the metal particles that was obtained by the introduction of promoting cations in Pt/zeolite-Y (see Chapter 2) could be transferred to other support materials, such as an all-silica one. For this purpose, we have studied a series of Pt/SiO_2 catalysts loaded with monovalent (Na^+, Cs^+) and divalent (Mg^{2+}, Ba^{2+}) cations. It will be shown that the promoting effect also correlates with the Lewis acidity of the cations under study, although the promoting effect is less pronounced than previously observed for zeolite-based materials.

2 Experimental section

2.1 Catalyst preparation

The microporous silica material ITQ-1 has been synthesised according to a recipe of Camblor and co-workers.[7-9] SBA-15, MCM-41 and MCM-48 materials were used as mesoporous silica supports and were prepared according to the method of, respectively, Van der Voort *et al.*,[10-11] Mokaya and Jones[12] and Baltes *et al.*[16] Amorphous SiO_2 was used as a macroporous support and obtained from Aldrich (Davisil 645). The same material was used to prepare $Na\text{-}SiO_2$, $Cs\text{-}SiO_2$, $Mg\text{-}SiO_2$ and $Ba\text{-}SiO_2$ by dry impregnation with aqueous solutions of the corresponding metal nitrates. The following materials were used for this purpose: $NaNO_3$ (Merck, p.a.), $CsNO_3$ (Acros, 99.9%), $Mg(NO_3)_2.6H_2O$ (Acros, 99%) and $Ba(NO_3)_2$ (Merck, p.a.).

Next, 1 wt% supported Pt particles were prepared *via* a dry impregnation step of the support materials with the appropriate aqueous solutions of $Pt(NH_3)_4(NO_3)_2$. After impregnation and drying at 353 K in N_2 (quality 4.0; Hoekloos) for 8 h, calcination was carried out by drying in a high air flow (30 ml/min) during 12 h followed by increasing the temperature to 573 K at a heating rate of 0.2 K/min, where it was kept for 8 h to achieve complete removal of NH_3/NO_3 prior to reduction. Reduction was performed in a 60 ml/min H_2 (quality 5.0; Hoekloos) flow with a ramp of 5 K/min to 573 K, which was kept for 1 h. After reduction and flushing with N_2 at room temperature, passivation was carried out by increasing the O_2 flow to 10 ml/min to prevent aggregation of Pt particles.

2.2 Catalyst characterisation

X-ray fluorescence (XRF) was carried out on all samples to determine the Pt and cation loadings using a Spectro X-lab 2000 instrument (Spectro). N_2 (quality 4.0;

Hoekloos) physisorption was performed at 77 K with a Micromeritics ASAP 2400 apparatus. Prior to these measurements, the samples were degassed for 24 h at 573 K in vacuum. Surface area, pore volume and pore size distribution were calculated with standard BET theory. High-resolution transmission electron microscopy (HRTEM) was done with a Philips CM 30 UT electron microscope equipped with a field emission gun as the source of electrons, operated at 300 kV. Samples were mounted on a microgrid carbon polymer supported on a copper grid by placing a few droplets of a suspension of ground sample in ethanol on the grid, followed by drying at ambient conditions. Extended X-ray absorption fine structure (EXAFS) measurements were carried out at the ESRF (Grenoble, France) on the CRG DUBBLE beamline (BM26A). The samples were prepared by pressing 0.12 g to 0.14 g powder to a self-supporting wafer. Next, the wafer was placed in a treatment cell. Prior to measurement, the sample was dried at 423 K for 30 min in a flow of dry He and then slowly heated to 573 K under a flow of 10 % H_2 in He to reduce the passivated Pt. Finally, the samples were measured at liquid N_2 temperature. EXAFS data analysis was carried out with the XDAP program.[14]

Infrared (IR) measurements were performed on self-supporting catalyst wafers that were pressed from 0.01-0.05 g of calcined and reduced sample material. A pressure of 3 bar was applied during 10 s to prevent destruction of the pore structure of the support.[15] The wafer was placed in an IR transmission cell equipped with CaF_2 windows as previously described.[16] The cell was evacuated to 10^{-8} bar followed by drying of the wafer at 323 K overnight prior to reduction by a 10 ml/min flow of H_2 (quality 4.6; Hoekloos). During reduction the temperature was raised from 323 K to 573 K where it was maintained for 1 h. Next, the system was switched to vacuum and after 1 h at 573 K, cooled to 323 K at a rate of 3 K/min. In the next step, the catalyst wafer was exposed to 10% CO (quality 4.7; Hoekloos) in He (quality 4.6; Hoekloos) at a pressure of 0.2 bar. After 30 min of static pressure, the system was re-evacuated and after another 30 min, temperature programmed desorption (TPD) was started by increasing the temperature from 323 to 573 K (3 K/min), where it was maintained for 30 min. IR spectra were recorded on a Perkin-Elmer 2000 FTIR instrument with a data point resolution of 4 cm^{-1}. For each spectrum, 25 scans were co-added. As a background, the spectrum of the catalyst wafer was taken after drying, reduction and cooling down to 323 K, 2 min prior to CO exposure. During CO adsorption and TPD, time-resolved scanning was carried out by automatically

acquiring spectral data every 2 min using the Perkin-Elmer Time-Base software. Intensity data were acquired by calculating the integrated area of baseline corrected spectra using the Perkin-Elmer Spectrum software.

3 Results and discussion

3.1 Catalyst characterisation

The physicochemical properties of the catalyst materials under study as obtained with N_2 physisorption, XRF, HRTEM and EXAFS are summarised in Table 3.1. The surface area of Pt/ITQ-1 was 418 m^2/g with a mean pore diameter of 3.2 nm and a micropore volume of 0.18 ml/g. The surface area of the mesoporous Pt/ MCM-41, Pt/ MCM-48 and Pt/ SBA-15 was 947, 690 and 678 m^2/g, respectively. This is a reduction of about 10-20 % compared to the BET results obtained prior to Pt impregnation and it is attributed to blocking of some of the pore architecture. The corresponding pore diameters were 2.7, 3.0 and 5.8 nm. The results for Pt/SBA-15 pointed to a significant amount of 1 nm micropores, next to the 5.8 nm

Table 3.1: Physicochemical properties of the catalysts under study.

Sample	Pt loading [wt%] [a]	Pt particle size [nm] [b]	N [c]	Surface area [m^2/g] [d]	Pore volume [ml/g] [d]	Mean pore diameter [nm] [d]
Pt/ITQ-1	1.4	1	6.5	418	0.18	3.2
Pt/MCM-41	0.7	1-4	8.2	947	1.08	2.7
Pt/MCM-48	1	1-4	7.6	690	1.15	3
Pt/SBA-15	0.7	1	6.5	678	0.90 (0.17 micro)	5.8
Pt/SiO_2	0.9	1-4	7.9	542	0.23	16
Pt/Na-SiO_2	1.8	1-2	-	125	< 0.01	12
Pt/Cs-SiO_2	1.2	1-10	8.8	102	< 0.01	26
Pt/Mg-SiO_2	1.7	1-3	-	209	< 0.01	7.5
Pt/Ba-SiO_2	1.3	1-3	7	193	< 0.01	18

[a] As determined by X-ray fluorescence (XRF).

[b] As determined from high resolution transmission electron microscope (HRTEM) pictures.

[c] Coordination number of the Pt-Pt contributions as determined from extended X-ray absorption fine structure spectroscopy (EXAFS) measurements.

[d] As determined by N_2 physisorption measurements.

mesopores.[10-11] The amorphous SiO_2 samples exhibited the expected low pore volumes (< 0.1 ml/g) and average mean pore diameters larger than 10 nm. The Pt content of the different catalyst materials as determined by XRF varied between 0.7 wt% Pt (Pt/SBA-15) and 1.7 wt% Pt (Pt/Mg-SiO_2). The estimated amount of cations in the Pt/Na-SiO_2 and Pt/Mg-SiO_2 samples was 0.5 wt%, while for Pt/Cs-SiO_2 and Pt/Ba-SiO_2 a content of 4 wt% was determined with XRF. The HRTEM pictures revealed that the Pt nanoparticles of the all-silica catalysts are well-dispersed. The majority of the particles were about 1 nm with some larger Pt-agglomerates for Pt/MCM-41, Pt/MCM-48 and Pt/SiO_2. The metal ion-impregnated Pt/SiO_2 samples showed Pt clusters of 1-3 nm for Pt/Na-SiO_2, Pt/Mg-SiO_2 and Pt/Ba-SiO_2, while for Pt/Cs-SiO_2 particles up to 10 nm were present. The same observation of larger Pt-particles was made in Chapter 2 on the Pt/Cs-Y catalysts. To illustrate the Pt particle size and distribution, a selection of HRTEM micrographs of Pt/ITQ-1, Pt/MCM-41, Pt/Na-SiO_2 and Pt/Ba-SiO_2 is presented in Figure 3.1.

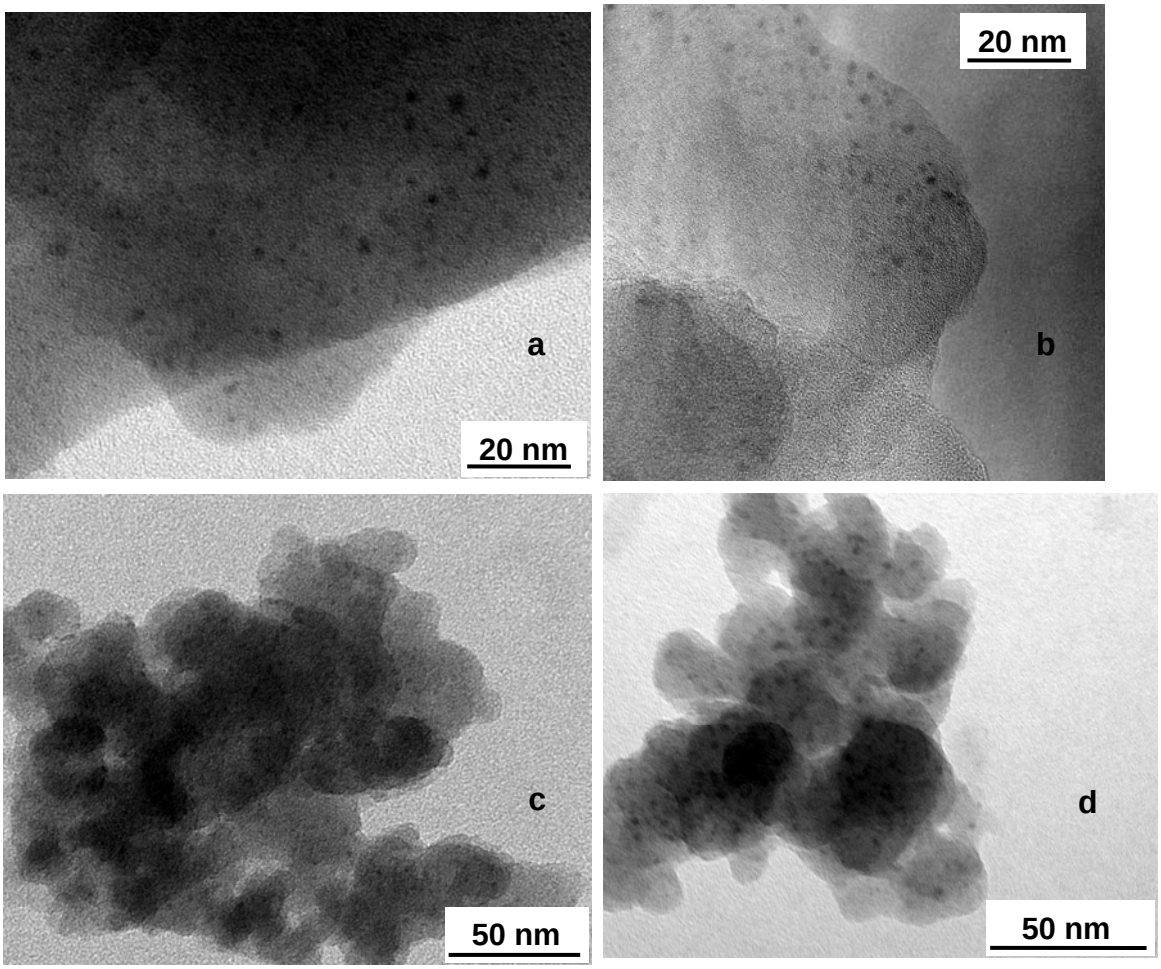

Figure 3.1: HRTEM micrographs of (a) Pt/ITQ-1, (b) Pt/MCM-41, (c) Pt/Na-SiO_2 and (d) Pt/Ba-SiO_2.

The Pt coordination numbers determined with EXAFS are in close agreement with the results of HRTEM. For Pt/ITQ-1 and Pt/SBA-15, a coordination number of about 6.5 was found, which corresponds to an average Pt particle size of 1.1 nm, while the values of 7-8 obtained for Pt/MCM-41, Pt/MCM-48 and the Pt/SiO_2 samples point to an average diameter of about 1.5 nm.

3.2 Infrared CO adsorption experiments

The results of the IR-CO temperature programmed desorption are shown in 3D projection in Figures 3.2 and 3.3. The corresponding band maxima, the half band width (HBW) of the linear band and the linear-to-bridge (L:B) intensity ratio at

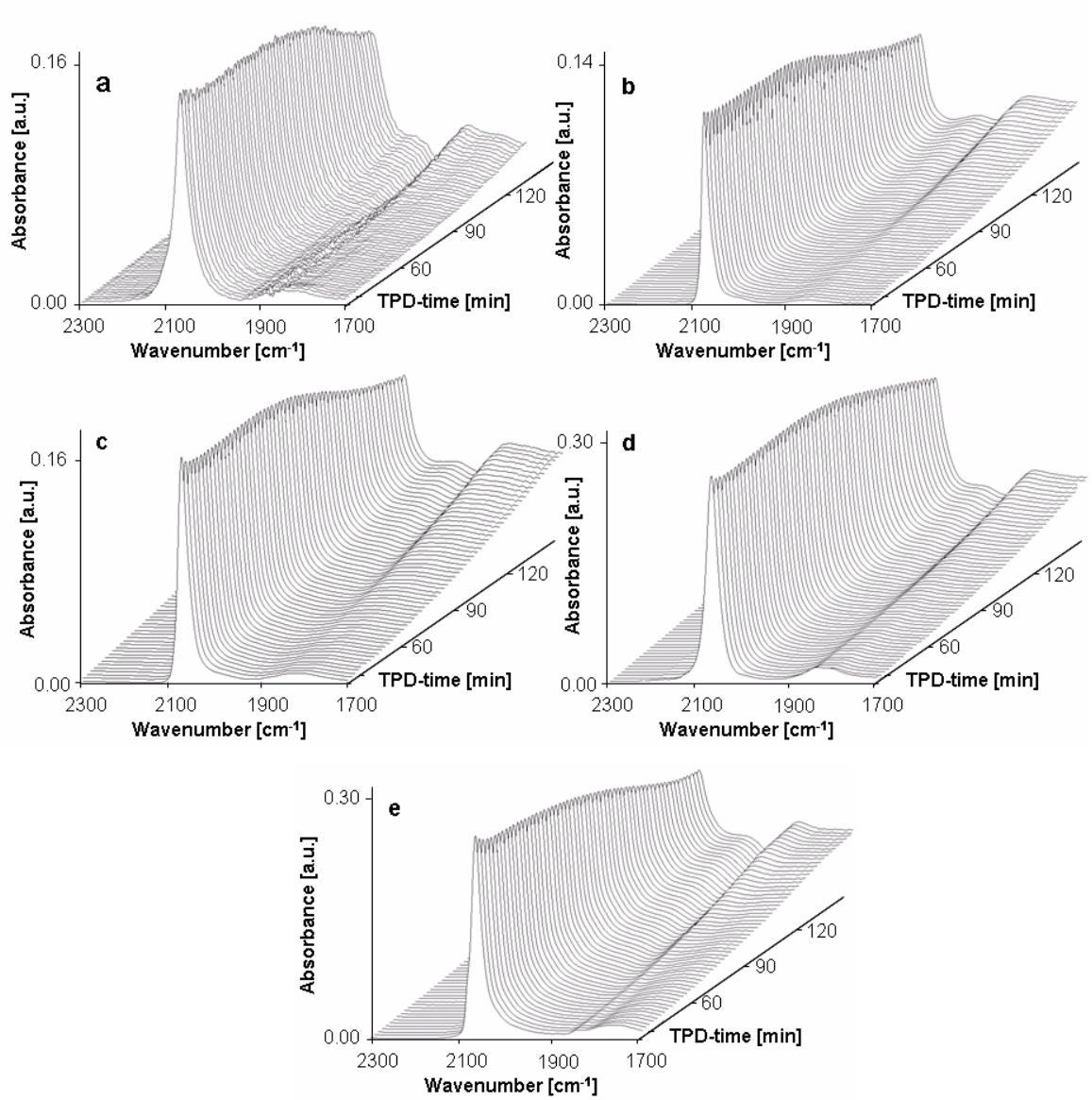

Figure 3.2: Time-resolved IR spectra during temperature programmed CO desorption from (a) Pt/ITQ-1, (b) Pt/MCM-41, (c) Pt/MCM-48, (d) Pt/SBA-15 and (e) Pt/SiO_2.

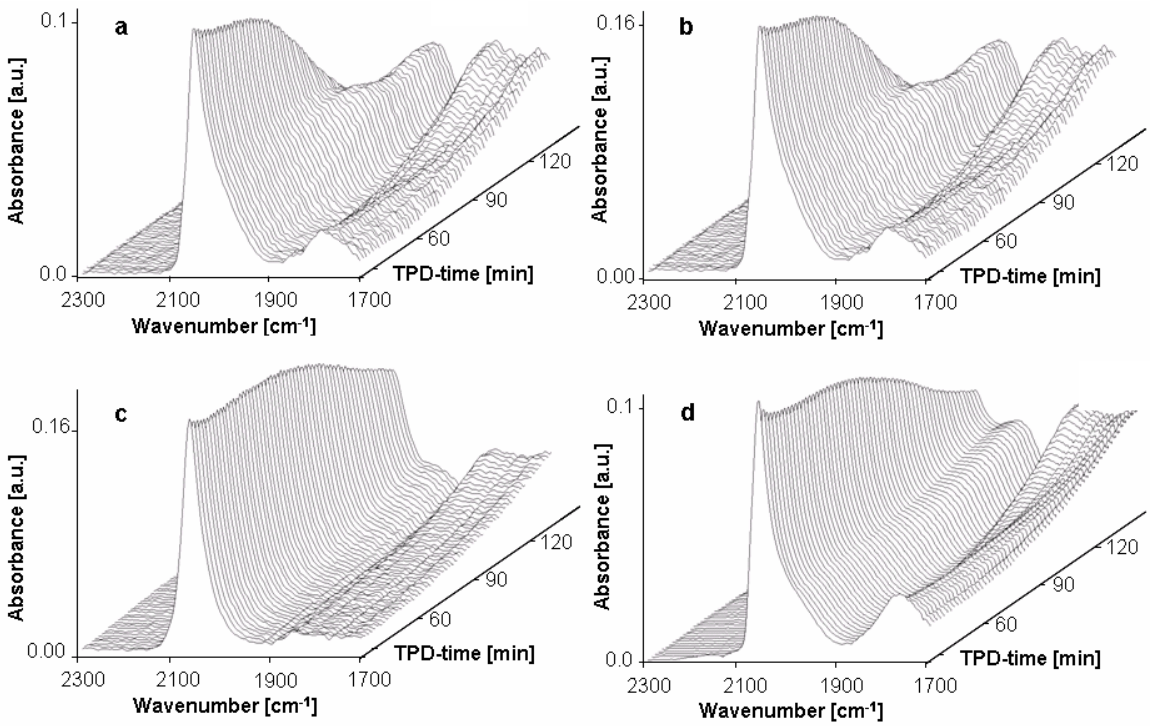

Figure 3.3: Time-resolved IR spectra during temperature programmed CO desorption from (a) Pt/Na-SiO_2, (b) Pt/Cs-SiO_2, (c) Pt/Mg-SiO_2 and (d) Pt/Ba-SiO_2.

selected temperatures are listed in Table 3.2. All catalysts show a strong IR-absorption band in the range 2100-2000 cm^{-1} and a weaker one at around 1800 cm^{-1}. As reported in Chapter 2 and in the literature, the high wavenumber band is commonly assigned to the linear Pt-bonded C≡O stretching vibration, while the lower frequency components are attributed to bridge coordinated types of CO.[16-21] At higher temperature the band patterns become more complex due to reorientation of the CO as a result of changing interactions. This was as well observed in Chapter 2 and by Hippe and co-workers.[21] In what follows, we will discuss the effects of the pore curvature and the promoting elements separately.

3.2.1 Pore curvature effects

In order to study the effect of the pore curvature of the support material on the electronic properties of the supported Pt nanoparticles, the IR-CO-TPD results of the all-silica microporous (Pt/ITQ-1), mesoporous (Pt/MCM-41, Pt/MCM-48 and Pt/SBA-15) and macroporous (Pt/SiO_2) catalysts have been compared. The linear coordinated CO stretching band is smooth and fairly symmetrical for all compounds.

Table 3.2: Maxima of the linear and bridge Pt-coordinated C≡O stretching bands at different temperatures during TPD.

Sample	HBW [cm^{-1}] [a]	L:B [b]	Linear Pt−C≡O band [cm^{-1}] at				Pt−C≡O band [cm^{-1}] at [c]		Bridge Pt−C≡O band [cm^{-1}] at			
			323 K	373 K	473 K	573 K	473 K	573 K	323 K	373 K	473 K	573 K
Pt/ITQ-1	37	10.3	2071	2069	2060	2050	1950	1950	1829	1820	1839	1832
Pt/MCM-41	33	14.1	2070	2069	2062	2061	1938	1938	1850	1840	1812	1812
Pt/MCM-48	28	11.5	2070	2069	2061	2053	1940	1937	1816	1819	1829	1830
Pt/SBA-15	29	12.4	2069	2068	2060	2046	1936	1936	1826	1825	1825	1828
Pt/SiO_2	29	11.1	2070	2069	2063	2052	1940	1939	1833	1820	1818	1818
$Pt/Na\text{-}SiO_2$	65	4.0	2055	2052	2035	-	1961	1948	1767	1768	1790	1820
$Pt/Cs\text{-}SiO_2$	83	3.6	2033	2029	1997	-	1950	1951	1786	1786	1785	1790
$Pt/Mg\text{-}SiO_2$	54	8.9	2066	2065	2058	2041	1940	1941	1815	1815	1815	1816
$Pt/Ba\text{-}SiO_2$	53	4.4	2064	2063	2054	2046	1950	1936	1763	1765	1816	1819

[a] Half band width (HBW) of the linear Pt−C≡O band at 323 K.

[b] Linear-to-bridge (L:B) band intensity ratio at 323 K.

[c] Band appearing upon heating pointing to the formation of bridge bonded C≡O, affected by neighbouring cations.

Besides, as listed in Table 3.2, the HBW at 323 K is rather small (28-37 cm^{-1}), which points to a single type of linear Pt-coordinated C≡O and hence to a more or less uniform Pt-particle size. This is in line with the results from HRTEM and EXAFS.

At low temperature, the band around 1800 cm^{-1} is also virtually symmetrical, which suggests mainly one type of bridge bonded CO. At these conditions, the integrated band intensity is less then 10 % of that of the linear coordinated band (*i.e.* L:B ratio > 10, Table 3.2) for all catalyst materials, indicating a limited presence of bridged conformations. Furthermore, above 423 K, an absorption band at around 1940 cm^{-1} grows in, pointing to the formation of bridge-bonded CO. At identical conditions, the position of the linear C≡O band at 323 K is practically the same for all catalyst materials and the shift to lower wavenumber upon increasing the temperature is small (17-23 cm^{-1}). Cooling down to ambient temperature after TPD resulted in a small blue shift of the C≡O band, but different from what has been reported for Pt/SiO_2 by Barth and Ramachandran,[20] a gain in intensity was not observed. According to literature,[17] frequency shifts of 20-30 cm^{-1} can be largely attributed to changes in temperature and for that reason we conclude that the effect of the pore curvature on the C≡O stretching vibration is small. Hence, assuming that the C≡O force constant is inversely proportional to the Pt−C(O) bond strength, one would expect that the CO desorption shows the same picture for all catalyst materials. However, as can be seen from Figure 3.2, the IR-desorption patterns are not identical. The main difference is observed in the decrease of the linear band above 523 K. As will be shown later, this is not only caused by CO desorption, but also partly by the conversion of linear into bridge bonded CO conformations, as expressed by the small increase in intensity of the band at 1800 cm^{-1}. The reduction in intensity of the linear CO band follows the order Pt/MCM-41 > Pt/MCM-48 ≈ Pt/SBA-15 > Pt/SiO_2, which is the inverse ranking of the corresponding mean pore diameter (Table 3.1), although the Pt/ITQ-1 material seems not to follow this trend. In principle, two non-bonding effects might play a role here. The first one is the Coulomb interaction between CO and framework oxygen atoms. Regarding the small pore diameter of particularly, Pt/MCM-41, Pt/MCM-48 and Pt/ITQ-1 in relation to the 1 nm Pt particle size, it is plausible to assume that such an electrostatic interaction will play the largest role in the microporous and mesoporous supports. Since these interactions are repulsive, it explains the higher desorption rate for the smaller pore diameter supports. Indeed, one could argue that the small pore volume

of ITQ-1 should have been attended with a larger effect, but this can be explained by assuming the Pt nanoparticles to be partly present outside the micropores. The second effect is the increasing contact area of the Pt particles and the support when the pore curvature increases, as schematically visualised in Figure 3.4.

In this model, a larger contact area will result in a larger electron withdrawing influence of the acidic support sites on the Pt nanoparticles. As a consequence, the back donation to CO decreases and the Pt−C(O) bond strength becomes weaker, which results in a higher CO desorption rate as observed. According to the results of Chapter 2 and of Koningsberger *et al.*,[3] a decrease in back donation might also cause a reduced presence of bridge bonded Pt−C≡O, but, as can be seen in Table 3.2, the linear to bridge intensity ratio (L:B) is about the same for all catalyst materials. In principle, a decreased back donation to CO and repulsive O···O interactions might lead to a higher C≡O frequency, but as already deducted such correlation is absent. It confirms the conclusion from Chapter 2, that a high C≡O stretching frequency is not by definition related to a weak Pt−C(O) bonding and *vice versa*. This is also in accordance with the conclusion of Wasileski *et al.*,[22] that there is no simple correlation between the field dependent Pt bonded C≡O vibration frequency and the Pt−C(O) bonding energy.

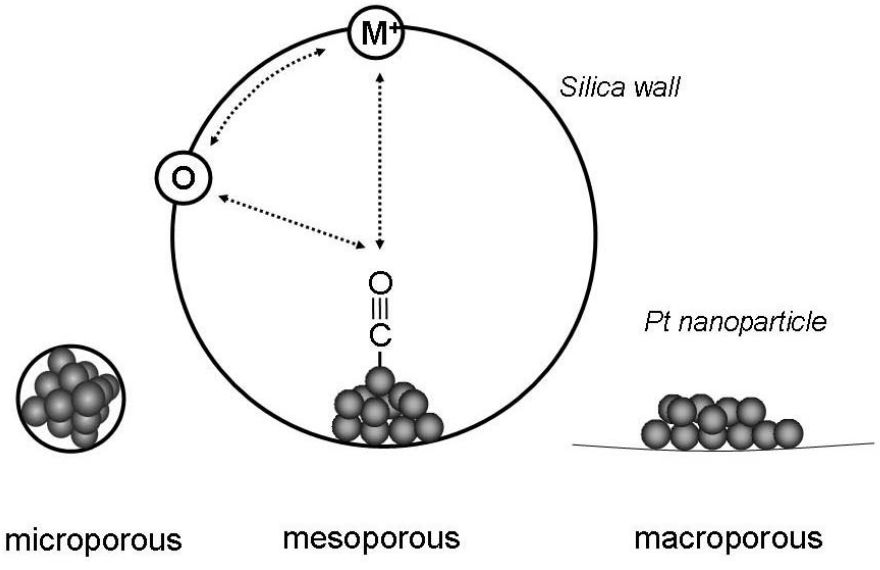

Figure 3.4: Schematic representation of a supported Pt nanoparticle in different silica cages and the corresponding non-bonding electrostatic interactions between the silica wall and a linearly adsorbed CO molecule. Reference is made to the related materials under study based on their mean average pore diameter.

Next, we calculated the surface coverage of the different catalyst materials as a function of the desorption temperature from the integrated intensities of all bands, according to the procedure described in Chapter 2. The result is shown in Figure 3.5. Consistent with the TPD patterns in Figure 3.2, all catalysts show a decrease in coverage at higher temperature, but the effect is smaller. This is due to the fact that the intensity decrease observed for the linear band in the TPD pattern (Figure 3.2) is partly compensated by the conversion of linear to bridge-bonded CO. According to our conclusions from the study on zeolite-supported Pt nanoparticles in Chapter 2, one could expect the relatively high coverage on Pt/SiO_2 to be attended with a smaller L:B ratio and a lower linear (Pt−)C≡O stretching frequency, but this is not the case. It implies that, next to cation-induced changes of the electronic charge on the Pt-particles, another effect plays a role in the CO adsorption capacity of supported Pt particles. Apparently, this effect is also not directly linked to the pore curvature of the support.

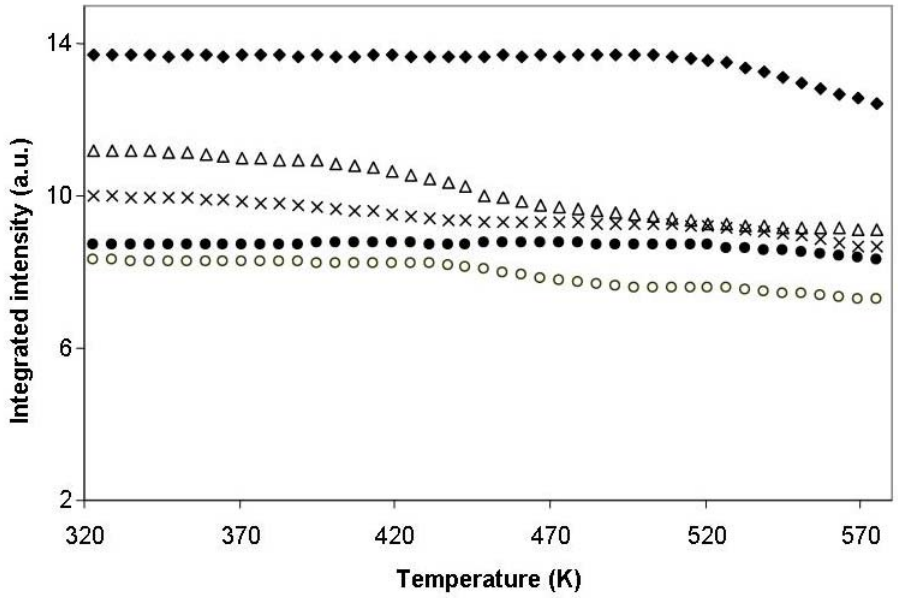

Figure 3.5: CO coverage on all silica-supported Pt nanoparticles as a function of the desorption temperature: (o) Pt/ITQ-1, (Δ) Pt/MCM-41, (•) Pt/MCM-48, (x) Pt/SBA-15 and (♦) Pt/SiO_2.

3.2.2 Chemical composition effects

In order to study chemical composition effects on the electronic properties of supported Pt nanoparticles, IR CO-TPD patterns of cation-containing $Pt/M\text{-}SiO_2$ catalysts ($Pt/Na\text{-}SiO_2$, $Pt/Cs\text{-}SiO_2$, $Pt/Mg\text{-}SiO_2$ and $Pt/Ba\text{-}SiO_2$) have been

measured, together with the reference Pt/SiO_2 material. The results have been compared to the data reported in Chapter 2 for the corresponding zeolite-supported Pt nanoparticles; *i.e.*, Pt/H-Y, Pt/Na-Y, Pt/Cs-Y, Pt/Mg-Y and Pt/Ba-Y. The IR CO-TPD results of both series of samples show a striking resemblance. Upon introduction of a cation, alike the Pt/M-Y catalysts, the $Pt/M\text{-}SiO_2$ materials exhibit much broader and irregularly shaped bands (Figure 3.3). This is illustrated by the HBW of 53-83 cm^{-1} at 323 K, which is considerably larger than the HBW of 29 cm^{-1} as observed for Pt/SiO_2 (Table 3.2). One explanation could be the presence of different CO−Pt adsorption sites. However, this is unlikely, since the HRTEM and EXAFS results show that, except for $Pt/Cs\text{-}SiO_2$, the average Pt particle size and distribution is about the same for Pt/SiO_2, $Pt/Na\text{-}SiO_2$, $Pt/Mg\text{-}SiO_2$ and $Pt/Ba\text{-}SiO_2$ (1-3 nm). For that reason we assign the observed band broadening to different C≡O orientations as a result of local non-bonding electrostatic interactions within the support. As outlined in Chapter 2 for Pt/M-Y catalyst systems, attractive ion-dipole interactions with charge compensating framework cations play a major role in this process. It also explains the larger complexity of the Pt−C≡O bands as a result of the presence of both cation-affected and “free” C≡O positions. Besides, the increasing band complexity at higher temperature can be attributed to reorientation of C≡O as a result of changing interactions. Identical to the Pt/M-Y catalysts, this phenomenon is particularly visible in the IR-CO-TPD pattern of $Pt/Na\text{-}SiO_2$, $Pt/Cs\text{-}SiO_2$ and $Pt/Ba\text{-}SiO_2$ from the increasing intensity of the band at 1950 cm^{-1}. This band has been tentatively assigned by Gandao *et al.*[21] to bridge bonded Pt−CO species affected by (Mg^{2+}) cations in the near vicinity of the supported Pt particles.

The positions of the Pt−C≡O vibration bands during TPD are listed in Table 3.2. Again, alike for the Pt/M-Y catalyst systems, the linear C≡O band position decreases upon introduction of the metal cations in the same order as their position in the periodic system; *i.e.*, Na > Cs and Mg > Ba. Besides, the red shifts show the same trend as for the Pt/M-Y samples studied in Chapter 2. Once more, this points to a correlation between the (Pt−)C≡O vibrational frequency and the electronic properties of the supported Pt nanoparticles as induced by the monovalent and divalent cations. This is illustrated by the plot of the red shift of the linearly Pt-coordinated C≡O bands compared to gas phase C≡O (positioned at 2143 cm^{-1}) versus the cation radius-to-charge ratio of the four different elements in Figure 3.6.[23-24] Evidently, the

Pt/M-SiO_2 samples show the same trend as the Pt/M-Y catalysts, confirming the correlation of a large red shift with a large cation radius-to-charge ratio.

Similar conclusions can be drawn for the effect of the cations on the IR linear to bridge (L:B) intensity ratio. Alike the Pt/M-Y compounds, the L:B values of the Pt/M-SiO_2 catalysts at 323 K (3.6-8.9) are lower than the L:B value of Pt/SiO_2 (11.1). Plotting of the L:B intensity ratio as a function of the Lewis acidity of the cations, as shown in Figure 3.7, reveals exactly the same trend as the one found in Chapter 2 for the Pt/M-Y samples. As previously explained, the Kamlet-Taft parameter α is a measure for the Lewis acidity of the cations and reflects the ability of a cation to accept an electron pair. Therefore, weak Lewis acid elements, such as Na^+ and Cs^+, have a small α-value and induce a relatively large electron charge on the framework oxygen atoms and hence on the supported Pt nanoparticles. For these elements, the net result is an increasing occupation of the d-levels, an increasing back donation in the CO molecular orbital with 2π* character and eventually an increasing red shift of the linear C≡O band and a decreasing infrared L:B ratio. Obviously, the effect of an element with a high α-value, such as Mg^{2+}, is much smaller and in line with the results of an IR-CO adsorption study on the promoting effect of manganese in titania-supported cobalt Fischer-Tropsch catalysts.[25]

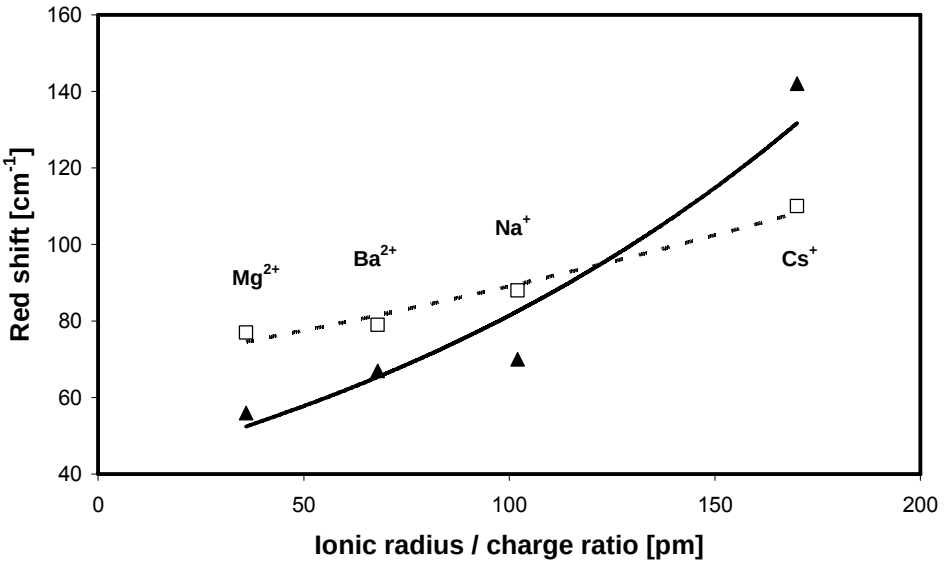

Figure 3.6: Red shift of the C≡O stretching vibration of linear bonded CO on cation impregnated (□) Pt/M-SiO_2 and (▲) Pt/M-Y catalysts compared to the gas phase C≡O frequency as a function of the cation radius-to-charge ratio.

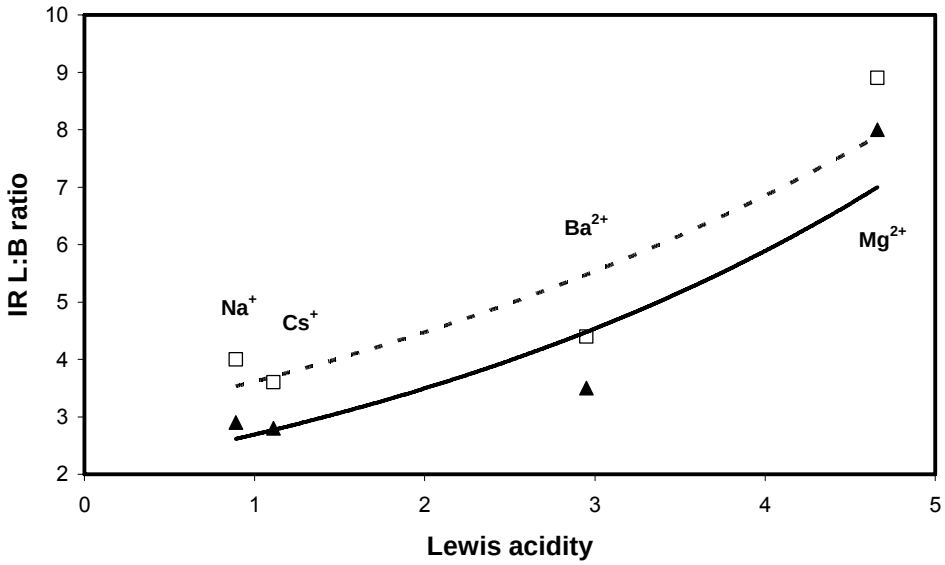

Figure 3.7: IR L:B intensity ratio as a function of the Lewis acidity expressed by the Kamlet Taft parameter α of the cation Na^+, Cs^+, Mg^{2+} and Ba^{2+} promoting the series of (□) Pt/M-SiO_2 and (▲) Pt/M-Y catalysts.

Finally, we calculated the CO surface coverage of the Pt/M-SiO_2 catalysts from the integrated C≡O band intensities as a function of the desorption temperature. The results are shown in Figure 3.8. As appears, the CO coverage (*i.e.* the summed integrated area of all CO bands) decreases only slightly with the temperature and less than suggested by the 3D TPD patterns in Figure 3.3. It follows that desorption

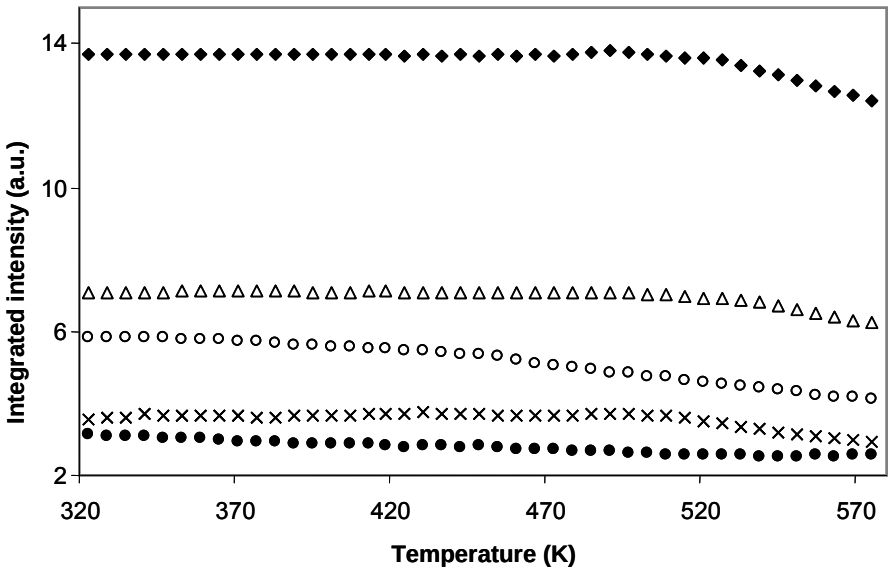

Figure 3.8: CO coverage on supported Pt nanoparticles as a function of the desorption temperature: (♦) Pt/SiO_2, (•) Pt/Na-SiO_2, (x) Pt/Cs-SiO_2, (Δ) Pt/Mg-SiO_2 and (o) Pt/Ba-SiO_2.

is minimal and that the linear bonded CO converts to the 2- and 3-fold coordinated form. Furthermore, the relative amount of adsorbed CO is the highest on Pt/Mg-SiO_2 and the lowest on Pt/Na-SiO_2 and Pt/Cs-SiO_2 with the value for Pt/Ba-SiO_2 in between. It is clear that, even though the coverage for Pt/Cs-SiO_2 is probably relatively too low, due to the larger Pt nanoparticles and hence a smaller Pt-surface area, the CO coverage correlates inversely proportional with the L:B ratio (Table 3.2). These results are identical to what we observed for the Pt/M-Y compounds and confirm the earlier conclusion that promoting elements can be used to affect the electron density of supported Pt particles.

4 Conclusions

The results of this characterisation study demonstrate that time-resolved IR spectroscopy is a useful tool to unravel electronic properties of supported Pt nanoparticles through the study of their effect on the temperature programmed desorption of CO as probe molecule. The new data largely confirm the conclusions of Chapter 2 on promotion effects in zeolite-supported Pt nanoparticles. IR parameters, like the CO surface coverage or the position, shape and relative intensity of the linear and bridge Pt-bonded C≡O stretching vibrations, can be used to determine the electronic properties of supported Pt nanoparticles. It is concluded that pore curvature effects are very small. The band positions, shifts and L:B ratio differ hardly, although the desorption seems to decrease with the mean pore diameter due to repulsive non-bonding interactions and/or the larger contact area between the Pt-particles and the support. The results for the cation-containing Pt/M-SiO_2 catalysts are consistent with the results obtained in Chapter 2 for zeolite-supported Pt nanoparticles. The red shift of the linear Pt-coordinated C≡O vibration compared to that of gas-phase CO increases with an increasing cation radius-to-charge ratio, while a decrease in the L:B ratio correlates with a decreasing Lewis acidity, as expressed by the Kamlet-Taft parameter α. The latter can be attributed to an increasing electron charge on the framework oxygen atoms and hence to an increasing electron density on the supported Pt nanoparticles upon decreasing α-value. Furthermore, the correlation of the CO coverage with the electron density on Pt is present though less prominent as for zeolite-supported Pt nanoparticles.

References

[1] Kustov, L.M.; Ostgard, D.; Sachtler, W.M.H. *Catal. Lett.* **1991**, *9*, 121.

[2] Miller, J.T.; Koningsberger, D.C., *J. Catal.* **1996**, *162*, 209.

[3] Koningsberger, D.C.; Ramaker, D.E.; Miller, J.T.; de Graaf, J.; Mojet, B.L., *Top. Catal.* **2001**, *15*, 35.

[4] Arena, G.E.; Centi, G., *Top. Catal.* **2004**, *30-31*, 147.

[5] Sobczak, I.; Grams, J.; Ziolek, M., *Micropor. Mesopor. Mat.* **2007**, *99*, 345.

[6] Stakheev, A. Y.; Zhang, Y.; Ivanov, A.V.; Baeva, G.N.; Ramaker, D.E.; Koningsberger, D.C., *J. Phys. Chem. C* **2007**, *111*, 3938.

[7] Camblor, M.A. ; Corell, C.; Corma, A.; Diaz-Cabanas, M.J.; Nicolopoulos, S.; Gonzalez-Calbet, J.M.; Vallet-Regi, M., *Chem. Mater.* **1996**, *8*, 2415.

[8] Corma, A.; Catlow, C.R.A.; Sastre, G., *J. Phys. Chem. B* **1998**, *102*, 7085.

[9] Camblor, M.A. ; Corma, A.; Diaz-Cabanas, M.J.; Baerlocher, C., *J. Phys. Chem. B* **1998**, *102*, 44.

[10] Van Der Voort, P.; Ravikovittch, P.I.; de Jong, K.P.; Benjelloun, M.; Van Bavel, E.; Janssen, A.H.; Neimark, A.V.; Weckhuysen, B.M.; Vansant, E.F., *J. Phys. Chem. B* **2002**, *106*, 5873.

[11] P. Van Der Voort, P.I. Ravikovitch, K.P. de Jong, A.V. Neimark, A.H. Janssen, M. Benjelloun, E. van Bavel, P. Cool, B.M. Weckhuysen, E.F. Vansant, Chem. Comm. (2002) 1010.

[12] Mokaya, R.; Jones, W., *Chem.Comm.* **1997**, 2185.

[13] Baltes, M. ; Cassiers, K.; Van der Voort, P.; Weckhuysen, B.M.; Schoonheydt, R.A.; Vansant, E.F., *J. Catal.* **2001**, *197*, 160.

[14] Vaarkamp, M. ; Linders, J.C.; Koningsberger, D.C., *Physica B* **1995**, *208/209*, 9825.

[15] Geidel, E. ; Lechert, H.; Dobler, J.; Jobic, H.; Calazferri, F.; Bauer, F., *Micropor. Mesopor. Mat.* **2003**, *65*, 31.

[16] Vaarkamp, M.; Mojet, B.L.; Kappers, M.J.; Miller, J.T.; Koningsberger, D.C., *J. Phys. Chem.* **1995**, *99*, 16067.

[17] Sheppard, N.; Nguyen, T.T., *Adv. Infrared Raman Spectrosc.* **1978**, *5*, 67.

[18] Hippe, C.; Lamber, R.; Schulz-Ekloff, G.; Schubert, U., *Catal. Lett.* **1997**, *43*, 195.

[19] Bourane, A.; Bianchi, D., *J. Catal.* **2003**, *218*, 447.

[20] Barth, A.; Ramachandran, A., *J. Catal.* **1990**, *125*, 467.

[21] Gandao, Z.; Coq, B.; de Ménorval, L.C.; Tichit, D., *Appl. Catal. A:General* **1996**, *147* 395.

[22] Wasileski, S.A.; Weaver, M.A.; Koper, M.T.M., *J. Electroanal. Chem.* **2001**, *500*, 344.

[23] Greenwood, N.N.; Earnshaw, A., *Chemistry of The Elements*, Pergamon Press, Oxford, **1984**.

[24] Marcus, Y., *Ion properties*, Marcel Dekker, New York, Basel, Hong Kong, **1997**, p. 193.

[25] Morales, F.; de Smit, E.; de Groot, F.M.F.; Visser, T.; Weckhuysen, B.M. *J. Catal.* **2007**, *246*, 91.

Chapter 4

Atomic XAFS as a tool to probe the electronic properties of supported noble metal nanoclusters

Abstract

In this study, we confirmed by X-ray absorption spectroscopy the observations of Chapters 2 and 3 that an increasing electron charge on the framework oxygen atoms of the support, induced, for example by promoters, is causing an increasing electron charge on the supported Pt nanoparticles. It was observed that the intensity of the experimental Pt atomic X-ray absorption fine structure (AXAFS) was enhanced for electron-poor Pt particles and *vice versa*. This finding correlated well with the linear-to-bridge intensity ratio of the CO IR signal for a broad range of supported Pt catalysts going from promoted zeolite Y (with monovalent, *i.e.*, H^+, Na^+, K^+ and Rb^+, and divalent cations, *i.e.*, Mg^{2+}, Ca^{2+}, Sr^{2+} and Ba^{2+}), to all-silica microporous (ITQ-1), mesoporous (MCM-41, MCM-48 and SBA-15) and macroporous (SiO_2) supports, as well as to a macroporous SiO_2 support impregnated with monovalent (Na^+, Cs^+) and divalent (Mg^{2+}, Ba^{2+}) cations. It demonstrates that Atomic XAFS is a very useful technique for probing electronic properties of supported metal nanoclusters. Its advantages over CO IR spectroscopy are that no probe molecule is required and that real-time measurements under reaction conditions are possible.

1 Introduction

Supported noble metal nanoclusters find widespread applications in heterogeneous catalysis as their catalytic activity can be altered by changing the support composition and architecture or by adding the appropriate promoting elements.[1-7] These effects are related to changes in the electronic properties of the noble metal, as measured by *e.g.* IR spectroscopy after the adsorption of simple probe molecules, such as CO. It is generally accepted that the ratio of linear-to-bridge metal coordinated CO reflects the electronic properties of the adsorbing noble metal nanocluster, and this ratio increases with increasing ionisation potential of the metal particle.[8-12] In Chapters 2 and 3, this trend in CO IR signal was confirmed with a series of model Pt catalysts varying by their support composition and porosity.

Another attractive, but almost unexplored technique for probing the electronic structure of supported noble metal nanoclusters is atomic X-ray absorption fine structure spectroscopy (AXAFS). This feature has been first recognised by Holland *et al.*[13] but its further development was done by the groups of Rehr, Baberschke, O'Grady, Ramaker and Koningsberger.[12-19] Whereas extended X-ray absorption fine structure spectroscopy (EXAFS) is known to originate from the scattering of the outgoing electron against the potential of neighbouring atoms, AXAFS represents the scattering against the potential of the electron cloud of the absorber atom itself. The embedded potential of probed atoms is dependent on the chemical and electronic environment of the atoms and can be influenced by the support characteristics. The intensity and position of the AXAFS peak is a function of the bonding of the absorbing atom with its environment. Therefore, any change in the support oxide altering the embedded potential of the absorbing noble atom will be reflected in its AXAFS spectrum.

Unfortunately, the introduction of AXAFS as a powerful new tool for studying heterogeneous catalysts is hampered by the lack of sufficiently broad experimental data to support the relation between the AXAFS intensity of catalytic systems and the corresponding changes in the electronic properties. Here, we show for a wide set of different support oxides, ranging from microporous (H-USY and zeolite Y exchanged with H^+, Na^+, K^+, Rb^+, Mg^{2+}, Ca^{2+}, Sr^{2+} or Ba^{2+}) over mesoporous (SBA-15 and MCM-41) to macroporous (SiO_2 and SiO_2 loaded with Cs^+ or Ba^{2+}) support oxides, that AXAFS accurately probes the electronic properties of supported Pt

nanoclusters. For this purpose, the AXAFS intensities of the 14 different supported Pt catalysts are compared with the corresponding linear-to-bridge Pt-coordinated CO ratios, as obtained by IR spectroscopy on the same set of samples, after adsorption of CO at room temperature in the same spectroscopic *in situ* cell.

2 Experimental section

2.1 Catalyst preparation

The synthesis of the series of zeolite Y oxide supports exchanged with H^+, Na^+, K^+, Rb^+, Mg^{2+}, Ca^{2+}, Sr^{2+} or Ba^{2+} has been described in Chapter 2, while the details of the preparation of the mesoporous (SBA-15 and MCM-41) and macroporous (SiO_2 and SiO_2 loaded with Cs^+ or Ba^{2+}) support oxides can be found in Chapter 3. The H-USY support was purchased by the company Amoco (LZY-84 type).

1 wt% supported Pt particles were prepared *via* a dry impregnation step of the support oxide materials with the appropriate aqueous solutions of $Pt(NH_3)_4(NO_3)_2$. After impregnation and drying at 353 K in N_2 for 12 h, calcination was carried out by drying in a high air flow during 12 h at 393 K followed by increasing the temperature to 573 K. Reduction was performed in pure H_2 at 573 K for 2 h. After reduction and flushing with N_2 at room temperature, passivation was carried out by admitting a small amount of air to the samples.

2.2 Catalyst characterisation

The Pt loading and Pt particle size of the obtained materials were characterised in detail with XRF, EXAFS and TEM using the same procedures and equipments as the ones described in Chapters 2 and 3.

CO adsorption IR measurements were performed on self-supporting catalyst wafers in a transmission cell like it was explained in Chapters 2 and 3. After heating in vacuum, reduction in H_2 at 573 K for 1 h and additional evacuation at 573 K for 1 h, the catalyst was exposed to a static pressure of 20 mbar CO at room temperature, followed by evacuation. All IR measurements were duplicated in order to ensure the reproducibility of the obtained results.

Pt L_3-edge EXAFS data were collected on self-supporting catalyst wafers in a transmission cell, identical to that used for the IR measurements with the exception that the CaF_2 windows have been replaced by Be windows. The measurements

have been performed at station X1.1 of Hasylab (Hamburg, Germany) and at beamline BM26A (DUBBLE CRG) at the ESRF (Grenoble, France), both using a double crystal monochromator equipped with Si{111} crystals. Reduction of the higher harmonic radiation in the spectrum at Hasylab was established by detuning the second crystal to 60 % of the maximum intensity, and at the DUBBLE station by using a secondary mirror. All samples have been reduced at 573 K for 1 h in a H_2/He flow (10 %). After cooling the samples to RT, they are cooled further to liquid nitrogen (LN) temperature to reduce the Debye-Waller factor. Three spectra are obtained and averaged, to improve the signal-to-noise ratio. The XAFS analysis is explained in the next paragraph.

2.3 AXAFS data analysis

The AXAFS contribution can be isolated from the total XAFS data by subtracting the EXAFS contributions from the experimental XAFS data.[20] Thus, after X-ray absorption measurement, a precise background subtraction was performed, one which optimises the AXAFS and EXAFS contributions in the XAFS data, while leaving the double electron excitations mostly in the background. Details on this procedure and the parameters definition can be found elsewhere.[21-23] The AXAFS contribution was then isolated by subtracting the calculated Pt-Pt and Pt-O contributions from the raw EXAFS data. The error for the isolation of the AXAFS contribution is estimated to be around 10%.[24]

The data analysis procedure performed on all the samples is illustrated for one sample, namely Pt/K-Y. Data analysis was performed on the averaged spectrum using the XDAP program.[25] The background subtraction is shown step by step in Figure 4.1. The pre-edge background was calculated by a modified Victoreen and subtracted from the raw data (Figure 4.1a). The post-edge background was calculated using a careful subtraction approach. A spline technique has been used with criteria to minimise the double electron excitation (DEE) contribution and maximise the AXAFS contribution. In Figure 4.1b, three different background approximations are plotted with smoothing factors (SM) of 0.80, 1.05 and 1.30. The DEE contribution appears as a small step at around 170-200 eV after the edge. With an SM factor of 1.05 the DEE contribution is minimised, whereas the SM factor of 0.80 does not maximise the EXAFS contributions and an SM factor of 1.3 leaves the

DEE in the spectrum. This is also emphasised in Figure 4.1c, where the corresponding k^3-weighted Fourier transforms (FT) of the Chi function, $\chi(k)$, are plotted. The DEE contributions are seen at 0.3 Å < R < 1.0 Å, while the AXAFS contribution are highlighted at 0.8 Å < R < 1.6 Å and the EXAFS contributions at higher R values. Figure 4.1c clearly shows the optimised AXAFS contribution around R = 1.4 Å, with SM = 1.05. The post-edge background together with the pre-edge-subtracted raw data is displayed in Figure 4.1d. Figure 4.2 shows the sequence for the removal of the EXAFS contributions from the signal. Figure 4.2a reflects the Chi plot, $\chi(k)$, corresponding to the background subtraction performed in Figure 4.1d.

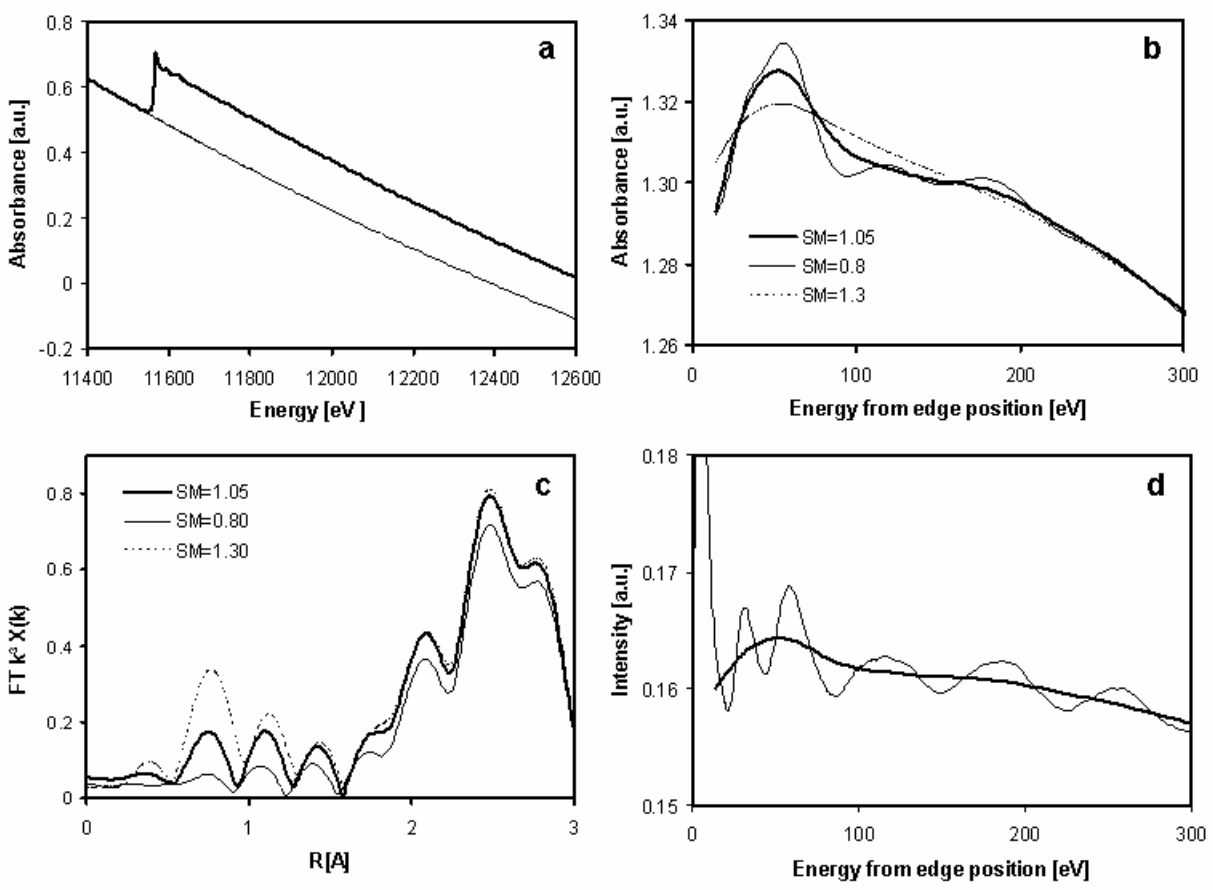

Figure 4.1: AXAFS data analysis – Optimised background subtraction for maximised EXAFS and AXAFS signal and minimised double electron excitations: (a) Averaged raw data obtained on Pt/K-Y (thick line) and calculated pre-edge background by a modified Victoreen (thin line), (b) Post-edge background calculated with the spline technique with SM factors of 0.80, 1.05 and 1.30, (c) Corresponding Fourier transform with k^3-weighting (3.0 $Å^{-1}$ < k < 14 $Å^{-1}$) and, (d) Pre-edge background-subtracted absorption coefficient $\mu(x)$ and post-edge background obtained with a smoothing factor SM of 1.05.

The difference file technique of the XDAP program is used to fit the data in R-space. The fitting is performed in the R-range between 1.6 Å and 3.2 Å on the k^1-weighted Fourier transformed data in the k range from 3.0 $Å^{-1}$ to 14 $Å^{-1}$ (Figure 4.2b). Care is taken to produce a good quality fit for both k^1- and k^3-weighted FT's, which is illustrated in Figures 4.2c and 4.2d. Figure 4.3 shows the FT of the difference file, where the Pt-Pt and Pt-O EXAFS signals were removed. As the AXAFS contribution in the data ranges from k equal to 3.0 $Å^{-1}$ to 8.0 $Å^{-1}$, this range is used to express the AXAFS contribution in the FT plot. The latter can be seen at R values below 1.6 Å. The reminder of the signal, R above 3 Å, is due to the EXAFS signal of higher Pt shells.

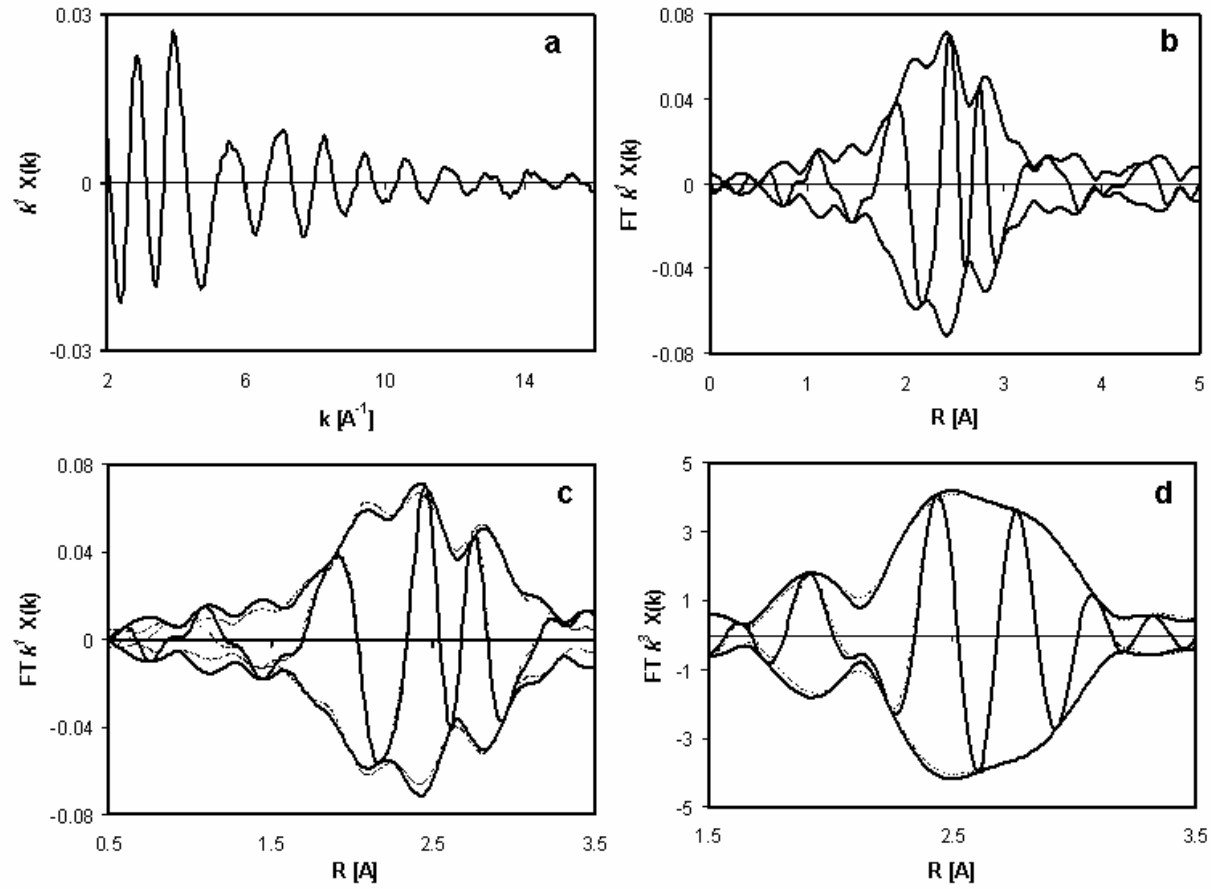

Figure 4.2: AXAFS data analysis – Fitting of the Pt-Pt and Pt-O EXAFS contributions: (a) k^1-weighted Chi-plot, k^1 χ(k), of the background subtracted data, (b) Corresponding k^1-weighted Fourier transform using k ranging from 3.0 $Å^{-1}$ to 14 $Å^{-1}$, (c) k^1-weighted Fourier transformed raw data using k ranging from 3.0 $Å^{-1}$ to 14 $Å^{-1}$ (full line) and its fit in the R-space from 1.6 Å to 3.2 Å (dotted line) and, (d) k^3-weighted Fourier transformed raw data using k ranging from 3.0 $Å^{-1}$ to 14 $Å^{-1}$ (full line) and its fit in the R-space from 1.6 Å to 3.2 Å (dotted line).

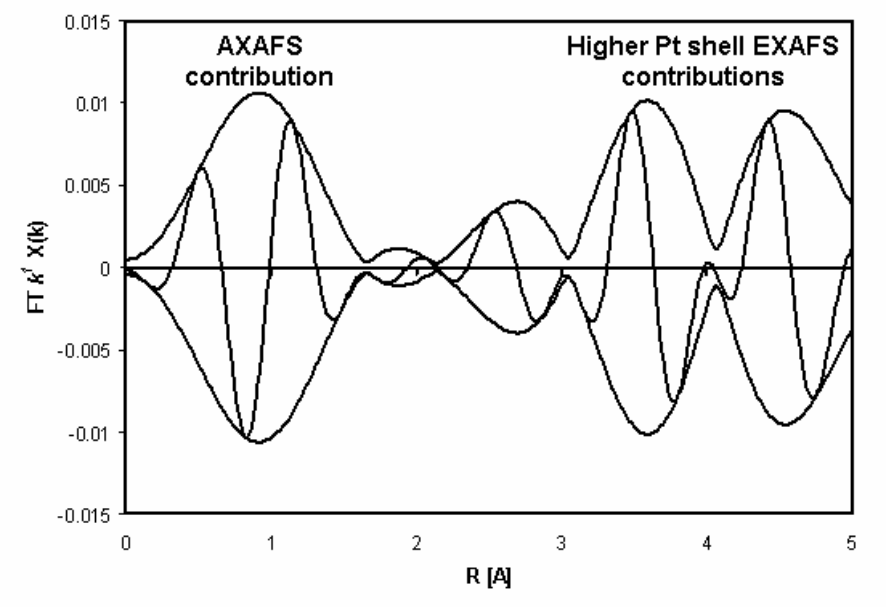

Figure 4.3: AXAFS data analysis – AXAFS contributions: k^1-weighted Fourier transform of the difference file using k ranging from 3.0 Å^{-1} to 8.0 Å^{-1}. The fitted Pt-O and Pt-Pt from 1.6 Å < R < 3.2 Å were removed.

3 Results and discussion

3.1 Catalyst characterisation

The results of the samples characterisation are summarised in Table 4.1. The Pt loading was measured by XRF and was found to vary between 0.7 wt% Pt and 1.3 wt% Pt. The Pt particle size and distribution were verified by EXAFS and TEM. Well-defined supported Pt nanoclusters were observed on each of the support oxides. It was noticed that the microporous supports contain mainly 1 nm Pt clusters, whereas the Pt clusters in the mesoporous and macroporous supports have dimensions around 1.5-2 nm.

3.2 Infrared CO adsorption experiments

Figure 4.4 shows some representative Pt C≡O IR spectra for the samples Pt/K-Y, Pt/Ca-Y, Pt/SiO_2 and Pt/MCM-41. The IR spectra are characterised by a strong IR absorption band at around 2000 cm^{-1} and a weaker one at around 1800 cm^{-1}. The former band is assigned to the stretching vibration of a linearly (L) Pt-coordinated C≡O, whereas the latter band is due to bridge (B) Pt-C≡O stretching vibrations.[26-28] It is clear that the IR L:B intensity ratio (Table 4.1) obtained by integrating the

Table 4.1: Summary of the characterisation of the supported Pt catalysts by X-ray fluorescence (XRF), high resolution transmission electron microscopy (HRTEM), CO infrared (IR) spectroscopy and X-ray absorption spectroscopy (XAFS).

Sample	Pt loading [wt%] [a]	Pt particle size [nm] [b]	L:B [c]	EXAFS analysis results					AXAFS intensity [x 10^{-2}]
				Scatterer	N	$\Delta\sigma^2$ [10^{-3} Å^2]	R [Å]	E_0 [eV]	
Pt/H-USY	1.1	≤ 1	14.0	Pt	5.84	4.3	2.74	1.2	2.60
				O	1.01	3.2	2.52	10.0	
Pt/SiO_2	0.9	1 to 4	10.0	Pt	7.90	1.3	2.76	2.3	1.90
				O	0.80	9.0	2.42	15.5	
Pt/SBA-15	0.9	≤ 1	10.0	Pt	6.45	4.4	2.76	2.3	2.00
				O	0.65	9.0	2.03	-9.8	
Pt/MCM-41	0.7	1 to 4	14.0	Pt	8.18	1.9	2.76	1.7	2.20
				O	1.15	9.0	2.48	12.0	
Pt/Cs-SiO_2	1.1	1 to 4	3.6	Pt	8.74	2.0	2.76	1.3	1.30
				O	0.45	5.7	2.13	-13.0	
Pt/Ba-SiO_2	0.9	1 to 3	2.9	Pt	6.96	4.1	2.74	1.7	1.09
				O	0.25	15.0	2.11	-13.0	
Pt/H-Y	1.2	≤ 1	10.0	Pt	5.44	3.4	2.74	1.9	2.20
				O	0.22	3.0	2.10	-12.3	
Pt/Na-Y	1.0	≤ 1	2.9	Pt	5.74	4.6	2.73	2.5	1.06
				O	0.56	3.8	2.07	-15.0	
Pt/K-Y	1.1	≤ 1 (main fraction 3 (traces)	2.7	Pt	6.22	4.4	2.74	2.2	0.94
				O	0.26	34.1	2.07	-13.0	
Pt/Rb-Y	1.0	≤ 1 (main fraction 3 (traces)	2.8	Pt	7.12	6.1	2.72	1.9	1.37
				O	0.4	56.2	2.00	-12.0	
Pt/Mg-Y	1.3	≤ 1 (main fraction 10 (traces)	8.0	Pt	5.81	6.1	2.73	2.0	1.95
				O	0.4	10.0	2.19	-10.3	
Pt/Ca-Y	1.2	≤ 1 (main fraction 5 (traces)	4.5	Pt	6.73	5.1	2.74	2.5	1.25
				O	0.3	52.5	2.03	-13.0	
Pt/Sr-Y	0.9	≤ 1 (main fraction 5 (traces)	4.0	Pt	5.14	3.1	2.74	1.9	1.30
				O	0.48	13.3	2.10	-12.0	
Pt/Ba-Y	1.0	≤ 1	3.5	Pt	5.05	4.7	2.73	2.7	1.16
				O	0.42	2.1	2.09	-13.0	

[a] As determined by XRF, [b] As determined from HRTEM pictures, [c] CO IR linear- to-bridge (L:B) band intensity ratio at 323 K.

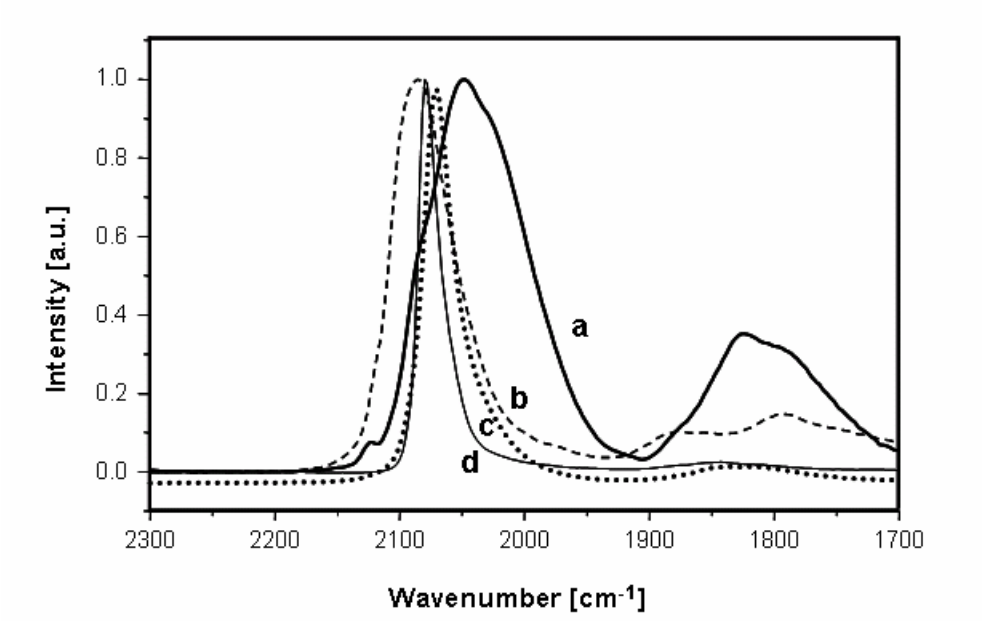

Figure 4.4: IR spectra of CO adsorbed on (a) Pt/MCM-41, (b) Pt/SiO_2, (c) Pt/Ca-Y and (d) Pt/K-Y.

spectra decreases in the order: Pt/MCM-41 (14) > Pt/SiO_2 (10) > Pt/Ca-Y (4.5) > Pt/K-Y (2.7), reflecting an increasing electron density on the supported Pt nanoclusters. The assumption made is that the extinction coefficients for adsorbed C≡O are influenced to the same extent for the linearly and bridged Pt-coordinated C≡O stretching vibrations, and the error is estimated to be around 10 %.

3.3 AXAFS experiments

The AXAFS spectra obtained following the procedure described in paragraph 2.3 are given as example for Pt/K-Y, Pt/Mg-Y, Pt/SiO_2 and Pt/MCM-41 in the R-range from 0 Å to 1.5 Å in Figure 4.5. One can notice that the AXAFS signal of the different supported Pt nanoclusters differ in their AXAFS intensity, as well as in the peak centroid. A decrease in the AXAFS intensity results in a shift of the peak centroid to higher R values and *vice versa*. The AXAFS intensity decrease follows the same order as the IR L:B intensity ratios; *i.e.*, Pt/MCM-41 ($0.22.10^{-3}$) > Pt/SiO_2 ($0.19.10^{-3}$) > Pt/Ca-Y ($0.125.10^{-3}$) > Pt/K-Y ($0.094.10^{-3}$). The AXAFS intensities obtained from the XAFS data of the different supported Pt catalysts are listed in Table 4.1.

The change in the intensity of the Fourier transformed AXAFS peak of Pt can be directly related to a change in the interatomic potential of the Pt atoms averaged

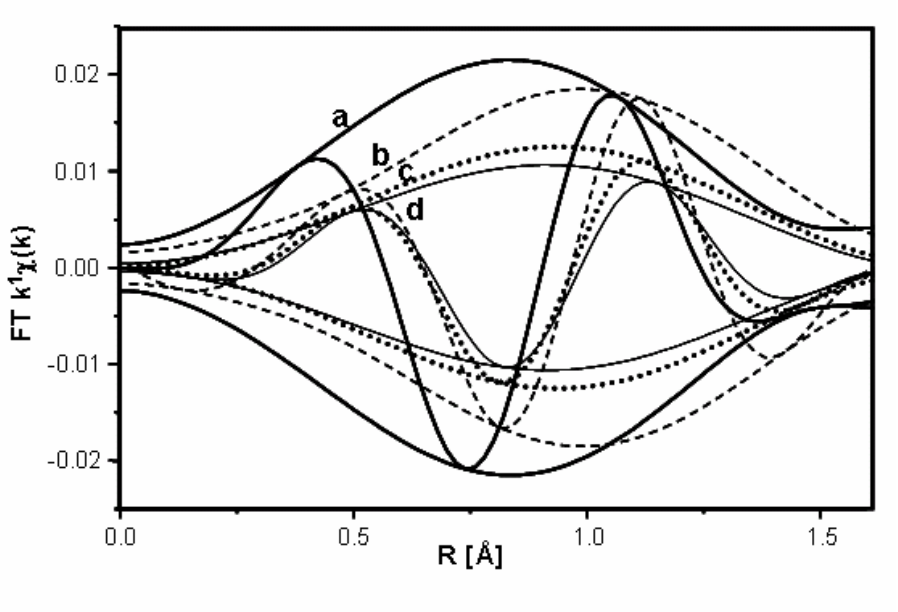

Figure 4.5: k^1-weighted Fourier transforms in the k range 2.5-8 $Å^{-1}$ of the AXAFS spectra of (a) Pt/MCM-41; (b) Pt/SiO_2; (c) Pt/Ca-Y and (d) Pt/K-Y.

over the whole Pt metal particle. The change in interatomic potential is caused by an increase or decrease in electron charge (more or less electron-rich) of the support oxygen atoms. The electron charge of the support oxygen atoms in turn is determined by the Madelung potential of the support oxide, which depends on the composition of the support material. Thus, a high intensity of the AXAFS contribution corresponds to an electron-poor Pt particle and *vice versa*.[12,22]

It is possible to compare the AXAFS intensities and the IR L:B ratios for the 14 different supported Pt catalysts under study. Table 4.1 lists the respective values and Figure 4.6 plots the AXAFS peak intensity of the different samples *versus* their corresponding IR L:B ratios. The IR L:B ratios spans a range of more than 10 units, whereas the AXAFS intensities change between $0.094.10^{-3}$ and $0.26.10^{-3}$. From Figure 4.6, it is evident that the AXAFS intensity decreases with decreasing IR L:B ratio and that both the AXAFS peak intensity and the IR L:B ratio can be considered as complementary measures for the electron charge of the Pt nanoclusters. In other words, both the AXAFS peak intensity and the IR L:B decrease with increasing electron richness of the Pt nanoclusters.

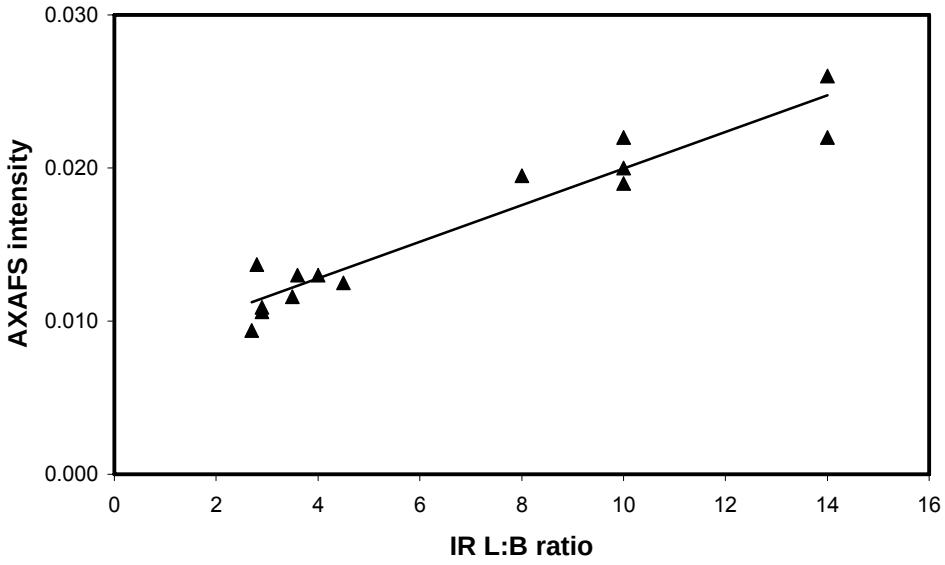

Figure 4.6: AXAFS peak intensity of supported Pt nanoclusters as a function of the corresponding CO IR L:B intensity ratio.

4 Conclusions

In summary, AXAFS is a very useful and sensitive technique for probing the electronic properties of supported noble metal nanoclusters and can in principle be applied to clusters of any atom amenable to the XAFS technique. In addition, the obtained information is fully consistent with CO IR measurements, but more importantly the technique has the advantage that it does not need any probe molecule. As a consequence, AXAFS can be used in the future to probe the electronic properties of supported noble metal nanoparticles under reaction conditions in real time, hopefully delivering mechanistic insight on the working catalyst.

References

[1] Linic, S.; Barteau, M.A., *J. Am. Chem. Soc.* **2004**, *126*, 8086.

[2] Bell, A.T., *Science* **2003**, *299*, 1688.

[3] Wei, J.M.; Iglesia, E, *Angew. Chem. Int. Ed.* **2004**, *43*, 3685.

[4] Carrettin, S.; Concepcion, P.; Corma, A.; Nieto, J.M.L.; Puntes, V.F., *Angew. Chem. Int. Ed.* **2004**, *43*, 2538.

[5] Chen, M.S.; Goodman, D.W., *Science* **2004**, *306*, 252.

[6] Guzman, J.; Gates, B.C., *J. Am. Chem. Soc.* **2004**, *126*, 2672.

[7] Derrouiche, S.; Grevejat, P.; Bianchi, D., *J. Am. Chem. Soc.* **2004**, *126*, 13010.

[8] Mojet, B.L.; Miller, J.T.; Koningsberger, D.C., *J. Phys. Chem. B* **1999**, *103*, 2724.

[9] van Santen, R. A., *J. Chem. Soc.*, *Faraday Trans. 1* **1987**, *83*, 1915.

[10] Crowell, J. E.; Garfunkel, E. L.; Somorjai, G. A., *Surf. Sci.* **1982**, *121*, 303.

[11] Sheu, L. L.; Karpinski, Z.; Sachtler, W. M. H., *J. Phys. Chem.* **1989**, *93*, 4890.

[12] Mojet, B.L.; Miller, J.T.; Ramaker, D.E.; Koningsberger, D.C., *J. Catal.* **1999**, *186*, 373.

[13] Holland, B.W.; Pendry, J.B.; Pettifer, R.F.; Bordas, J., *J. Phys. C* **1978**, *11,* 633.

[14] Rehr, J.J.; Booth, C.H.; Bridges, F.; Zabinsky, S.I., *Phys. Rev. B* **1994**, *49*, 12347.

[15] Wende, H.; Baberschke, K., *J. Electron. Spectrosc. Relat. Phenom.* **1999**, *101-103*, 821.

[16] Ramaker, D.E.; Mojet, B. L.; O'Grady, W. E.; Koningsberger, D. C., *J. Phys.: Condens. Mater.* **1998**, *10*, 8753.

[17] Ramaker, D.E.; de Graaf, J.; van Veen, J.A.R.; Koningsberger, D.C., *J. Catal.* **2001**, *203*, 7.

[18] Koningsberger, D.; Mojet. B.; Miller, J.; Ramaker, D., *J. Synchr. Rad.* **1999**, *6*, 135.

[19] Ramaker, D.E.; O'Grady, W.E., *J. Synchr. Rad.* **1999**, *6*, 800.

[20] Koningsberger, D.C.; Mojet, B.L.; van Dorssen, G.E.; Ramaker, D.E., *Top. Catal.* **2000**, *10*, 143.

[21] Ramaker, D.E.; van Dorssen, G.E.; Mojet, B.L.; Koningsberger, D.C., *Top. Catal.* **2000**, *10*, 157.

[22] Koningsberger, D.C.; de Graaf, J.; Mojet, B.L.; Ramaker, D.E.; Miller, J.T., *Appl. Catal. A: General* **2000**, *191*, 205.

[23] Van Dorssen, G.E., Koningsberger, D.C.; Ramaker, D.E. *J. Phys. Cond. Matter.* **2002**, *14*, 13529.

[24] Tromp, M.; van Bokhoven, J.A.; Slagt, M.Q.; Klein Gebbink, J.M.; van Koten, G.; Ramaker, D.E.; Koningsberger, D.C., *J. Am. Chem. Soc.* **2004**, *126*, 4090.

[25] Vaarkamp, M.; Linders, J. C.; Koningsberger, D. C., *Physica B* **1995**, *208/209*, 159.

[26] Hippe, C.; Lamber, R.; Schulz-Ekloff, G.; Schubert, U., *Catal. Lett.* **1997**, *43*, 195.

[27] Sheppard, N.; Nguen, T.T., *Adv. Infrared Raman Spectrosc.* **1978**, *5,* 67.

[28] Bourane, A., Dulaurent, O.; Bianchi, D., *J. Catal.* **2000**, *196,* 115.

Chapter 5

Promotion effects in the oxidation of CO over zeolite-supported Rh nanoparticles

Abstract

Rh-particles with an average diameter smaller than 1.5 nm have been supported on a series of zeolite Y samples. These zeolite materials contained different monovalent (H^+, Na^+, K^+, Rb^+ and Cs^+) and divalent (Mg^{2+}, Ca^{2+}, Sr^{2+} and Ba^{2+}) cations and were used as model systems to investigate the effect of promoter elements in the oxidation of CO over supported Rh-particles in excess of oxygen. Infrared (IR) spectroscopy was carried out to monitor the electronic changes in the local environment of Rh-adsorbed CO. It was found that the bands corresponding to two Rh *gem*-dicarbonyl species, $Rh^+(CO)_2$-$(O_z)_2$ and $Rh^+(CO)_2$-$(O_z)(H_2O)$, shift to lower wavenumbers with increasing ionic radius-to-charge ratio of the cation. In addition, the relative intensity of the bridge bonded CO as compared to the total absorbance of Rh-bonded CO species decreases with increasing Lewis acidity, as expressed by the Kamlet-Taft parameter α of the cation. This trend could be directly correlated to the Rh CO oxidation activity, since low temperatures at 50 % CO conversion corresponded with catalyst materials with a high contribution of bridge bonded CO species and hence with small α values. A lower Lewis acidity causes an increased electron density on the framework oxygen atoms and thus an increased electron density on the zeolite-supported Rh-particles. Comparable trends have been observed in Chapter 2 on a similar series of cation containing zeolite-supported Pt catalyst materials.

1 Introduction

The catalytic activity of supported nanometer-size metal particles is generally recognised to be influenced by the chemical composition of support materials due to weak, medium or strong metal-support interactions. Amongst these supported metal catalysts, Rh plays an important role due to its versatile catalytic behaviour. For example, Rh supported on zeolites has been investigated for the hydroformylation of alkenes,[1] the hydrogenation of arenes, CO or CO_2,[2] the carbonylation of methanol,[3] and the conversion of synthesis gas into hydrocarbons or oxygenates.[4] However, its best known application is in the three-way exhaust automotive catalyst, where it is used for its capacity to reduce NO_x in excess of oxygen to a higher level than Pd or Pt.[5] In this specific system, the support is usually a complex mixture of metal oxides (*e.g.* Al_2O_3, SiO_2, ZrO_2 and CeO_2) and promoters (*e.g.* Ba, K and La). Several studies have shown that these supports influence the Rh metal dispersion as well as its reducibility. It was also shown by the groups of Mariadassou[6,7] and Yu Yao[8] that these Rh properties directly influence the type of kinetics taking place on the Rh active sites during the oxidation of CO.

The goal of this work is to elucidate Rh-support interactions in a systematic manner by studying Rh-based model catalysts making use of zeolites as supports in which different monovalent (H^+, Na^+, K^+, Rb^+ and Cs^+) and divalent (Mg^{2+}, Ca^{2+}, Sr^{2+} and Ba^{2+}) cations are present. The leading idea, inspired by the work mainly performed in Chapter 2 on zeolite-supported Pt nanoparticles, is that the electronic properties and related CO oxidation activity behaviour of Rh particles encaged in zeolite Y would be influenced by promoter elements added to the support material. By using CO as probe molecule in combination with infrared spectroscopy (IR), it will be shown that an increasing electron density on the supported Rh nanoparticles, indirectly induced by alkali and earth alkaline metal ions via the framework oxygen atoms, promotes the CO oxidation activity. The results will be further compared to the ones related to the zeolite-supported Pt materials. The work therefore provides guidelines for the development of improved three-way exhaust catalytic converters containing lower amounts of noble metals.

2 Experimental section

Prior to preparation and characterisation, it should be emphasised that the CO stretching vibration of Rh-chemisorbed CO is not only sensitive to the support characteristics, but also to a large number of experimental parameters. According to literature, the loading, dispersion, particle size and coordination number of Rh, its precursor, the reduction temperature and CO exposure pressure can affect the observed IR data, whereas sample pretreatment, CO exposure temperature, CO adsorption and CO interaction with support cations may play a role as well.[9-17] To prevent erroneous assignments and conclusions, special attention has been paid to keep the experimental parameters and the instrumental settings as far as possible identical.

2.1 Catalyst preparation

The starting material for ion exchange was a Na-Y material from AKZO Nobel with a Si:Al ratio of 2.3. The zeolite support materials with H^+, K^+, Rb^+, Cs^+, Mg^{2+}, Ca^{2+}, Sr^{2+}, and Ba^{2+} were obtained by five consecutive ion exchanges for 24 h with an aqueous 0.1 M solution of NH_4NO_3 (Acros, p.a.), KCl (Acros, p.a.), RbCl (Acros, 99+ %), CsCl (Acros, 99+ %), $MgCl_2$ (Acros, p.a.), $CaCl_2$ (Aldrich, 98+ %), $SrCl_2$ (Acros, 99.99 %), and $BaCl_2$ (Aldrich, 99.999 %), respectively. The pH of the solution was kept between 6.5 and 7.5 and the zeolite material was separated from the solution through centrifugation for 30 min at 4000 rpm. The samples were then washed chlorine-free with deionised water, which was examined with $AgNO_3$, before being dried at 323 K for 48 h. The crystallinity, before and after ion exchange, was verified by X-Ray Diffraction (XRD) on the Rh/RbY sample as a method check that the ion exchange method does not modify the crystalline structure of the zeolite support. This point was extensively checked for all samples studied in Chapter 2.

Before impregnation, the support was dried under vacuum at 473 K for 2 h. $RhCl_3.2H_2O$ (Alfa, 99.9 %) was chosen as the precursor and incipient wetness as the impregnation method. In this combination, the Rh ion complex is small enough to enter the zeolite channel and it minimises a decrease in the concentration of the charge compensating ion.[15] The target Rh loading was 0.5 wt %. The concentration of the precursor solution was calculated taking into account the change in material density caused by the introduction of the cations. After impregnation, the powder

was dried for 12 h at room temperature and for 8 h at 353 K in an oil bath under flowing N_2 (quality 4.0; Linde). It was then pressed at 8 bar, grinded and sieved to pellets of 212 to 425 µm diameter. The calcination was carried out in a tubular reactor in a high air flow (1335 ml/min). The temperature was first increased to 423 K at a rate of 5 K/min, where it was kept for 8 h, and then further to 573 K at a rate of 0.2 K/min where it was maintained for 1 h. Following cooling, the pellets were reduced in a H_2 (quality 5.0; Linde) flow (380 ml/min) at 573 K for 2 h after a temperature ramp-up of 5 K/min. Finally, the Rh particles were stabilised by a short surface re-oxidation at room temperature to prevent agglomeration.

2.2 Catalyst characterisation

Rh and cation loadings of the samples were determined making use of Atomic Emission Spectroscopy (AES) with an Inductively-Coupled Plasma (ICP) as atomisation source on a Shimadzu ICPS-8100 machine. For this purpose, the catalysts were dissolved in a mixture of hydrofluoric, nitric and hydrochloric acids.

High Resolution Transmission Electron Microscopy (HRTEM) was performed with a Philips CM 30 UT electron microscope equipped with a field emission gun as the electron source operated at 300 kV. Samples were mounted on a micro-grid made of carbon polymer supported on a copper mesh by placing a few droplets of a suspension of ground sample in ethanol on the grid, followed by drying at ambient conditions. Based on the TEM pictures, the particle size distribution for all particles larger than 1 nm was evaluated by using the analySIS software (Philips). The size distribution was calculated on the basis of the average diameter of at least 150 particles found in one TEM picture. In order to verify the consistency of this methodology, two different TEM pictures from the same sample were analysed and very similar results for both the average particle size and the standard deviation were obtained. In the same way, we also confirmed that the Rh-nanoparticles were not sintering during the heat treatments; *i.e.*, throughout the reduction, evacuation and temperature programmed desorption processes.

Extended X-ray Absorption Fine Structure (EXAFS) measurements were carried out in the CRG DUBBLE (BM26A) beamline at the ESRF synchrotron (Grenoble, France). The beamline was equipped with a double Si{111} crystal monochromator. Measurements were performed in transmission mode and ion chambers were used

for detection with a gas fill to absorb 20 % in the first and 80 % in the second ion chamber. Reduction of the higher harmonic radiation was established using a vertically focusing Pt/Si mirror installed behind the monochromator. The samples were prepared by hand pressing 0.5 g powder into a self-supporting wafer. This wafer was then placed in a treatment cell and reduced in a flow of 10 % H_2 in He for 15 min at 423 K and for 30 min at 573 K or 623 K, the temperature ramp-up rate being 5 K/min. Afterwards, the cell was evacuated for 30 min at 573 K before being measured under active vacuum at liquid N_2 temperature. Each measurement was repeated two times at the Rh K-edge. The EXAFS data analysis was carried out with the XDAP program.[18] The EXAFS data was extracted from the averaged absorption spectra through pre-edge subtraction using a modified Victoreen curve and then through background subtraction employing cubic spline routines with a continuously adjustable smoothing factor. Finally, the average spectrum was normalised by dividing the data by the absorption intensity at 50 eV after the edge.[19] The obtained Chi (χ) function was analysed by multiple shells data fitting in the k-space with a k^3-weighting. The reliability of the fitted parameters was then verified with the goodness of fit for the k^1-weighted Chi (χ) function. References were created for the phase-shifts and backscattering amplitudes corrections of Rh-Rh, Rh-Cl and Rh-O contributions based on experimental absorption spectra measured on a Rh foil (Aldrich, 12 µm thick, 99.9 %) and on $RhCl_3.2H_2O$ (Aldrich, 98 %) and Rh_2O_3 (Aldrich, 99.8 %) pressed powders. The obtained Rh-Rh coordination numbers were used to evaluate the average Rh particle size.

IR measurements were performed on self-supporting catalyst wafers that were pressed from 0.01 to 0.02 g of the passivated and finely grained sample material. A pressure of no more than 3 bar was applied during 10 s to prevent destruction of the pore structure of the support. The wafer was placed in an IR transmission cell equipped with CaF_2 windows. The cell was evacuated to 2 x 10^{-8} bar at 323 K for at least 1 h prior to reduction by a 40 ml/min to 60 ml/min flow of H_2 (quality 5.0; Linde). During reduction, the temperature was raised from 323 K to 573 K at 3 K/min; it was maintained for 1 h at 573 K. The system was then switched back to vacuum for 1 h at 573 K, before being cooled down to 323 K at a rate of 3 K/min. A first spectrum was taken under vacuum and served as background reference for the catalyst wafer. Next, 10 % CO (quality 2.0; Linde) in He (quality 4.6; Linde) was introduced in the cell until a stable pressure of *circa* 0.06 bar was reached. After 30 min of static

CO exposure, the cell was evacuated to a pressure of 2 x 10^{-6} bar for 30 min at 323 K before the Temperature Programmed Desorption (TPD) was started by increasing the temperature up to 573 K at a rate of 3 K/min. IR spectra were recorded every 2 min on a Perkin-Elmer 2000 FTIR instrument with a data point resolution of 4 cm^{-1} and an accumulation of 25 scans with wavenumbers ranging from 4000 cm^{-1} to 1300 cm^{-1}. The data acquisition was performed automatically using the Perkin-Elmer Time-Base software. The reproducibility of all IR-TPD measurements was verified by repeating the experiments in two ways: (1) on two different wafers from the same sample and (2) on the same wafer by applying the same procedure two times in a row without opening the IR cell. Band positions and corresponding intensity data were estimated by peak fitting of the baseline corrected spectra using the Grams AI software. After evaluation of the different peak profiles, it was concluded that the Voigt profile was giving the best fits for well-defined maxima as well as for shoulders. Each spectrum was fitted with 7 to 8 Voigt-type peaks depending on its shape in the 2200-1550 cm^{-1} range. It should be noted that the peak positions obtained were very consistent, while repeating the fitting with different starting conditions. The same is valid for the integrated intensity of the peaks situated between 2200 and 2020 cm^{-1}. The broad and overlapping peaks below 2020 cm^{-1} hampered evaluation of the integrated areas of the individual components with great precision.

2.3 Catalytic testing

The zeolite-based Rh catalysts were tested for the oxidation of CO in a U-tube reactor equipped with a thermocouple placed in the catalytic bed, a furnace and mass flow controllers. For this purpose, 20 mg of each catalyst diluted with 200 mg of SiC was loaded in the reactor. The reacting gas consisted of 2000 ppm of CO (10 % CO, quality 2.0; in He, quality 4.6; Linde) in 10 % of O_2 (quality 5.0; Linde) and N_2 (quality 4.0; Linde) as balance. The total flow rate was 100 ml/min and the heating rate was 5 K/min. The CO conversion was calculated between 278 K and 773 K from FT-IR spectra measured every 25 to 35 s in a transmission flow cell using a Midac M2000 FT-IR spectrometer in the range of 2700-1985 cm^{-1} accumulating 4 scans at a resolution of 4 cm^{-1}.

3 Results and discussion

3.1 Catalyst characterisation

First, the results from ICP-AES, EXAFS and HRTEM were evaluated to determine the Rh particle size, distribution and loading as well as the rate of cation exchange of the zeolite support. The data have been summarised in Tables 5.1 and 5.2. In addition, a selection of TEM pictures with corresponding particle size distributions are presented in Figure 5.1.

The results of the ICP-AES analysis (Table 5.1) revealed that the amount of Rh in the different zeolite samples varies between 0.2 and 0.5 wt%, while the percentage of support Na^+ ions exchanged by 1/n M^{n+} ions reaches 65 to 83 %. The latter values are not as high as the 98 % ion exchange ratios reported in Chapter 2

Table 5.1: Summary of the synthesised Rh-based catalysts and their main characteristics.

Sample	ICP-AES		TEM		EXAFS	
	Na^+ exchange [%]	Rh [wt%]	Particle size [nm]	Average particle size [nm]	Rh-Rh coordination number	Average particle size [nm] [a]
Rh/H-Y	NA	0.21	< 5	2.5	7	~ 1.3
Rh/Na-Y	100	0.33	< 6	3.1	6.5	~ 1.2
Rh/K-Y	78	0.32	< 5	2.7	6.3	~ 1.1
Rh/Rb-Y	65	0.36	< 3	1.3 [b]	5.8	~ 1.0
Rh/Cs-Y	72	0.49	< 6	2.6	6.4	~ 1.1
Rh/Mg-Y	66	0.32	< 4	2.2	5	~ 0.9
Rh/Ca-Y	77	0.38	< 6	2.7	6.1	~ 1.1
Rh/Sr-Y	83	0.39	< 3	1.9	1.8 [c]	< 0.6
Rh/Ba-Y	83	0.45	< 4	1.5	3.7	~ 0.7

[a] Average particle size based on the work done by van Zon *et al.*[20] and by Gloor and Prins.[21]

[b] The TEM pictures of this sample were much better, which allowed us to see smaller particles and gives a lower average particle size.

[c] The fit on this sample was not as good as on the others. The magnitude of the EXAFS Fourier Transform around 2.69 Å was however very similar to the one obtained on Rh/Ba-Y, which points to comparable Rh particle sizes.

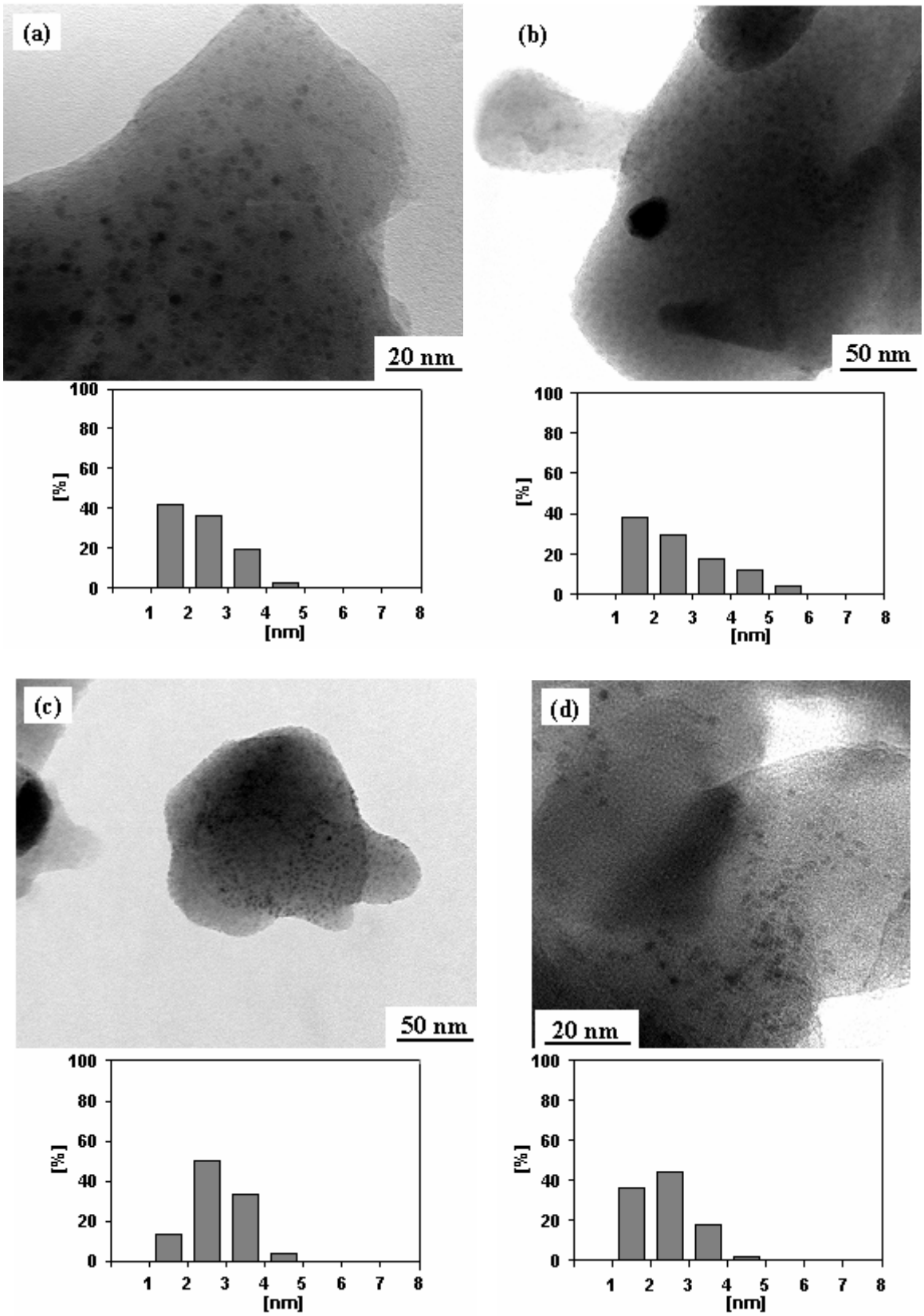

Figure 5.1: TEM pictures and their corresponding particle size distributions based on 150 particles, the ones smaller than 1 nm being excluded. Pictures have been taken on samples as prepared: (a) Rh/H-Y, (b) Rh/Cs-Y, (c) Rh/K-Y and on a sample after CO exposure and temperature programmed desorption: (d) Rh/K-Y.

or by Gijzeman *et al.*[22] for Pt-based zeolites, but in line with the results of Kamble and co-workers.[23]

As illustrated by the TEM data of Rh/H-Y, Rh/Cs-Y and Rh/K-Y in Figure 5.1, it was not possible to exclusively obtain Rh-particles smaller than 1 nm. On the other hand, the particle size distribution graphs indicate that the Rh dispersion is about the same for all samples with an average particle diameter of 1.3-3.1 nm (Table 5.1). Furthermore, comparison of pictures (c) and (d) in Figure 5.1 leads to the conclusion that sintering of the Rh-nanoparticles did not take place during the heat treatments applied in the reduction and the TPD.

The Rh-Rh coordination numbers (N) obtained through EXAFS data analysis (Table 5.1) point to an average particle size in the range 0.7-1.3 nm, which is significantly smaller than the values derived from TEM. This virtual discrepancy between the results of both techniques is a well-known phenomenon, observed on various catalytic systems.[17,24-25] Jentys demonstrated that, in case the majority of the particles are small (*i.e.* N < 10.5), the EXAFS technique is more reliable than TEM or XRD.[26] Therefore, we conclude that most of the supported Rh-particles are smaller than 1 nm and mainly located in the zeolite supercages.

Detailed analysis of the EXAFS spectra (Table 5.2) revealed, next to the main absorption signal from the first Rh-Rh shell, some small Rh contributions, which may originate from oxygen or chlorine.[20-21] In order to identify and quantify them, the difference file technique was applied.[19,20,27] This method started with the removal of the first Rh-Rh shell contribution from the Chi (χ) function. Next, the sign of the imaginary part of the residual signal was examined after phase correction, using Rh_2O_3 and $RhCl_3$ as references. This is illustrated by Figure 5.2 for the Rh/Na-Y sample, where the imaginary part after subtraction of the Rh-Rh contribution and correction for the Rh-Cl phase showed a positive maximum between 2.2 and 2.5 Å confirming that there is some chlorine interacting with Rh. However, regarding the small coordination number of 0.4 (Table 5.2) as compared to the one of the precursor salt, *i.e.*, 6, we conclude that its amount is small. Similar results were observed on the Rh/K-Y and Rh/Rb-Y, whereas for all other samples the remaining signal did not even show reliable evidence to fit any chlorine scatterer. Moreover, the slight asymmetry in the difference signal (as highlighted by the arrows in Figure 5.2) shows that oxygen scatterers also contribute to this signal. This contribution

Table 5.2: EXAFS fitting parameters obtained in the k-range, with a k^3-weighting, where N are first shell coordination numbers, DW are Debye Waller factors, R are bond distances and E_0 are energy shifts compared to the reference compounds.

Sample	Scatterer	N	DW [Å^2]	R [Å]	E_0 [eV]	k range [Å^{-1}] [a]
Rh/H-Y	Rh	7.0	0.0015	2.67	11.4	4.06-15.26
Rh/Na-Y	Rh Cl	6.5 0.4	0.0044 0.0000	2.64 2.36	6.6 1.8	4.23-14.04
Rh/K-Y	Rh Cl	6.3 0.5	0.0035 0.0000	2.64 2.42	9.3 − 5.0	4.14-14.56
Rh/Rb-Y	Rh Cl	5.8 0.5	0.0030 0.0000	2.64 2.42	7.8 − 3.4	4.17-14.70
Rh/Cs-Y	Rh	6.4	0.0018	2.66	4.5	4.24-15.33
Rh/Mg-Y	Rh	5.0	0.0034	2.66	5.3	4.15-15.30
Rh/Ca-Y	Rh	6.1	0.0016	2.67	6.2	4.19-15.70
Rh/Sr-Y	Rh O	1.8 3.0	0.0008 0.0000	2.66 2.75	9.0 − 0.4	4.04-13.92
Rh/Ba-Y	Rh O	3.7 2.2	0.0040 0.0000	2.66 2.76	7.6 − 5.1	4.10-14.59

[a] The k-range was chosen to match nodes of the Chi function.

Typical errors are of the order of 10 % for the Rh-Rh coordination numbers and 20 % for the Rh-O and Rh-Cl ones, 5% for the Debye Waller factors, 1-2 % for the bond distances and 10 % for the energy shifts.[19,21]

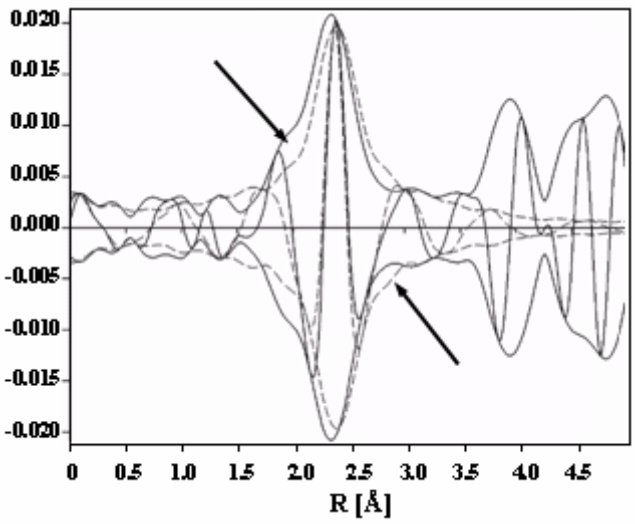

Figure 5.2: k^1-weighted Fourier transform of the EXAFS signal obtained on the Rh/Na-Y sample after removal of the Rh-Rh contributions and phase correction against the $RhCl_3$ reference (full line) and its corresponding fitted Rh-Cl contribution (dashed line).

could only be fitted on the two samples with the smallest average particle size (*i.e.*, Rh/Sr-Y and Rh/Ba-Y). There are two possible sources for this oxygen-Rh interaction:[16,21] (a) oxygen from the support at a distance varying between 2.5 Å and 2.8 Å, termed 'long oxygen' or (b) oxidised Rh with a Rh-O bond length between 2.1 Å and 2.2 Å, being called 'short oxygen'. Assuming that our samples have been fully reduced before EXAFS measurement, it is expected that the main portion comes from long oxygen neighbours. However, the presence of Rh oxide in the analysed samples after reduction cannot be totally excluded from the difference file signal. Moreover, it has been shown that it is difficult to fully reduce Rh on certain types of support oxides, such as alumina, ceria, zirconia and zeolites,[6-8,17,28-30] particularly, when the particles are very small and hence strongly interacting with the support.[6,31-32]

It should also be emphasised that the Rh-Rh bonding distances found are all shorter than the one obtained in a Rh crystal. This is in agreement with the contractions observed on small particles measured under vacuum conditions.[17,24-25,33-34] Finally, the Rh-Cl bonding distances appear a little long (ranging from 2.36 Å in Rh/Na-Y to 2.42 Å in Rh/K-Y and Rh/Rb-Y) compared to the Rh-Cl bond distance in $RhCl_3$, which is 2.31 Å, or in $[Rh(CO)_2Cl]_2$ where bonds of 2.33 Å and 2.38 Å have been found.[20,27] It has however been shown, that, after reduction, chlorine tends to stay on the Rh on silica supports, but migrates away from the Rh surface on alumina supports. Since our samples have a Si:Al ratio of 2.7, it suggests a situation in between.[27,29] A last striking point comes from the Debye-Waller factors for the light scatterers, which are equal to zero. Nevertheless, such values have also been reported by other groups.[20,27]

3.2 Infrared spectroscopy

The changes in the IR spectra, observed during the CO TPD experiments are illustrated by the time-resolved graph in Figure 5.3 for the catalyst Rh/Cs-Y. Each spectrum is separated from the next one by 2 min. Upon exposure to CO (t = 2 min), absorption bands of Rh-bonded CO species immediately show up between 2100 cm^{-1} and 1700 cm^{-1}, next to the CO gas phase band at 2143 cm^{-1}. All Rh-CO bands reach their maximum after 5 min to 10 min and remain constant in position and intensity during exposure and vacuum treatment (t = 30-60 min). In time, bands

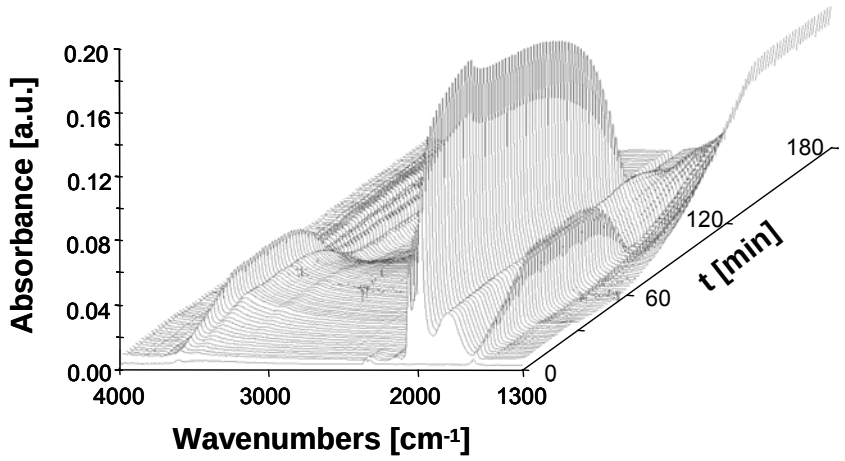

Figure 5.3: CO IR spectra measured during 30 min exposure to 0.23 bar CO, followed by 30 min vacuum at 323 K and temperature programmed desorption from 323 K to 573 K at 3 K/min on Rh/Cs-Y. Each spectrum is separated from the previous one by 2 min.

also slowly grow in around 1640 cm^{-1} and 3400 cm^{-1}, which start to disappear at about 400 K during TPD (t = 85 min). In accordance with Lefevbre *et al.*,[35] we assign these bands to traces of water adsorbed on the zeolite support. This was confirmed by additional IR experiments, where the bare support material was reduced, exposed to CO and subsequently submitted to TPD. The IR spectra obtained, revealed that the water bands originate from a slow diffusion of water into the cell during CO exposure since the same time-resolved spectral pattern was obtained, but without the presence of CO bands. It also implies that the occurrence of dehydroxylation reactions of the support[23] or the formation of carbonates[23,36-39] can be excluded. Further exposure of the wafers to various pressure levels of ambient air revealed that the diffusion under the normal experimental conditions was very small. Moreover, it turned out that the Rh-CO band positions and intensities are not affected at those low diffusion levels.

As illustrated by the time-resolved IR graphs of Rh/H-Y, Rh/Na-Y, Rh/Cs-Y and Rh/Ba-Y in Figure 5.4, the catalysts not only exhibit clearly different band patterns, but also a different behaviour upon TPD. Except for Rh/H-Y, CO appears to be fully desorbed from the samples of the Rh/M^{+}-Y series before the temperature of 573 K was reached. On the contrary, there is still CO adsorbed on the samples of the Rh/M^{2+}-Y series at this temperature.

Prior to desorption, all catalysts show relatively sharp absorption bands in the range 2150-1900 cm^{-1} and a much broader pattern in the region 1900-1700 cm^{-1}.

The former are generally attributed to linear Rh-bonded CO vibrations and the latter to bridge Rh-coordinated CO. The presence of both types of species in Rh supported on macroporous materials[6,9-10,12-14,28,30-31,40-49] and zeolites[13-14,16,29,50] has been widely reported.

The region 1900-1700 cm^{-1}

As can be seen from Figure 5.4, the bandwidth, symmetry and relative absorption intensity of the bridge-bonded CO band differ significantly depending on the cation of the support material. For Rh/H-Y (Figure 5.4 a) and the Rh/M^{2+}-Y series (*e.g.* Rh/Ba-Y in Figure 5.4 d), the band is less intense and broader while, for the latter ones, the asymmetry points to at least two different types of bridge Rh-coordinated CO species. It is commonly known, that the position and shape of the corresponding bands may change as a function of parameters such as the Rh loading, particle size, dispersion and the type of support. It follows that overlapping

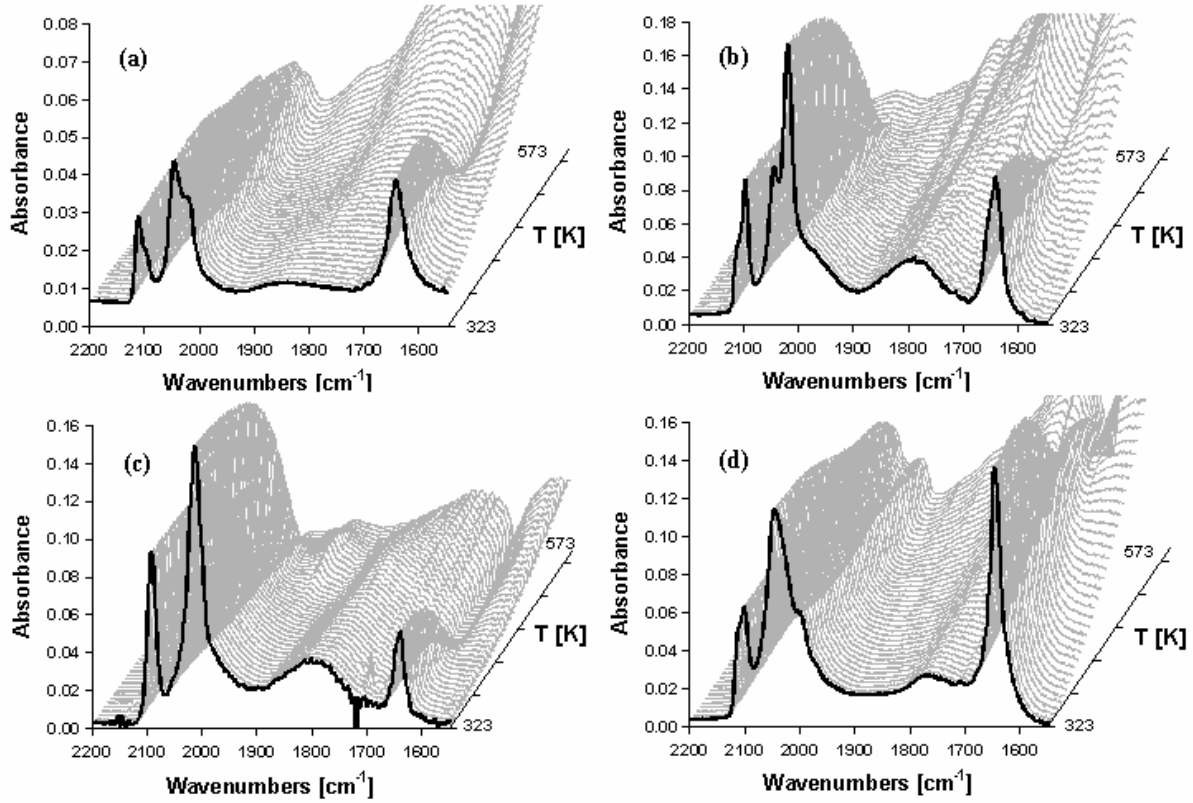

Figure 5.4: CO IR spectra after 30 min exposure to 0.23 bar CO and 30 min vacuum at 323 K during the temperature programmed desorption from 323 K to 573 K obtained on (a) Rh/H-Y, (b) Rh/Na-Y, (c) Rh/Cs-Y and (d) Rh/Ba-Y samples. Each spectrum is separated from the previous one by 2 min or 6 K.

bands can originate from CO bridge bonded to for instance two different Rh crystal faces or to small Rh clusters of different size. Finally, referring to literature, it is concluded that the absence of a separate band maximum around 1900-1920 cm^{-1} is in line with the EXAFS data, pointing to the presence of mainly small particles with an average diameter less than 1.5 nm.

The region 2150-1900 cm^{-1}

It is evident from Figure 5.4 that several peaks contribute to the CO absorption pattern in the region 2150-1900 cm^{-1}. This is particularly clear in the spectra of Rh/Na-Y (Figure 5.4 b) where at least 5 different contributions can be distinguished. Alongside the narrow peaks around 2100 cm^{-1} and 2040 cm^{-1}, a broad absorption band appears to be overlapping at about 2000 cm^{-1}. Based on the position and width of this band, as well as on the fact that it disappears if the sample is oxidised in an oxygen flow for 1 h at 573 K, it can be concluded that the band corresponds to CO adsorbed in a bridge position on slightly oxidised Rh particles, where the Rh oxidation state lies between 0 and +1.[6,41-42] The presence of the latter is not an uncommon phenomenon in supported Rh catalysts even after calcination and reduction.[6,28,31-32,41]

Closer examination of the sharp bands between 2150 cm^{-1} and 2000 cm^{-1}, revealed that 4 resolved bands are present for all samples except for the Rh/Cs-Y catalyst (Figure 5.4 c). Furthermore, the relative intensities vary considerably, depending on the cation introduced in the zeolite support material. Literature is not uniform in the assignment of the different peaks. For Rh supported on zeolite Na-Y, all authors reported the presence of two types of *gem*-dicarbonyls giving rise to 4 IR bands with maxima in the range 2118-2020 cm^{-1}.[13-17,35] The respective band positions for this catalyst are in good agreement with what we observe. The literature on Rh on other supports, such as alumina, silica, ceria, zirconia, titania and other types of zeolites, also describes the presence of a *gem*-dicarbonyl structure, *i.e.*, $Rh^{+}(CO)_2$. This species is formed when small Rh particles are exposed to CO, through the disruption of the small Rh metal clusters into isolated Rh cations with the participation of the OH groups of the support.[13,51] It results in two bands in the CO IR spectrum, one in-phase CO stretching vibration between 2118 cm^{-1} and 2070 cm^{-1} and one out-of-phase stretching vibration between 2053 cm^{-1} and 2007 cm^{-1}.[6,9-15,27-

[28,30-32,40-43,45-53] Next to these, linearly bonded CO adsorbed on Rh metallic particles has been reported to give rise to a band between 2075 cm^{-1} and 2031 cm^{-1}, whereas CO linearly adsorbed on oxidised Rh^{1+} or Rh^{2+} crystallites is attended with a band between 2135 cm^{-1} and 2110 cm^{-1}.[6,9,12-14,16,29-31,40-48,50] In order to unambiguously assign the 4 bands observed in the spectra of our catalysts, two additional tests have been performed (data not shown for brevity).

In the first experiment, the Rh/Na-Y sample was oxidised in air for 1 h at 573 K and then measured in the IR cell following the procedure described above except for the reduction step. Comparison of the CO IR spectra obtained on the reduced and oxidised catalyst highlighted that a band at 2134 cm^{-1} showed up. It can be associated to CO linearly bonded to Rh^{2+} or Rh^{3+}.[13,15,17,41-42,50] Furthermore, the absorption intensity around 2070 cm^{-1} (linear CO on Rh^0) and below 1950 cm^{-1} (bridge CO) was reduced, whereas the 4 bands between 2130 cm^{-1} and 2000 cm^{-1} were unchanged in intensity and position. In the second experiment, the CO gas was introduced in the cell on the reduced Rh/Na-Y sample at liquid nitrogen temperature. Next to the intense peak of the linear CO on Rh^0, two broad bands showed up at 1980 cm^{-1} and 1800 cm^{-1}, that can be easily attributed to CO bridge bonded to oxidised and metallic Rh, respectively. As the CO cannot disrupt the Rh particles at such low temperature, *gem*-dicarbonyl structures cannot be formed and hence no twin bands are present, which is in agreement with studies from Primet[13] and Zaki *et al.*.[30]

Combining the results of these experiments leads to the conclusion that the bands between 2130 cm^{-1} and 2000 cm^{-1} originate from two types of *gem*-dicarbonyls, which differ in the way they are bonded to the support.[14-17,29,35,54] One type has its Rh atom attached to an oxygen of the zeolite framework and to a water molecule, denoted as $Rh^{+}(CO)_2$-$(O_z)(H_2O)$, and the other one has its Rh bonded to two oxygen atoms of the support, $Rh^{+}(CO)_2$-$(O_z)_2$. The former one exhibits its in-phase and out-of-phase CO stretching bands at 15-25 cm^{-1} higher wavenumbers than the latter one. Furthermore, it can be concluded that CO linearly bonded to metallic Rh, if present, gives rise to a band between 2070 cm^{-1} and 2040 cm^{-1}. Finally, the IR data demonstrate as well that the Rh particles must be very small. The prominent bands are due to *gem*-dicarbonyl contributions and these species are merely formed when the Rh particles are smaller than 1 nm in diameter, while particles larger than 2 nm should only give rise to ‘single’ linear and bridge bonded

CO bands.[13,16,30,51] This is fully in line with the small Rh-Rh coordination numbers extracted from the EXAFS data and not conflicting with the presence of some larger particles, which appeared on the TEM pictures.

Influence of the support composition

As already mentioned in the discussion about Figure 5.4, the IR spectra of the catalysts vary as a function of the cation introduced in the zeolite material. This is better visualised by Figure 5.5 where the IR spectra recorded after CO exposure and 30 min vacuum at 323 K are juxtaposed and normalised by their maximum absorbance. Figure 5.5 a shows the Rh/M^+-Y series and it is clear that all CO vibration frequencies are red shifting with increasing cation radius, *i.e.*, H < Na < K < Rb < Cs. At the same time, the relative intensities of the absorption bands are changing: the ones of the $Rh^+(CO)_2$-$(O_z)(H_2O)$ carbonyls are decreasing in intensity, while those of $Rh^+(CO)_2$-$(O_z)_2$ are more pronounced for the larger cations than for the proton-exchanged support. Additionally, the two bands around 2100 cm^{-1} and the ones around 2030 cm^{-1} get closer to each other when going from Rh/H-Y to Rh/Cs-Y. In the same way, the spectral differences for the Rh/M^{2+}-Y series are presented in Figure 5.5 b. For these catalysts, however, there is not a clear trend. The two bands around 2100 cm^{-1} are equally broad for all samples but the two extremes (Rh/Mg-Y and Rh/Ba-Y) present broader peaks around 2020-2000 cm^{-1}. A more detailed interpretation is not possible without a better insight into the position, shape and intensity of the different band components. For that reason peak fitting of

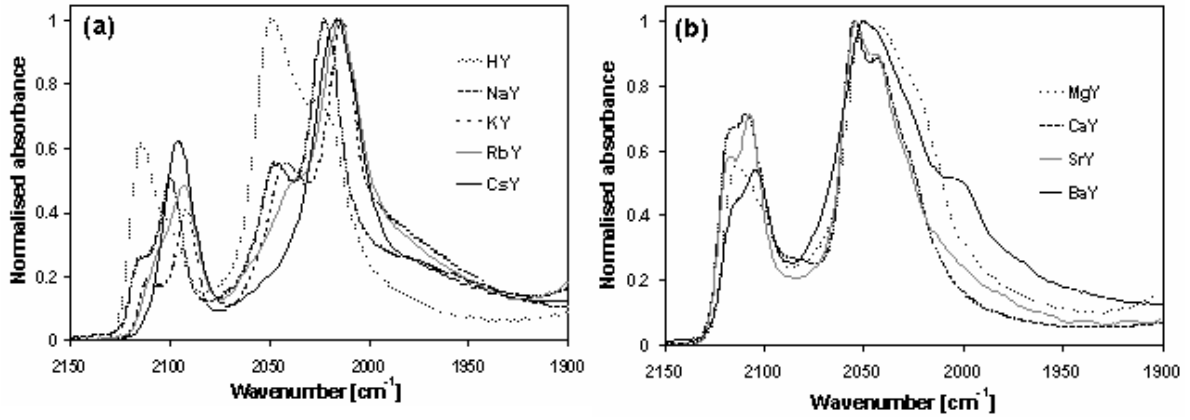

Figure 5.5: CO IR spectra, normalised to their maximum absorbance, after 30 min exposure to 0.23 bar CO followed by 30 min vacuum at 323 K for (a) the Rh/M^+-Y series and (b) the Rh/M^{2+}-Y series.

the spectra was carried out on the IR spectra recorded after CO exposure and 30 min vacuum. Figure 5.6 illustrates the results for Rh/Na-Y, Rh/Cs-Y, Rh/Sr-Y and Rh/Mg-Y, while Table 5.3 summarises the maxima obtained for the Rh-adsorbed CO species on all samples. It was found that, next to the water peak at 1640 cm^{-1}, the spectra are best fitted with 4 sharp and 2 or 3 broad peaks. Next, in continuation to the previous conclusions, the bands at around 2110 cm^{-1} and 2050 cm^{-1} can be assigned to the in-phase and out-of-phase CO stretching vibration of the $Rh^{+}(CO)_2$-$(O_z)(H_2O)$ species, the bands at around 2100 cm^{-1} and 2025 cm^{-1} to the in-phase and out-of-phase CO mode of the $Rh^{+}(CO)_2$-$(O_z)_2$ configuration and the broad peaks at 1995 cm^{-1} and 1800 cm^{-1} to CO bridge-bonded to oxidised and metallic Rh, respectively. Clear evidence for a band around 2070 cm^{-1} of CO linearly bonded to metallic Rh was not derived from the peak fitting. It should be noted, however, that such a band if present, will largely coincide with the out-of-phase CO stretching band of the $Rh^{+}(CO)_2$-$(O_z)(H_2O)$ species. Therefore, CO linearly bonded to Rh^0 might as well be present, although in a limited amount.

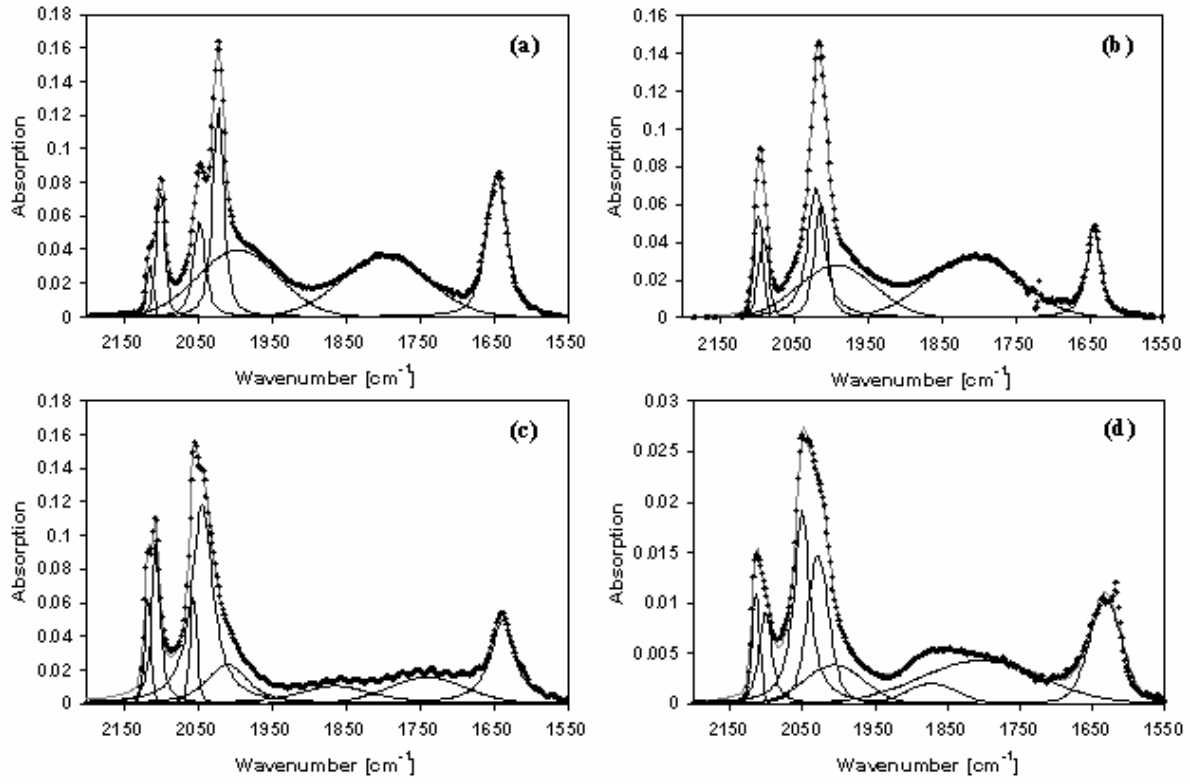

Figure 5.6: CO IR spectrum after 30 min exposure to 0.23 bar CO and after 30 min vacuum at 323 K on (a) Rh/Na-Y, (b) Rh/Cs-Y, (c) Rh/Sr-Y and (d) Rh/Mg-Y with their fitted bands.

Table 5.3: Rh related band positions in the CO IR spectrum after 30 min exposure to 0.23 bar CO and 30 min vacuum at 323 K.

Sample	CO band position [cm^{-1}]					
	$Rh^+(CO)_2(O_z)(H_2O)$ (sym)	$Rh^+(CO)_2(O_z)_2$ (sym)	$Rh^+(CO)_2(O_z)(H_2O)$ (as)	$Rh^+(CO)_2(O_z)_2$ (as)	$Rh_n^{\delta+}$-CO	Rh_n^0-CO
Rh/H-Y	2114	2100	2049	2025	1990	1843
Rh/Na-Y	2114	2100	2048	2022	1995	1797
Rh/K-Y	2109	2092	2042	2014	1999	1812
Rh/Rb-Y	2105	2092	2041	2014	1986	1821
Rh/CsY	2098	2091	2020	2013	1992	1807
Rh/Mg-Y	2114	2101	2051	2028	2007	1871 1804
Rh/Ca-Y	2118	2106	2056	2042	2019	1879 1751
Rh/Sr-Y	2118	2106	2056	2043	2010	1864 1740
Rh/Ba-Y	2115	2103	2049	2030	1991	1864 1751

$Rh^+(CO)_2(O_z)(H_2O)$ refers to a Rh *gem*-dicarbonyl species bonded to one oxygen of the zeolite framework and $Rh^+(CO)_2(O_z)_2$ to a Rh *gem*-dicarbonyl species bonded to two oxygens of the support. $Rh_n^{\delta+}$-CO is representing CO in a bridge position on slightly oxidised Rh and Rh_n^0-CO a CO molecule bonded in n-fold bridge position to metallic Rh.

The curve fitting results confirm that bridge bonded CO on Rh metal exhibits one band for the M^+-Y support series and two for the M^{2+}-Y ones. It is also evident that the intensity ratio of the *gem*-dicarbonyl CO bands and hence the presence of both species, are affected by the promoter cation. However, the mutual intensity ratio of the twin in-phase and out-of-phase vibration bands of the same *gem*-dicarbonyl remains more or less the same. Overall, it averages 0.4 for the $Rh^+(CO)_2$-$(O_z)_2$ carbonyls bands and 0.3 for the $Rh^+(CO)_2$-$(O_z)(H_2O)$ ones. The relative integrated band intensities for a *gem*-dicarbonyl species can be used to estimate the angle, α, between the two CO dipoles: $A_{as} / A_{sy} = tg^2 (\alpha / 2)$.[11,14,39,42,50,53] The application of this formula gives an angle of about 116° for the former species and 123° for the latter one. Miessner and co-workers reported a bond angle of 114° for Rh supported on Na-X,[14] while Lefevbre and Ben Taârit calculated an angle of 112° for $Rh^+(CO)_2$-$(O_z)_2$ and about 90° for $Rh^+(CO)_2$-$(O_z)(H_2O)$.[35] The former is in good agreement with our results, especially when one takes into account the possible influence of the zeolite structure and composition on the $Rh(CO)_2$ angle.[35] On the contrary, the bond angle that we calculated for $Rh^+(CO)_2$-$(O_z)(H_2O)$ seems too large. A plausible explanation is an overestimation of the out-of-phase vibration band intensity as result of an underlying contribution of CO linearly bonded to metallic Rh. This phenomenon has also been observed by Hecker and Bell[49] and by Primet.[13]

The CO peak positions of the M^+-Y samples series, as listed in Table 5.3, show a clear decrease in wavenumber for the *gem*-dicarbonyl species when going from the smallest cation (H^+) to the largest one (Cs^+). In the M^{2+}-Y series, it is not as clear, but overall a trend is present as visualised in Figure 5.7. The full symbols (◆, ■, ▲, and ●) represent the red shift of the Rh *gem*-dicarbonyls bands compared to the CO gas phase vibration as a function of the cation radius divided by its charge. It can be seen that the red shift increases as a function of the promoter ionic radius-to-charge ratio. This observation is valid for all linearly bonded CO species resolved in the spectra. In literature, shifts of the carbonyl vibration band as a function of the Rh environment have been attributed to electronic effects and to the back-bonding ability of the metal.[14,23,35] In agreement with our results, Miessner *et al.* found that the addition of Na to a titania support resulted in a significant shift to lower wavenumbers.[14] Several other observations are relevant to the interpretation of Figure 5.7. First of all, samples with identical support and different Rh metal

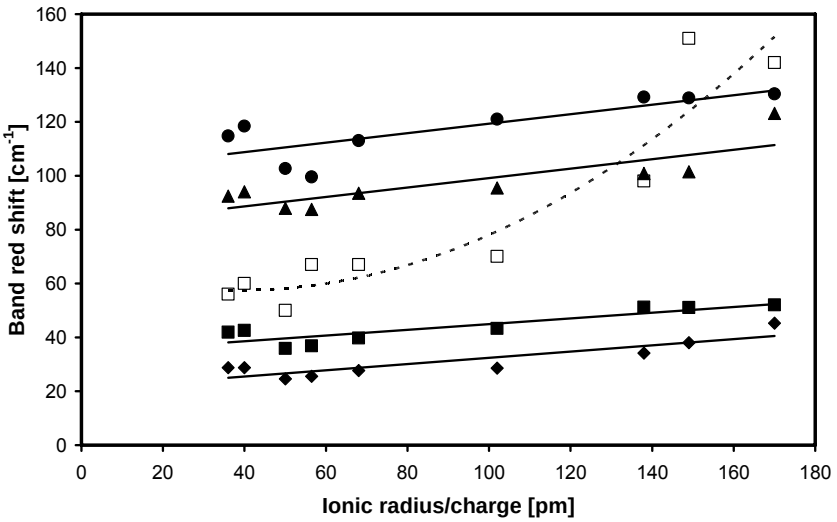

Figure 5.7: CO IR band red shift versus the CO vibration in the gas phase as a function of the cation ionic radius-to-charge ratio: for the (◆, ■) in-phase and (▲, ●) out-of-phase stretching vibrations of $Rh^{+}(CO)_2(O_z)(H_2O)$ and $Rh^{+}(CO)_2(O_z)_2$ *gem*-dicarbonyls, respectively, and, as a reference, for the (□) Pt-CO linear vibration observed in Chapter 2.

dispersions were found to have the same carbonyl IR band positions.[17] Second, a variation in metal loading as high as 0.9 wt % resulted in very small shifts in wavenumber (3-5 cm^{-1}).[14] Finally, these CO band positions are independent of the CO coverage.[9,42] We can therefore conclude that the trend in the Rh *gem*-dicarbonyl band positions is due to differences in support composition. A trend in the band position of the bridge bonded species (Table 5.3) has not been observed. Most likely, this is due to the fact that the effect of the support on the Rh particles is not as large as for isolated Rh cations. Besides, the band originates from several configurations, which can be differently influenced by the cation.

In the discussion of Figures 5.4 and 5.6, we already highlighted that the relative intensities of the bands corresponding to linearly bonded CO (*i.e.*, in the form of *gem*-dicarbonyls) and bridge bonded CO seem to depend on the support composition, *i.e.*, the cation present. Furthermore, the intensities of the two bands related to the CO bridge bonded to Rh particles seem to be correlated. When compared to the total absorption intensity, the bridge bonded contributions on metallic Rh (1800 cm^{-1}) and on slightly oxidised Rh (2000 cm^{-1}) are both much larger on the Rh/Na-Y sample than on catalysts containing more acidic cations (Figure 5.6). This is further illustrated in Figure 5.8. The full symbols (▲) represent the

relative intensity of the bridge-bonded CO-bands as compared to the total IR absorption in the region 2150-1700 cm^{-1} as a function of the support cation Lewis acidity, as expressed by the Kamlet-Taft parameter α.[55] The Lewis acidity of hydrogen is unknown, but its value is supposed to be much higher than for the other cations. It is clear that the relative amount of bridge bonded species is decreasing and hence the relative amount of *gem*-carbonyls formed is increasing with increasing Lewis acidity of the promoting cation. This trend can be explained by the fact that more basic cations will push electrons towards the framework oxygen of the support, which in turn causes the Rh nanoparticles to have a higher electron-density. This gives rise to a larger back-donation to the adsorbed CO π-orbitals, thus enhancing the possibility for bridge bond formation. Another interpretation can be made based on the work of Zaki *et al.*, who concluded that the acidity of the support OH-groups controls the Rh particle disruption and thus the formation of Rh *gem*-dicarbonyls.[30] In the same way, Iordan and co-authors reported that the addition of K to a Rh/Al_2O_3 catalyst material suppressed the CO-induced Rh particle disruption.[47] It should be noted that the Rh particle size might have an influence on the formation of carbonyls.[13,16,30,51] However, such an impact was not observed due to the fact that the size of the Rh particles is in average smaller than 1.5 nm. Finally, as already mentioned before, the presence of incompletely reduced Rh (*i.e.*, a broad band at 2000 cm^{-1}) might be due to the effect of chlorine residuals,[6,31,32,41] which

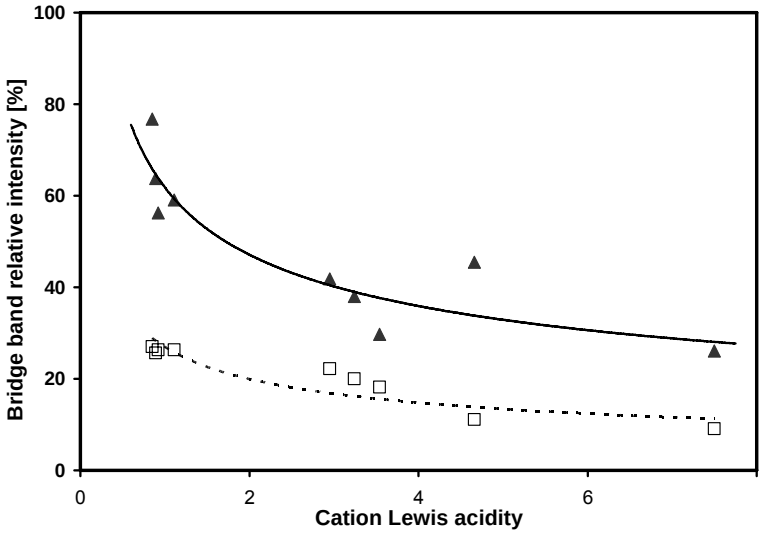

Figure 5.8: Relative intensity of the bridge bonded CO as compared to the total absorbance of (▲) Rh- and (□) Pt-bonded CO species as a function of the cation Lewis acidity of the support promoter. The Pt-related data have been taken over from Chapter 2.

would affect the trend in Figure 5.8. This can nevertheless be excluded as the same trend is observed in case the bridge bonded CO's on Rh metal or on slightly oxidised Rh are considered separately and relative to the total intensity of the CO-Rh bands. Moreover, during the reduction process, the changes in the white line intensity of the XANES signal at the K-edge as a function of temperature were very similar. So, differences in reducibility are absent amongst the samples under study. It can therefore be concluded that the trend observed in Figure 5.8 is directly linked to the support composition effect through: (1) differences in the electron back-donation capability of the Rh (influencing the amount of bridge bonded CO), and (2) differences in the OH-group acidity of the support (having an impact on the carbonyls formation).

3.3 CO oxidation activity

The CO IR study discussed above shows that the support composition has a clear impact on the electronic properties of supported Rh nanoparticles. It is therefore interesting to correlate these observations with the catalytic activity of the samples in the oxidation of CO. As an example, Figure 5.9 is showing the CO conversion for the fresh Rh/Ca-Y sample in excess of oxygen as a function of temperature upon heating and cooling. The hysteresis seen between the two curves is not uncommon for the CO oxidation reaction. It can be explained by heating and

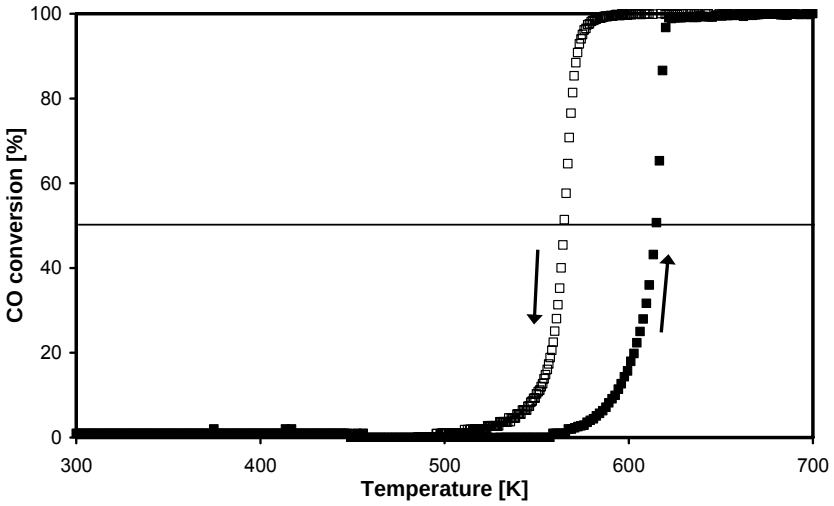

Figure 5.9: CO conversion as a function of temperature on Rh/Ca-Y upon (■) heating and (□) cooling at a rate of 3 K/min.

cooling.[56-58] This is confirmed by the fact that, upon cycling, the changes in the Rh oxidation state or by differences in CO and O coverage upon hysteresis remains, but the curves tend to shift to slightly lower temperatures with the cycle number due to sintering of the Rh particles.

The temperature at 50 % CO conversion (T_{50}) upon heating the catalyst powder has been taken as a measure for the catalytic activity. Comparison of the T_{50}-values of all catalyst materials under study expressed as the ▲-symbols in Figure 5.10 shows that this parameter varies for the different samples. It is also clear that T_{50} can be directly correlated to the results of the IR measurements: the catalytic activity increases with decreasing T_{50} and increasing relative intensities of the bridge bonded CO. In principle, the difference in experimental conditions does not allow a direct correlation between the CO species present on the Rh surface during the static CO IR measurements, taken in the absence of oxygen, and the catalytic test for the CO oxidation reaction done in large excess of oxygen. However, based on the relation found in the CO IR study between the relative amount of bridge species and the Lewis acidity of the promoting cation, it can be concluded that the formation of bridge bonded species is directly linked to the electron density of the Rh catalyst. This has a direct influence on its catalytic activity. These results are in agreement with the studies of Anderson[48] and Dent *et al.*[45], who reported that carbonyl species have low activity in the CO oxidation and CO/NO reactions, respectively. The former

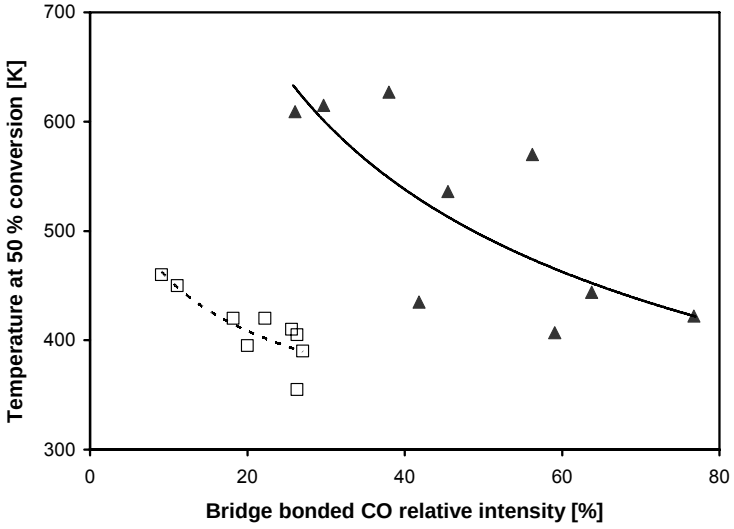

Figure 5.10: Temperature at 50 % conversion for the CO oxidation reaction as a function of the relative CO IR absorption intensity of the bridge bonded CO (▲) on Rh and (□) on Pt. The latter data points have been extracted from Chapter 2.

author added that, at high O_2/CO ratios, small clusters were formed with bridge adsorption sites. They also agree with the work of Iordan and co-authors, who found that the addition of K to Rh/Al_2O_3 catalysts promoted the CO decomposition as result of an enriched electron density of the Rh metal active sites.[47] Moreover, Miessner *et al.* reported a direct relation between the IR data and the Rh activity in the CO hydrogenation reaction, but did not compare it to the bridge bonded CO.[14] Finally, the presence of chlorine might have some impact on the Rh catalytic activity, especially at low temperature.[6,31-32,42,59] However, EXAFS, XANES and CO IR data analysis revealed that its impact, if any, is about the same on all samples.

3.4 Comparison between the chemistry of supported Pt and Rh nanoparticles

To determine whether the promoting effect of the different cations on the Rh catalysts is similar to what we observed on the corresponding Pt/M^+-Y and Pt/M^{2+}-Y samples studied in Chapter 2, we compared the results of both studies. For that purpose, we added the data of the Pt-catalysts to Figures 5.7, 5.8 and 5.10 (see □ symbols). In Figure 5.7, the red shifts of the Rh *gem*-dicarbonyl bands as a function of the radius-to-charge ratio of the promoting cation (◆, ■, ▲, and ● symbols) are compared to the ones of the linearly bonded CO on Pt (□ symbols). Obviously, it would have been more logical to compare these data to CO linearly bonded to Rh, but as explained previously, it was not possible to extract this band from the spectra. It is nevertheless clear that the red shift is increasing with increasing cation radius-to-charge ratio for both noble metal catalysts. At first glance, the more pronounced effect for the Pt series seems to contradict intuition, in view of the isolated Rh atoms as opposed to the larger Pt particles. There are, however, some fundamental differences. Firstly, the Rh might be less sensitive to the support, because the bands under consideration originate from Rh in a +1 oxidation state whereas Pt is metallic. This means there are less electrons available for back-donation to CO from the Rh. Secondly, the Rh *gem*-dicarbonyl species undergo some constraints because the Rh cation is directly bonded to the zeolite matrix.[36]

Figure 5.8 represents the relative intensity of the bridge-bonded CO band as compared to the total absorption of Rh and Pt metal-bonded CO species as a function of the cation Lewis acidity. The trends for both Rh (▲) and Pt (□) are again similar but this time, the differences in the Rh series are more pronounced. This

disparity may be caused by the intervention of two parameters in the case of Rh, *i.e.*, electron density on the metal and acidity of the support, instead of one in the case of Pt, *i.e.*, electron density.

Figure 5.10 shows the temperature at 50 % CO conversion under large excess of oxygen as a function of the relative intensity of the bridge bonded CO in the static CO IR measurements. Although the data points of the Rh catalyst series are more scattered and the influence of the cation is larger for Rh as for Pt, the trend is once more equivalent for both noble metals.

4 Conclusions

The following conclusions can be drawn from this work:

(1) Exposure of zeolite-supported Rh nanoparticles to CO gives rise to more complex IR spectra than for zeolite-supported Pt nanoparticles.

(2) This increased complexity is due to the fact that CO modifies the state of the supported Rh particles upon adsorption, the smallest particles being disrupted into isolated Rh cations giving rise to Rh *gem*-dicarbonyl species.

(3) $Rh^{+}(CO)_2$ species exhibit typical narrow IR bands, which are sensitive to the support composition. This is demonstrated by ion exchanging the zeolite with different monovalent and divalent cations. It was observed that the IR red shift, as compared to the vibration frequency of CO in the gas phase increases with increasing ionic radius to charge ratio of the promoter. The same trend, but to a larger extent, was also observed for zeolite-based Pt particles.

(4) The relative intensity of the bridge bonded CO as referred to the total absorbance of the Rh-bonded CO species, decreases with increasing Lewis acidity of the promoting cation. This is similar to what has been observed on zeolite Y-supported Pt nanoparticles with alkali and alkaline earth promoters. However, the differences are more pronounced for the Rh catalysts, due to the larger contribution of bridge bonded CO in these samples.

(5) This last trend is directly correlated to the Rh catalytic activity for the CO oxidation reaction, since the temperature at 50 % CO conversion is lower for larger relative intensities of the bridge bonded CO. Again, the differences are more pronounced for the zeolite Y-supported Rh catalysts than for Pt ones.

References

[1] (a) Davis, M. E.; Rode, E.; Taylor, D.; Hanson, B. E., *J. Catal.* **1984**, *86*, 67. (b) Atsushi, A.; Rao, L.-F.; Kosugi, N.; Kuroda, H.; Ichikawa, M., *Appl. Catal.* **1989**, *50*, 295.

[2] (a) Weber, W. A.; Gates, B. C., *J. Catal.* **1998**, *180*, 207. (b) Boutros, M.; Launay, F.; Nowicki, A.; Onfroy, T.; Herledan-Semmer, V.; Roucoux, A.; Gédéon, A., *J. Mol. Catal. A: Chem.* **2006**, *259*, 91. (c) Lee, T. J.; Gates, B. C., *J. Mol. Catal.* **1992**, *71*, 335. (d) Bando, K. K.; Soga, K.; Kunimori, K.; Ichikuni, N.; Okabe, K.; Kusama, H.; Sayama, K.; Arakawa, H., *Appl. Catal. A: General* **1998**, *173*, 47. (e) Bando, K. K.; Soga, K.; Kunimori, K.; Arakawa, H., *Appl. Catal. A: General* **1998**, *175*, 67. (f) Bando, K. K.; Ichikuni, N.; Soga, K.; Kunimori, K.; Arakawa, H.; Asakura, K., *J. Catal.* **2000**, *194*, 91.

[3] (a) Denley, D. R.; Raymond, R. H.; Tang, S. C., *J. Catal.* **1984**, *87*, 414. (b) Andersson, S. L. T., *J. Catal.* **1981**, *71*, 233. (c) Bódis, J.; Zsakó, J.; Németh, C.; Mink, J., *Vibr. Spectrosc.* **1995**, *9*, 197.

[4] (a) Siri, G. J.; Guerrero-Ruiz, A.; Rodriguez-Ramos, I.; Terreros, P., *Appl. Catal. A: General* **1993**, *107*, 59. (b) Treviño, H.; Hyeon, T.; Sachtler, W. M. H., *J. Catal.* **1997**, *170*, 236. (c) Xua, B.-Q.; Suna, K.-Q.; Zhua, Q.-M.; Sachtler, W. M. H., *Catal. Today* **2000**, *63*, 453.

[5] (a) Gandhi, H. S.; Graham, G. W.; McCabe, R. W., *J. Catal.* **2003**, *216*, 433. (b) Taylor, K. C.; Schlatter, J. C., *J. Catal.* **1980**, *63*, 53. (c) Taylor, K. C., *Catal. Rev.-Sci. Eng.* **1993**, *35*, 457.

[6] Fontaine, C.; Krafft, J.-M.; Thomas, C.; Djéga-Mariadassou, G., *Phys. Chem. Chem. Phys.* **2006**, *8*, 3732.

[7] Manuel, I.; Chaubet, J.; Thomas, C.; Colas, H.; Matthess, N.; Djéga-Mariadassou, G., *J. Catal.* **2004**, *224*, 269.

[8] Yu Yao, Y.-F., *J. Catal.* **1984**, *87*, 152.

[9] Yang, A. C.; Garland, C. W., *J. Phys. Chem.* **1957**, *61*,1504.

[10] Yates, D. J. C.; Murrell, L. L.; Prestridge, E. B., *J. Catal.* **1979**, *57*, 41.

[11] Ivanova, E.; Mihaylov, M.; Thibault-Starzyk, F.; Daturi, M.; Hadjiivanov, K., *J. Catal.* **2005**, *236*, 168.

[12] Chafik, T.; Kondarides, D. I.; Verykios, X. E., *J. Catal.* **2000**, *190*, 446.

[13] Primet, M., *J. Chem. Soc., Faraday Trans. 1* **1978**, *74*, 2570.

[14] Miessner, H.; Gutschick, D.; Ewald, H.; Müller, H., *J. Mol. Catal.* **1986**, *36*, 359.

[15] Shannon, R. D.; Vedrine, J. C.; Naccache, C.; Lefebvre, F., *J. Catal.* **1984**, *88*, 431.

[16] Bergeret, G.; Gallezot, P.; Gélin, P.; Ben Taârit, Y.; Lefebvre, F.; Naccache, C.; Shannon, R. D., *J. Catal.* **1987**, *104*, 279.

[17] Tomczak, D. C.; Lei, G. D.; Schünemann, V.; Treviño, H.; Sachtler, W. M. H., *Micropor. Mater.* **1996**, *5*, 263.

[18] Vaarkamp, M.; Linders, J. C.; Koningsberger, D. C., *Physica B* **1995**, *208/209*, 159.

[19] Koningsberger, D. C.; Mojet, B. L.; van Dorssen, G. E.; Ramaker, D. E., *Top. Catal.* **2000**, *10*, 143.

[20] van Zon, J. B. A. D.; Koningsberger, D. C.; van't Blik, H. F. J.; Sayers, D. E., *J. Chem. Phys.* **1985**, *82*, 5742.

[21] Gloor, A. P.; Prins, R., *J. Phys. Chem.* **1994**, *98*, 9865.

[22] Gijzeman, O. L. J.; Mens, A. J. M.; Van Lenthe, J. H.; Mortier, W. J.; Weckhuysen, B. M., *J. Phys. Chem. B* **2003**, *107*, 678.

[23] Kamble, V.S.; Gupta, N. M.; Kartha, V. B.; Iyer, R. M., *J. Chem. Soc., Faraday Trans.* **1993**, *89*, 1143.

[24] Zhang, Y.; Toebes, M. L.; Van der Eerden, A.; O'Grady, W. E.; de Jong, K. P.; Koningsberger, D. C., *J. Phys. Chem. B* **2004**, *108*, 18509.

[25] Newton, M.A.; Dent, A. J.; Diaz-Moreno, S.; Fiddy, S. G.; Jyoti, B.; Evans, J., *Chem. Eur. J.* **2006**, *12*, 1975.

[26] Jentys, A., *Phys. Chem. Chem. Phys.* **1999**, *1*, 4059.

[27] van 't Blik, H. F. J.; van Zon, J. B. A. D.; Huizinga, T.; Vis, J. C.; Koningsberger, D. C.; Prins, R., *J. Am. Chem. Soc.* **1985**, *107*, 3139.

[28] Martinez-Arias, A.; Soria, J.; Conesa, J. C., *J. Catal.* **1997**, *168*, 364.

[29] Wong, T. T. T.; Stakheev, A. Y.; Sachtler, W. M. H., *J. Phys. Chem.* **1992**, *96*, 7733.

[30] Zaki, M.I.; Tesche, B.; Kraus, L.; Knözinger, H., *Surf. Interface Anal.* **1988**, *12*, 239.

[31] Force, C.; Belzunegui, J. P.; Sanz, J.; Martínez-Arias, A.; Soria, J., *J. Catal.* **2001**, *197*, 192.

[32] Newton, M.A.; Jyoti, B.; Dent, A. J.; Fiddy, S. G.; Evans, J., *Chem. Commun.* **2004**, 2382.

[33] Oudenhuijzen, M. K.; Van Bokhoven, J. A.; Miller, J. T.; Ramaker, D. E.; Koningsberger, D. C., *J. Am. Chem. Soc.* **2004**, *127*, 1530.

[34] Newton, M.A.; Dent, A. J.; Diaz-Moreno, S.; Fiddy, S. G.; Evans, J., *Angew. Chem. Int. Ed.* **2002**, *41*, 2587.

[35] Lefevbre, F.; Ben Taârit, Y., *Nouv. J. Chim.* **1984**, *8*, 387.

[36] Martra, G.; Ocule, R.; Marchese, L.; Centi, G.; Coluccia, S., *Catal. Today* **2002**, *73*, 83.

[37] Rakic, V. M.; Hercigonja, R. V.; Dondur, V. T., *Micropor. Mesopor. Mat.* **1999**, *27*, 27.

[38] Klepel, O.; Hunger, B., *J. Therm. Anal. Calorim.* **2005**, *80*, 201.

[39] Yagi, F.; Tsuji, H.; Hattori, H., *Microporous Mater.* **1997**, *9*, 237.

[40] Lavalley, J. C.; Saussey, J.; Lamotte, J.; Breault, R.; Hindermann, J. P.; Kiennemann, A., *J. Phys. Chem.* **1990**, *94*, 5941.

[41] Trautmann, S.; Baerns, M., *J. Catal.* **1994**, *150*, 335.

[42] Rice, C. A.; Worley, S. D.; Curtis, C. W.; Guin, J. A.; Tarrer, A. R., *J. Chem. Phys.* **1981**, *74*, 6487.

[43] Almusaiteer, K. A.; Chuang, S. S. C., *J. Phys. Chem. B* **2000**, *104*, 2265.

[44] Kusama, H.; Bando, K. K.; Okabe, K.; Arakawa, H., *Appl. Catal. A: General* **2001**, *205*, 285.

[45] Dent, A. J.; Evans, J.; Fiddy, S. G.; Jyoti, B.; Newton, M. A.; Tromp, M., *Angew. Chem. Int. Ed.* **2007**, *46*, 5356.

[46] Dujardin, C.; Mamede, A.-S.; Payen, E.; Sombret, B.; Huvenne, J.P.; Granger, P., *Top. Catal.* **2004**, *30/31*, 347.

[47] Iordan, A.; Zaki, L. I.; Kappenstein, C.; Géron, C., *Phys. Chem. Chem. Phys.* **2003**, *5*, 1708.

[48] Anderson, J. A., *J. Chem. Soc., Faraday Trans.* **1991**, *87*, 3907.

[49] Hecker, W. C.; Bell, A. T., *J. Catal.* **1983**, *84*, 200.

[50] Miessner, H.; Burkhardt, I.; Gutschick, D.; Zecchina, A.; Morterra, C.; Spoto, G.J., *J. Chem. Soc., Faraday Trans. 1.* **1989**, *85*, 2113.

[51] van't Blik, H. F. J. ; van Zon, J. B. A. D.; Huizinga, T.; Vis, J. C.; Koningsberger, D. C.; Prins, R., *J. Phys. Chem.* **1983**, *87*, 2264.

[52] Burkhardt, I.; Gutschick, D.; Lohse, U.; Miessner, H., *J. Chem. Soc. Chem. Comm.* **1987**, 291.

[53] Vayssilov, G. N.; Rösch, N., *J. Am. Chem. Soc.* **2002**, *124*, 3783.

[54] Gélin, P.; Dutel, J.-F.; Ben Taârit, Y., *J. Chem. Soc. Chem. Comm.* **1990**, 1746.

[55] Marcus, Y. *Ion Properties*; Marcel Dekker: New York, Basel, Hong Kong **1997**, p 193.

[56] Makeev, A.G.; Slinko, M.M.; Janssen, N.M.H.; Cobden, P.D.; Nieuwenhuys, B.E., *J. Chem. Phys.* **1996**, *105*, 7210.

[57] Hrncír, T.; Nahasil, V., *Surf. Sci.* **2002**, *507-510*, 859.

[58] Ioannides, T.; Efstathiou, A.M.; Zhang, Z.L.; Verykios, X.E., *J. Catal.* **1995**, *156*, 265.

[59] Fontaine-Gautrelet, C.; Krafft, J.-M.; Djéga-Mariadassou, G.; Thomas, C., *J. Catal.* **2007**, *247*, 34.

Chapter 6

Promotion effects in the reduction of NO by CO over zeolite-supported Rh nanoparticles

Abstract

Rh nanoparticles supported on a series of zeolite Y samples containing different monovalent (H^+, Na^+, Rb^+, and Cs^+) and divalent (Mg^{2+}, Ca^{2+}, Sr^{2+}, and Ba^{2+}) cations were used as model systems to investigate the effect of promoter elements in the reduction of NO by CO. Infrared (IR) spectroscopy with NO as a probe molecule allowed to monitor the electronic changes in the local environment of Rh. It was found that the bands corresponding to linearly adsorbed NO, *i.e.*, linear and dinitrosyl species, shift to lower wavenumbers with increasing ionic radius-to-charge ratio of the cation. In addition, the relative intensity of the bridge bonded NO as compared to the total absorbance of Rh-bonded NO species decreased with increasing Lewis acidity, as expressed by the Kamlet-Taft parameter α of the cation. Interestingly, the same trends have been observed in Chapter 5 for the same type of measurements performed with CO as IR probe molecule and could be related to the Rh activity for the CO oxidation reaction. The samples of this study also showed different activities. However, the observations made by NO IR spectroscopy could not be correlated to the catalytic reduction of NO by CO on the Rh surface. Additionally, it was observed that the NO conversion reached 50 % at a temperature 10-20 K lower than the conversion of CO. Besides, the reaction was accompanied by the formation of N_2O.

1 Introduction

Emissions from cars have been regulated in Europe since the 1970 Directive 70/220/EEC showing, amongst others, increasingly stricter requirements concerning the abatement of nitrogen oxides (NO_x).[1-2] For this purpose, Rh has been until today the precious metal of choice in three way catalysts (TWC) applications where it is used to reduce NO with CO or hydrocarbons.[3-13] It has been selected for its high activity and selectivity towards N_2 formation, its good thermal stability and its non-negligible resistance to poisons in spite of its elevated and highly fluctuating price. The need for an enhanced catalytic performance has pushed the catalyst material designers to develop better support materials as they have been shown to have a strong influence on the precious metals catalytic activity, their dispersion, their valence state and their aging behaviour, *i.e.*, their tendency to sinter, get poisoned and be involved in solid state reactions.[9,14-19] Promoters, such as alkali and alkaline earth metals, have been introduced to improve the TWC activity.[7-8,10,12,20-22]

In Chapters 2 to 5, it has been shown that these promoting elements have a direct impact on the electron density of Pt and Rh nanoparticles, which was directly reflected in their catalytic activity for the CO oxidation reaction. As Rh is mainly introduced in TWC for the reduction of NO_x and as it has been observed that the effect of Ba can be different on Pt- and Rh-based catalysts,[21] it is therefore of utmost interest to verify in a systematic manner how promoters, favouring the CO oxidation in excess of oxygen, influence the reduction of NO. The NO reduction by CO was also shown to be sensitive to the Rh particle size and the CO oxidation to be structure dependent.[5,23-26] Additionally, it was demonstrated that alkali metals promoting Rh/Al_2O_3 catalysts had an influence on the precious metal dispersion when applied by wet impregnation.[27] Furthermore, we demonstrated in Chapter 3 that the trends observed in the CO IR signal for two series of zeolite Y and silica supported Pt catalysts were similar. Therefore, it was decided to study the NO reduction by CO by means of Rh dispersed on the same series of zeolite Y supports with a varying composition, the charge compensating cation being modified via ion-exchange.

The goal of this work is to elucidate support effects on the activity of Rh for the NO reduction reaction by CO in a systematic manner. For this purpose, we have studied Rh-based model catalysts making use of zeolites as supports in which

different monovalent (H^+, Na^+, Rb^+ and Cs^+) and divalent (Mg^{2+}, Ca^{2+}, Sr^{2+} and Ba^{2+}) cations are present. By using NO as probe molecule in combination with IR spectroscopy, it will be shown that an increasing electron density on the supported Rh nanoparticles, indirectly induced by alkali and earth alkaline metal ions via the framework oxygen atoms, promotes the bonding of NO in a bridge position. However, as opposed to the clear effect of the cation promoters on the activity of Pt and Rh for the CO oxidation reaction in excess of oxygen, no systematic effect on the activity of Rh for the NO reduction by CO reaction could be observed.

2 Experimental section

2.1 Catalyst preparation

The starting material for ion exchange was a Na-Y material from AKZO Nobel with a Si:Al ratio of 2.3. The zeolite support materials with H^+, Rb^+, Cs^+, Mg^{2+}, Ca^{2+}, Sr^{2+}, and Ba^{2+} were obtained by five consecutive ion exchanges for 24 h with an aqueous 0.1 M solution of NH_4NO_3 (Acros, p.a.), RbCl (Acros, 99+ %), CsCl (Acros, 99+ %), $MgCl_2$ (Acros, p.a.), $CaCl_2$ (Aldrich, 98+ %), $SrCl_2$ (Acros, 99.99 %), and $BaCl_2$ (Aldrich, 99.999 %), respectively. The pH of the solution was kept between 6.5 and 7.5 and the zeolite material was separated from the solution through centrifugation for 30 min at 4000 rpm. The samples were then washed chlorine-free with deionised water, which was checked with $AgNO_3$, before being dried at 323 K for 48 h.

Before impregnation with a $RhCl_3.2H_2O$ (Alfa, 99.9 %) solution, the support was dried under vacuum at 473 K for 2 h. The target Rh loading by dry incipient impregnation was 0.5 wt%. The concentration of the precursor solution had to be calculated taking into account the change in material density caused by the introduction of the cations. After impregnation, the powder was dried for 12 h at room temperature and for 8 h at 353 K in an oil bath under flowing N_2 (quality 4.0; Hoekloos). The calcination was carried out in a tubular reactor in a high air flow (1335 ml/min). The temperature was first increased to 423 K at a rate of 5 K/min, where it was kept for 8 h, and then further to 573 K at a rate of 0.2 K/min where it was maintained for 1 h. Following cooling, the pellets were reduced in a H_2 (quality 5.0; Hoekloos) flow (380 ml/min) at 573 K for 2 h after a temperature ramp-up of

5 K/min. Finally, the Rh particles were stabilised by a short surface re-oxidation at room temperature, which should keep them from agglomerating.

2.2 Infrared spectroscopy measurements

IR measurements were performed on self-supporting catalyst wafers that were pressed from 0.01 g to 0.02 g of the passivated and finely grained sample material. A pressure of no more than 3 bar was applied during 10 s to prevent destruction of the pore structure of the support. The wafer was placed in an IR transmission cell equipped with CaF_2 windows. The cell was evacuated to less than 10^{-6} bar at 323 K for at least 1 h prior to reduction by a 40 ml/min to 60 ml/min flow of H_2 (quality 5.0; Hoekloos). During reduction, the temperature was raised from 323 K to 573 K at 3 K/min; it was maintained for 1 h at 573 K. The system was then switched back to vacuum for 1 h at 573 K, before being cooled down to 323 K at a rate of 3 K/min. A first spectrum was taken under vacuum and served as background reference for the catalyst wafer. Next, 10 % NO (quality 4.7; Linde AG) in He (quality 4.6; Linde AG) was introduced in the cell until a stable pressure of *ca.* 0.06 bar was reached. After 30 min of static NO exposure, the cell was evacuated to a pressure of 2 x 10^{-6} bar for 30 min at 323 K before the Temperature Programmed Desorption (TPD) was started by increasing the temperature up to 573 K at a rate of 3 K/min. IR spectra were recorded every 2 min on a Perkin-Elmer 2000 FTIR instrument with an optical resolution of 4 cm^{-1} and an accumulation of 25 scans with wavenumbers ranging from 4000 cm^{-1} to 1300 cm^{-1}. The data acquisition was performed automatically using the Perkin-Elmer Time-Base software. The reproducibility of all IR-TPD measurements was verified by repeating the experiments in two ways: (1) On two different wafers from the same sample and (2) on the same wafer by applying the same procedure two times in a row without opening the IR cell. Band positions and corresponding intensity data were estimated by peak fitting of the baseline corrected spectra using the Grams AI software. After evaluation of the different peak profiles, it was concluded that the Voigt profile was giving the best fits for well-defined maxima as well as for shoulders. Each spectrum was fitted with 5 to 6 Voigt-type peaks depending on its shape in the 2100-1300 cm^{-1} wavenumbers range. It should be noted that the peak positions obtained were very consistent, while repeating the fitting with different starting conditions.

Additional IR measurements were carried out to determine the rotational fine structure of vapour phase bands at an optical resolution of 0.5 cm^{-1} and co-adding 100 scans per spectrum.

2.3 Catalytic testing

The zeolite-based Rh catalysts were tested for the reduction of NO by CO in a U-tube reactor equipped with a thermocouple placed in the catalytic bed, a furnace and mass flow controllers. For this purpose, 20 mg of each catalyst diluted with 200 mg of SiC was loaded in the reactor. The reacting gas consisted of 2000 ppm of NO (10 % NO in He; quality 4.6; Linde AG) and 2000 ppm of CO (10 % CO in He; quality 4.6; Linde AG) with N_2 (quality 4.0; Linde AG) as balance. The total flow rate was 100 ml/min and the heating rate was 5 K/min. The NO and CO conversions and N_2O production were calculated between 278 K and 773 K from IR spectra measured every 25 s in a transmission flow cell using a Midac M2000 FT-IR spectrometer in the range 2700-1300 cm^{-1} accumulating 4 scans at an optical resolution of 4 cm^{-1}.

3 Results and discussion

3.1 Catalyst characterisation

All Rh-based model catalysts have been used and characterised in Chapter 5. A summary of their characteristics is given in Table 6.1. X-Ray Diffraction (XRD) measurements before and after ion exchange confirmed that the crystalline structure of the starting zeolite Na-Y material was not dramatically modified by the introduction of the new cations. The Rh and cation loadings of the different materials were determined making use of Atomic Emission Spectroscopy (AES) with an Inductively-Coupled Plasma (ICP) as atomisation source. The amount of Rh in the different zeolite samples varied between 0.2 wt% and 0.5wt% and the percentage of Na^+ ions exchanged by 1/n M^{n+} ions reached 65 to 83 %. The combination of Extended X-ray Absorption Fine Structure (EXAFS) measurements and High Resolution Transmission Electron Microscopy (HRTEM) pictures revealed that the mean Rh particle size was in the range 0.7-1.3 nm with some larger particles being in average 2-3 nm in diameter. Furthermore, it was concluded that the Rh dispersion

Table 6.1: Summary of the synthesised model catalysts and their main characteristics.

Sample	ICP-AES		TEM		EXAFS	
	Na^+ exchange [%]	Rh [wt%]	Particle size [nm]	Average particle size [nm]	Rh-Rh coordination number	Average particle size [nm] [a]
Rh/H-Y	NA	0.21	< 5	2.5	7	~ 1.3
Rh/Na-Y	100	0.33	< 6	3.1	6.5	~ 1.2
Rh/Rb-Y	65	0.36	< 3	1.3 [b]	5.8	~ 1.0
Rh/Cs-Y	72	0.49	< 6	2.6	6.4	~ 1.1
Rh/Mg-Y	66	0.32	< 4	2.2	5	~ 0.9
Rh/Ca-Y	77	0.38	< 6	2.7	6.1	~ 1.1
Rh/Sr-Y	83	0.39	< 3	1.9	1.8 [c]	< 0.6
Rh/Ba-Y	83	0.45	< 4	1.5	3.7	~ 0.7

[a] Average particle size based on the work done by van Zon *et al.*[28] and by Gloor and Prins.[29]

[b] The TEM pictures of this sample were much better, which allowed us to see smaller particles and gives a lower average particle size.

[c] The fit on this sample was not as good as on the others. The magnitude of the EXAFS Fourier Transform around 2.69 Å was however very similar to the one obtained on Rh/Ba-Y, which points to comparable Rh particle sizes.

was about the same for all samples and that the majority of the supported Rh-particles were located in the supercages of zeolite Y.

3.2 Infrared spectroscopy

General observations

The IR spectroscopic changes of the catalysts during exposure to NO and the subsequent evacuation and temperature programmed desorption (TPD) are illustrated by the 3D graph in Figure 6.1 for the Rh/Ca-Y catalyst. The first spectrum is taken prior to introducing NO into the cell. Next, upon exposure to NO (t = 2 min), several peaks show up and grow in intensity during the 30 min of exposure. After switching to vacuum (t = 32 min) the bands at around 2230 cm^{-1} disappear

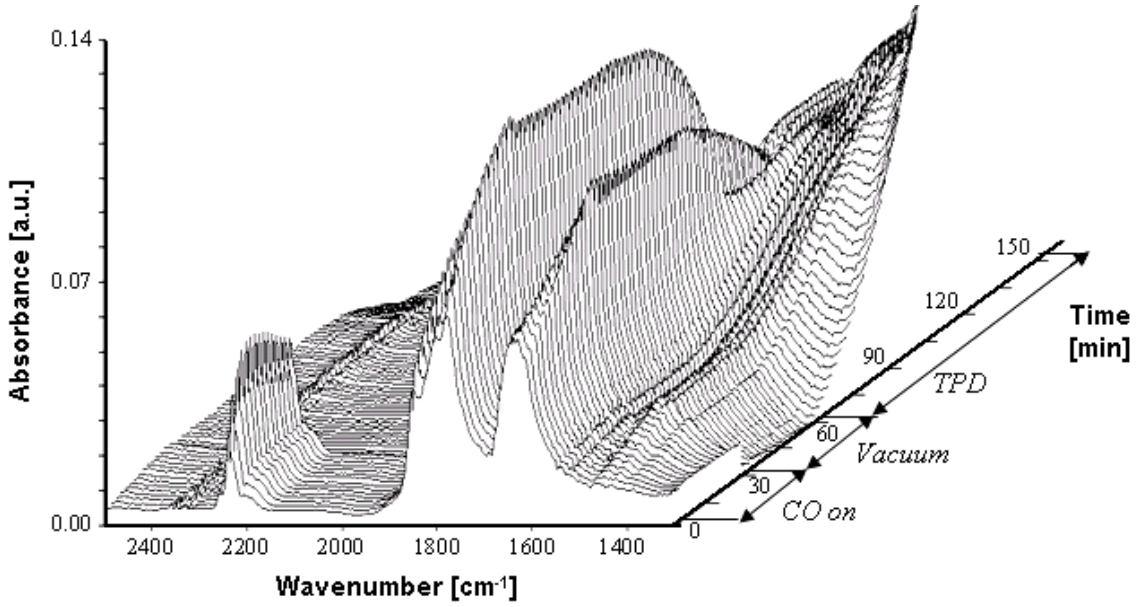

Figure 6.1: NO IR spectra measured during 30 min exposure to 0.06 bar NO, followed by 30 min vacuum at 323 K and temperature programmed desorption from 323 K to 573 K at 3 K/min on Rh/Ca-Y. Each spectrum is separated from the previous one by 2 min.

instantaneously, while the peaks in the range 2000-1400 cm^{-1} disappear during the TPD step (t = 62-154 min).

Closer examination of the bands in the region 2300-2200 cm^{-1} and their additional scanning at higher spectral resolution revealed a rotational fine structure pattern with its centre at 2224 cm^{-1} and a peak of "normal" shape around 2240 cm^{-1}. The former is characteristic for gas phase N_2O and is assigned accordingly.[30-34] Referring to the literature, the latter is ascribed to N_2O adsorbed on the support cations,[32,34-35] while the blue shift compared to the vapour phase frequency of N_2O is the result of the bonding through the nitrogen end of the molecule. The correctness of this assignment is further confirmed by the fact that identical band patterns were observed when the bare supports were exposed to NO. This is illustrated in the 3D graph of bare Ca-Y in Figure 6.2. In this specific case, as well as for the Sr-Y support, the band around 2240 cm^{-1} shifted to around 2250 cm^{-1} in agreement with the work of Chao and Lunsford[32] and an additional small peak appeared at about 2265 cm^{-1}. Both bands can be attributed to the N-N stretching vibration of adsorbed N_2O, but for different adsorption sites.[34,36] The observation that the peaks disappear upon evacuation is in accordance with their assignment since molecular N_2O is known to weakly bind to cations.[32,34,36]

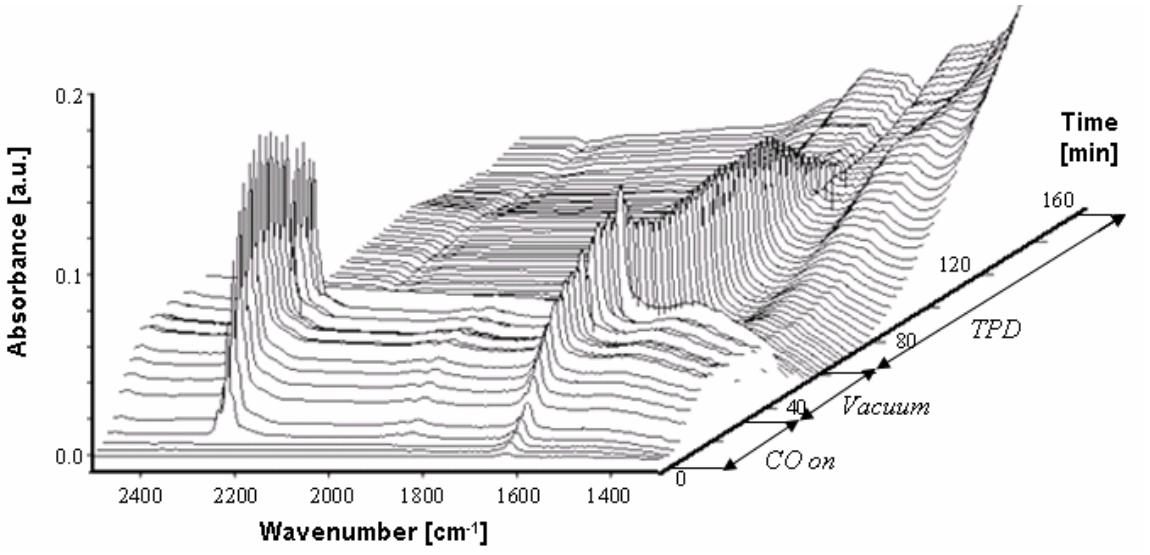

Figure 6.2: NO IR spectra measured during 30 min exposure to 0.06 bar NO, followed by 30 min vacuum at 323 K and temperature programmed desorption from 323 K to 573 K at 3 K/min on bare Ca-Y support. Each spectrum is separated from the previous one by 2 min.

The formation of N_2O

In order to determine the origin of N_2O, the IR cell was filled with NO gas and the spectrum was recorded with high resolution. As expected, the characteristic gas phase rotational fine structure pattern of the N=O vibration at 1876 cm^{-1} was present, but also weak bands with rotational fine structure at 2224 cm^{-1} and 1616 cm^{-1}. These bands can be assigned to gas phase N_2O and NO_2, respectively.[26,31-34,37-38] Both species are known to be formed through disproportionation of NO at high pressures in the gas bottle. However, based on the band intensities and the corresponding extinction coefficients, the concentration of N_2O and NO_2 were calculated to be less than 2 to 4 %.[36,39] It should nonetheless be noted that N_2O and NO_2 might as well be produced in the tubing to the cell, by the Rh catalyst and/or by the zeolite support materials. Comparison of the different spectra revealed that the intensity of the band of adsorbed N_2O around 2240 cm^{-1} was about the same for the catalysts and the corresponding supports, but slightly enhanced compared to the vapour phase band. On the one hand, this could indicate supplementary formation of N_2O by the studied materials, but it might also be the result of a larger extinction coefficient upon adsorption. A band corresponding to gaseous NO_2 was not observed in the spectra of the catalysts or the bare supports. Instead, in some of the spectra, a peak around 1455 cm^{-1} showed up; it disappeared

at high temperatures. In accordance with literature, this points to the adsorption of NO_2 by the support material in the form of stable nitrito compounds, nitrites or nitrates.[30-32,34-35,37,40-43] Therefore, we assign the band to nitrites or nitrates adsorbed on the cation or on extra-framework Al sites of the support.[32,34,37,42] No correlation between the intensities of the 1450 cm^{-1} and 2240 cm^{-1} bands was found.

In the literature, the production of N_2O by supported Rh catalysts has been reported at temperatures above 400 K in the presence of a reductant such as CO or H_2.[26,44-49] On three-way catalysts (TWC), the N_2O formation is limited to the temperature just after light-off.[5] At room temperature, Rh ions in zeolite Y are active for the reduction of NO by CO, mainly forming N_2O, although reduced Rh is, in principle, not active.[35] On Rh/Al_2O_3 catalysts, NO was shown to produce N_2O between about 350 K and 600 K in the absence of a reductant.[30,50] But, reducing agents are assumed to be absent in our cell as vacuum is applied after reduction with H_2 for 1 h at 573 K and the temperature during NO exposure does not exceed 323 K. The formation of N_2O has additionally been attributed to the reaction of a NO molecule with an adsorbed N-atom or to the disproportionation of Rh dinitrosyls.[30,35,44-45,50-52] The latter, as will be shown in the next section, are present in the studied systems. Regarding the former, Wallace *et al.* demonstrated that NO already dissociates on a Rh{111} single crystal at room temperature.[53] It has also been reported that the N_2O and NO_2 are formed simultaneously and that the generation of NO_x^- can be accompanied by the observation of N_2O.[30,34-35] On the other hand, Szanyi and co-authors[37] as well as Chao and Lunsford[32] concluded that the adsorption of NO on zeolite Na-Y at room temperature only yields to physically adsorbed NO. In contrast, the latter authors observed that NO disproportionated into NO_2 and N_2O on Ca-Y at room temperature and on Na-Y and on decationated Y at 195 K but not on H-Y at these temperatures.[32] Disproportionation was reported as well for alkali metal ion-exchanged ZSM-5 zeolites at 226 K.[36] Finally, Sedlmair *et al.* observed the formation of nitrates and nitrites on Ba-Y upon contact with NO at 323K.[42] In our study, the exposure to NO at 323 K of the bare Na-Y, Rb-Y and Cs-Y supports gave no bands attributable to adsorbed NO_x, whereas for H-Y, Mg-Y, Ca-Y, Sr-Y and Ba-Y, a broad band at *ca.* 1450 cm^{-1} of varying intensity was present. Hence, the formation of NO_2 and N_2O by the support and/or the supported Rh nanoparticles cannot be fully excluded for this series of samples.

It should be noted that, during NO exposure of the catalysts or the bare supports, a peak around 1640 cm^{-1} slowly grows up, at the same time as one around 3600-3300 cm^{-1}. As reported in Chapter 5, this is due to the diffusion of traces of water into the cell. Possibly, a band related to adsorbed NO_2 coincides with this water peak. Nonetheless, this could not be unambiguously concluded from the spectra of the bare support materials since residual water in zeolites can react with NO_2 to form nitrates.[31,34]

Adsorbed NO species

Figure 6.1 shows that the band positions and intensities in the range 2000-1400 cm^{-1} remain practically the same during the 30 min vacuum period (t = 32-62 min). It implies that all adsorbed species related to these bands are strongly bonded at 323 K. Upon TPD (t = 62-145 min), the intensity of the 1640 cm^{-1} band slowly decreases and disappears around 450 K. All other bands remain unaffected up till 450 K and for that reason we conclude they originate from adsorbed NO-species, which all desorb before the temperature of 573 K is reached. This is not only the case for the Rh/Ca-Y, but for all catalysts that have been studied, as illustrated by Figure 6.3 for Rh/Mg-Y, Rh/H-Y, Rh/Na-Y, and Rh/Ca-Y. In these TPD graphs, each spectrum is separated from the next one by 2 min or 6 K. Apart from Rh/H-Y, NO is fully desorbed around 473 K from the Rh/M^{+}-Y catalysts, while, from the Rh/M^{2+}-Y catalysts, complete desorption is only achieved above 523 K. A similar behaviour, but with a shift to higher temperatures, has been observed in Chapter 5 for CO IR TPD measurements on the same samples. The shape and relative intensity of the NO bands vary considerably depending on the type of support. During TPD, the 2 peaks around 1850 cm^{-1} and 1770 cm^{-1} lose intensity at the same speed, whereas the bands between 1650 cm^{-1} and 1450 cm^{-1} show a different behaviour. The assignment of the bands is rather difficult and requires a more detailed spectral analysis.

Assignment of the peaks in the region 2000-1300 cm^{-1}

In order to facilitate the interpretation of the 2000-1300 cm^{-1} spectral region, curve fitting was applied to the background-subtracted and baseline-corrected IR

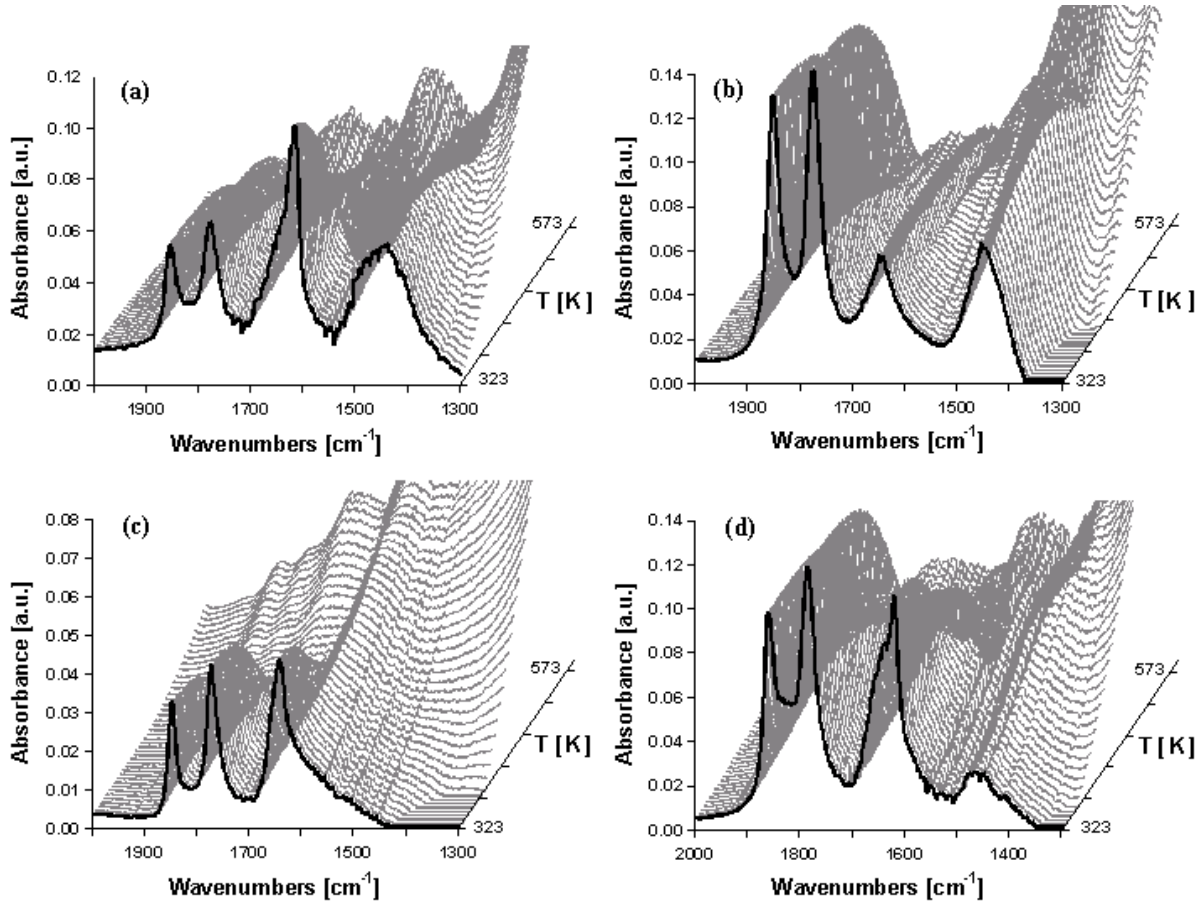

Figure 6.3: NO IR spectra measured after 30 min exposure to 0.06 bar NO and 30 min vacuum at 323 K during TPD from 323 K to 573 K at 3 K/min obtained on (a) Rh/Mg-Y, (b) Rh/H-Y, (c) Rh/Na-Y and, (d) Rh/Ca-Y samples. Each spectrum is separated from the previous one by 2 min or 6 K.

spectra recorded after NO exposure and 30 min vacuum at 323 K. The results obtained for Rh/Mg-Y, Rh/H-Y, Rh/Na-Y, and Rh/Ca-Y are shown in Figure 6.4. All spectra appear to be nicely fitted with 5-6 peaks of which the corresponding peak positions have been listed in Table 6.2, together with the curve-fitting results for the other catalysts. Based on previous discussions and literature the band around 1640 cm^{-1} is assigned to the OH-deformation vibration of water. It is as well observed in the spectra obtained for the NO-exposed bare support materials between 1655 cm^{-1} and 1620 cm^{-1}, depending on the cation used as a promoter (Table 6.2). Although highly back-bonded NO adsorbed on Rh^{30} or $Rh\text{-}NO^{\delta-}$ [25,44,50-51] may give rise to an absorption band in the same region, this is rejected as the peak is present in the spectra of the NO-exposed bare supports. For the same reason, the band around 1450 cm^{-1} is assigned to NO_x stored on the support material.

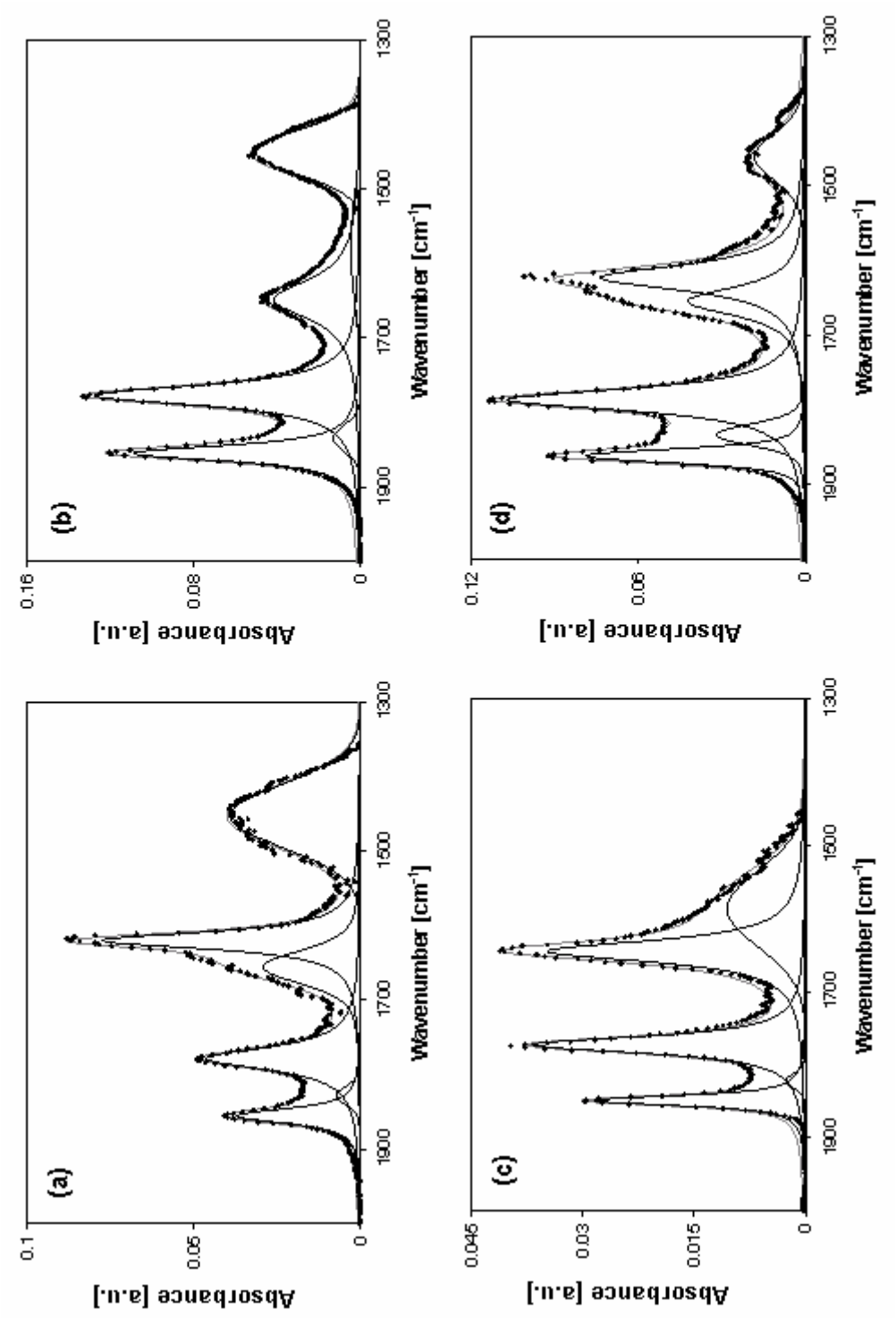

Figure 6.4: NO IR spectra after 30 min exposure to 0.06 bar NO and 30 min vacuum at 323 K with the fitted bands on (a) Rh/Mg-Y, (b) Rh/H-Y, (c) Rh/Na-Y and, (d) Rh/Ca-Y samples.

Table 6.2: Band positions in the NO IR spectrum after 30 min exposure to 0.06 bar NO and 30 min vacuum at 323 K.

Sample	Band position [cm^{-1}]					
	$Rh^+(NO)_2$ (sym)	$Rh^0(NO)$	$Rh^+(NO)_2$ (as)	Rh_n^0-NO [a]	Water	M-NO_x^- [b]
Rh/H-Y	1855	1835	1777	1580	1648	1451
Rh/Na-Y	1849	1822	1773	1587	1645	-
Rh/Rb-Y	1835	1791	1751	1593	1649	-
Rh/Cs-Y	1829	1773	1740	1584	1646	-
Rh/Mg-Y	1856	1829	1779	1656	1621	1453
Rh/Ca-Y	1862	1834	1787	1655	1623	1462
Rh/Sr-Y	1862	1841	1783	1602	1641	1463
Rh/Ba-Y	1854	1827	1775	1598	1649	1482

[a] Rh_n^0-NO is a NO molecule bonded in n-fold bridge position to metallic Rh.

[b] M-NO_x^- are nitrites or nitrates adsorbed on alkali or alkaline earth cations.

Next, the relatively weak band at around 1800 cm^{-1}, and the stronger ones at 1850 cm^{-1}, 1780 cm^{-1} and 1630 cm^{-1} can be attributed to different adsorbed NO species. For these peaks, a variety of assignments has been reported in the literature. On Rh{111} single crystals, for instance, NO bands at 1850 cm^{-1} and 1645 cm^{-1} have been ascribed to linearly and bridge bonded NO, respectively.[53-54] The same species have been proposed for peaks in the range 1840-1800 cm^{-1} and 1694-1620 cm^{-1}, respectively, in the spectra of supported Rh catalysts.[30,47,51,55-57] In contrast, the band at *ca.* 1650 cm^{-1} has also been assigned to Rh-$NO^{\delta-}$, often referred to as Rh-NO^- "low".[25-26,43-44,47,50-51,56] However, in this study, the band was broad and, for that reason, attribution to bridge bonded NO or to highly back-bonded NO seems more plausible.[25,50,56] Besides, referring to the review of Hadjiivanov,[34] Rh-$NO^{\delta-}$ species are usually found at higher wavenumbers, whereas perturbed or "bent" NO molecules bonded to Rh^0 or Rh^+ do absorb in this region of the spectrum. Furthermore, for Rh supported on a dealuminated zeolite Y, Miessner and co-workers assigned the band around 1840 cm^{-1} to linearly bonded NO and the one between 1694 cm^{-1} and 1636 cm^{-1} to bridge bonded species.[57] The bands were only present for samples with larger Rh crystallites, which is in agreement with our TEM

observations showing the presence of some larger Rh particles. Therefore, we assign the weak band in the range 1841-1773 cm^{-1} to NO linearly bonded to reduced Rh and the broader "non-water" band between 1656 cm^{-1} and 1580 cm^{-1} to NO bridge bonded to Rh.

Finally, the two prominent peaks at around 1850 cm^{-1} and 1780 cm^{-1}, which evolve identically during TPD, can be attributed to, respectively, the symmetrical and anti-symmetrical stretching vibrations of $Rh^{+}(NO)_2$.[25,34-35,44,50,57-59] Supported Rh nanoparticles of less than 2 nm are known to easily disintegrate into isolated Rh cations under NO atmosphere; a process, which is similar to what happens in a CO atmosphere with the participation of adsorbed O atoms or of OH groups from the support. Additionally, this reaction can also occur via the oxidation of the Rh surface during the reduction of NO to N_2O or the dissociation of NO.[25,44,57,60-62] Dinitrosyls can be found on both oxidised and reduced Rh surfaces.[34,44,57] As opposed to the CO IR study performed in Chapter 5, which showed 2 types of Rh dicarbonyls, only one type of Rh dinitrosyls was observed on the cation-exchange zeolite Y. This is completely in line with the studies of Miessner *et al.* who also reported two different dicarbonyl species and only one kind of dinitrosyls.[57,63]

Like for the Rh dicarbonyls, the intensity ratio of the two nitrosyls bands can be used to calculate the angle θ between the 2 adsorbed NO molecules, where $I_{asym}/I_{sym} = \tan^2(\theta/2)$.[34,58] For our catalysts, this resulted in an angle of about 110°. This is slightly larger than the 103.5° bond angle reported by Ivanova and Hadjiivanov for Rh supported on a H-MFI zeolite,[58] but identical to the results of Miessner *et al.* for Rh on highly dealuminated zeolite Y.[57] Besides, the presence of these species already at low temperature is in accordance with the small average Rh particle size as determined with EXAFS.[57]

To verify the correctness of our assignments, some of the catalysts were re-analysed with IR after exposure to pure oxygen at 573 K for 2 h. To illustrate the results, the spectrum obtained for Rh/Mg-Y is shown in Figure 6.5, together with the data of the reduced sample as already presented in Figure 6.4 a. The spectra have been normalised to the intensity of the Rh dinitrosyls bands and, for both, the fitted curves have been included. First of all, the bands at *ca.* 1800 cm^{-1} and around 1600 cm^{-1}, assigned to $Rh^0(NO)$ species, either strongly decreased in intensity or even disappeared. Obviously, this is the result of the oxidative conditions and confirms the correctness of the assignment. Secondly, the position and the relative

intensity of the bands at around 1850 cm^{-1} and 1780 cm^{-1}, attributed to Rh dinitrosyls, remained the same, which is a further validation of this assignment.[34,44,57] Thirdly, the band around 1450 cm^{-1}, attributed to NO_x storage by the support, also decreased in intensity. There is no clear explanation for this phenomenon, but it is not in contradiction with the attribution either. Finally, a new band is observed around 1915 cm^{-1}, which can be ascribed to NO linearly bond to oxidised Rh. In the literature, this band is often erroneously denoted Rh-NO^+, but it is at too low wavenumbers to be assigned to adsorbed NO^+. Therefore, it should be written Rh^+-NO.[34,37,39,41-42] The band has been reported between 1900 cm^{-1} and 1931 cm^{-1}.[25,30,35,43-44,46,50,55-57] It was shown to be a dominant species in the absence of reduced Rh, upon addition of oxygen or, at higher temperatures, upon prolonged exposure of Rh to NO due to its decomposition and the accumulation of oxygen atoms on the Rh surface. Miessner *et al.* also demonstrated that this band shows up on reduced samples with larger Rh particles upon heating in a NO atmosphere at the expense of the linear and bridge bonded NO adsorbed on reduced Rh.[57] This is in agreement with the decrease in intensity of the Rh^0(NO)-related bands at 1850 cm^{-1} and 1600 cm^{-1}.

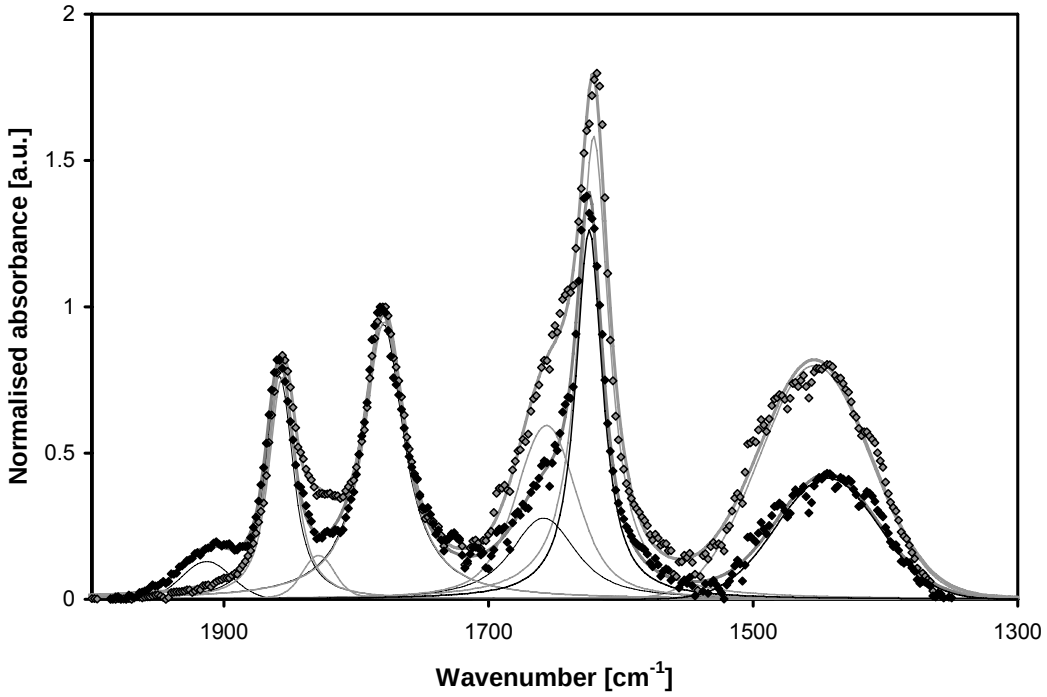

Figure 6.5: NO IR spectrum after 30 min exposure to 0.06 bar NO and 30 min vacuum at 323 K on the reduced (grey trace) and on the oxidised (black trace) Rh/Mg-Y sample with their fitted bands. For a better visibility, the traces have been normalised to the height of the nitrosyls bands.

Influence of the support composition

The samples promoted by alkali metal ions show a clear decrease in wavenumber for the Rh (di)nitrosyls peak positions when going from the smallest cation (H^+) to the largest one (Cs^+) (Table 6.2). For the alkaline earth promoters, it is not as obvious, but overall a trend is present as visualised in Figure 6.6. The full symbols represent the red shift of the Rh (di)nitrosyls bands, *i.e.* symmetrical and asymmetrical stretching vibrations of $Rh^+(NO)_2$ (◆ and ▲, respectively) and linear Rh^0-NO (■), compared to the NO gas phase vibration (1876 cm^{-1}) as a function of the cation radius divided by its charge. It can be seen that the red shift increases with the promoter ionic radius-to-charge ratio. The trend is slightly more pronounced for the linearly bonded NO to metallic Rh than for the cationic Rh dinitrosyls. The same difference was noticed in Chapter 5, when series of Pt and Rh supported on promoted zeolite Y were studied by CO IR, *i.e.*, the difference in the vibration frequency shift of the CO linearly bonded to Pt was larger than the one of the Rh *gem*-dicarbonyl species. Chafik and co-authors observed that the bands were blue-shifted when Rh was influenced by an electron-donor. On the contrary, the nitrosyls of metals with less d-type electrons, *i.e.*, Rh^+ compared to Co^{2+}, were found at higher wavenumbers.[35] This can be related to a stabilisation of the dinitrosyls by a π back-donation.[34-35,57] Stretching vibration shifts have also been observed for NO molecules adsorbed on the cations incorporated in zeolites.[36] They were explained by changes in the electric field in the zeolite pores. In the latter study of Katoh *et al.*, however, the smallest shifts were observed for the largest cations. This can be due to a direct absorption through the O-end of the molecule on the cations. In our case, the NO is adsorbed on the Rh through the N-end and interacts with the cations *via* the O-end of the molecule, which could explain the opposite trend. The bonding through the N-end might also explain why the band corresponding to the NO_x-type of species at around 1450 cm^{-1} shows an upward wavenumber shift from Mg^{2+} to Ba^{2+} (Table 6.2).[34] For Rh/Na-Y, Rh/Rb-Y and Rh/Cs-Y, a NO_x-band from nitrates/nitrites is absent unless it is hidden in the peak corresponding to bridge bonded NO between 1500 cm^{-1} and 1570 cm^{-1}. This assumption would however be in contradiction with the work of Sedlmair *et al.* who observed Ba-nitrates at higher wavenumbers than Na-nitrates.[42] Therefore we conclude that nitrates are absent for these catalysts.

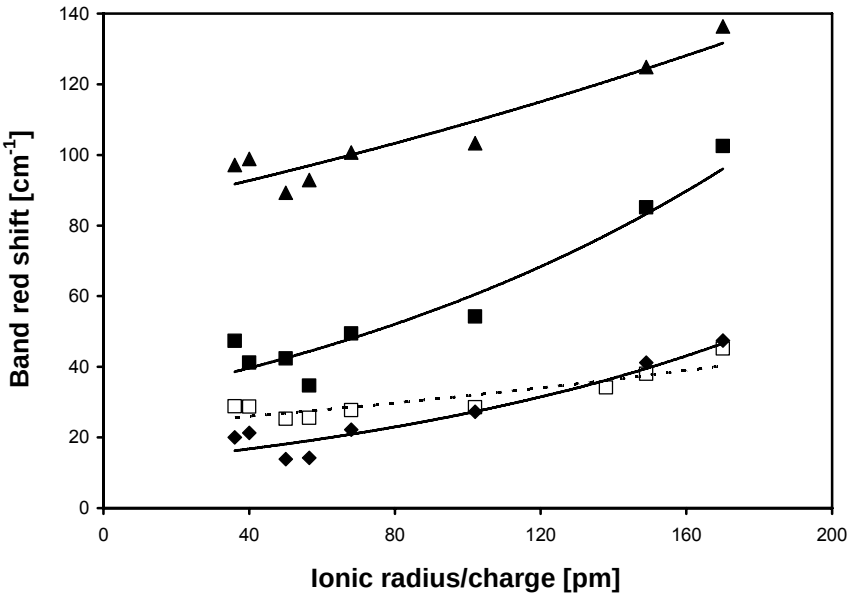

Figure 6.6: NO IR band red shift versus the NO vibration in the gas phase as a function of the cation ionic radius-to-charge ratio for the (◆) symmetrical and (▲) asymmetrical vibrations of the Rh di-nitrosyls ($Rh^{+}(NO)_2$), and for the (■) linearly bonded NO ($Rh^{0}(NO)$. For comparison, the CO IR band red shift for the (□) symmetrical Rh di-carbonyl ($Rh^{+}(CO)_2$) obtained in Chapter 5 has been added.

From literature, it is known that dinitrosyls bond angles can vary between 100° and 140°.[34] We observed differences in bond angle depending on the cation promoting the Rh nanoparticles. However, no relationship could be found between the properties of the cation and the angle between the Rh dinitrosyls.

The comparison of the spectra in Figure 6.4 shows that the relative intensity of the (di)nitrosyls bands and the bridge bonded NO varies from sample to sample. In Figure 6.7, we highlight that the intensity of the bridge bonded NO (▲ symbols), related to the total intensity of the bands corresponding to Rh-adsorbed NO species, is decreasing with increasing support cation Lewis acidity, as expressed by the Kamlet-Taft parameter α.[64] As already discussed in a Chapter 5, this trend can be explained by the fact that more basic cations are pushing electrons towards the framework oxygen of the support, which in turn causes the Rh nanoparticles to have a higher electron-density. This gives rise to a larger back-donation to the π-orbitals of adsorbed NO, thus enhancing the possibility for bridge bond formation. It should be noted, however, that the OH-group acidity of the support might play a role here as well, since they are known to influence the formation of the $Rh^{+}(NO)_2$ species.[44]

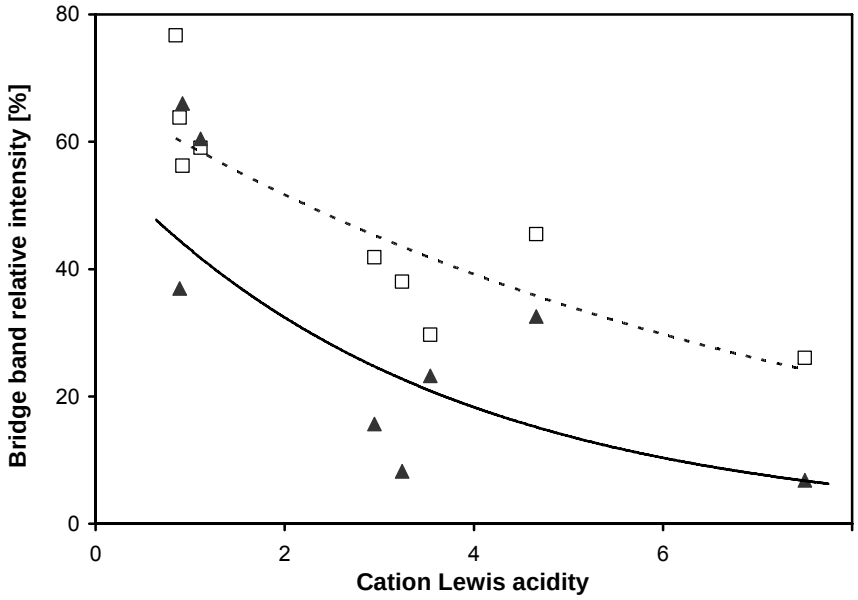

Figure 6.7: Relative intensity of the bridge bonded NO as compared to the total absorbance of Rh-bonded NO species as a function of the cation Lewis acidity of the support promoter (▲). As a comparison, the relative intensity of the bridge bonded CO as compared to the total absorbance of the Rh-bonded CO species obtained in Chapter 5 has been added (□).

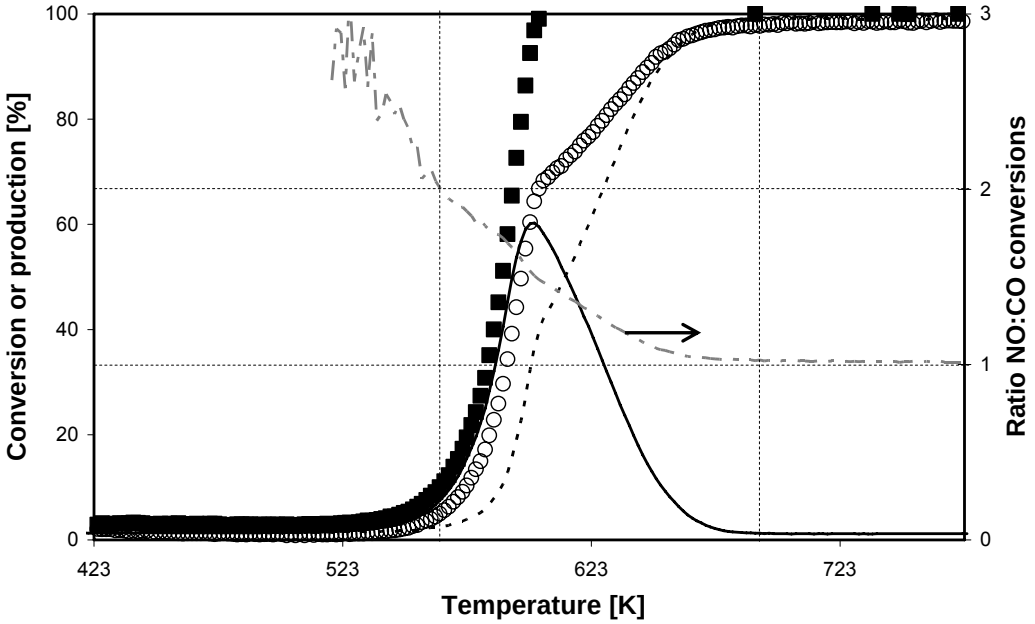

Figure 6.8: Conversion of NO (■) and CO (○) as well as the production of N_2O (full line) and N_2 (dotted line). The production in N_2O has been calculated from IR spectra and expressed in percentage of the maximum of N_2O that could be formed based on the NO feed. The N_2 production has been extracted from the NO conversion and N_2O production. The ratio of the NO conversion to the CO conversion has been added on the secondary Y-axis (grey line).

3.3 NO reduction activity

The series of samples studied by NO IR has also been tested for their activity in the stoichiometric NO-CO reaction. Typical light-off curves are illustrated in Figure 6.8 for the Rh/Na-Y sample. As can be seen, N_2O (full line) is the main product of the reduction of NO (■) by CO (○) upon light-off. The maximum in N_2O production is obtained when NO reaches at least 90 % conversion. At that temperature, the CO conversion and the N_2 production curve (dotted line) show an inflection point, while the NO conversion keeps a sigmoid shape, indicating a change in reaction mechanism. Different reaction mechanisms have been proposed for the CO-NO reaction on Rh,[30,46-47,51,65-66] but, usually, the following series of reactions is accepted:

$$NO_g + * \leftrightarrow NO_{ads} \quad (1)$$

$$CO_g + * \leftrightarrow CO_{ads} \quad (2)$$

$$NO_{ads} + * \rightarrow N_{ads} + O_{ads} \quad (3)$$

$$N_{ads} + NO_{ads} \rightarrow N_2O_g + 2 * \quad (4)$$

$$2\ N_{ads} \rightarrow N_{2g} + 2 * \quad (5)$$

$$O_{ads} + CO_{ads} \rightarrow CO_{2g} + 2 * \quad (6)$$

where $*$ is a free adsorption site on the Rh surface, the g-subscript is referring to a molecule in the gas phase and the ads-subscript to an adsorbed molecule or atom. Our results tend to indicate that the NO conversion initially proceeds following Reaction (3) and then, at higher temperatures, progressively shifts to Reaction (4). This is further confirmed by the ratio of the NO conversion versus the CO conversion, which is about 2 when the reaction starts, 1.3-1.5 when 50 % N_2 production is reached and decreases to 1 upon full conversion of CO and full selectivity to the N_2 product. As it has been shown that the oxygen atoms are directly reacting with CO via Reaction (6),[43] we can conclude that when the reaction starts, only one oxygen atom is left on the Rh surface for 2 NO molecules consumed, whereas, the production of N_2 instead of N_2O, leaves one oxygen atom for each NO molecule that disappears. As NO tends to adsorb preferentially on Rh,[30,51] this transition from N_2O to N_2 production is completely in line with the work

of Permana *et al.*, who concluded that N_2O was being formed when NO mainly covers the surface whereas N_2 is the product when mainly CO is on the Rh surface.[66] The formation of N_2O is in agreement with the presence of dinitrosyls, which are believed to be an active species in the production of N_2O.[25,35,44,46,50] Besides, it is in accordance with our preparation method, which consists of a reduction followed by surface re-oxidation, as the production of N_2 requires reduced Rh sites.[30,35,44-45,47,50,60] A change in kinetic behaviour has also been observed by Newton and co-authors and was believed to originate from the formation of metallic Rh.[67] Finally, in line with the literature, no NO_2 formation was observed.[44,46,51]

A clear trend in the catalytic activity or the selectivity of the samples under study as a function of (1) the Lewis acidity of the promoting cation, (2) the formation of bridge bonded NO or of dinitrosyls or, (3) the desorption temperature in the NO TPD was not observed. This might be due to a complex influence of different parameters on the catalytic activity. As was shown in Chapter 5, the promoting cation can affect the electron density on the Rh but also the formation of carbonyls or nitrosyls. Most likely, the electron density of the Rh will influence the degree of charge transfer from the Rh to the antibonding π^* orbital of the adsorbed NO, which favours its dissociation following Reaction (3).[44,51] Additionally, it is known that the co-adsorption of NO and CO provokes large structural changes in Rh particles because NO promotes their oxidative disruption by CO and hinders their reductive agglomeration upon temperature increase.[25,43,46-47,60,62,67] A small difference in starting particle size, *i.e.* 0.8 nm *versus* 1.1 nm has been shown to have a dramatic influence on the selectivity and activity of the reaction, at the condition that the initial particles are small.[25-26] Larger particle sizes favour the NO dissociation.[43,55] As the average Rh particle size in the studied samples is varying between 0.6 nm and 1.3 nm, the influence of this parameter will most probably not be negligible. Furthermore, the Rh state is influenced by the NO-CO reaction; *i.e.* adsorbed O from dissociated NO oxidises Rh^0 to Rh^+, adsorbed CO reduces Rh^+ to Rh^0, and oxidised Rh is less active for the NO reduction.[46,67] As we observed in Chapter 5 that the Rh particles are difficult to fully reduce, this factor might also have an influence on the catalytic results for the NO-CO reaction. Finally, it has been shown that Rh-$NO^{\delta-}$ species are predisposed for dissociation,[25-26,30,44,51] but we did not observe such species during the NO IR measurements even if, in the cited references, they were not absolutely associated with the co-adsorption of NO with CO.

3.4 Comparison with the results from previous Chapters

In Figures 6.6, 6.7 and 6.9, the results of this study can be compared to the results of the previous work performed on Rh and Pt supported nanoparticles.

Figure 6.6 shows that the band maxima of linearly Rh-bonded CO (represented by the symmetrical Rh *gem*-dicarbonyl stretching vibration, ☐ symbols) as well as the linear Rh bonded NO (represented by Rh^0(NO), ■ symbols) are more red-shifted when the radius-to-charge ratio of the promoting cation is increasing. Besides, larger band shift differences are observed for the linear Rh-NO species as a function of the cations compared to the differences in shift for the Rh *gem*-dicarbonyl species. This is in agreement with observations from Chafik *et al.*[44]

In Figure 6.7, we can see that for samples promoted by cations with a stronger Lewis acidity, the tendency to form bridge bonded species is decreasing. This suggests that, when the electron density of the Rh is increased, it tends to donate back more electrons to the adsorbed NO or CO molecule.

Finally, Figure 6.9 shows that, for the CO oxidation in excess of oxygen on Rh (☐ symbols) or Pt (△ symbols) nanoparticles, there is a clear influence of the promoter, which could not be observed for the stoichiometric reduction of NO by CO

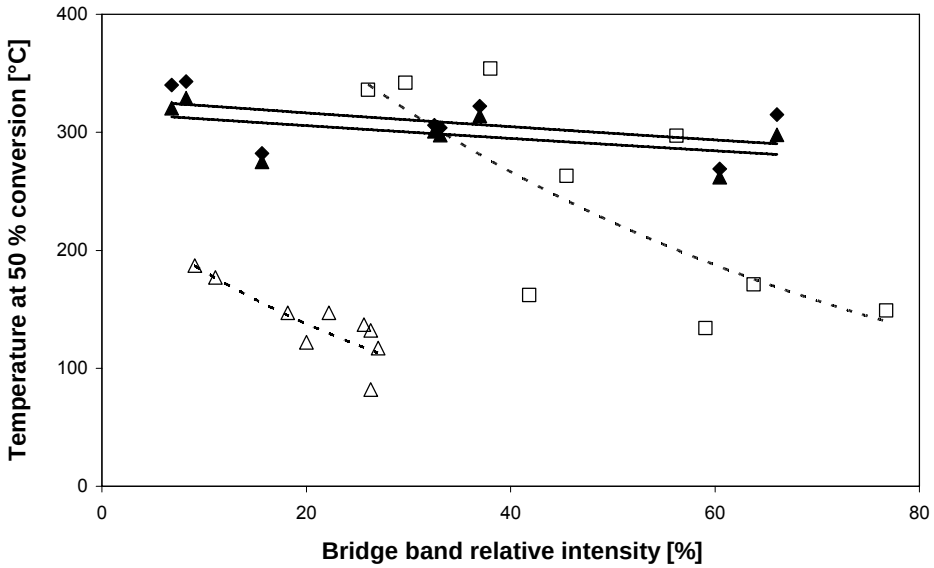

Figure 6.9: Temperature at 50 % NO (▲) and CO (◆) conversion for the stoichiometric reduction of NO by CO reaction as a function of the relative NO IR absorption intensity of the bridge bonded NO. As a comparison, the temperature at 50 % CO conversion for the CO oxidation in excess of oxygen as a function of the relative CO IR absorption intensity of the bridge bonded CO has been added for Pt (△) and Rh (☐) catalysts (Chapter 5).

(◆ and ▲ for CO and NO, respectively). For all samples, except for Rh/Ca-Y and Rh/Sr-Y, the temperature at 50 % CO conversion is higher when NO is used as an oxidant than when O_2 is used. This can be explained by the competitive adsorption of CO and NO.

4 Conclusions

The following conclusions can be drawn from this work:

(1) Under NO exposure, the small Rh particles tend to disintegrate and form Rh dinitrosyls.

(2) The NO IR bands corresponding to the linearly bonded NO on Rh are red-shifted to a larger extent, as compared to the NO vibration in the gas phase, when the radius-to-charge ratio of the cation promoter is larger.

(3) The relative intensity of the IR band corresponding to the bridge bonded NO as compared to the total absorbance related to Rh-bonded NO species is increasing with decreasing Lewis acidity of the promoting cation.

(4) The NO reduction by CO was accompanied by N_2O formation upon light-off. At temperatures above 623-673 K, full selectivity to N_2 was reached. It was not possible to derive a clear correlation with properties of the promoting cation from the present study, probably due to the impact of different factors such as the electron density of the Rh, the Rh particle size and the Rh oxidation state during reaction.

References

[1] European Union *Motor vehicles with trailers: polluting emissions*, Gateway website: http://europa.eu/scadplus/leg/en/lvb/l21047.htm; July **2007**.

[2] Schulte-Braucks, R. *European emissions legislation for mobile sources*, CAPoC7 Conference, Brussels, August **2006**.

[3] Gandhi, H. S.; Graham, G. W.; McCabe, R. W., *J. Catal.* **2003**, *216*, 433.

[4] Taylor, K. C.; Schlatter, J. C., *J. Catal.* **1980**, *63*, 53.

[5] Taylor, K. C., *Catal. Rev.-Sci. Eng.* **1993**, *35*, 457.

[6] Tollefson, J., *Nature* **2007**, *450*, 334.

[7] Thomas, J. M.; Thomas, W. J. (Eds.), *Principles and Practice of Heterogeneous Catalysis*, Wiley-VCH, Weinheim; **1996**.

[8] Webster, D. E., *Top. Catal.* **2001**, *16/17*, 33.

[9] Ertl, G.; Knozinger, H.; Weitkamp, J. (Eds.), *The Handbook of Heterogeneous Catalysis*, Wiley-VCH, Weinheim; Volume 4, **1997**.

[10] Twigg, M. V., *Appl. Catal. B: Environ.* **2007**, *70*, 2.

[11] Koltsakis, G. C.; Stamatelos, A. M., *Prog. Energy Combust. Sci.* **1997**, *23*, 1.

[12] Collins, N. R.; Twigg, M. V., *Top. Catal.* **2007**, *42-43*, 323.

[13] Skoglundh, M.; Fridell, E., Top. Catal. **2004**, *28*, 79.

[14] Fontaine, C.; Krafft, J.-M.; Thomas, C.; Djéga-Mariadassou, G., *Phys. Chem. Chem. Phys.* **2006**, *8*, 3732.

[15] Manuel, I.; Chaubet, J.; Thomas, C.; Colas, H.; Matthess, N.; Djéga-Mariadassou, G., *J. Catal.* **2004**, *224*, 269.

[16] Yu Yao, Y.-F., *J. Catal.* **1984**, *87*, 152.

[17] Zaki, M. I.; Tesche, B.; Kraus, L.; Knözinger, H., *Surf. Interface Anal.* **1988**, *12*, 239.

[18] Nagai, Y.; Hirabayashi, T.; Dohmae, K.; Takagi, N.; Minami, T.; Shinjoh, H.; Matsumoto, S., *J. Catal.* **2006**, *242*, 103.

[19] Matsumoto, S.; Shinjoh, H., *Adv. Chem. Eng.* **2007**, 33, 1.

[20] Iordan, A.; Zaki, L. I.; Kappenstein, C.; Géron, C., *Phys. Chem. Chem. Phys.* **2003**, *5*, 1708.

[21] Shinjoh, H.; Tanabe, T.; Sobukawa, H.; Sugiura, M., *Top. Catal.* **2001**, *16/17*, 95.

[22] Shinjoh, H.; Isomura, N.; Sobukawa, H.; Sugiura, M., *Stud. Surf. Sci. Catal.* **1998**, *116*, 83.

[23] Hopstaken, M. J. P.; Niemantsverdriet, J. W., *J. Chem. Phys.* **2000**, *113*, 5457.

[24] Bagot, P. A. J., *Mat. Sci. Techn.* **2004**, *20*, 679.

[25] Newton, M.A.; Dent, A. J.; Fiddy, S. G.; Jyoti, B.; Evans, J., *J. Mat. Sci.* **2007**, *42*, 3288.

[26] Araya, P.; Gracia, F.; Cortés, J.; Wolf, E. E., *Appl. Catal. B: Environ.* **2002**, *38*, 77.

[27] Haber, J.; Nattich, M.; Machej, T., *Appl. Catal. B: Environ.* **2008**, *77*, 278.

[28] van Zon, J. B. A. D.; Koningsberger, D. C.; van't Blik, H. F. J.; Sayers, D. E., J. Chem. Phys. **1985**, *82*, 5742.

[29] Gloor, A. P.; Prins, R., *J. Phys. Chem.* **1994**, *98*, 9865.

[30] Granger, P.; Praliaud, H.; Billy, J.; Leclercq, L.; Leclercq, G., *Surf. Interface Anal.* **2002**, *34*, 92.

[31] Li, G.; Larsen, S.C; Grassian, V. H., *J. Mol. Catal. A: Chem.* **2005**, *227*, 25.

[32] Chao, C.-C.; Lunsford, J. H., *J. Am. Chem. Soc.* **1971**, *93*, 71.

[33] Bennici, S.; Gervasini, *A*., *Appl. Catal. B: Environ.* **2006**, *62*, 336.

[34] Hadjiivanov, K. I., *Catal. Rev.-Sci. Eng.* **2000**, *42*, 71.

[35] Iizuka, T.; Lunsford, J. H., *J. Mol. Catal.* **1980**, *8*, 391.

[36] Katoh, M.; Yamazaki, T.; Kamijo, H.; Ozawa, S., *Zeolites* **1995**, *15*, 591.

[37] Szanyi, J.; Kwak, J. H.; Moline, R. A.; Peden, C. H. F., *Phys. Chem. Chem. Phys.* **2003**, *5*, 4045.

[38] Goodman, A. L.; Underwood, G. M.; Grassian, V. H. J., *Phys. Chem. A* **1999**, *103*, 7217.

[39] Li, G., *FT-IR studies of zeolite materials: Characterization and environmental applications*, PhD Thesis in Chemistry from the University of Iowa; May **2005**.

[40] Song, W.; Li, G.; Grassian, V. H.; Larsen, S. C., *Environ. Sci. Technol.* **2005**, *39*, 1214.

[41] Li, G.; Larsen, S.C; Grassian, V. H., *Catal. Lett.* **2005**, *103*, 23.

[42] Sedlmair, C.; Gil.; B.; Seshan, K.; Jentys, A.; Lercher, J. A., *Phys. Chem. Chem. Phys.* **2003**, *5*, 1897.

[43] Srinivas, G.; Chuang, S. S. C.; Debnath, S., *J. Catal.* **1994**, *148*, 748.

[44] Chafik, T.; Kondarides, D. I.; Verykios, X. E., *J. Catal.* **2000**, *190*, 446.

[45] Newton, M.A.; Dent, A. J.; Diaz-Moreno, S.; Fiddy, S. G.; Evans, J., *Angew. Chem. Int. Ed.* **2002**, *41*, 2587.

[46] Almusaiteer, K. A.; Chuang, S. S. C., *J. Phys. Chem. B* **2000**, *104*, 2265.

[47] Dujardin, C.; Mamede, A.-S.; Payen, E.; Sombret, B.; Huvenne, J.P.; Granger, P., *Top. Catal.* **2004**, *30/31*, 347.

[48] Mulukutla, R. S.; Shido, T.; Asakura, K.; Kogure, T.; Iwasawa, Y., *Appl. Catal. A: Gen.* **2002**, *228*, 305.

[49] Shimokawabe, M.; Umeda, N., *Chem. Lett.* **2004**, *33*, 534.

[50] Newton, M. A.; Dent, A. J.; Fiddy, S. G.; Jyoti, B.; Evans, J., *Phys. Chem. Chem. Phys.* **2007**, *9*, 246.

[51] Hecker, W. C.; Bell, A. T., *J. Catal.* **1983**, *84*, 200.

[52] Djéga-Mariadassou, G.; Fajardie, F.; Tempère, J.-F.; Manoli, J.-M.; Touret, O.; Blanchard, G., *J. Mol. Catal. A: Chem.* **2000**, *161*, 179.

[53] Wallace, W. T.; Cai, Y.; Chen, M. S.; Goodman, D. W., *J. Phys. Chem. B* **2006**, *110*, 6245.

[54] Gonzalez, S.; Sousa, C.; Illas, F., *J. Phys. Chem. B* **2005**, *109*, 4654.

[55] Dent, A. J.; Evans, J.; Fiddy, S. G.; Jyoti, B.; Newton, M. A.; Tromp, M., *Angew. Chem. Int. Ed.* **2007**, *46*, 5356.

[56] Mergler, Y. J.; Ramsaransing, D. R. G.; Nieuwenhuys, B. E., *Rec. Trav. Chim. Pays-Bas* **1994**, *113*, 431.

[57] Miessner, H.; Burkhard, I.; Gutschick, D., *J. Chem. Soc., Faraday Trans.* **1990**, *86*, 2329.

[58] Ivanova, E.; Hadjiivanov, K., *Phys. Chem. Chem. Phys.* **2003**, *5*, 655.

[59] Miessner, H.; Burkhard, I.; Gutschick, D.; Zecchina, A.; Morterra, C.; Spoto, G., *J. Chem. Soc., Faraday Trans.* **1990**, *86*, 2321.

[60] Campbell, T.; Dent, A. J.; Diaz-Moreno, S.; Evans, J.; Fiddy, S. G.; Newton, M. A.; Turin, S., *Chem. Commun.* **2002**, 304.

[61] Berkó, A.; Solymosi, F., *J. Catal.* **1999**, *183*, 91.

[62] Solymosi, F.; Bánsági, T.; Novák, E., *J. Catal.* **1988**, *112*, 183.

[63] Miessner, H.; Burkhardt, I.; Gutschick, D.; Zecchina, A.; Morterra, C.; Spoto, G., *J. Chem. Soc., Faraday Trans. 1* **1989**, *85*, 2113.

[64] Marcus, Y. *Ion Properties*; Marcel Dekker: New York, Basel, Hong Kong **1997**, p 193.

[65] Zhdanov, V.P.; Kasemo, B., *Surf. Sci. Rep.* **1997**, *29*, 31.

[66] Permana, H.; Simon Ng, K. Y.; Peden, C. H. F.; Schmieg, S. J.; Lambert, D. K.; Belton, D. N., *J. Catal.* **1996**, *164*, 194.

[67] Newton, M. A.; Jyoti, B.; Dent, A. J.; Fiddy, S. G.; Evans, J., *Chem. Comm.* **2004**, 2382.

Chapter 7

Concluding remarks and perspectives

1 Concluding remarks

The ***goal*** of this PhD thesis was to systematically study the fundamental issue of metal-support interactions for Pt- and Rh-based catalysts. Therefore, ***model catalysts*** made of well-defined Pt or Rh nanoparticles dispersed on various oxide supports, differing in their chemical composition and pore architecture, were prepared. The composition effect was mainly examined with a series of zeolite Y supports containing different alkali or alkaline earth metal ions and further confirmed with promoted macroporous SiO_2. The impact of the support porosity was investigated thanks to all silica supports varying by their pore size. All samples were first thoroughly ***characterised*** for their precious metal and promoter loadings, catalyst particle size and the integrity of their support. The electronic properties of the supported Pt and Rh nanoparticles were then studied by IR spectroscopy and, for Pt, further confirmed by AXAFS, a direct measurement technique of the electron density. Finally, the impact of the support composition on the catalytic activity of Pt and Rh was evaluated for two simple reactions relevant to the automotive exhaust gas converters: the CO oxidation in excess of oxygen and the NO reduction by CO in stoichiometric conditions. The complete experimental plan, including tested samples and used techniques, is summarised in Table 7.1.

The ***main results*** of this study are compiled in Tables 7.2 and 7.3. For all catalyst materials, the IR spectra showed clear differences that could be directly related to properties of the promoting cations. The NO or CO probe molecules were adsorbed on the Pt or Rh surface in linear or bridge positions. In the case of Rh, hiding the linear contribution, *gem*-dicarbonyl and dinitrosyl species were also observed. It was found that the band maximum of all the linearly metal-coordinated species were more red-shifted compared to that of the gas-phase probe molecule when the cation radius-to-charge ratio was increasing. This trend was the most pronounced for CO adsorbed on Pt supported on the series of zeolite materials, then for CO adsorbed on Pt supported on silica, followed by NO adsorbed on Rh and finally, the least pronounced for CO adsorbed on Rh supported on zeolites. These shifts in linear band position, including *gem*-dicarbonyl and dinitrosyl species, are most probably due to the interaction of the oxygen-end of the adsorbed molecule with the cation promoters. They are therefore influenced by the porosity of the support leading to smaller shifts when the distance to the promoter increases, *i.e.* for

Table 7.1: Summary of the studies performed in this PhD (for details, see Chapters 2 to 6).

Study the effect of the	Support	Metal	Characterisation techniques								Catalytic reaction	
			XRF	ICP-AES	HR-TEM	XRD	BET	EXAFS	IR	AXAFS	$CO + O_2$	CO + NO
Support composition	Zeolite Y ion-exchanged with: • H^+, Na^+, K^+, Rb^+, Cs^+, Mg^{2+}, Ca^{2+}, Sr^{2+}, and Ba^{2+}	Pt	✓		✓	✓	✓	✓	CO	✓	✓	
	• H^+, Na^+, (K^+), Rb^+, Cs^+, Mg^{2+}, Ca^{2+}, Sr^{2+}, and Ba^{2+}	Rh		✓	✓	✓		✓	CO NO		✓	✓
	SiO_2 impregnated with: Na^+, Cs^+, Mg^{2+}, and Ba^{2+}	Pt	✓		✓			✓	CO	✓	✓	
Support porosity	ITQ-1 (microporous)	Pt	✓		✓		✓	✓	CO	✓		
	MCM-41, MCM-48, and SBA-15 (mesoporous)	Pt	✓		✓		✓	✓	CO	✓		
	Amorphous SiO_2 (macroporous)	Pt	✓		✓		✓	✓	CO	✓		

Table 7.2: Relation between IR and catalytic activity results and promoter properties on supported Pt and Rh catalysts (for details, see Chapters 2, 3, 5 and 6).

Metal	IR observation		Cation property		e^- density	Activity
Pt	CO linear band red shift	↗↗↗	Radius:Charge	↗	-	-
	CO linear-to-bridge band intensity ratio	↗	Lewis acidity	↘	↗	$CO + O_2$ ↗
Rh	CO carbonyls band red shift	↗	Radius:Charge	↗	-	-
	CO bridge bands relative intensity	↗↗	Lewis acidity	↘	↗	$CO + O_2$ ↗
	NO (di)nitrosyls band red shift	↗↗	Radius:Charge	↗	-	-
	NO bridge band relative intensity	↗↗	Lewis acidity	↘	↗	CO + NO ?

↗ and ↘ are increasing and decreasing trends, respectively

↗ to ↗↗↗ indicate a moderately to strongly increasing trend

? means that the impact was not clear

smaller pore curvatures. But these shifts are also a function of the type of probe molecule and the amount of d-electrons of the metal on which the probe molecules are adsorbed. The latter will indeed influence the back donation to the π orbital of the adsorbed CO or NO. In agreement with this statement, molecules adsorbed on Pt (with 9 d-electrons) exhibit larger band shifts than when bonded to Rh (with 8 d-electrons). Additionally, the band shifts for dinitrosyls, which are bonded to Rh^+, are smaller than for linearly bonded NO on Rh^0. Finally, the shifts of the Rh dinitrosyls are larger than the ones of the Rh *gem*-dicarbonyls, which can be explained by the presence of one more electron in NO. Besides the band shifts, the relative intensity of the bridge bonded probe molecule as referred to the total absorbance of the metal-bonded CO or NO molecules was decreasing for increasing Lewis acidity of the promoting cation, as expressed by the Kamlet-Taft parameter α. A decreasing α results in an increasing electron charge on the framework oxygen atoms of the support and therefore in an increasing electron charge on the supported precious metal nanoparticles. When the electron density of the Pt or Rh is increased, it tends to donate back more electrons to the adsorbed NO or CO molecule. The differences in the Rh series are more pronounced. This disparity may be caused by the intervention of two parameters in the case of Rh, *i.e.*, electron density on the metal

and acidity of the support, instead of one in the case of Pt, *i.e.*, electron density. Furthermore, for the Pt samples, it was found that the CO coverage increased with increasing electron density on the Pt nanoparticles. A slightly higher desorption rate during CO IR TPD was observed for the micro- and mesoporous supports, probably due to larger non-bonding electrostatic interactions between CO and the pore walls. But no systematic shift from linear to bridge bonded CO could be observed upon a decrease of the radius of curvature, which would indicate an increasing electron charge on the supported Pt nanoparticles. So, pore size effects are very small.

Finally, as highlighted in Table 7.2, it was possible to correlate the above observations with the activity of the Pt or Rh catalysts for the CO oxidation reaction in excess of oxygen, *i.e*. the $T_{50\%}$ for CO oxidation decreases with electron density on the precious metal nanoparticles. Concerning the stoichiometric NO reduction by CO on Rh, no clear trend could be extracted. We assume that this difference is due to other important factors affecting the Rh catalytic activity, such as its oxidation state and its particle size.

As shown in this work, IR spectroscopy is a powerful method to characterise the electron density of supported nanoparticles. It, however, presents at least one disadvantage as it is an indirect measurement method requiring a probe molecule like CO or NO. Consequently, it cannot be used for measurements in realistic reaction conditions. Therefore, AXAFS, a novel spectroscopic method has been explored for directly probing the electronic properties of supported Pt nanoparticles in porous oxides. Table 7.3 demonstrates that IR and AXAFS measurements both

Table 7.3: Relation between IR, AXAFS and CO oxidation results on supported Pt catalysts (for details, see Chapters 2 to 4).

Technique	Property	Observation	
CO IR	CO linear-to-bridge band intensity ratio	Small	Large
	CO coverage	High	Low
AXAFS	Peak intensity	Low	High
	Peak centroid position	Far from 0	Closer to 0
Catalysis	Activity for the CO oxidation reaction	High	Low
Conclusion	Electronic density of Pt	e^- rich	e^- poor

give information on the electron density of the Pt nanoparticles, which can be directly correlated to their catalytic activity. In other words, as the CO IR linear-to-bridge band intensity ratio increases, so does the AXAFS peak intensity, while the promoting cation is more acidic and the Pt particles become electron poor.

In ***conclusion***, the results of this detailed characterisation study demonstrate that time-resolved IR spectroscopy and AXAFS are useful and complementary tools to unravel electronic properties of supported nanoparticles. AXAFS could even, in principle, be applied to clusters of any atom amenable to the XAFS technique and this under *operando* conditions. IR bridge band relative intensities could be correlated to the Lewis acidity of the promoting cation and to the catalytic activity of the Pt and Rh metals for the CO oxidation reaction in excess of oxygen, more basic cations being recommended. For the stoichiometric NO reduction by CO on Rh, such relationship between electron density and activity was not observed. In general, the support pore curvature effects were limited to some repulsive interactions whereas the support composition effect was large. Finally, the results obtained with the promoted macroporous silica supports as opposed to the zeolite samples demonstrate that results from one support type to another can be transposed for Pt, thus providing further guidelines for the design of improved automotive catalysts. For Rh nanoparticles, such substitution might be more difficult.

2 Perspectives

The conclusions concerning the impact of support composition and porosity were clear for dispersed Pt nanoparticles. The effect of the support on Rh seems to be more complex in view of the scattered data points. In particular, the results of the IR TPD and catalytic activity measurements did not show a clear correlation. There might be several reasons for it. First of all, the exposure of small Rh nanoparticles to CO and NO gives rise to Rh particle disruption and to formation of *gem*-dicarbonyls and dinitrosyls, giving more complex IR spectra than for Pt nanoparticles. Thus, the uncertainty on the data was larger for Rh than for Pt. In this view, a study based on alumina or silica supports might be more appropriate as 2 types of Rh *gem*-dicarbonyls are for instance observed with zeolites, while only one type is seen for alumina.[1] Additionally, the extent of this disruption phenomenon depends on the Rh particle size and can exhibit large variations for small differences in size, especially

for *ca.* 1-nm-wide particles in a NO-containing CO atmosphere.[2] Furthermore, as shown by Figure 7.1, it is not yet clear to which proportion these structural changes are affected by the support composition. It indeed seems that the Rh-Rh coordination number ($N_{Rh\text{-}Rh}$), which is the measure of the particle size, tend to decrease more under CO atmosphere when the support is promoted by more basic cations but these experiments should be repeated with particles of exactly the same size. So, a method allowing a better control of the Rh clusters diameter would be preferable. Finally, Rh can be difficult to get in a reduced state[3] and this state can be modified by NO and CO adsorption at the same time as its structure.[4] The different adsorption sites will form different adsorbed species with varying activities. So, the oxidation state and particle size of Rh as well as the adsorbed species should ideally be measured in *operando* conditions. This point is partially illustrated by Figures 7.2 and 7.3, which respectively show observed differences in adsorbed species and light-off between the first and second catalytic cycles for the CO oxidation in excess of oxygen on Rh/K-Y and Rh/Na-Y samples. During the first run, the Rh/Na-Y catalyst lights off at a much lower temperature than during the second catalytic cycle (Figure 7.3). In the case of Rh/K-Y, the first light-off curve (Figure 7.2 c) is similar to

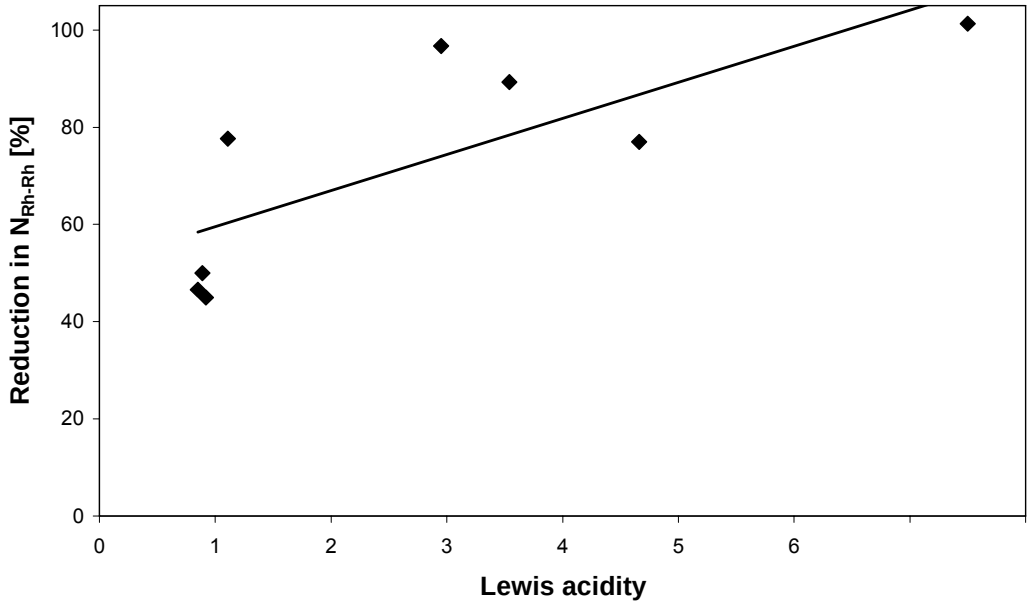

Figure 7.1: Reduction in the Rh-Rh coordination number obtained upon exposure of the samples to 10 % NO in He at room temperature *versus* Lewis acidity of the cation promoting the zeolite Y support. The reference Rh-Rh coordination numbers were measured on the reduced samples under vacuum (*cf.* Chapter 5).

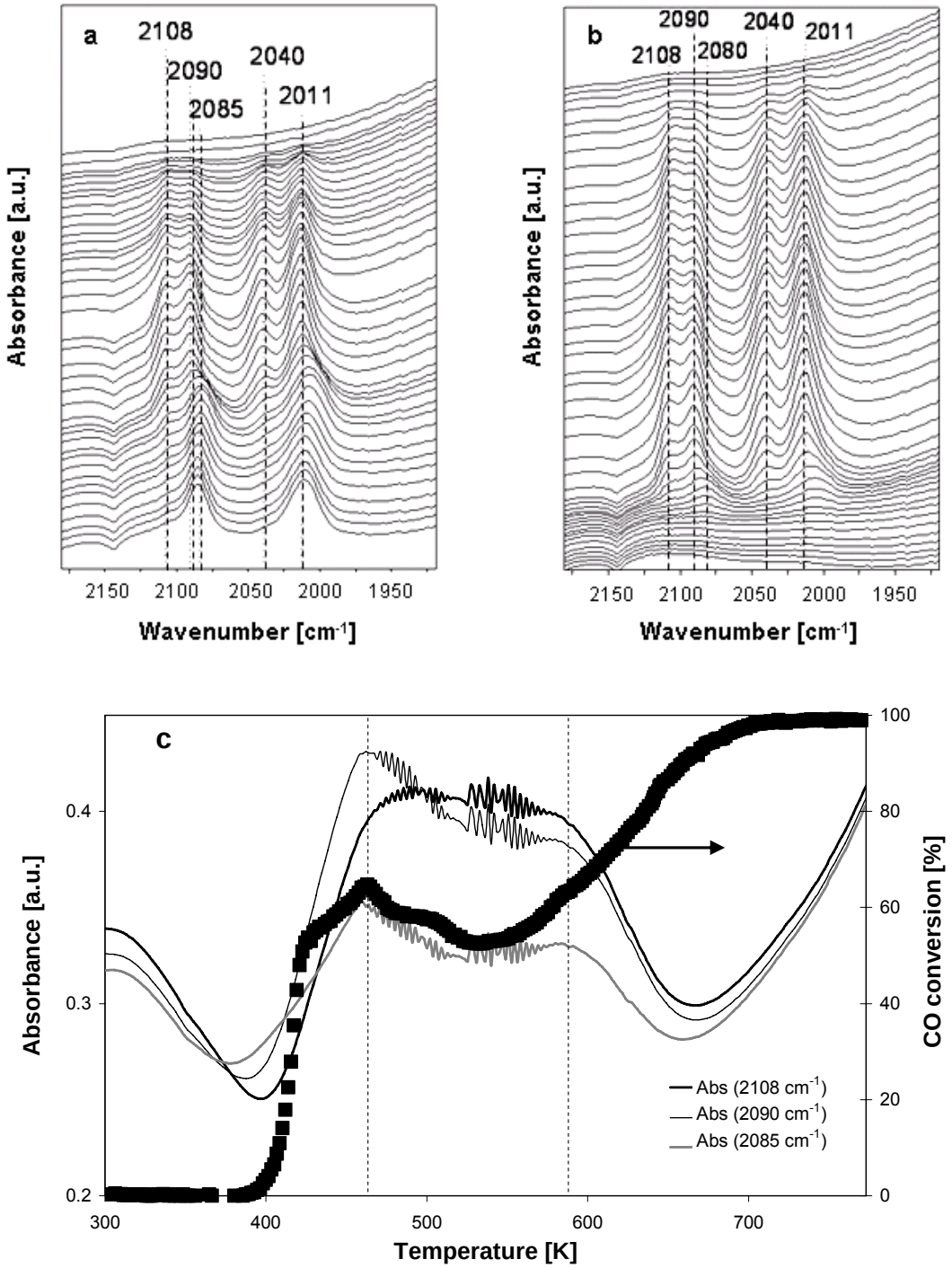

Figure 7.2: DRIFTS spectra recorded during the (a) 1st and (b) 2nd cycles of the CO oxidation light-off in excess of oxygen on Rh/K-Y and, (c) absorbance profiles of the $Rh^{+}(CO)_2$ and gas phase CO IR bands corresponding to (a) with the associated CO conversion as a function of temperature.

the one of Rh-NaY and the decrease in activity above *ca.* 460 K seems to correspond to the disappearance of, for instance, the Rh^0-CO species at 2085 cm^{-1},[1] which cannot be separated from the band at 2090 cm^{-1} with an absorbance profile

plot (Figure 7.2 a and c). This more active species is not present at the start of the second cycle (Figure 7.2 b). At this point a more in depth multivariate curve resolution (MCR) analysis would be useful.[5]

In conclusion, further work on the effect of the support composition on Rh nanoparticles should be carried out in *operando* conditions with a starting support giving less complex IR spectra and with Rh particles of precise size. Moreover, a last point would merit more attention: the suppression of the N_2O formation observed upon light-off of the NO reduction by CO reaction. This gas should indeed be avoided as it is a major greenhouse gas.

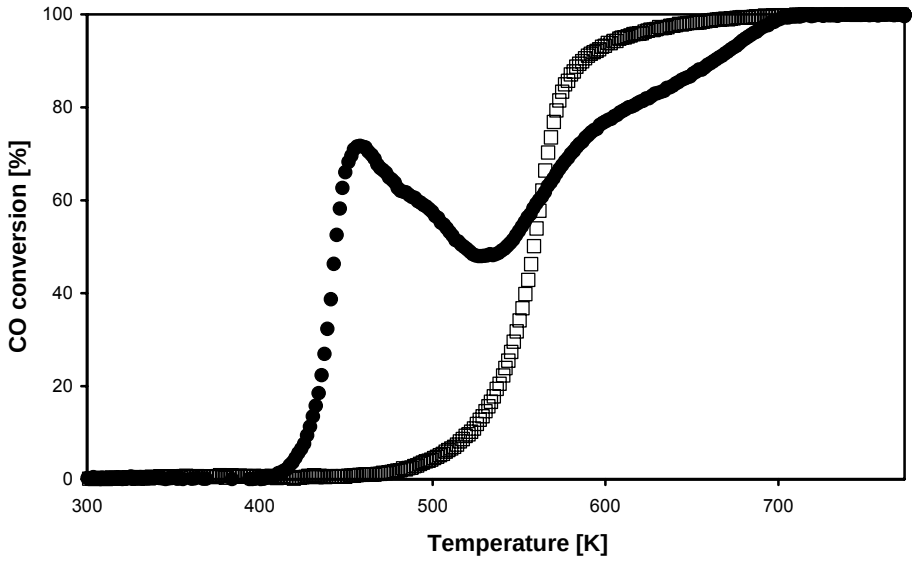

Figure 7.3: Light-off curves for the CO oxidation in excess of oxygen in the (●) 1st and 2nd (□) catalytic cycle on Rh/Na-Y.

References

[1] Primet, M., *J. Chem. Soc., Faraday Trans. 1* **1978**, *74*, 2570.

[2] Newton, M.A.; Dent, A. J.; Fiddy, S. G.; Jyoti, B.; Evans, J., *J. Mat. Sci.* **2007**, *42*, 3288.

[3] Manuel, I.; Chaubet, J.; Thomas, C.; Colas, H.; Matthess, N.; Djéga-Mariadassou, G., *J. Catal.* **2004**, *224*, 269.

[4] Almusaiteer, K. A.; Chuang, S. S. C., *J. Phys. Chem. B* **2000**, *104*, 2265.

[5] Tauler, R.; de Juan, A. *Multivariate curve resolution homepage*: www.ub.edu/mcr/welcome.html.

Samenvatting

De katalyse van auto-uitlaatgassen is een goed ontwikkelde technologie, die alleen nog met nieuwe wetenschappelijke inzichten kan worden verbeterd. Ideeën leidend tot deze technische voortgangen kunnen verkregen worden door te werken met modelsystemen. Een dergelijke aanpak beperkt het aantal mogelijke parameters dat invloed heeft op de resultaten, het vereenvoudigt de interpretatie van die resultaten en maakt de extrapolatie naar complexere systemen mogelijk. Het doel van het onderzoek, beschreven in dit proefschrift, was om een beter inzicht te krijgen in de metaal-drager interacties van Pt- en Rh-gebaseerde uitlaatgaskatalysatoren door gebruik te maken van modelkatalysatoren met goed gedefinieerde Pt en Rh nanodeeltjes afgezet op dragermaterialen met verschillende chemische samenstelling en poriestructuur. De elektronische eigenschappen van deze gedragen Pt en Rh nanopartikels zijn met twee technieken onderzocht: Infrarood spectroscopie (IR) in combinatie met CO of NO als probemoleculen en X-stralen Absorptie Fijn Structuur spectroscopie (XAFS). Daarnaast is de katalytische werking van de materialen met twee, voor de auto-uitlaatgaszuivering relevante reacties, de CO oxidatie en de NO reductie door CO, geëvalueerd. Door het combineren van alle experimentele resultaten was het mogelijk om relaties te leggen tussen de chemische samenstelling van de drager, de elektronendichtheid van de gedragen Pt en Rh nanodeeltjes alsmede hun katalytische activiteit.

Hoofdstuk 2 beschrijft een systematisch onderzoek van de Pt-drager interacties op basis van een reeks van zeoliet-Y dragers met verschillende monovalente (H^+, Na^+, K^+, Rb^+, en Cs^+) en divalente (Mg^{2+}, Ca^{2+}, Sr^{2+}, en Ba^{2+}) kationen. Daartoe zijn Pt nanopartikels, afgezet in de superkooi van zeoliet-Y, bestudeerd met CO IR spectroscopie op 323 K en tijdens temperatuur geprogrammeerde desorptie (TPD). De trends in de verschuiving naar lager golfgetal van de Pt-CO IR absorptiebanden en in de verandering van de intensiteitsverhouding van de lineaire versus de gebrugde Pt-CO band konden gerelateerd worden aan de intrinsieke eigenschappen van de promotor kationen, zoals de Lewis zuurheid. Bovendien was het mogelijk

om, voor de verschillende materialen, de veranderingen in het CO IR absorptiepatroon te koppelen aan de temperatuur waarop de katalysator actief werd in de oxidatie van CO.

De in Hoofdstuk 2 verkregen inzichten zijn in **Hoofdstuk 3** verder uitgebreid met onderzoek aan het effect van de poriegrootte van het dragermateriaal op de elektronische eigenschappen van de gedragen Pt nanodeeltjes. Daarvoor zijn geheel uit silica bestaande dragers met allerlei poriegrootten onderzocht: ITQ-1 als voorbeeld van een microporeus materiaal, Si-MCM-41, Si-MCM-48 en Si-SBA-15 als mesoporeuze materialen, en een amorf SiO_2 als macroporeuze drager. Tevens is het, in Hoofdstuk 2 voor de zeolite Y reeks geconstateerde promotor effect bestudeerd aan 4 Pt/SiO_2 katalysatoren, geïmpregneerd met respectievelijk Na^+, Cs^+, Mg^{2+} en Ba^{2+} als promotor element. Zowel de poriegrootte als de chemische samenstelling van de katalysatoren kon met de katalytische activiteit van de monsters worden gecorreleerd. De invloed van de promotor-elementen blijkt voor zeoliet-Y en de SiO_2 dragers vergelijkbaar.

Uit de resultaten die verkregen werden met het onderzoek beschreven in de Hoofdstukken 2 en 3 kan worden afgeleid dat IR spectroscopie een krachtige methode is om de elektronendensiteit van gedragen Pt nanopartikels te bepalen. Deze techniek heeft echter als nadeel dat het een indirecte meetmethode is die gebruik maakt van probe-molecule, zoals CO of NO. IR spectroscopie is daarom niet bruikbaar om de elektronische eigenschappen van de gedragen Pt nanopartikels onder realistische reactiecondities te meten. Daarom is, in **Hoofdstuk 4**, de bruikbaarheid van een nieuwe spectroscopische techniek onderzocht om de elektronische eigenschappen van Pt nanopartikels in poreuze oxiden op een directe manier te bepalen. De voorgestelde methode is gebaseerd op Atomische X-stralen Absorptie Fijn Structuur spectroscopie (AXAFS) en werd op de bovengenoemde 14 gedragen Pt katalysatoren toegepast. De intensiteit van het AXAFS signaal kon direct gecorreleerd worden met de, in Hoofdstukkken 2 en 3 bepaalde intensiteitverhoudingen van de lineaire versus de gebrugde CO IR absorptiebanden. Aangezien deze AXAFS methode geen probe molecule vereist, biedt het de mogelijkheid om de elektronische eigenschappen van metaal-nanopartikels te bepalen onder reële reactieomstandigheden en als functie van de reactietijd.

Geïnspireerd door de veelbelovende resultaten uit Hoofdstuk 2 werd in **Hoofdstuk 5** de wetenschappelijke aanpak uitgebreid tot Rh nanopartikels

gedragen op een reeks van zeoliet-Y dragers met dezelfde alkali en aardalkali elementen als promotoren. Daartoe werd een ionenuitwisselingsstap uitgevoerd aan een NaY zeoliet als startmateriaal met H^+-, K^+-, Rb^+-, Cs^+-, Mg^{2+}-, Ca^{2+}-, Sr^{2+}- of Ba^{2+}-ion bevattende oplossingen. Vervolgens werden goed gedefinïeerde Rh deeltjes met een gemiddelde diameter tussen 1 nm en 1.5 nm afgezet op het drageroppervlak. Net als voor de Pt gedragen katalysatoren werd de invloed van de chemische samenstelling van het dragermateriaal op de CO adsorptie eigenschappen van Rh bestudeerd met behulp van IR spectroscopie. Deze gegevens werden daarna gecorreleerd met de CO oxidatie-activiteit van de gedragen Rh nanodeeltjes.

Aangezien Rh een heel belangrijke katalysator is voor de NO reductie-reactie in de zuivering van auto-uitlaatgassen werd de lijn van het in Hoofdstuk 5 uitgevoerde onderzoek doorgetrokken naar de studie van de reductie van NO met Rh/zeoliet-Y modelkatalysatoren. Analoog aan het eerdere gebruik van CO als probe molecule werd in dit onderzoek NO in combinatie met IR spectroscopie toegepast om het effect van de promotoren op de elektronische eigenschappen van Rh in kaart te brengen. De resultaten hiervan zijn weergegeven in **Hoofdstuk 6.** De NO-IR absorptiebanden bleken dezelfde trends te vertonen in bandverschuiving en in verandering van intensiteitsverhouding lineair/gebrugd, als voor Pt-CO en Rh-CO. De invloed van de promotoren op de katalytische activiteit van gedragen Rh nanopartikels blijkt echter veel complexer te zijn.

Tenslotte werden, in **Hoofdstuk 7**, algemene conclusies getrokken uit het gehele onderzoekswerk. Allereerst werd bewezen dat AXAFS en IR spectroscopie, in combinatie met een probe molecule zoals CO en NO, krachtige en complementaire technieken zijn waarmee de elektronendichtheid van gedragen metaal nanodeeltjes kan worden bepaald. Alle onderzochte katalysatormaterialen toonden duidelijk verschillende IR spectra. In deze spectra schuift de positie van de lineair-gebonden NO of CO band meer naar lager golfgetal naarmate de verhouding van de diameter tot de lading van het promotorende kation groter wordt. Die trend is voor Pt op zeolietdragers meer uitgesproken dan voor de Rh katalysatoren. Daarnaast neemt de relatieve intensiteit van de bruggebonden CO of NO moleculen af met toenemende Lewis zuurheid van het promotor-kation, zoals uitgedrukt door de α Kamlet-Taft parameter. Een verlaging van α leidt tot een toename in de elektronenlading van de zuurstofatomen van de dragerstructuur en daarom tot een

toename in de elektronenlading van de gedragen metaal nanopartikels. Als de elektronendichtheid op Pt of Rh stijgt, neemt ook de neiging toe om meer elektronen aan de geadsorbeerde NO of CO moleculen terug te geven. Deze zogenaamde 'back donation' trend is voor gedragen Rh katalysatoren het best zichtbaar. Bij gedragen Pt-gebaseerde katalysatoren stijgt de CO bedekkingsgraad met toenemende elektronendichtheid van de Pt nanopartikels. Verder is aangetoond dat het effect van de poriegrootte van het dragermateriaal beperkt is. Een belangrijk resultaat is dat er een relatie kon worden gelegd tussen de werking van Pt of Rh gedragen katalysatoren, hun activiteit in de CO oxidatie, en de elektronendichtheid van de metaal nanopartikels. Een dergelijke duidelijke correlatie kon niet worden vastgesteld voor de stoichiometrische reactie tussen NO en CO. Dit verschil kan worden toegeschreven aan veranderingen in de oxidatiegraad en de deeltjesgrootte van de Rh partikels bij hogere temperatuur.

Annex

List of acronyms, special units and chemicals

ABS	Anti-lock Braking System
ACEA	European Automobile Manufacturers Association
AES	Atomic Emission Spectroscopy
Al_2O_3	Alumina or aluminium oxide
$Al_2O_3.TiO_2$	Aluminium titanate
AXAFS	Atomic X-ray Absorption Fine Structure spectroscopy
A/F	Air/Fuel ratio
$BaCl_2$	Barium chloride
BaO	Barium oxide
BET	Brunauer, Emmett and Teller
$CaCl_2$	Calcium chloride
CAFE	Clean Air For Europe
CDPF	Catalysed Diesel Particulate Filter
CeO_2	Ceria or cerium oxide
CH_4	Methane
CNG	Compressed Natural Gas
cpsi	Cells per square inch
CO	Carbon monoxide
CO_2	Carbon dioxide
CR-DPF	Continuous Regeneration Diesel Particulate Filter
CsCl	Caesium chloride
CZ	CeO_2-ZrO_2 or ceria-zirconia solid solution
DEE	Double Electron Excitation
DOC	Diesel Oxidation Catalyst
DPF	Diesel Particulate Filter

DPNR	Diesel Particulate-NO_x Reduction
DRIFTS	Diffuse Reflectance Infrared Fourier Transform Spectroscopy
EEA	European Environment Agency
EEV	Enhanced Environmentally friendly Vehicles
EGR	Exhaust Gas Re-circulation
EU	European Union
EXAFS	Extended X-ray Absorption Fine Structure
FT	Fourier Transform
GHG	Greenhouse Gas
HC	Hydrocarbons
HCl	Hydrogen chloride
HC-SCR	Selective Catalytic Reduction by HC
H_2	Molecular hydrogen
H_2S	Hydrogen sulphide
HBW	Half Band Width
HRTEM	High-Resolution Transmission Electron Microscopy
ICP	Inductively-Coupled Plasma
IR	Infrared spectroscopy
KCl	Potassium chloride
La_2O_3	Lanthanum oxide
LNT	Lean NO_x-Trapping
MCR	Multivariate Curve Resolution
$MgCl_2$	Magnesium chloride
N_2	Molecular nitrogen
NaCl	Sodium chloride
NH_3	Ammonia
NH_3-SCR	Selective Catalytic Reduction by NH_3
NO	Nitric oxide or nitrogen monoxide
NO_x	Nitrogen oxides
NO_2	Nitrogen dioxide
NSR	NO_x Storage-Reduction
N_2O	Nitrous oxide
OBD	On-Board Diagnostic

OSC	Oxygen Storage Capacity
PdO	Palladium oxide
PGM	Platinum Group Metals
PM	Particulate Matter
$PM_{2.5}$	PM with an aerodynamic diameter < 2.5 µm
PM_{10}	PM with an aerodynamic diameter < 10 µm
RbCl	Rubidium chloride
Rh_2O_3	Rhodium oxide
SEM	Scanning Electron Microscope
SiC	Silicon carbide
SO_2	Sulphur dioxide
SO_3	Sulphur trioxide
SO_x	Sulphur oxides
$SrCl_2$	Strontium chloride
SSA	Specific Surface Area
T_{50} or $T_{50\%}$	Temperature at which 50 % conversion is reached for a given reactant
TEM	Transmission Electron Microscopy
THC	Total Hydrocarbons
TiO_2	Titania or titanium oxide
TPD	Temperature Programmed Desorption
TWC	Three-Way Catalyst
VOC	Volatile Organic Compounds
V_2O_5	Vanadia or vanadium oxide
WO_3	Tungsten oxide
XAFS	X-ray Absorption Fine Structure
XRD	X-Ray Diffraction
XRF	X-Ray Fluorescence
Y_2O_3	Yttria or yttrium oxide
ZrO_2	Zirconia or zirconium oxide
$2MgO.2Al_2O_3.5SiO_2$	Cordierite

Acknowledgements

Looking back to this very special and rich-in-learning experience, I find out that I have to thank many people who have been involved at different levels during this PhD work. It was a very challenging project because of my particular position as a student and as a project leader. So, without support, I would never have succeeded in obtaining this PhD degree.

Bert, aan deze onderneming zou ik nooit hebben durven denken had je het zelf niet aan mij voorgesteld. Achteraf gezien ben ik blij dat ik jouw voorstel aanvaard heb. Ik ben me er ook bewust van dat ik die kans geen tweede keer had kunnen krijgen en daarvoor ben ik jou zeer erkentelijk. Daarenboven wil ik jou erg bedanken voor je doorlopende steun, voor je begrip en voor het in mij gestelde vertrouwen.

Matsumoto san, I would like to thank you for having given me this great opportunity within Toyota, but also for your enthusiasm and continuous support. I really enjoyed the scientific discussions we had and I am happy that I now exactly understand the purpose of my work.

Tom, jij bent er altijd voor mij geweest. Ik ga de levendige discussies over infrarode spectra die wij samen gehad hebben nooit vergeten. Dankzij jou weet ik nu wat een samenwerking in onderzoek kan zijn. Jouw begrip, respect en relativeringkracht zijn voor mij een enorme steun geweest.

I am also thankful to the Toyota colleagues with whom we build a real global research group on exhaust catalysis: Hirata san, Ikeda san, Hara san, Takahashi san, Shinjoh san, Nagai san, Tanabe san… Thank you!

Fouad, Ana, Andrew and Ad, thanks a lot for the support you gave in performing part of the experimental work. It has been a very rich experience to work with people having very different approaches and backgrounds.

For the experimental work, I am additionally grateful to Patricia Kooyman (Delft University of Technology) and Cor van der Spek (Utrecht University) for performing HRTEM measurements, to Diek Koningsberger (Utrecht University) for helping me with the EXAFS as well as AXAFS analysis, to Ad Mens (Utrecht University) for carrying out the N_2 sorption measurements, to Pascal Van der Voort (Gent University, Belgium) for assistance in preparing the Si-MCM-41, Si-MCM-48 and Si-SBA-15 materials, Hermenigildo Garcia (Universidad Politecnica de Valencia, Spain) for providing the ITQ-1 material and to Nobuyuki Takagi (Toyota Motor Corporation, Japan) for the ICP-AES measurements.

Dymph en Monique, bedankt voor jullie vriendelijkheid en de administratieve hulp.

Thanks a lot to my colleagues from the department of Inorganic Chemistry and Catalyst at Utrecht University and from the Advanced Technology Division at Toyota Motor Europe nv/sa. You made my time in Utrecht and in Zaventem less lonely.

Finalement, mes dernières pensées vont à ma famille et à mes amis. Chers parents, je vous remercie pour l'environnement dans lequel vous m'avez élevée. Je suis sûre que cet univers rempli de livres, de voyages et de débrouillardise a largement contribué à ma curiosité, mon esprit critique et ma ténacité. Chers sœurs, cousins, oncles, tantes et grand-père, merci pour les belles réunions au cours desquelles je pouvais me ressourcer. Chers amis, je vous suis infiniment reconnaissante pour les bons moments passés ensembles, pour les «exploits» sportifs partagés et pour la tendresse que vous m'avez témoignée. Sans vous, je n'aurais pas pu m'évader et trouver la chaleur et l'équilibre dont j'avais besoin.

Muriel Lepage

Curriculum vitae

Muriel Lepage was born in Namur (Belgium) on May 13th, 1975. In 1998, she obtained, from the University of Liège (Belgium), a master degree in Chemical Engineering with great distinction. Her research project was focussing on the hydrothermal aging of epoxy resins. During her studies, she has also been a laboratory assistant for the classes on thermodynamics applied to thermal machines in 1997 and she worked for an American water bottling company on quality control in the period 1996-1997. From 1999 to mid 2001, she has been a project engineer at IMEC, a research and development centre in microelectronics located in Leuven (Belgium). She was developing plasma etching processes for dielectric materials, such as silicon dioxide, SiOC and polymeric isolators. She then moved to Toyota Motor Europe nv/sa in Zaventem (Belgium), where she was initially responsible for the system implementation and data collection related to the End of Live Vehicle Directive.

From 2005 until now, she has been working as a Senior Engineer responsible for the follow-up of research collaborations with European Universities on automotive exhaust catalysis and for the review of new technologies in Europe. In August 2005, she additionally joined the department of Inorganic Chemistry and Catalysis at the University of Utrecht as a PhD student under the supervision of prof. dr. ir. B. M. Weckhuysen.

List of publications

Visser, T.; Nijhuis, T. A.; van der Eerden, A. M. J.; Ji, Y.; Ikeda, Y.; Lepage, M.; Weckhuysen, B. M., *Promotion effects in the oxidation of CO over zeolite-supported Pt nanoparticles*, Stud. Surf. Sci. Catal. **2005**, *158*, 1239.

van der Eerden, A. M. J.; Visser, T.; Nijhuis, T. A.; Ikeda, Y.; Lepage, M.; Koningsberger, D. C.; Weckhuysen, B. M., *Atomic XAFS as a Tool to Probe the Electronic Properties of Supported Noble Metal Nanoclusters*, J. Am. Chem. Soc. **2005**, *127*, 3272.

Visser, T.; Nijhuis, T. A.; van der Eerden, A. M. J.; Jenken, K.; Ji, Y.; Bras, W.; Nikitenko, S.; Ikeda, Y.; Lepage, M.; Weckhuysen, B. M., *Promotion Effects in the Oxidation of CO over Zeolite-Supported Pt Nanoparticles*, J. Phys. Chem. B **2005**, *109*, 3822.

Lepage, M.; Visser, T.; Soulimani, F.; Beale, A. M.; Iglesias-Juez, A.; van der Eerden, A. M. J.; Weckhuysen, B. M., *Promotion Effects in the Oxidation of CO over Zeolite-Supported Rh Nanoparticles*, J. Phys. Chem. **2008**, *112*, 9394.

Lepage, M.; Visser, T.; van der Eerden, A. M. J.; Soulimani, F.; Weckhuysen, B. M., *Pore curvature and support composition effects on the electronic properties of supported Pt catalysts: An infrared spectroscopy study with CO as probe molecule*, Vibr. Spectrosc. **2008**, *8*, 92.

Lepage, M.; Visser, T.; Soulimani, F.; Iglesias-Juez, A.; Weckhuysen, B. M., *IR spectroscopic study of the effect of cation promoters in the reduction of NO by CO over zeolite-supported Rh catalysts*, submitted to Vibr. Spectrosc.

Lepage, M.; Matsumoto, S.; Visser, T.; Weckhuysen, B. M., *Automotive catalysis: From engine exhaust emissions over current catalyst technology to new scientific challenges*, submitted to ChemCatChem.